UNIVERSIDADE DE LISBOA

INSTITUTO SUPERIOR TÉCNICO

The Effect of Dual Doping in the Thermoelectric Properties of Tetrahedrite

Duarte Nuno Mendonça Costa Moço

Supervisor: Doctor António Cândido Lampreia Pereira Gonçalves

Co-Supervisors: Doctor Luís Filipe da Silva dos Santos

Doctor Elsa Maria Simões Branco Lopes

Thesis approved in public session to obtain the PhD Degree in

Chemistry

Jury final classification: **Pass with Distinction**

2023

TÉCNICO LISBOA

UNIVERSIDADE DE LISBOA

INSTITUTO SUPERIOR TÉCNICO

The Effect of Dual Doping in the Thermoelectric Properties of Tetrahedrite

Duarte Nuno Mendonça Costa Moço

Supervisor: Doctor António Cândido Lampreia Pereira Gonçalves

Co-Supervisors: Doctor Luís Filipe da Silva dos Santos

Doctor Elsa Maria Simões Branco Lopes

Thesis approved in public session to obtain the PhD Degree in

Chemistry

Jury final classification: **Pass with Distinction**

Jury

Chairperson: Doctor Mário Nuno de Matos Sequeira Berberan e Santos, Instituto Superior Técnico, Universidade de Lisboa

Members of the Committee:

Doctor António Cândido Lampreia Pereira Gonçalves, Instituto Superior Técnico, Universidade de Lisboa

Doctor Maria Amélia Martins de Almeida, Instituto Superior Técnico, Universidade de Lisboa

Doctor Andrei Kavaleuski, Laboratório Associado CICECO – Instituto de Materiais de Aveiro, Universidade de Aveiro

Doctor André Miguel Trindade Pereira, Faculdade de Ciências, Universidade do Porto

Funding Institution – FCT: Fundação para a Ciência e a Tecnologia

2023

TÉCNICO LISBOA

I. RESUMO

Os geradores termoelétricos são dispositivos capazes de reconverter calor residual em eletricidade, sendo assim uma potencial fonte de energia verde. Porém, apesar de serem uma fonte de energia confiável para locais remotos e/ou não tripulados, como naves espaciais ou expedições polares, exigindo pouca ou nenhuma manutenção e não produzindo nenhum poluente ou ruído adicional durante o seu funcionamento, o seu uso não está mais disseminado devido ao elevado custo e alta toxicidade dos materiais termoelétricos atualmente disponíveis comercialmente, geralmente à base de Bi, Pb e Te.

Na busca por materiais termoelétricos mais baratos e menos tóxicos, a tetraedrite, $Cu_{12}Sb_4S_{13}$, destaca-se como uma boa alternativa para uma gama de temperaturas médias. Este mineral de ocorrência natural é abundante na terra, tem baixa toxicidade e boas propriedades termoelétricas no estado natural (zT=0.6 a 700K). Embora a sua performance ainda não possa competir com materiais termoelétricos comerciais (com $zT \geq 1.0$), a dopagem isovalente pode ser usada para alcançar um zT mais próximo de 1.

Durante a última década um extenso esforço de investigação foi realizado para melhorar o desempenho termoelétrico da tetraedrite por ajuste de composição, mas a maioria dessa investigação focou-se na dopagem de um único elemento. Este projeto explora os efeitos da dopagem simultânea com Níquel e Selénio nas propriedades termoelétricas da tetraedrite.

Caracterização por difração de raios X, espectroscopia de Raman e SEM-EDS revelaram uma formação bem-sucedida de uma fase maioritária de tetraedrite em amostras com diferentes teores de níquel e selénio em diferentes etapas de síntese: fusão, recozimento e prensagem a quente.

Foi possível melhorar significativamente o desempenho termoelétrico através da dupla dopagem de Ni e Se, havendo uma amostra que se destacou significativamente nesta família de composições, $Cu_{11.5}Ni_{0.5}Sb_4S_{12.5}Se_{0.5,}$ apresentado um alto fator de potência (1279.99 $\mu W/m.K^2$ a 300 K), que, depois de estimar-se a condutividade térmica pela lei de Wiedemann-Franz e assumindo κ_L=0.5 W/m.K, um valor típico para tetraedrite não-dopada, obteve-se uma figura de mérito de zT = 0.33 a 300 K, que é um dos mais altos para este tipo de materiais termoelétricos à temperatura ambiente.

Palavras-chave: Tetrahedrite, termoeletricidade, dopagem química, reação de estado sólido, materiais sustentáveis.

II.ABSTRACT

Thermoelectric generators are a promising heat harvesting devices capable of converting waste heat into electricity. However, albeit being a reliable power source for remote and/or unmanned locations, like spacecrafts or polar expeditions, requiring little to no maintenance and not producing any additional pollutants or noise in their operation, they have failed to find widespread application due to expensiveness and high toxicity of current commercially available thermoelectric materials, generally based on Bi, Pb and Te.

In the search of cheaper and less toxic thermoelectric materials, tetrahedrite, $Cu_{12}Sb_4S_{13}$, is one of the most notable alternatives for medium temperature range. This naturally occurring mineral is earth abundant, has low toxicity and has good thermoelectric properties in the natural state (zT=0.6 at 700K). While this performance cannot yet compete with commercial thermoelectric materials (with $zT \geq 1.0$), isovalent doping can be used to improve it, to near unity zT.

During the last decade, an important and extensive research effort has been carried out to improve the thermoelectric performance of tetrahedrite by composition tuning, but most of it has been conducted by single element doping. This project explores the effects of doping simultaneously with Nickel and Selenium in thermoelectric properties of tetrahedrite.

X-ray diffraction, Raman spectroscopy and SEM-EDS characterization revealed successful formation of main tetrahedrite phases in samples with different Nickel and Selenium content at different synthesis stages: casting, annealing, and hot-pressing.

It was possible to significantly improve thermoelectric performance via simultaneous Ni and Se doping, with one sample standing out from this family of materials, $Cu_{11.5}Ni_{0.5}Sb_4S_{12.5}Se_{0.5}$, with a high power factor (1279.99 $\mu W/m \cdot K^2$ at 300 K), and after estimating the thermal conductivity using the Wiedemann-Franz law and assuming a κ_L=0.5 W/m.K, typical for undoped tetrahedrite, a figure of merit of zT = 0.33 at 300 K is obtained, which is one of the highest for this type of thermoelectric materials at room temperature.

Keywords: Tetrahedrite, thermoelectrics, chemical doping, solid state reaction, sustainable materials.

III.AKNOWLEDGEMENTS

I would like to express my deep gratitude and appreciation to all those who have supported and guided me throughout my doctoral journey.

First and foremost, I am immensely grateful to my supervisor Prof. Doctor António Pereira Gonçalves and co-supervisors Prof. Doctor Luís Filipe Santos and Doctor Elsa Branco Lopes for their unwavering support, insightful expertise, and invaluable guidance throughout the entire duration of my research. Their incisive constructive feedback, experience, constant encouragement, and patience have been instrumental in shaping this work and my journey into mastering all the nuances of thermoelectrics and solid-state chemistry. I would like to add a special thanks to Prof. Doctor G. Jeffrey Snyder and Prof. Doctor Duncan Zavanelli, for their kind and much appreciated availability to provide insightful assistance and wisdom on this field of research.

I would like to acknowledge the support and camaraderie of my fellow graduate students and colleagues, José F. Malta, Tiago Alves, Helena Ferreira, Rodrigo Coelho, Beatriz Santos, Cristiana Rodrigues and Filipe Figueiredo. Their companionship, stimulating discussions, and shared experiences have enriched my journey and provided a sense of community throughout this demanding process.

My deepest and sincerest appreciation goes to my long-time girlfriend, Catarina Dorisa Silva for her unconditional love, unwavering support, extraordinary patience and understanding throughout this challenging endeavour, without whom I would not have had the courage to set out on this journey and certainly would not have made it this far. I would like to thank her for all the late and the sleepless nights she endured, all the presentations she spectated and all my endless stress-filled venting ramblings she put up with. Her continued support and faith in me have been my greatest motivation and constant source of inspiration.

My dearest appreciation goes to my late father, Francisco Costa Moço, who was a source of encouragement and inspiration. And while he, unfortunately, is no longer able to witness the conclusion of this journey, I hope the gratitude I seek to express with these few lines can somehow reach him, for he is extremely missed.

I am also grateful for my family's support and patience. To my mother, brother, grandmother, uncles, aunts and cousins, as well as my girlfriend's family, who throughout this project they have shown their utmost understanding for all the missed family events, busy schedules and overworked weekends.

I extend my heartfelt appreciation to the faculty members and researchers in the Centro de Ciências e Tecnologia Nuclear from Instituto Superior Técnico, for their contributions to my academic development. Their lectures, seminars, and discussions have broadened my knowledge and nurtured my passion for my field of study. And to the entire institution, for providing me with the necessary resources, facilities, and financial support, which enabled me to conduct my research effectively. The technical staff and administrative personnel have been incredibly helpful and accommodating throughout my time here, and I thoroughly appreciate their assistance.

I am indebted to the funding organization Fundação para a Ciência e Tecnologia, for their financial support, which made this research possible. Their belief in the significance of this work has been both motivating and enabling.

Lastly, I want to acknowledge the countless individuals who have crossed my path during this journey. From friends and mentors to acquaintances and strangers, each interaction has shaped my experiences and influenced my personal and professional growth. And although I cannot name every person who has contributed to this thesis, I am deeply grateful for the collective impact of all those who have touched my life in various ways.

IV.INDEX

V.FIGURES INDEX

VI. TABLE INDEX

VII. LIST OF ABBREVIATIONS

BSE- Backscattered Electrons

DOS- Density of States

EDS- Energy Dispersive X-Ray Spectroscopy

GGA- Generalized Gradient Approximation

PF- Power Factor

SE- Secondary Electrons

SEM- Scanning Electron Microscopy

TEG- Thermoelectric Generator

TEM- Thermoelectric Material

TEC- Thermoelectric Cooler

VIII. LIST OF SYMBOLS

B – Thermoelectric quality factor

d – Spacing or grating constant in a crystal structure

e – Charge of a single electron

E_C – Energy of a channel

E_F – Fermi energy

$\boldsymbol{F}_{1/2}[x]$ – Fermi-Dirac integral

h – Thickness of the sample-bar

$\hbar$ – Planck constant,

I – Electrical current

k_B – Boltzmann constant

L – Lorenz number

l' – Distance between the contacts of voltmeter wires in the surface of a sample

m^* – Effective mass

m_e – Electron mass

n – Charge carrier concentration

Q – Heat flow

dQ/dx – Heat Flux

q – electric charge

R_h – Hall resistance

S – Seebeck coefficient

$S_{A,B}$ – Seebeck coefficient in respect to materials A and B assembled in a thermocouple

t - Relaxation time

T – Absolute temperature

ΔT – Temperature difference

dT/dx – Temperature gradient

ΔV – Potential difference

w – Width of the sample-bar

x – Stoichiometric content of Ni in samples following formula $Cu_{12-x}Ni_xSb_4S_{13-y}Se_y$

y – Stoichiometric content of Se in samples following formula $Cu_{12-x}Ni_xSb_4S_{13-y}Se_y$

z – Integer value representing diffraction order

zT – Figure of merit

ϵ - Energy variable

θ – Incidence angle of the x-ray radiation on the sample in X-ray Diffraction

κ – Thermal conductivity

κ_T – Total thermal conductivity

κ_E – Electrical component of the thermal conductivity

κ_L – Lattice component of the thermal conductivity

λ – Wavelength of incident radiation in X-ray Diffraction

λ_0 – Wavelength of incident radiation in Raman spectroscopy

λ_1 – Wavelength of scattered radiation in Raman spectroscopy

μ – Charge carrier mobility

μ^* - Chemical potential

μ_h – Hall mobility

μ_w - Weighted mobility

Π – Peltier coefficient

$\Pi_{A,B}$ – Peltier coefficient in respect to materials A and B assembled in a thermocouple

ρ – Electrical resistivity

σ – Electrical conductivity

τ – Thomson coefficient

Δv – Wavenumber

χ – Field-cooled magnetic susceptibility

1.INTRODUCTION

1.1 HISTORY OF THERMOELECTRICS AND MAIN MOTIVATORS

There are a set of energy transport phenomena that occurs in solid materials that involve a response of the electron system to a temperature gradient, collectively called thermoelectric effects. These effects centre on the electron, a subatomic particle with negative charge that carries electric current. In solids, the vast quantity of electrons present is in thermal equilibrium, suggesting that they also carry heat and entropy. This means that outside the thermal equilibrium or, in other words, in the presence of a temperature gradient, electrons move from the hot side to the cold side producing in the end an electric voltage. This behaviour, explains why thermal and electrical phenomena are coupled together and are thus called thermoelectric effects.(1)

The first recorded mention of a thermoelectric effect dates back to 1794, in an experiment carried out by Alessandro Volta, best known for the invention of the first electric battery, the voltaic pile. In his records, Volta connected two wires made of the same metal, but at different temperatures to a dissected frog leg, which made the leg muscles contract and twitch, that is to say, Volta was able to produce enough electrical charge to make the muscles in the frog leg spasm. However, despite this first mention, the discovery of this particular phenomenon, is accredited to the German physicist, Thomas Johann Seebeck, who in 1821, in his study of magnetic fields, devised an experiment where he could create a magnetic field by heating up one side of wires or rods of bismuth or antimony and copper, thus becoming known as the Seebeck effect**.**(2)

In 1834 another thermoelectric effect was discovered, the Peltier effect, named after the French physicist Jean Charles Athanase Peltier, who discovered that if two different metal wires were connected in a closed circuit with an electrical current, the junctions between these two metal wires would either heat up or cool down, depending on the direction of the current.

Later, the Thomson effect, named after William Thomson, also known as Lord Kelvin, was added to the list of thermoelectric phenomena. Thomson made an expansion to both the Seebeck and Peltier effects, based on the variations of Seebeck coefficient with a gradient of temperature in a material when crossed by an electrical current. He remarked that, depending on the direction of the current passing through the material, heat evolved differently throughout the circuit made by a single material, resulting in points equidistant to the heat

source, having different temperatures depending on the direction of the electrical current on that point.[3,4]

The first practical application of thermoelectric effects occurred during World War II, when the Soviet Union, inspired by the physicist Abram Fedorovich Ioffe, produced a 2-4 Watt thermoelectric generator to be included in a “partisan mess kit”, capable of powering a small radio with the heat of a small cooking fire. During the 1950s and 60s there was a significant effort to develop this technology, originally for military applications and later for civilian applications, driven by major advances in semiconductor technology, which lead to the discovery of more efficient thermoelectric semiconductor alloys and advances in thermoelectric theory. As the proven efficiency in laboratory of these thermoelectric devices kept increasing, many appliance corporations like Westinghouse, as well as universities and national research laboratories thought that thermoelectrics could transcend conventional heat engines, thus investing heavily on researching thermoelectric applications, peaking by mid 60s. At this point, thermoelectric devices were majorly used in niche sectors like aerospace field being used in both cooling and powering systems, but also to a minor extent, found applications in optoelectronics and small refrigerators. However, by the end of the 60’s, progress began to slow down, as increasing efficiency became significantly more arduous, leading to many researchers believing there was a un upper limitation to the potential efficiency and overall performance of thermoelectric devices, ultimately resulting in a sharp decline over the course of a three-decade period, as companies abandoned research due to the limited application in only niche sectors and low expectations to improve efficiency.[5,6]

Despite the decreased interest of major companies in this field of research, between 1963 and 1983, major breakthroughs were achieved in thermoelectricity, with successful transition from the laboratory to practical applications. Most notably, the combination of a nuclear heat source and a thermoelectric generator (TEG), resulted in a long-life power source that required no maintenance or human intervention, usable in inaccessible and hostile environments, known as radioisotope thermoelectric generators, which have been critical in NASA missions to the moon, Mars, and outer-planetary exploration missions like Voyager I and II, but also used in a variety of other fields, to name a few: buoys, unmanned lighthouses, polar stations, and even as a very successful and safe nuclear-powered thermoelectric cardiac pacemaker battery.[7–12]

However, in recent years a “renaissance” occurred in the field of thermoelectric, with a significant rise in popularity after decades of stagnant research. After major breakthroughs in

the field of material science, the pool of thermoelectric materials (TEMs) available for study exploded from a small group to a veritable ocean of potential material combinations, with new ones being discovered every year. Advances in simulation software, coupled with better understanding of the behaviour of subatomic particles, have provided more accurate predictive modules that hastened the discovery of novel materials with high thermoelectric properties. Coupled with growing global environmental concerns, rising energy demand, climate change and dwindling accessible natural resource reserves, which forced today's societies to re-evaluate their dependence on fossil fuel and current energy production technologies, which in turn, led to the rise of popularity of thermoelectrics and other green energy sources. Originally, the focus of thermoelectric research was about application as a reliable energy source or cooling system for long remote operations. Nowadays, the focus has shifted toward the efficiency angle, due to the society's growing need for more efficient, cost-effective, less fuel-consuming and less pollutant-emitting operations across all aspects of society, be it in the industry, transportation or domestic sector.[13]

Thus, the scientific community is now driven to seek new, sustainable, and more efficient ways to produce electricity. Following this motivation, the research of TEMs has grown in popularity, with the focus of discovering novel, cheaper and sustainable materials to make thermoelectric devices more affordable, cost-effective, and easier to widely implement in electricity generation from heat or use electricity to extract heat. In terms of energy generation, this means that waste heat (the energy lost in the form of heat that is prevalent in nearly all forms of energy production, with some studies estimating that 52% of total global energy produced is wasted as heat[14–16]) could be harvested to produce electricity, through TEGs[17], thus increasing the overall efficiency of any process that releases waste heat.

1.2 THERMOELECTRIC EFFECTS

While extremely interchangeable, there are three known distinct phenomena that correlate charge carrier transport and thermal gradient within a solid, which are named after their discoverers: the Seebeck effect, Peltier effect, and Thomson effect. These effects are all reversible.

1.2.1 Seebeck effect

The first discovered thermoelectric effect, at its core, is a phenomenon wherein a solid conducting material exhibits a charge carrier concentration gradient, i.e., a small voltage, when subjected to a temperature gradient.

To further elucidate and substantiate this phenomenon, an effective and simplistic approach involves employing a thermocouple system. This system comprises two dissimilar conductive materials, denoted as A and B, interconnected at two junctions to establish electrical series connection and thermal parallel connection. In practical terms, assuming wires of materials A and B, the ends of the A wire are connected to the corresponding independent B wire ends, thereby forming a complete open circuit. Subsequently, if the junctions experience different temperatures, for instance, junction 1 being heated by a small flame, resulting in T1>T2, applying a voltmeter across the open circuit—specifically, the ends of the independent B wires—will indicate the presence of voltage.

The underlying cause of this voltage formation stems from the movement of charge carriers within conductive materials induced by heat, which can be considered kinetic vibrational energy. Thus, electrons in the hotter region migrate towards cooler regions within the conductive material to exchange energy, just obeying the laws of thermodynamics. Consequently, these electrons lose a portion of their vibrational energy, reducing their kinetic energy and thus leading to an increased concentration of electrons in colder regions and a decreased concentration in warmer regions. This disparity in electron concentration manifests as a voltage, the Seebeck voltage, which is defined as the net thermal electromotive force established under open circuit conditions.[3,4,7]

Therefore, the Seebeck effect comprises of net conversion of thermal energy into electrical energy with the emergence of a voltage. It was found that for small temperature

differences between the junctions of the dissimilar conductive materials, the change in voltage (ΔV) formed was proportional to the temperature difference (ΔT=T2-T1), thus:

$$\Delta V \propto \Delta T \leftrightarrow \Delta V = -S_{A,B}.\Delta T \qquad (1)$$

with $S_{A,B}$, a proportionality coefficient, be labelled the Seebeck coefficient, the sign of which is determined by the materials (A and B) used on the circuit. Per convention, the sign of $S_{A,B}$ is set as positive if the induced current flows from A to B on the cold junction. The Seebeck coefficient can also be expressed as a flux of entropy per carrier per unit charge.[18,19]

In the analysis of a single material, the determination of the Seebeck coefficient necessitates comparative measurements with respect to a well-characterized reference material, denoted as X. This practice stems from the fact that in thermocouples, experiments have demonstrated that the thermal electromotive force or voltage (V) occurring at the junctions between various material pairs can be combined in the following manner[20]:

$$V_{A,B}(T_1, T_2) = V_{A,X}(T_1, T_2) - V_{B,X}(T_1, T_2) \qquad (2)$$

1.2.2 Peltier effect

The Peltier effect was the second discovered effect and is essentially the inverse of the Seebeck effect. In simple terms, when a current is applied to a solid conductive material, it develops a temperature gradient.

To illustrate the Peltier effect using the previously described thermocouple system, instead of maintaining an open circuit, the ends of the independent B wires are connected to a direct current source. Thermometers positioned at both junctions between the A and B wires would reveal that one junction is increasing in temperature while the other is decreasing, exhibiting a balanced rate of heating and cooling. In other words, one junction emits heat while the other absorbs an equivalent amount of heat. This phenomenon occurs because, although the thermocouple system maintains a constant overall temperature, charge carriers transport heat throughout the circuit. As these carriers pass through the junctions, they undergo changes in entropy, resulting in the absorption or emission of energy in the form of heat.

It is worth mentioning that observing the Peltier effect in metals is challenging due to the concurrent occurrence of Joule heating. This phenomenon arises from the passage of electrons through the metal, generating heat. Consequently, heat is simultaneously produced by the circuit, absorbed at one junction, and emitted at the other. In certain circumstances, this makes it only possible to discern variations in the quantity of heat emitted at a junction when the direction of the current changes.[3,4,7]

Similar to the Seebeck effect, experimental observations of the Peltier effect have shown that the heat absorbed or emitted at a junction (Q) is proportional to the current (I) passing through that junction, thus a proportionality coefficient, the Peltier coefficient ($\Pi_{A,B}$), can be obtained through the formula:

$$\Pi_{A,B} = \frac{Q}{I} \qquad (3)$$

1.2.3 Thomson effect

While the Seebeck and Peltier effects are inversely related, representing the intricate connection between heat and charge carrier transport in solid conductive materials, the Thomson effect can be regarded as an extension of these phenomena.

The Thomson effect pertains to the manner in which heat is transported within a conductive solid material while an electric current passes through it. To explain this phenomenon in a simplified manner, consider a homogeneous conductive material, such as a wire, through which a current is flowing. If a small section of the wire is exposed to a direct heat source, the wire naturally heats up, and the heat conducts throughout the length of the wire in both directions. Logically, one would assume that two points (A and C) to either side of the position of the heat source (B), if they are equidistant to B, they would have the same temperature, however if current is passing through the wire, the temperature in point A and C will often be different. Assuming the current direction is from A to C, if the temperature at point C is higher than at point A, it signifies that heat has been absorbed in the A-B segment of the wire and evolved in the B-C segment. This is referred to as a positive Thomson effect. Conversely, if, with the same current direction, the temperature at point A is higher than at point C, it means that heat is being evolved in the A-B segment and absorbed in the B-C segment of the wire, thus denoting a negative Thomson effect. Whether the Thomson effect is positive or negative depends on the Thomson coefficient of the material. It is worth noting that certain materials may possess a null Thomson coefficient, resulting in both points A and C having the same temperature, with no heat being absorbed or evolved in the process.[3,4,7]

By establishing a reversible thermoelectric circuit, William Thomson accomplished the correlation between the Seebeck (*S*) and Peltier coefficients (*Π*) based on the principles elucidated by the first and second laws of thermodynamics. This correlation can be mathematically expressed by the following formula:

$$\Pi = S.T = \frac{Q}{I} \qquad (4)$$

that can be expanded to express heat flux (dQ/dx) observed in the Thomson effect as a function of the gradient of temperature and current:

$$\frac{dQ}{dx} = \tau . I . \frac{dT}{dx} \qquad (5)$$

where, τ is the proportionality coefficient for the Thomson effect, the Thomson coefficient.

1.3 THERMOELECTRIC MATERIALS

All materials exhibit thermoelectric effects to some extent, with varying effectiveness or practical utility, thereby qualifying the most effective and most practical as thermoelectric materials (TEMs). The degree to which these effects are manifested is commonly evaluated using a measure known as the figure of merit, denoted as zT. This dimensionless parameter was originally introduced by Ioffe et al.[21] in 1959 and is calculated using the following formula:

$$zT = \frac{S^2 \cdot \sigma}{\kappa} T \qquad (6)$$

where S represents Seebeck coefficient, σ the electrical conductivity, T the absolute temperature and κ the thermal conductivity and serves as a facilitated form of comparison between different materials, with higher values correlating to higher thermoelectric performances.

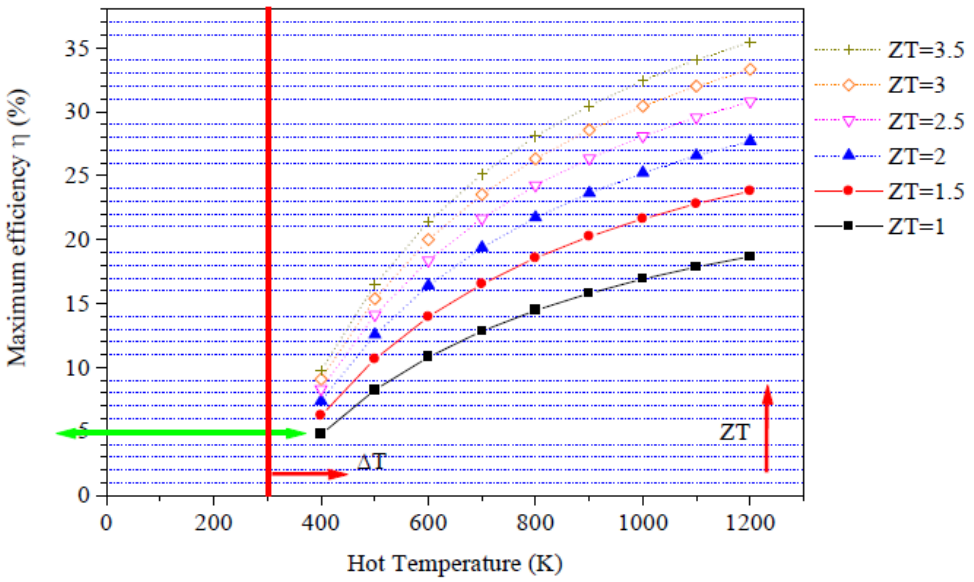

Fig. 1 Maximum efficiency (%) achievable for a thermoelectric device with an average zT between 1.0 and 3.5 with the cold side at approximately room temperature (≈300K) as a function of temperature of the hot side (K).[22]

To contextualize this parameter, in order to achieve a 10% energy conversion efficiency, materials with an average zT≈ 1,0 require a temperature difference of ΔT>250 K, and those with an average zT≈ 2.0, the required temperature difference decreases to ΔT>150 K, as depicted in Fig. 1. In comparison, the Rankine cycle (Fig.2) which is prevalent method utilized for energy conversion in both power generation and in refrigeration, thermal

efficiency ranges from 10% with a ΔT=100K to nearly 50% with a ΔT=550K or higher. It has been demonstrated (Fig.3) that achieving the efficiency level of the Rankine cycle would require a zT ≥4.0.[23,24]

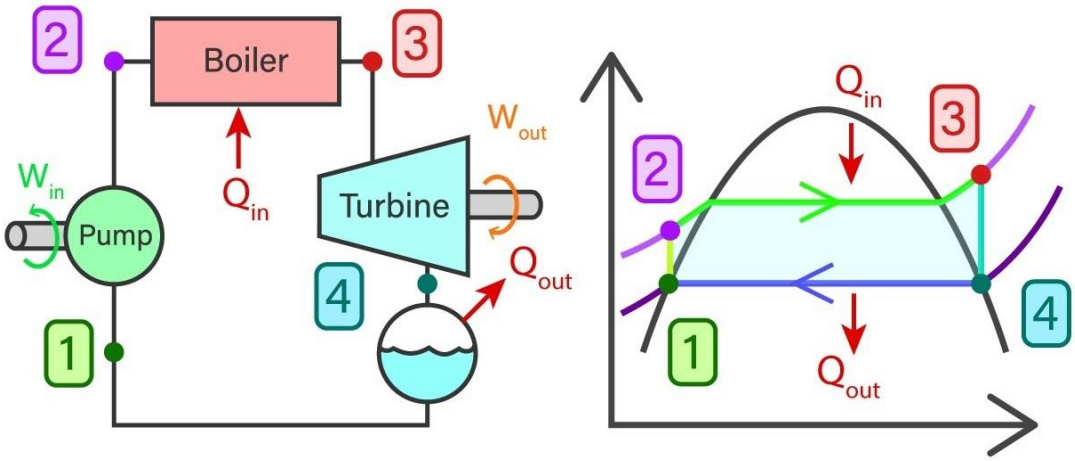

Fig. 2 Schematic of the ideal Rankine Cycle and corresponding T-S diagram.[25]

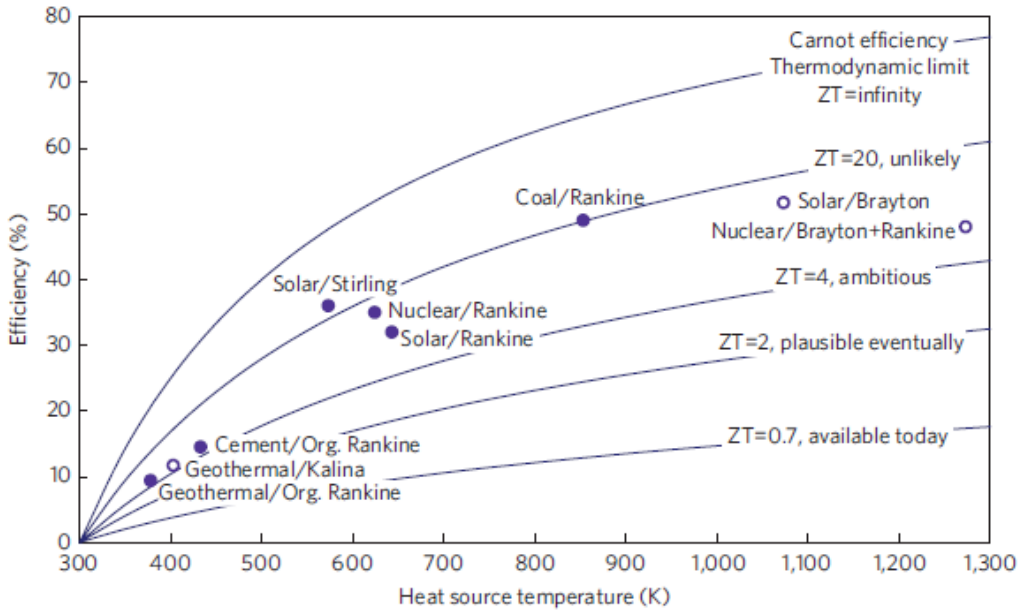

Fig. 3 Efficiency of mechanical engines compared to different thermoelectric estimates.[23]

It is pertinent to emphasize that although Rankine cycle-based devices exhibit significantly higher efficiency compared to thermoelectric devices, their operation necessitates the use of highly intricate and voluminous machinery. This machinery relies on numerous moving parts and the circulation of a working fluid (such as steam, water, refrigerants, or hydrocarbons), which, in turn, leads to requiring frequent maintenance and monitoring. On the other hand, thermoelectric devices are able to make direct energy

conversion simply through the passage of charge carriers through TEMs, so devices employing these materials would not only be considerably smaller and more compact than Rankine cycle-based devices, because they do not require tubes, compressors, turbines and other complex machinery, but also lack the moving parts and working fluid, thus being able of operating silently for long periods of time without maintenance or human interaction.

Achieving higher zT values poses a formidable challenge. The fundamental requirement for increasing zT involves simultaneously increasing electrical conductivity (σ) and Seebeck coefficient (S), while minimizing thermal conductivity (κ_T). However, due to the inherent interdependence of these properties, it becomes exceedingly difficult to manipulate them independently. Notably, materials with high electrical conductivity often exhibit elevated thermal conductivity as well. Nonetheless, by introducing simplifications to the calculations and assuming a simple parabolic band for electron energy levels, while disregarding electron-electron and proton-electron interactions, it becomes feasible to express these properties (S, σ, and κ_T) as functions of charge carrier concentration, n, using the following equations:

$$S = \frac{8 \cdot \pi^2 \cdot k_B^2}{3 \cdot e \cdot h^2} \cdot m^* \cdot T \cdot \left(\frac{\pi}{3 \cdot n}\right)^{2/3} \qquad (7)$$

$$\sigma = n \cdot e \cdot \mu \qquad (8)$$

$$\kappa_T = \kappa_L + \kappa_E = \kappa_L + L \cdot \sigma \cdot T \qquad (9)$$

where k_B is the Boltzmann constant, $\hbar$ is the Planck constant, e the electron charge, m^* the effective mass, μ the charge carrier mobility, L the Lorenz number, and κ_L and κ_E the lattice or phonon contribution and electrical contribution to thermal conductivity, respectively. With a constant Lorenz number being calculated through the formula:

$$L = \frac{\pi^2}{3}\left(\frac{\kappa_B}{e}\right)^2 = 2.44 \cdot 10^{-8}\, V^2/K^2 \qquad (10)$$

It is important to note, that by charge carriers, researchers are referring to both electron particles, carrying a negative charge, and quasiparticles called “holes”, that effectively represent the absence of an electron in a state, thus carrying a “positive” charge.[26,27] So, by combining these functions, it becomes possible to estimate a specific n for optimum conditions, as represented in Fig. 4.

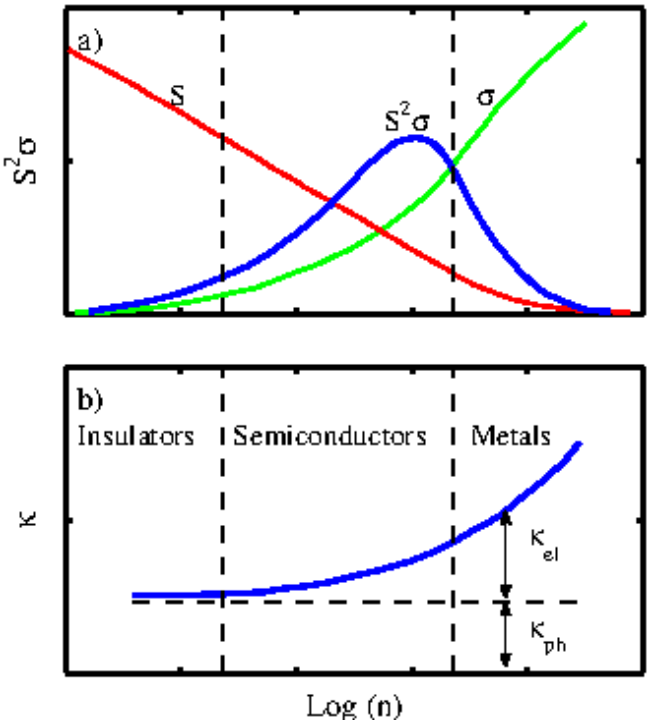

Fig. 4 Representation of the Seebeck coefficient (S), electrical conductivity (σ), power factor ($S^2\sigma$) and thermal conductivity (κ) as a logarithmic function of charge carrier concentration, (n).[28]

In this figure, it can be inferred that metals and insulators usually have bad thermoelectric properties, since they will either have high electrical conductivity but low Seebeck coefficient or high Seebeck coefficient but low electrical conductivity, respectively. Continuing the estimation, if a Boltzmann distribution is assumed instead of Fermi-Dirac, the optimum *n* is evaluated around 10^{19}–10^{20} cm^{-3}, which is close to the value characteristic of degenerate semiconductors. This explains why most thermoelectric materials are semiconductors, particularly degenerate semiconductors of high mobility, since the only way to maximize electrical conductivity with a set optimum *n*, according to (eq. 8) is by maximizing the charge carrier mobility.[1,29,30]

Even within this subsection of semiconductive materials exist a vast number of different naturally occurring minerals and artificially made materials with a wide range of different compositions, thus identification of those with high thermoelectric potential still proves quite challenging. There are however, two main methods to search for TEMs with potential high performance. The "phonon glass electron crystal" method, is based on the assumption that an ideal TEM should have a combination of glass-like thermal conductivity and crystal-like electronic properties (i.e. low thermal conductivity and high electrical conductivity)[3,27]. This combination of transport properties is more achievable with complex crystals structures where voids/vacancies and "rattlers" (heavy element atoms that can be incorporated into these voids)

would provide phonon scattering, reducing significantly the lattice thermal conductivity. The other method is the nanostructuring of TEMs, based on the assumption that nanostructures can enhance zT. The reasoning is that nanostructures provide quantum confinement, in other words, the spatial confinement of electron-hole pairs within the material, can enhance the density of states at the Fermi level, which improves the Seebeck coefficient and provides a way to tune this property disjointed from the electrical conductivity.[31–33] Also, in heavily doped semiconductors, the mean free path of electrons is significantly shorter than that of phonons. Therefore, the introduction of more interfaces through nanostructuring could help scatter more effectively the phonons, which due to the larger mean free path would be more affected than electrons, ultimately reducing the lattice thermal conductivity without affecting too much carrier mobility and electron conduction. For this purpose, the nanostructure should have one or more dimensions smaller than the mean free path of the phonons, while being larger than the mean free path of the charge carriers.[27]

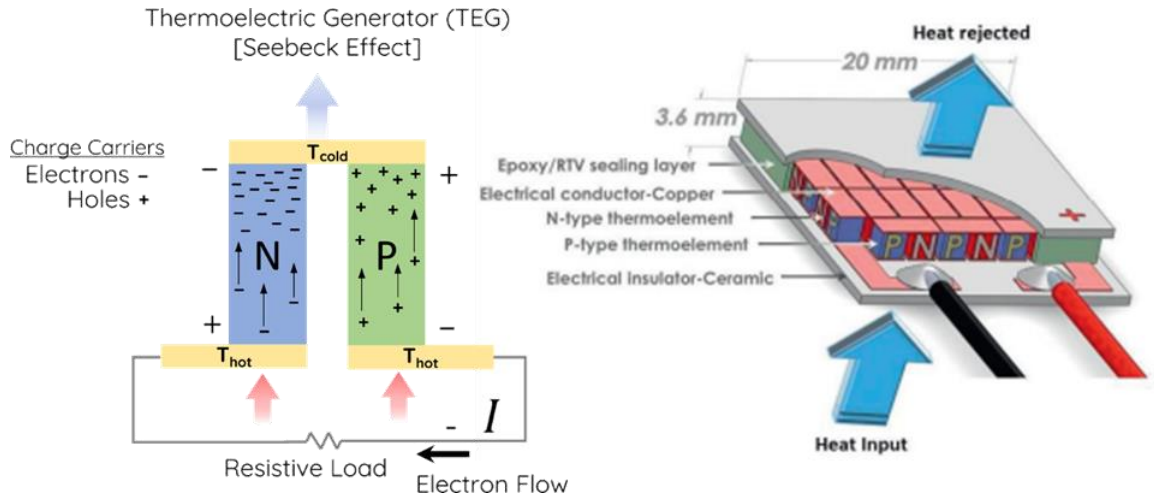

Fig. 5 Operation of a thermoelectric device: on the left, representation of the flow of charge carriers in a thermoelectric generator[34], on the right, schematic of a module of a thermoelectric device[35].

Thermoelectric devices usually consist of multiple n-type and p-type semiconducting legs that are assembled in an alternating arrangement and connected in series to form a circuit that can move current from the hot side to the cold side, with electrons on the n-type legs and holes in the p-type legs, following the heat flow (Fig. 5). Since the efficiency of these devices is based on the average figure of merit of the legs, in order to have the best performance for each situation it is necessary that the n-type and p-type material have similar values of zT in the range of operating temperatures. Thus, often new materials need to be discovered to find a suitable pair.

1.3.1 Inorganic Thermoelectric Materials

The most conventional inorganic TEMs are bismuth telluride (Bi_2Te_3), lead telluride (PbTe), silicon-germanium (SiGe), antimony telluride (Sb_2Te_3), tin telluride (SnTe) and their alloys. Bi_2Te_3, PbTe and SiGe were extensively studied in the early thermoelectric boom, due to their high thermoelectric performance: Bi_2Te_3 achieving zT 0.8-1.0 at room temperature and PbTe with a zT of 1.8 at 850K. Bi_2Te_3, Sb_2Te_3 and $BiSe_3$ are currently the most commonly used and have been extensively studied to increase their performance with some of the highest zT values reaching 1.7 (Fig. 6 and 7). However, despite high thermoelectric performances, concerns about a potential upcoming tellurium scarcity, which is frequently used in the making of current electronic devices, coupled with the high toxicity of heavy metals, most concerningly lead, are pushing the scientific community to search for cheaper and less toxic alternative materials for a wider range of applications. Other examples of studied inorganic thermoelectric material include chalcogenides, oxides, MgAgSb, skutterudites, clathrates and Half-Heusler's.[29,36–41]

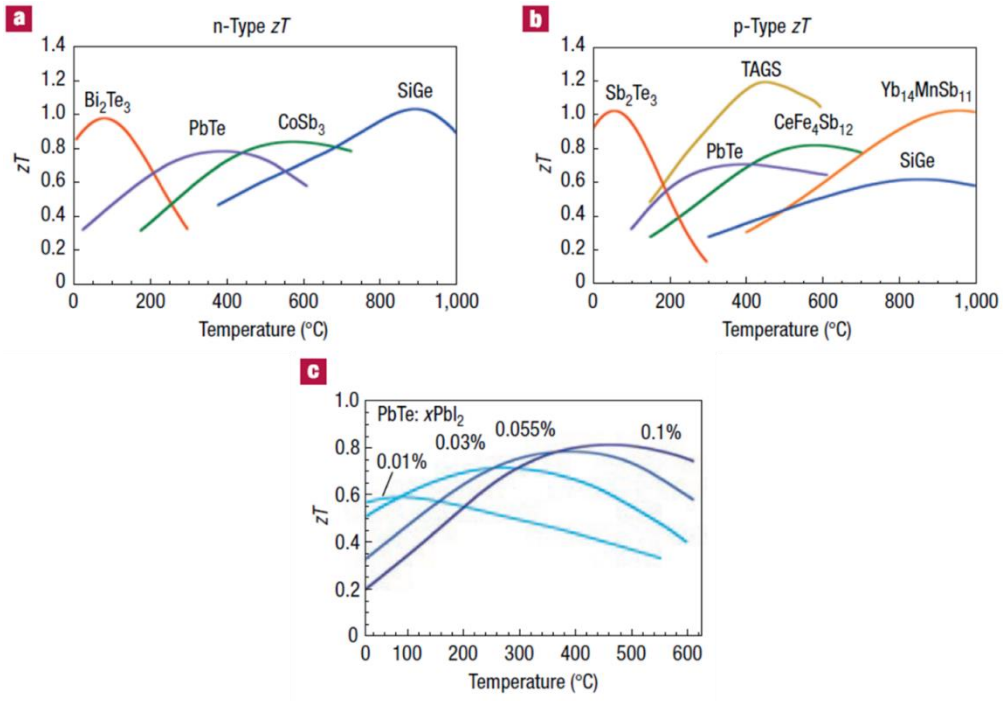

Fig. 6 Figure of merit of state-of-the-art commercial materials currently used or being developed by NASA for thermoelectric power generation: a), p-types; b), n-types and c) the effect of dopant concentration on the zT of PbTe alloy. With higher concentrations, the zT increases and peak shifts to higher temperatures.[42]

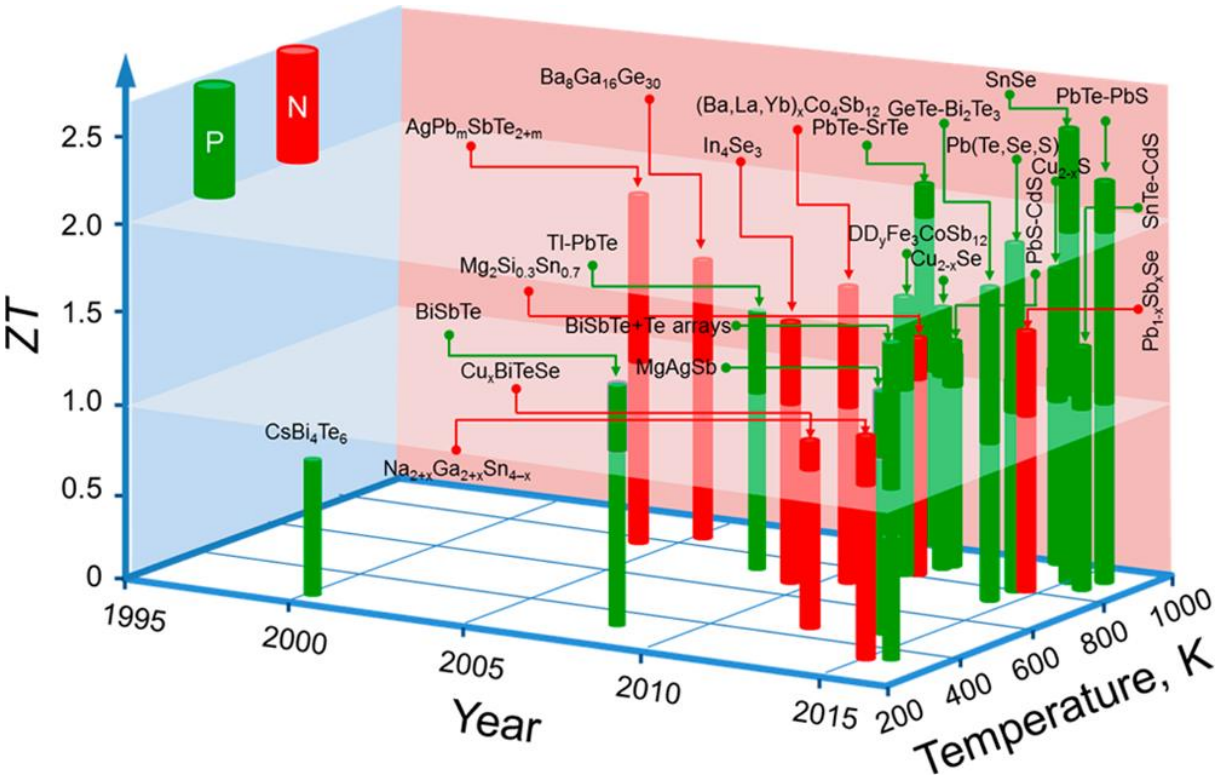

Fig. 7 Figure of merit of current state-of-the-art bulk thermoelectric materials represented as a function of temperature and year of publication. In green are represented p-type materials and in red the n-type.[43]

To improve the thermoelectric performance of inorganic materials the most common methods are doping/alloying and nanostructuring (Fig. 6C). Examples of nanostructured inorganic materials include silicon nanowires, nanotubes and quantum dots that are added to bulk thermoelectric material to improve the thermoelectric performance.[27,44,45]

It should be mentioned that the current record zT value in inorganic thermoelectric materials is 3.1 with SnSe[46–49]. However, a recent study by Hinterleitner, B. et al.[50] has suggested that a meta-stable thin-film Half-Heusler alloy, with the formula $Fe_2V_{0.8}W_{0.2}Al$, could potentially achieve a zT in the 5.0-6.0 range.

1.3.2 Organic Thermoelectric Materials

The early stages of thermoelectric research focused on inorganic materials, as they can be more easily and rapidly improved. Only in the recent decades organic TEMs, such as polymers, graphene, and carbon nanotubes, were identified and studied, as they have some advantages over their inorganic counterparts, namely: recyclability, flexibility, and price.

Because organic materials possess low thermal conductivity, the zT will be mostly dependent on the power factor (PF), which can be significantly increased in these materials. Improvements come from new molecular designs, or the manufacture of nanocomposites composed of conducting polymers or nanomaterials.

Polymer TEMs are divided into conducting and non-conducting. Conducting polymers are low cost, non-toxic and have low thermal conductivity, tending to perform better than non-conducting polymers due to their intrinsic electrical conductivity. The most researched conducting polymers are poly(3,4-ethylenedioxythiophene), polyaniline, and polypyrrole. On the other hand, non-conducting polymers often act as barriers to bundle-to-bundle hopping, which decrease thermoelectric performance. Nonetheless, both types are being extensively investigated to improve performance, often via doping or new designs.[51]

Graphene and carbon nanotubes are frequently used as fillers in polymer nanocomposites, since they have high electrical conductivity and their large surface area increases interference between polymer and carbon particles, providing a way to adjust the thermal conductivity and increase the properties of organic TEMs. Moreover, both are flexible, non-toxic, lightweight and have high mechanical strength.[47]

1.3.3 Inorganic-Organic Thermoelectric Materials

While inorganic thermoelectric materials, in general, achieve zT values 2-3 times higher than organic, the latter tends to be cheaper, more sustainable, and more mechanically flexible. Thus, hybrid materials are being developed, to combine the best properties of both types of materials, with the goal of producing a thermoelectric material with low thermal conductivity and high electrical conductivity and Seebeck coefficient.[47]

Most dominant approach for producing hybrid materials is integrating nanostructured inorganics (e.g.: Te, Bi_2Te_3) with conducting polymers. With this technique tellurium nanostructures coupled with carbon nanotubes and poly(3,4-ethylenedioxythiophene) polymers, managed to achieve a PF of 235 $\mu W/mK^2$, as reported by Ahn et al.[52,53], as well as SnSe incorporated with Te and poly(3,4-ethylenedioxythiophene): poly(styrenesulfonate) polymers that achieved a PF of 390 $\mu W/mK^2$.[49]

Other organic materials have also been employed to produce hybrid materials, i.e.: CH_3NH_3I was used in a multilayer composite with Sb_2Te_3, which achieved a PF of 1600 $\mu W/mK^2$ [54]; and graphene sheets combined with $Bi_{0.4}Sb_{1.6}Te_3$ demonstrated a PF of 4600 $\mu W/mK^2$.[55]

1.4 THERMOELECTRIC DEVICES

The utilization of heat for electricity generation or the application of electricity for cooling or heating purposes does not represent the novelty introduced by thermoelectric devices (Fig 8). In fact, the waning interest from both companies and the scientific community in thermoelectrics during the 1960s to 1990s can be attributed to the presence of alternative power generation and refrigeration methods that are often more efficient and cost-effective. Technologies based on the Rankine Cycle emerged as the favoured means of energy conversion. However, what sets thermoelectric devices apart is their ability to facilitate energy conversion through thermoelectric modules without the reliance on complex processes and bulky machinery to harness useful energy from heat. Consequently, these devices exhibit remarkable compactness compared to their counterparts. Moreover, devoided of moving parts, they operate silently, require minimal maintenance, and produce no pollutants. It is precisely these attributes that render thermoelectric devices the preferred choice for applications constrained by size, weight, portability, and accessibility limitations.

As mentioned before, thermoelectric devices can either employ the Seebeck effect to produce electricity by absorbing heat or employ the Peltier Effect to use electricity to produce cooling/heating. Thus, thermoelectric devices are split into two categories: generators (TEGs), for heat harvesting, and coolers (TECs), for cooling or heating. Conceptually, there is very little difference between the two types of devices, with both TEGs and TECs having a similar geometry as described in Fig.5. Aside from different soldering material/method employed in the contacts (to operate at different temperatures and voltages), the only major difference between them is whether there is an imposed passage of current or an imposed temperature difference.

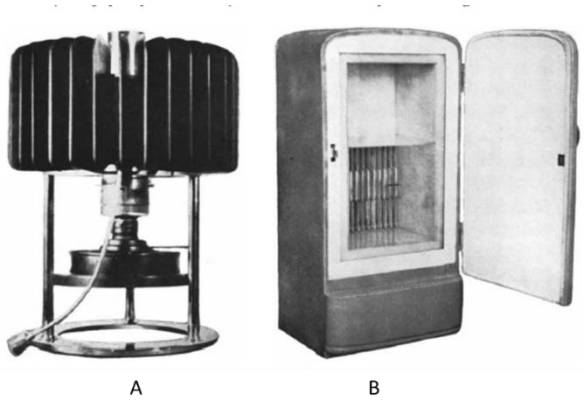

Fig. 8 Examples of thermoelectric applications from the 40s and 50s: A) a kerosene lamp chimney capable of powering a small radio, and B) a domestic refrigerator prototype.[6]

1.4.1 Generators

In what regards to the application of TEGs, there are two main motivations for their use: A) is the need for small and durable power sources for devices with very limited access or very limited size and weight restrictions; or B) to reduce energy waste in the form of waste heat.

Regarding this latter motivation, it is estimated that around two thirds of total primary energy global production is wasted. Heat is by far the most prevalent form in which the energy is lost, with waste heat accounting for approximately half of the entire primary energy produced, regardless of the sector: industry, transportation, domestic, etc. Which, effectively speaking, means that the entire global production energy has only a roughly 33% efficiency. From both an economic and a sustainable standpoint, it is crucial to mitigate this waste, increase the efficiency of our power generation methods, reduce fuel consumption, reduce overall production costs, and reduce pollutant emissions. TEGs, by harnessing waste heat to produce electricity, can help meet all these goals, with the added benefits of not producing any pollutants, requiring very little to no maintenance and being noise free, on account of not having moving parts. This, combined with their small size and modular design, makes them far easier to apply and customize, and easily be adaptable to a wide range of surfaces. On top of that, since TEGs only require a temperature difference to operate, these devices TEGs can be easily added to any existing operation system by installing in any equipment, machine or surface where it can be exposed to a temperature difference as a sustainable approach to improve efficiency in any existing process.[17,24,56–58]

For various decades, TEGs found niche application in the space sector or in remote locations due to being a reliable energy source that could go without maintenance for extended periods. Radioisotope Thermoelectric Generators (Fig.9), being the most notable application of TEGs, which is used to power space probes, rovers, satellites, uncrewed lighthouses, navigation beacons, equipment used in polar bases and, for several decades, heart pacemakers, which were only abandoned due to fear that pacemakers would be cremated with the corpse before removal, which would compromise the integrity of the radioactive heat sources[8–12]. In recent years, however several studies were published exploring the application of these devices to a wide range of applications, to name a few: automotive applications in car exhaust[59] and break systems[60]; industrial waste heat recovery[61]; wearable technology and internet of things applications[62,63]; medical sensors that rely on body heat[64]; and additions to solar collectors[35] and photovoltaic panels[65]. In the case of photovoltaic cells the heat

produced by solar radiation and the heat emitted by radiative cooling of photovoltaic cells during the night combined, resulting in solar panels capable of producing energy not just during the day but also at night.

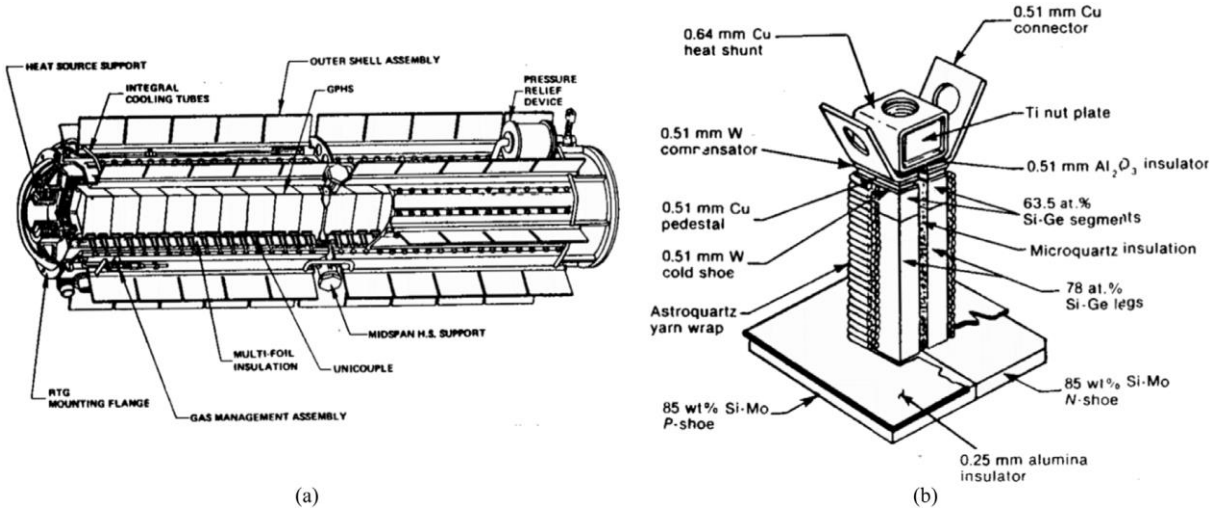

Fig. 9 The (a) overall structure of a general-Purpose Heat Source Radioisotope Thermoelectric generator and the schematic for the SiGe thermocouple components.[66]

However, despite these advantages and the potential application in all sectors and operations that involve generation of heat, this technology had some difficulty of expanding from niche applications. The problem stems from the expensiveness and toxicity of currently used TEMs, as well as the low energy conversion efficiency of TEGs, when compared with alternative energy converters. In conclusion in the present this technology is not sufficiently cost-effective to be widely applicable. As such, to expand TEGs beyond niche applications it is necessary to improve the cost-effectiveness by engineering better designs, developing new nanoscale structures and interfaces, and discovering novel inexpensive sustainable materials with high thermoelectric performances.[17,24,56–58]

1.4.2 Coolers

TECs compared to the commonly used vapour-compressing refrigeration systems, are smaller, have more flexible shapes that can be easily tailored to each specific situation, have no moving parts and no refrigerants, resulting in longer lifespan, less maintenance, and no risk of leaks. Since most currently used refrigerants still have a negative environmental impact, the absence of refrigerants makes TECs, in this aspect, a greener and more sustainable option. Also, with the amount of heat absorbed or emitted being proportional to the applied DC current, these devices are suitable to be used for temperature control with a remarkable precision, by accurately controlling the direction and amount of current applied.

Nonetheless, despite these advantages, TECs are not considered a viable alternative to vapor-compressing refrigeration in most situations due to the operational limits of the technology. Despite the amount of heat moved by these devices being proportional to the product of current and Peltier coefficient, as denoted by eq.3, there are two phenomena that offset this formula. The first is the generation of waste heat by the TEC itself due to Ohm's law and the second the thermal conduction within the device from the hot side to the cold side. The latter is naturally aggravated by the increase of temperature difference and is further intensified by the small dimensions of the device, in other words, a smaller distance between hot and cold regions. Eventually, the heat moved by the Peltier effect cannot offset the one moved in the opposite direction by these two phenomena and thus, a typical single-stage TEC can only achieve a maximum temperature difference of 70 ºC between the hot and cold side. Also, TECs can achieve a maximum of 10-15% efficiency in energy conversion, while the reverse Rankine cycle, which is the base process of the vapor-compressing refrigeration, can achieve an energy conversion of 40-60%, being the best option in most cases.

However, in situations where the efficiency is not the critical point, TECs are a valid option, as in portable coolers, humidifiers, and heat sinks in microprocessors. In the industrial sector, while not being able to compete with vapour-compressing refrigeration in dealing with large heat removal from macro equipment of the manufacturing process, TECs are still employed in both small and sensitive equipment like semiconductor diodes, laser equipment, power amplifiers, infrared detectors, charge-coupled devices and other electro-optic instruments[7], and large, even industrial size, electronics like telecommunications, vehicle cooling, mini refrigerators, incubators, military equipment, IT enclosures, personnel temperature control for full body military uniforms, astronaut suits, and bio/chemical hazard protection suits.[67] Their application in small delicate devices also translates into a wide range

of scientific research equipment, which coupled with low maintenance requirements, small size, flexible shape, and long lifespan makes this technology the most suitable for temperature regulation of the electronic systems.

1.5 TETRAHEDRITE AS A THERMOELECTRIC MATERIAL

As mentioned in chapter 1.3.1, many state-of-the-art TEMs are chalcogenides, which include, but are not limited to: Bi_2Te_3, PbTe, Sb_2Te_3 and SnTe. Because they have been one of the most extensively studied groups of materials and tend to display high thermoelectric performances. Chalcogenides represent a group of materials that have at least one chalcogen anion (element from the column 16 of the periodic table) combined with at least one more electropositive element. Although oxides fit the description of a chalcogenide, the term is commonly reserved to describe sulphides, tellurides, selenides, and polonides.

Currently, in thermoelectric applications, most of the commonly used chalcogenides are tellurides, but the growth of global tellurium demand and concerns about the application of heavy metals and other toxic elements, like thallium, lead or bismuth, have pushed the scientific community to discover other alternative materials that do not contain these elements.[24,45,68–70]

Sulphides were not originally explored for thermoelectrics due to the challenges they pose, namely: the low melting and boiling points of Sulphur limited the temperature range of applications (115-445ºC)[71,72]; also, light atomic weights and the tendency for intrinsically having either too high or too low charge carrier concentration, led to low conversion efficiencies. However, since mineral sulphides are not only naturally occurring but are also abundant on the crust of the Earth, it could mean not only cheaper TEMs, but also less complex production processes, with the added benefit that sulphide-based TEMs having lower toxicity and thus higher environment compatibility than other chalcogenides.[45] Amongst the novel sulphides being studied are: chalcocite, Cu_2S; colusites, $Cu_{26}V_2(Ge, Sn, As, Sb)_6S_{32}$; bornite, Cu_5FeS_4; and tetrahedrites, $Cu_{12}Sb_4S_{13}$.[29,36–38,73]

Tetrahedrites, $Cu_{12}Sb_4S_{13}$, the object of study of this project, is an earth-abundant mineral (Fig. 10)[74] that has drawn the attention of researchers due to its naturally good thermoelectric properties as a p-type semiconductor, with zt values of ~0.1[75] at 700 K, with synthetic tetrahedrite reaching zT value as high as 0.76 at 623 K.[76,77]. It is composed of significantly less toxic and more common elements than current commercial grade TEMs, with already a few studies carried out discussing the application of this mineral in TEGs[61,78,79] and in solar absorbers.[80,81]

Fig. 10 Natural tetrahedrite crystal. Origin :Peru.[82]

Tetrahedrite was named in 1875 and has been extensively studied in geology and mineralogy, and despite the knowledge that tetrahedrites had good thermoelectric properties since 1950, the main interest in this mineral is solely on being an economically attractive copper and antimony ore, which often also contains traces of silver and mercury.[82–84] Only recently, did the focus of research shifted to thermoelectric applications, after "re-discovering" the high thermoelectric properties and odd low thermal transport prompting further study of the crystal, electronic and thermal properties.

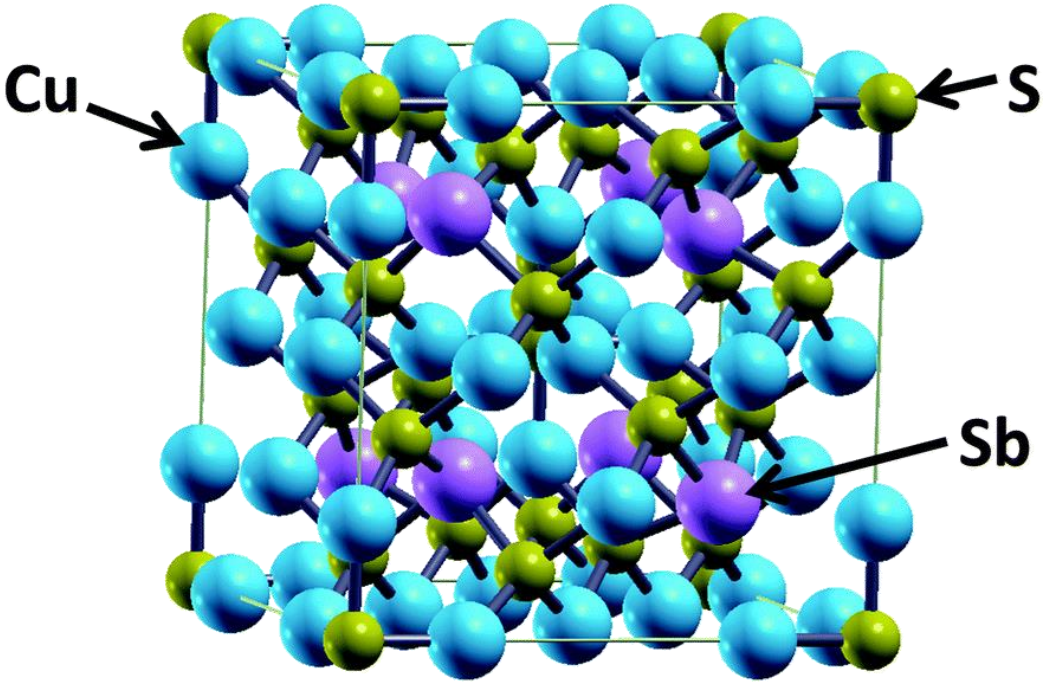

Fig. 11 Crystal structure of tetrahedrite ($Cu_{12}Sb_4S_{13}$).[77]

Although frequently represented by $Cu_{12}Sb_4S_{13}$, a more accurate chemical formula of tetrahedrites is $A_{12}X_4Y_{13}$, where A = Cu (with possible partial substitutions by transition metals, such as Ag, Zn, Fe, Ni, Co, Mn, or Hg); X = Sb (with possible partial substitution by As, Bi or Te); and Y = S (with possible partial substitution by Se). In natural tetrahedrites all these elements can be present, with a great amount of geology and mineralogy studies dedicated to tracing specific compositions to specific geological locations.(74)

The crystal structure of tetrahedrite (Fig.11) is cubic ($I\bar{4}3m$ space group), with 58 atoms per unit cell. The A, X and Y elements are distributed into 5 distinct crystallographic sites. For the sake of simplicity, taking into consideration the ternary tetrahedrite formula ($Cu_{12}Sb_4S_{13}$), the copper atoms possess two different chemical environments: Cu1, which is located in a tetragonal configuration with three S atoms and one Sb atom, and Cu2 that is arranged in a near coplanar triangle configuration with three S atoms. The S atoms are also distributed into two distinct chemical environments, with 12 of the 13 atoms arranged in a tetragonal configuration and the remaining S atom surrounded with six Cu atoms in octahedron configuration. This crystal configuration exhibits two main peculiarities: i) the Cu2 atoms are able to strongly vibrate around their equilibrium position, displaying large anisotropic atomic thermal displacement parameters; and ii) the tetrahedral environment of Sb atoms lacks a fourth S atom, which leads to the formation of 5s lone electron pairs in the Sb atom. These two peculiarities contribute both to a reduced lattice contribution to the thermal conductivity, as the interaction between them results in the modification of the Cu2 environment into an oversized atomic cage, effectively functioning as an anharmonic rattler scattering phonons, which, according to the Phonon Glass/Electron Crystal principle, leads to reduced thermal conductivity.(3,76,85–90)

Regarding the electronic properties, Candolfi, et al.(86) best explains them, after the simple assumption of all atomic bonds to be considered as purely ionic. From this assumption, the chemical formula can be written as $(Cu^{+})_{10}(Cu^{2+})_2(Sb^{3+})_4(S^{2-})_{13}$, which represents a total of 204 valence electrons. Following the Brillouin zone model, if the number of valence electrons are a multiple of the number of electrons of the 1st Brillouin zone, the material is a semiconductor or an insulator, otherwise it is considered a metal since it has accessible conduction bands. In the case of tetrahedrite, the space group $I\bar{4}3m$ has a body-centred lattice of cubic unit cell, making the first Brillouin zone a dodecahedron <110>, which contain 4 electrons(91), thus attesting to the semiconductor nature of the tetrahedrite.

However, from an electronic standpoint, the valence bands of tetrahedrite are not entirely filled, leaving two holes per formula unit, thus the prediction is that the ternary compound can behave as a p-type metal. Another argument to be made about the semiconductor-metallic behaviour of tetrahedrites stems from the real chemical formula that frequently diverges from the classical $(Cu^{+})_{10}(Cu^{2+})_{2}(Sb^{3+})_{4}(S^{2-})_{13}$, denoting different partial substitutions and different ratios of Cu and Sb atoms, following the ionic model.

Although the tendency is to have exactly 2 divalent cations per unit formula, the reality of situation is that by following the ionic model, for the chemical stability of the tetrahedrite, 26 positive charges are required, which can also be met with additional Cu or Sb atoms on the unit formula, like $(Cu^{+})_{14}(Sb^{3+})_{4}(S^{2-})_{13}$ and $(Cu^{+})_{12}(Sb^{3+})_{4.67}(S^{2-})_{13}$, or any combinations of additional Cu and Sb atoms, following the formula $Cu_{12+x}Sb_{4+y}S_{13.}$ These additional forms of tetrahedrite have already been confirmed experimentally[92–96] and some studies supporting this approach to improving thermoelectric performance.[97–100] These variations in the formula also change the number of valence electrons, which are, in general, between 204 and 208. Although indicative of semiconductor behaviour, any number in between attest a potential metallic behaviour, which seems to indicate that tetrahedrite can manifest p-type metallic behaviour for certain compositions that, although less energetically favourable than the standard two divalent cations per formula unit, are still possible.[89]

This change from metallic to semiconductor behaviour can be seen in the experimental work of Suekuni et al.[101] for $Cu_{12}Sb_{4}S_{13}$, Fig. 12, in which the transport and magnetic properties of ternary tetrahedrites were studied. The ternary tetrahedrites have a metallic-insulator shift in both the Seebeck coefficient, electrical resistivity and thermal conductivity dependence of temperature around the 85 K. Below this temperature there is a sharp increase in electrical resistivity, which combined with an increase in Seebeck coefficient from a 25 $\mu V\ K^{-1}$ at 85 K to 100 $\mu V\ K^{-1}$ at 60 K, brings confirmation of a semiconductor-like state at low temperatures.[102,103] Thermal conductivity also decreases below 85 K, which is associated with the increased in electrical resistivity that translates into lower electronic contributions to the thermal conductivity. Below the transition temperature the magnetic susceptibility drops, adopting an antiferromagnetic ordering.

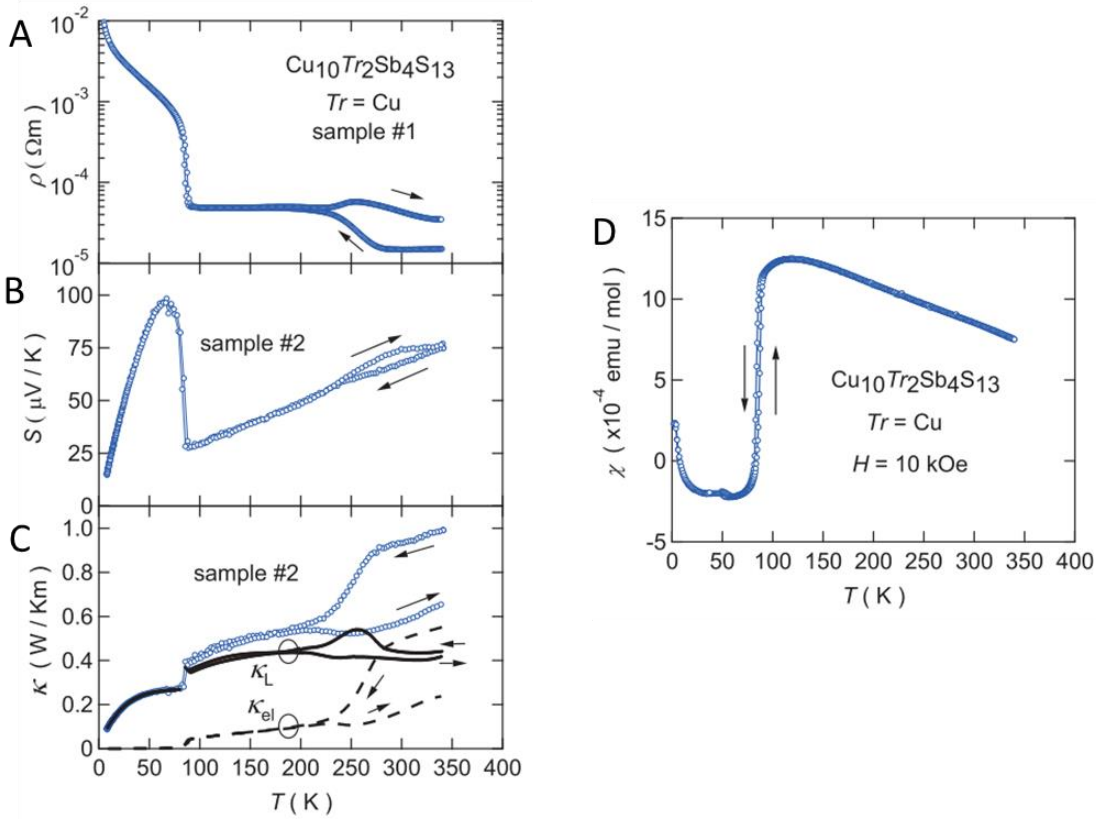

Fig. 12 Temperature dependence of (A) electrical resistivity ρ, (B) Seebeck coefficient S, (C) thermal conductivity κ and field-cooled magnetic susceptibility χ for tetrahedrite $Cu_{12}Sb_4S_{13}$[101]

In the same work[101], other tetrahedrites of the type $Cu_{10}Tr_2Sb_4S_{13}$ (Tr= Ni, Zn, Co, Fe or Mn) were also studied (Fig.13). It was shown that semiconductor-like behaviour was still observed in these quaternary tetrahedrites, which also exhibited very low thermal conductivities (in the order of 0.4 W/m.K). However, the presence of different metals leads to significant increase in the electrical resistivity and Seebeck coefficient, with the high electrical resistivity, unfortunately, preventing the possibility of high zT values. Thus, further optimization of the thermoelectric properties of this material requires the adjusting of the transition metal dopant content for, aiming for the hole concentration optimization, which translates into maximized PFs. This strategy for improving the thermoelectric efficiency has been at the centre of various studies[53,76,104–125], most notably the one carried out by Heo at al.[109] that claimed to have achieved a record high zT of 1.13 at 575K with the formula $Cu_{11}MnSb_4S_{13}$ (Fig.14A). However, this result lacks confirmation, as studies with similar compositions did not achieve the same zT, which could be attributed to differences in the synthesis procedure. Also studied was the performance of doped-tetrahedrite based nanocomposites, with two notable studies achieving a zT around 1.15 at 723 K (Fig.14 B and C) with a $Cu_{11.5}Ni_{0.5}Sb_4S_{13}$ based nanocomposite with 0.7%vol of BiI_3[126] and 0.3%vol of Nb_2O_3[127].

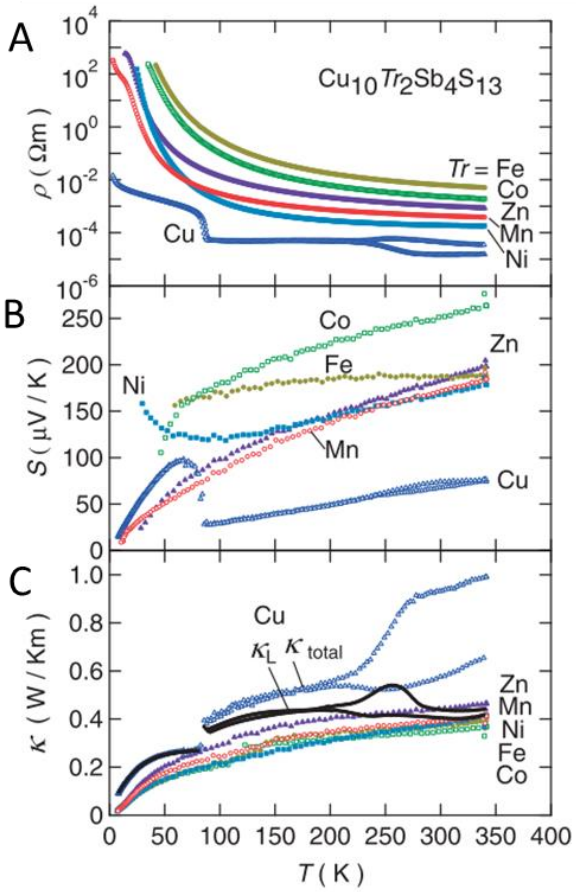

Fig. 13 Temperature dependence of (A) electrical resistivity ρ, (B) Seebeck coefficient S and (C) thermal conductivity κ for various tetrahedrites, $Cu_{10}Tr_2Sb_4S_{13}$ (Tr= Ni, Zn, Co, Fe or Mn)[101]

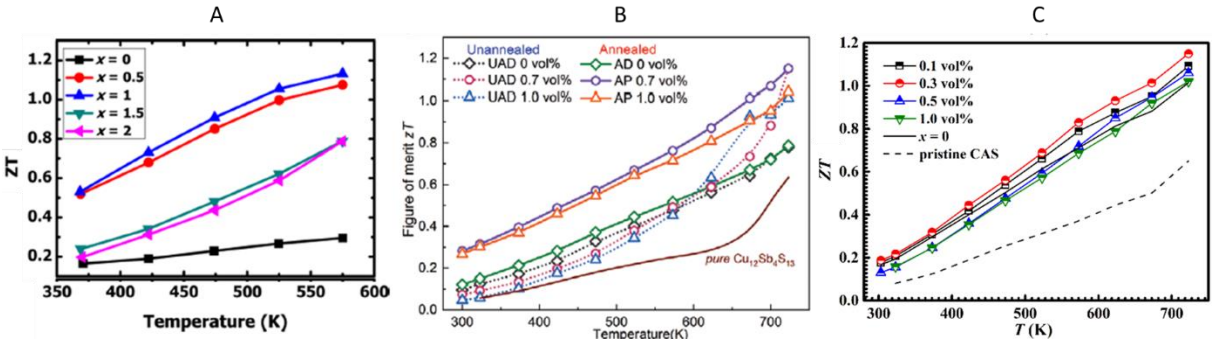

Fig. 14 Variation of zT with temperature for A) $Cu_{12-x}Mn_xSb_4S_{13}$[109], B) $Cu_{11.5}Ni_{0.5}Sb_4S_{13}$ samples with a %vol of BiI_3[126] and C) $Cu_{11.5}Ni_{0.5}Sb_4S_{13}$ samples with a %vol of Nb_2O_3[127].

Other studies focused on the effect of substituting Sb with other elements (Fig.15), such as: As, Si, Te and Bi.[128–137] With these dopants it was possible to achieve a max zT of 0.63 at 723K for $Cu_{12}Sb_{3.8}Si_{0.2}S_{13}$; 0.68 at 700K for $Cu_{12}Sb_2As_2S_{13}$, to 0.92 at 723 K for $Cu_{12}Sb_3TeS_{13}$ and 0.88 at 723 K for $Cu_{12}Sb_{3.9}Bi_{0.1}S_{13}$. Each of these elements were expected to improve the thermoelectric properties in a different way. Si doping was expected to increase charge carrier concentration as additional electrons would be introduced when replacing Sb^{3+}= [Kr] $4d^{10}$ $5s^2$ for Si^{+4}=$1s^2$ $2s^2$ $2p^6$, which should result in an increased number

of valence electron. In this case, however, charge concentration only increased moderately up to 0.2 Si stoichiometric content, thus a slightly higher zT over ternary tetrahedrite at 723K with zT=0.63. Since As belongs to the same group in the periodic table as Sb, it should have the same number of valence electrons and should have a smaller ionic radius thus producing a contraction of the unit cell resulting in a shortening of the energy band gap, this could mean that doping with As results in a tetrahedrite-tennantite ($Cu_{12}Sb_4S_{13}$- $Cu_{12}As_4S_{13}$) solution that is more conductive, which explains why $Cu_{12}Sb_2As_2S_{13}$ would display the best results, has it possess the optimum combination of increased electrical conductivity without a great increase in thermal conductivity. In the case of Te doping, the electronic configuration of Te^{3+}= [Kr] $4d^{10}$ $5s^2$ $5p^1$, has one more electron than Sb^{3+}, contributing to a higher charge carrier concentration, thus optimizing the PF. And similar to As, Bi belongs to the same group as Sb, also meaning the same number of valence electrons and no expected change to carrier concentration, however, since Bi has a larger ionic radius, its introduction in the structure causes lattice distortions and produces point defects, leading to the creation of Cu vacancies that can act has electron acceptors, thus increasing the hole concentration, nevertheless, this interference in the unit cell favours the occurrence of secondary phases that often have an adverse effect on the thermoelectric properties of the overall sample.

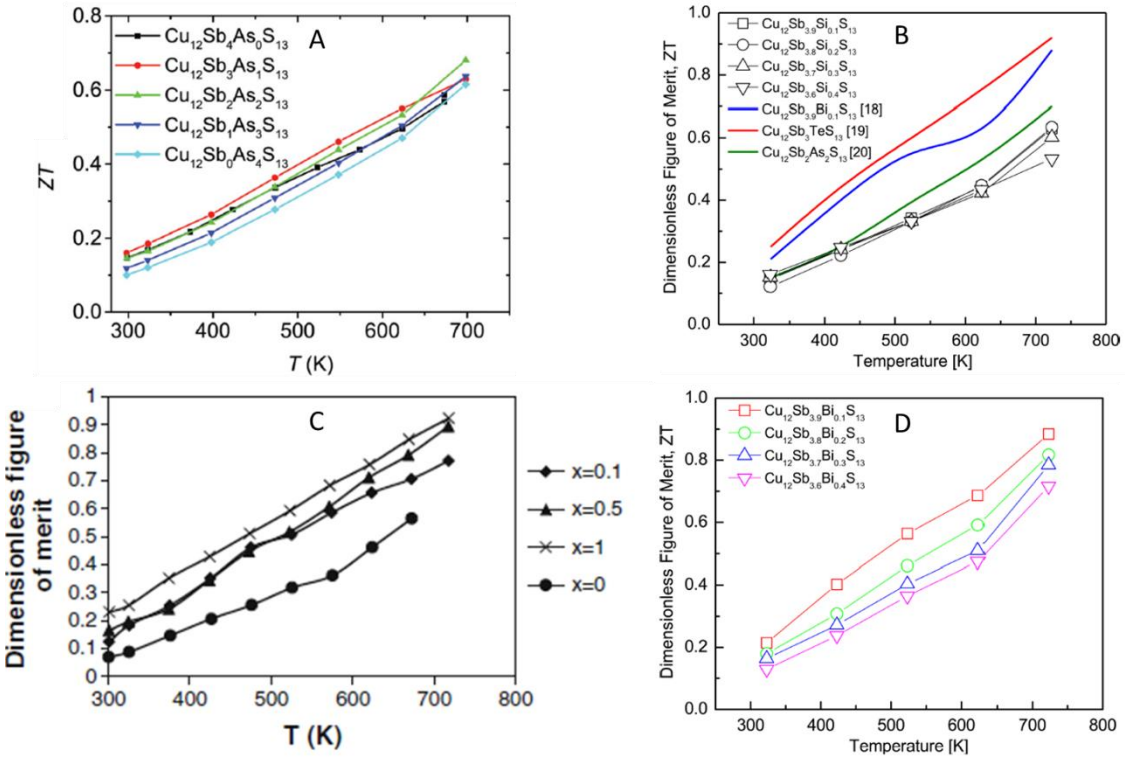

Fig. 15 Variation with temperature of the figure of merit ZT for various tetrahedrites doped on the Sb site: (A) $Cu_{12}Sb_{4-x}As_x$ S_{13}[128]; (B) $Cu_{12}Sb_{4-x}Si_x$ S_{13}[129]; (C) $Cu_{12}Sb_{4-x}Te_x$ S_{13}[130]; and (D) $Cu_{12}Sb_{4-x}Bi_x$ S_{13}[131].

The substitution of S for Se (Fig.16) was also studied[112,138–142] which resulted in a zT=0.86 at 720K for the formula $Cu_{12}Sb_4S_{12}Se$. This increase comes from a reduction of the total thermal conductivity, with contradictory results regarding the electrical conductivity measurements, which can be connected to the tendency of formation of secondary phases that increases with Se content increase.

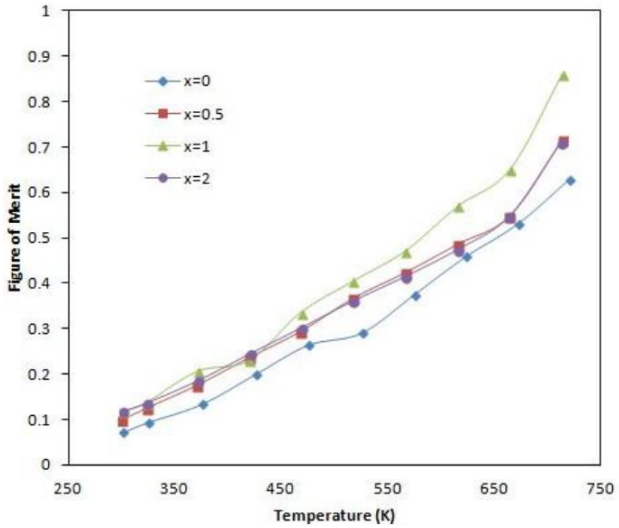

Fig. 16 Temperature dependence of the figure of merit (zT) of tetrahedrite doped with Se, $Cu_{12}Sb_4S_{13-x}Se_x$.[112]

Since substitutions of the three elements in tetrahedrite are able to improve its thermoelectric properties, this opens the possibility of further optimization of the thermoelectric efficiency via co-doping, with some studies already reported on the effect of different combinations of dopants.[134,135,137,140–142] Amongst them, figures of merit as high as 0.9 at 723K were achieved for $Cu_{11.975}Zn_{0.025}Sb_4S_{12.8}Se_{0.2}$[140], Fig. 17. Following this line of reasoning, the present project seeks to study the effects of co-doping with Ni and Se in tetrahedrite.

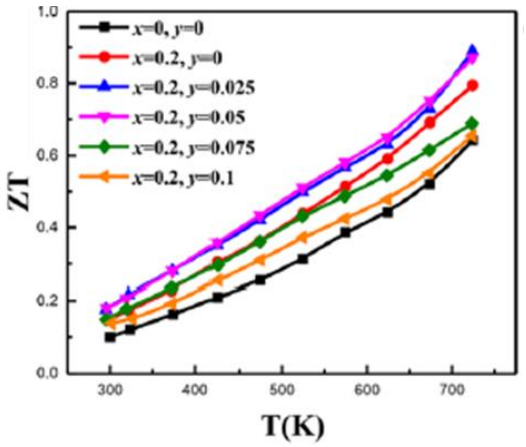

Fig. 17 Temperature dependence of the figure of merit (zT) of tetrahedrite doped with Se, $Cu_{12-x}Zn_xSb_4S_{12.8}Se_{0.2}$ [140]

2. METHODOLOGY AND EXPERIMENTAL PROCEDURE

2.1 BAND CALCULATIONS AND THERMOELECTRIC PROPERTIES SIMULATIONS METHODOLOGY

In order to provide a frame of reference to compare with later measurements of thermoelectric properties, simulations of the temperature-dependent behaviour of thermoelectric properties were carried out for tetrahedrites with different Ni and Se content, namely: Seebeck coefficient, electric resistivity, and thermal conductivity.

The method chosen in this study to make these simulations is based on the method used by Ravaji et al.[143] and Knízek et al[144], which combines the Wien2K software[145], for density of states simulation, with BoltzTraP software[146], for the actual simulation of thermoelectric properties.

2.1.1 Wien2K Package

The calculations were made using the Wien2k package. This program is based on the density-functional theory and uses the full-potential linearized augmented plane-wave method with the dual basis set. This method operates by partitioning the crystal unit cell into two parts: non-overlapping spheres centred around each atom, where there is rapid variation of wavefunctions, and the remaining interstitial region with constant potential. Then, each basis function is defined as a planewave in the interstitial region connected to a linear combination of atomic-like functions located in the spheres, this way it is possible to obtain an efficient representation throughout space.

The Wien2K package is a combination of several independent programs working interchangeably through C-Shell scripts. In Fig. 18 is represented a schematic of the various data flow lines and program usage transpiring in order to fulfil the calculations. The process is divided into two stages: initialization, which consists of running a few small auxiliary programs that prepare inputs for the main programs; and the SCF cycle, a self-consistency cycle, where the inputs defined in the initialization stage are run until the convergence criteria is met[145], after which a Density of States (DOS) diagram is obtained.

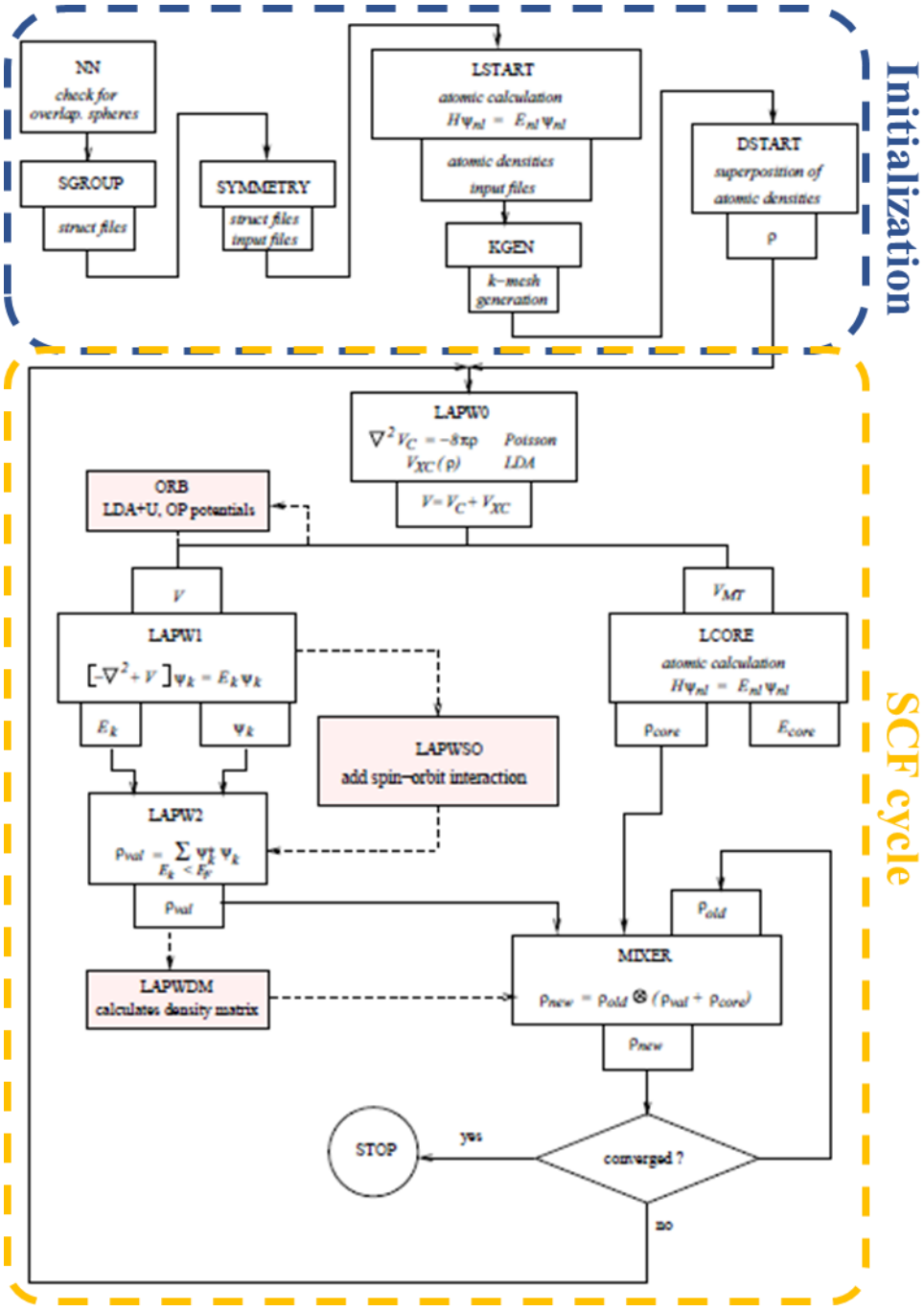

Fig. 18 Program flow in Wien2K.[145]

In order to carry out the calculations, some approximations were taken, namely: the exchange-correlation energy which was calculated using local spin-density approximation and the generalized gradient approximation (GGA), as well as the modified Becke-Johnson exchange potential. It should be added that GGA was calculated in accordance with the standard parametrization proposed by Perdew, Burke and Ernzerhof.[147] With the linearized augmented plane-wave method, the software performs the electronic structure calculations for crystals, solving the Kohn-Sham equations for the total energy, Kohn-Sham eigenvalues, and

ground state density to obtain energy bands of a many-electron system. To improve the description of 3d electrons, the GGA+U method was used. In this method, an orbital dependent potential is introduced for the chosen set of electron states, the 3d states of Cu and Ni in this case. This additional potential has an atomic Hartree–Fock form but with screened Coulomb and exchange interaction parameters. The fully localized limit version of the GGA+U method was employed. All calculations were performed to account for spin-polarization, with a plane wave cut off energy of 100 keV and a 9 x 9 x 9 k-point mesh in the reciprocal space of the first Brilloin zone.

Several compositions were simulated following the formula $Cu_{12-x}Ni_xSb_4S_{13-y}Se_y$, where x and y varied between the values 0.0, 0.5 and 1.0. Unfortunately, it was not possible to analyse the composition x and y equal to 1.5, because the size and complexity of unit cell necessary for the simulation is too big and becomes unsustainable with the available computational power to make the calculations, with the longest simulation having taken well over 1 month to converge.

2.1.2 BoltzTraP Simulations

The main objective of the BoltzTraP software is to bridge between DFT data and other simulations like phase field simulation. The code uses Fourier expansion and the simulated crystal structure from Wien2K in the calculations, with the space group symmetry being maintained by star function, until the extrapolated energies fit the energy-bands obtained in the DFT calculations of the Wien2K. Once the fit is complete, through Boltzmann transport theory it is possible to calculate the overall transport properties of the simulated material. This method has already been tested to calculate transport coefficients of intermetallic compounds, high-temperature superconductors and thermoelectric materials.[146,148–150]

To conduct these simulations, it was assumed a constant relaxation time for charge carriers, and by establishing a mesh of k-points (up to 5000) on the energy bands, it was possible to calculate electrical conductivity (σ), Seebeck coefficient (S) and thermal conductivity (κ) through the formulas:

$$\sigma_{i,j} = \frac{e^2 t}{\hbar^2} \int \frac{\partial \varepsilon}{\partial k_i} \frac{\partial \varepsilon}{\partial k_j} \left[-\frac{\partial f_{\mu^*(T;\varepsilon)}}{\partial \varepsilon} \right] \partial \varepsilon \qquad (11)$$

$$\kappa_{i,j} = \frac{\tau}{\hbar^2 T} \int \frac{\partial \varepsilon}{\partial k_i} \frac{\partial \varepsilon}{\partial k_j} (\varepsilon - \mu^*)^2 \left[-\frac{\partial f_{\mu^*(T;\varepsilon)}}{\partial \varepsilon} \right] \partial \varepsilon \qquad (12)$$

$$S_{i,j} = \frac{1}{eT} \frac{\int \frac{\partial \varepsilon}{\partial k_\beta} \frac{\partial \varepsilon}{\partial k_j} (\varepsilon - \mu^*) \left[\frac{\partial f_{\mu^*(T;\varepsilon)}}{\partial \varepsilon} \right] \partial \varepsilon}{\int \frac{\partial \varepsilon}{\partial k_i} \frac{\partial \varepsilon}{\partial k_j} \left[\frac{\partial f_{\mu^*(T;\varepsilon)}}{\partial \varepsilon} \right] \partial \varepsilon} \qquad (13)$$

Where ϵ, is the energy variable, T the absolute temperature, μ^*, chemical potential, e is the electron charge and τ the relaxation time.[143,151]

2.2 SYNTHESIS AND PROCESSING TECHNIQUES

The preparation methodology (Fig.19) is heavily based on previous similar studies[105,112,139], mainly following the synthesis methodology employed by Alves, et al.[141]. The procedure is the same for all samples and the conditions were kept as similar as possible. However, some adjustments in the temperature and duration (time) of the annealing step were taken in order to reduce the quantity of secondary phases in samples of specific compositions.

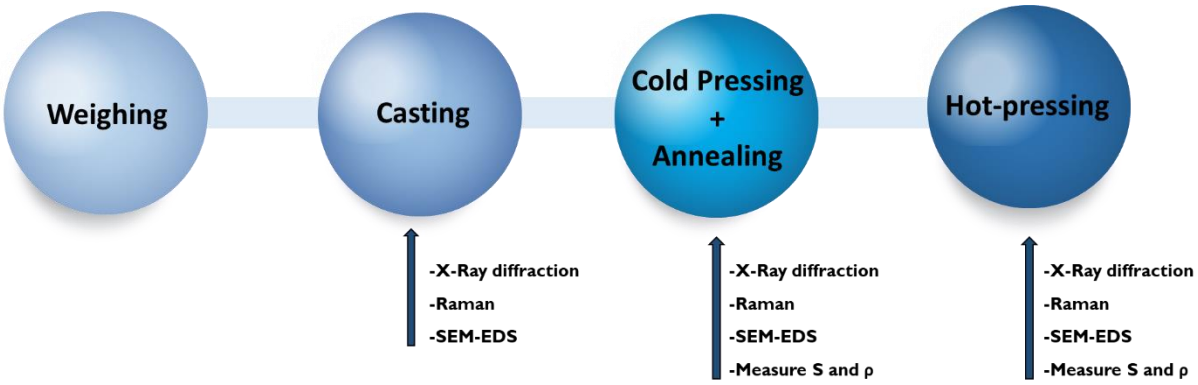

Fig. 19 Simplified schematic of the synthesis and characterization process.

2.2.1 Preparation by solid-state reaction (Casting and Annealing Steps)

$Cu_{12-x}Ni_xSb_4S_{13-y}Se_y$ ($0 \leq x \leq 1,5$; $0 \leq y \leq 1,5$) samples were synthesized by reacting the pure elements (Cu (99.99%), Ni (99.99%), Sb (99.99%), S (99.99%), Se (99.99%) from Sigma-Aldrich and Alfa Aesar) inside quartz ampoules sealed under vacuum (10^{-1} Torr). The amount of each element in each sample was calculated for the desired stoichiometric ratio to make a mixture with a total mass of 1.5g, except for sulphur, which, in an effort to offset losses due evaporation, was added an excess of ~1.0 wt%. The samples were submitted to a casting process with multiple steps: (I) were heated up to 920ºC at the rate of 4 ºC /min and kept at that temperature for 1 hour; (II) then cooled to 700 ºC at the rate of 11 ºC /min kept for 10 min; after which (III) were cooled to 650 ºC at the rate of 11 ºC /min kept for 20 min; and finally (IV) cooled to 400 ºC the rate of 4 ºC /min kept for 18 hours before removed.

After casting, the ampoules are broken, and the samples removed. Then for the annealing step, samples are crushed with a mortar, pestle into a fine powder and shaped into pellets by cold pressing with a hydraulic press. The obtained disks were sealed under vacuum (10^{-1} Torr) inside quartz ampoules and subjected to a temperature treatment at 450 ºC for 7 days. Samples with solely selenium doping underwent the 350 ºC annealing temperature for

14 days, due to a higher tendency to produce secondary phases. Similarly, samples of undoped tetrahedrite also underwent annealing at different conditions, 300 ºC for 14 days, to minimize the appearance of secondary phases.

2.2.2 Densification by hot-pressing

Hot-pressing is the pressing at high temperatures of a powder, allowing the production of fully dense powder compacts, with controlled microstructures, and minimal porosity (near 100% density).

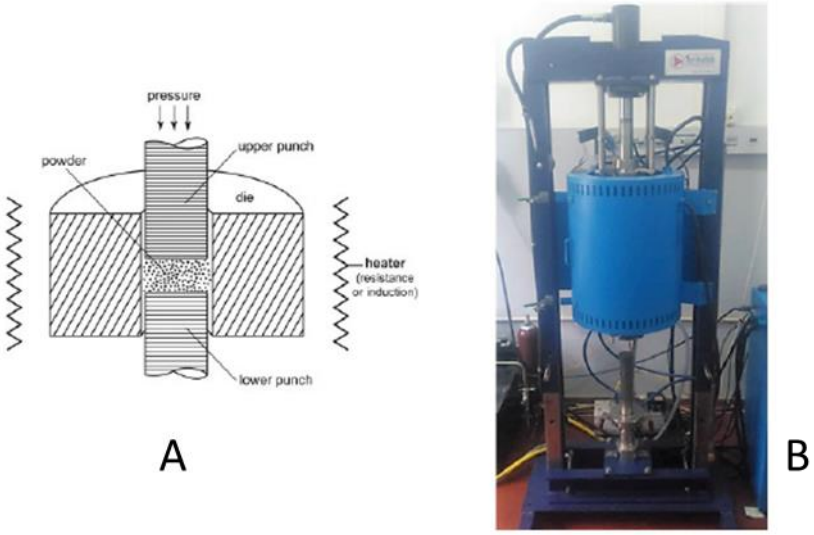

Fig. 20 A) Schematic of the setup of the powder loaded in the graphite mould , and B) Termolab SV-Prensa 200/2018 equipment.

After annealing, samples were crushed again with a mortar and pestle into a fine powder. Then, the powder was loaded into a graphite mould as shown in Fig. 20A, with two graphite sheets separating the powder from the upper and the lower punch, to prevent the adhesion of the final compacted sample and facilitate extraction without breaking. The equipment used was a Termolab SV-Prensa 200/2018 with single action pressing (only the upper punch moves, the other parts are stationary). The graphite mould with the powder was then loaded into the chamber which was evacuated and filled with an inert (Argon) atmosphere. The system was then heated through indirect resistance at the rate of 25 ^{o}C /min, the pressure was increased at the rate of 3MPa/min and were maintained at 575^{o}C and 56 MPa for 90 min, respectively. Finally, the samples were cooled to room temperature and the pressure released at the rates of 25 ^{o}C /min and 3MPa/min, respectively.

2.3 CHARACTERIZATION TECHNIQUES

2.3.1 Powder X-ray Diffraction

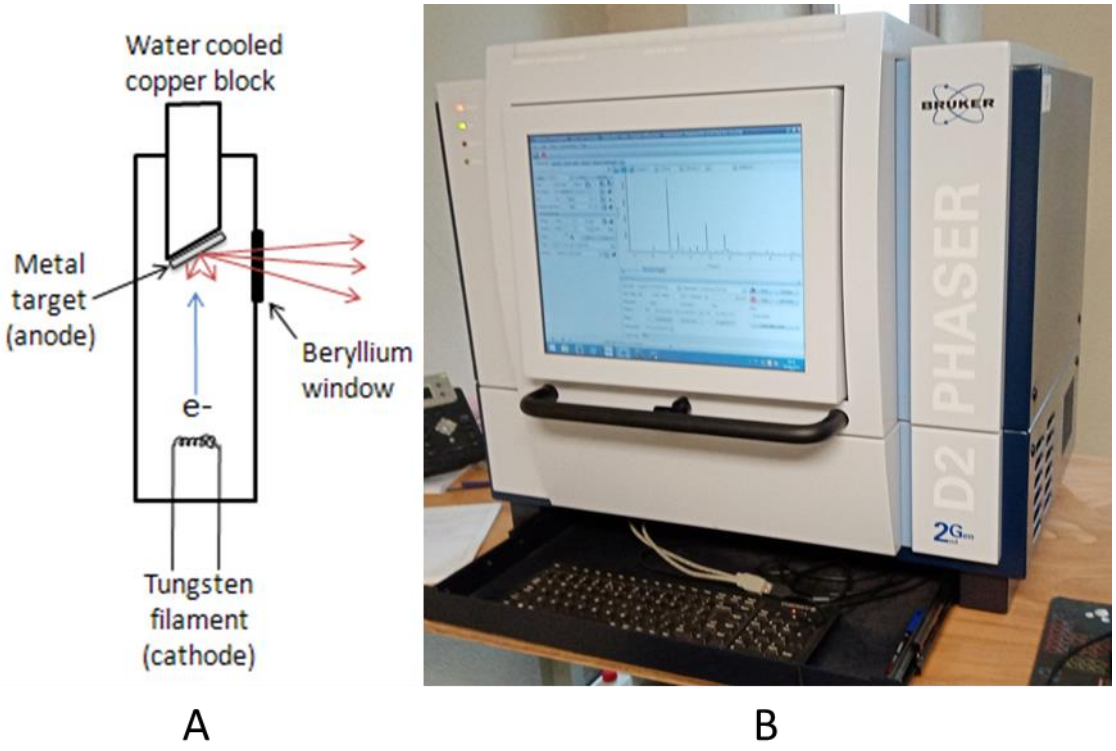

Fig. 21 A) Schematic of a typical X-ray tube, and B) D2 Phaser Bruker 2nd Gen equipment.

In 1912, Max von Laue discovered that crystalline structures are able to diffract X-ray wavelengths similar to the spacing of planes in a crystal lattice and because most materials have a unique diffraction pattern, X-ray diffraction became a common technique for phase identification and determining atomic spacing in crystal structures.

A typical X-ray diffractometer has four main components elements: a X-ray source, a sample holder, a X-ray detector, and a way to change the incidence angle at which the X-rays hit the sample surface. For the source, it is generally used a X-ray tube (Fig.21A). The tube contains a block of water-cooled copper that supports a metal target anode and a tungsten filament cathode in an evacuated atmosphere. When high voltage passes through the tungsten filament, it heats up and potential difference between the cathode filament and the anode, causes electrons to be ejected towards the metal target. The accelerated electrons knock core electrons out of the water-cooled metal target, and to fill the vacancies in the core orbitals, electrons from outer orbitals drop down to fill the vacancies, emitting X-rays in the process, which then exit through the beryllium window. The emitted X-ray radiation is in the form of a small spectrum of wavelengths designated “white radiation”, resulting in X-ray fluorescence.

Thus, to reduce fluorescence filters and monochromators are often used to thin out the "white radiation" to a desired characteristic wavelength.

When the monochromatic X-rays hit the surface of the sample, they are partially scattered by the atoms of the crystal structure, but the part that is not scattered passes through the first layer and is again partially scattered by the atoms of the new layer or passes through to the next layer, so on and so forth. The scattering and interference is what causes the diffraction and the signature pattern. Overall, for a material to diffract radiation it must be crystalline, in order to have an ordered regular arrangement of the atoms, and distance between layers, spacing or grating constant, *d*, must be similar to the wavelength of the incident radiation. When both these conditions are met, Bragg's law ($z\lambda=2d.\sin(\theta)$) can be applied and used to calculate the spacing, where θ is the incidence angle of the X-ray, λ the wavelength of the incident X-ray and *z*, the diffraction order represented by an integer value. Because the d-spacing is characteristic to each crystal, it can be used to identify the crystal phase, generally by comparison with reference patterns. The constructive interference of the diffracted radiation is what results in the diffraction pattern after reaching the detector.

Older diffractometers used to have a film as a detector. Nowadays, most modern equipment uses transducers as detectors. These devices produce electrical signals when exposed to radiation. Transducers often are used as photon counters, resulting in intensity being determined by the number of counts in a determined amount of time.[152–155]

The equipment used in this project was D2 Phaser Bruker 2nd Gen diffractometer (Fig. 21B). Because the focus is in studying the whole bulk material to have an overall understanding of the material, the samples were ground into a fine powder and placed on a silicon wafer, the sample holder for the equipment. To even the layer of agglomerated powder in the silicon sample holder, a few drops of acetone, combined with gentle stirring was applieded. The measuring conditions used were as follow: 35mA current; 40kV tension; through a 1 mm slit; measured in the in the 10º- 65º 2θ range; in 0,02º steps each taking 0.6 seconds.

Phase identification was performed using the Crystallography Open Database with the Diffrac.Eva software version 5.1.[156]. Cell parameters were extrapolated from the diffraction data and used in the Unit Cell software[157], that uses the non-linear least squares method, to calculate the lattice parameter of the Tetrahedrite phase.

2.3.2 Raman Spectroscopy

This non-destructive technique for chemical analysis is based on the interaction of light with chemical bonds within a material, providing information on the chemical structure, phase, polymorphy, crystallinity and molecular interactions.

This technique is based on Raman scattering, a phenomenon first observed by the Indian physicist C.V. Raman and his research partner K.S. Krishnan in 1928.[158] Raman scattering happens when light is scattered by the molecule, the photons transfer energy to electrons when hitting the molecular electron cloud leaving the molecule in a higher virtual energy state. However, these energy states are so short-lived, often called virtual states, that molecule almost immediately reverts back to the original lower energy state, re-emitting the photon as scattered light. In the bulk of the scattering events, the photon is re-emitted with the same energy and, by extension, the same wavelength, it had prior to hitting the molecule electron cloud. In other words, the scattered photon is equal to the incident photon, this form of scattering is called elastic or Rayleigh scattering. On the other hand, in the significantly smaller portion of the scattering events (approximately 1 in 10^7 photons)[155] where the scattered photon has a different energy and, thus, different wavelength, a form of scattering named inelastic scattering or Raman scattering. In one form of this scattering, the molecule instead of reverting back to the original vibrational energy state from the virtual energy state, it ends up being excited to a higher vibrational level (Stokes-Raman scattering) or being relaxed to a lower vibrational level (Anti Stokes-Raman scattering), resulting in the emission of a photon with less energy and a higher wavelength or with more energy and smaller wavelength than the incident photon, respectively, as it is shown in Fig. 22.

While in a quantum mechanics level, both forms of Raman scattering are equally likely to occur, since it is more likely for molecules to be in the lowest vibration energy state, Stokes Raman scattering ends up being the most probable to occur, thus having more intense signals than Anti-Stokes Raman. It should also be noted that not all vibration modes can be detected using Raman spectroscopy. Only when the molecular polarizability changes during a vibration, is it possible to detect this vibrational mode, often being referred to as “Raman Active” vibrational mode.

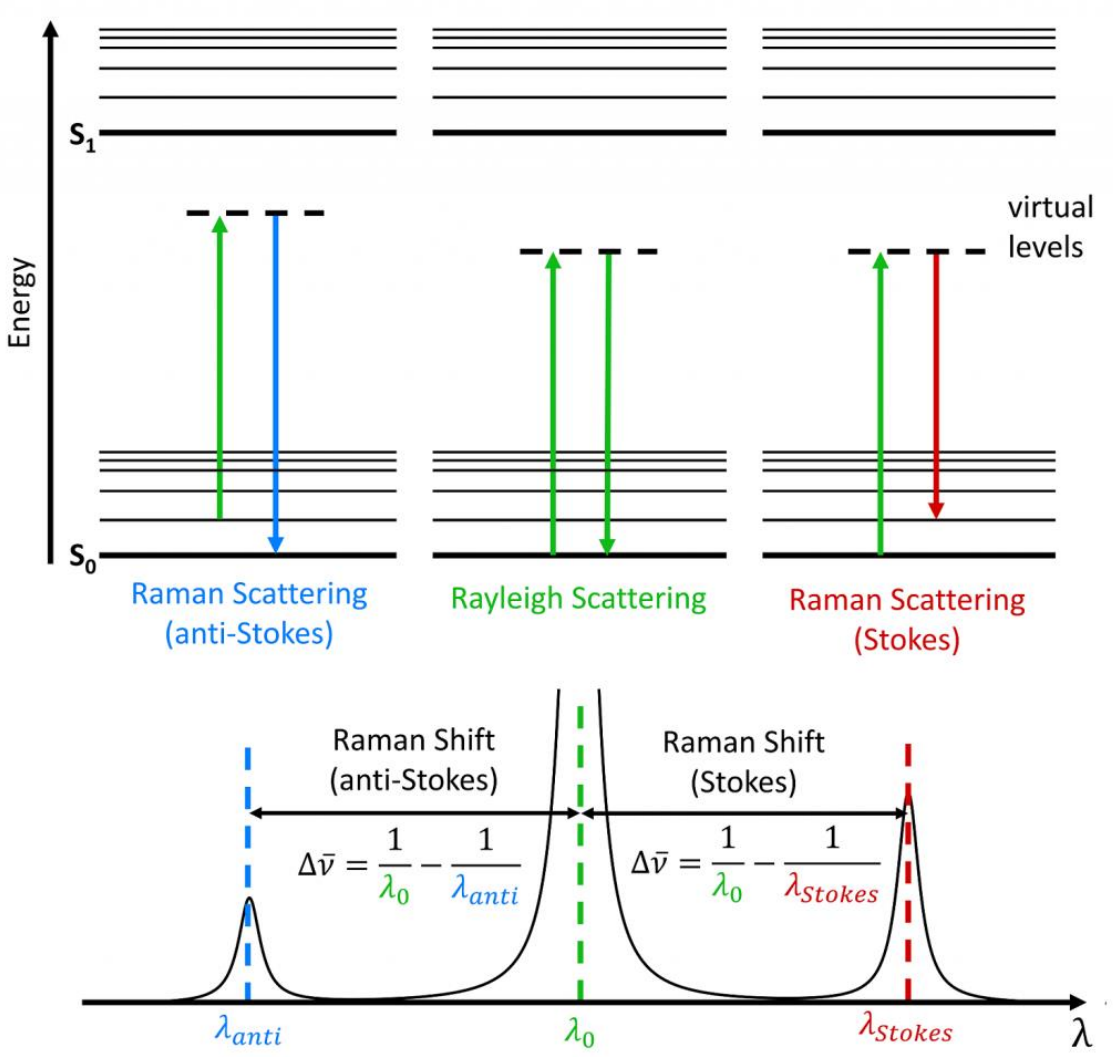

Fig. 22 Visual representation of the changes to the electron energy state in Rayleigh, Stokes Raman and Anti-Stokes Raman Scattering and respective position of the signal for each scattering in a Raman spectrum.

Because photons with different wavelengths will also have different energy that will result in excitation to different vibrational modes and so on, it becomes difficult to properly compare the patterns and extract proper information of the vibrational modes. Thus, what is actually used in Raman spectra is the Raman shift expressed in wavenumber ($\Delta\nu$, cm^{-1}), which is the difference between the inverse of incident wavelength, λ_0 and the inverse of the scattered wavelength, λ_1, following the formula:

$$\Delta\nu = \left(\frac{1}{\lambda_0} - \frac{1}{\lambda_1}\right) \qquad (14)$$

The position (Raman shift) of the peaks in the Raman spectra, or scatter, provides information about the molecule and permits the identification of phases and compounds in the sample.

At its core, a Raman spectrometer is composed of 4 main elements: laser source; sample illumination and collection system; spectral analyser; and detection and computer control and processing system. For Raman spectroscopy its necessary to have a highly monochromatic incident light, thus, it is commonly used a continuous-wave laser with a wavelength in the visible spectrum or close to the range. The laser beam then passes through a filter to reduce the beam to a single wavelength, which is then focused on the sample. The resulting Raman scattered light is collected by the lenses and passes through a filter to remove Rayleigh scattering which is more intense than Raman scattered light. Afterwards the filtered scattered light is diffracted in a grating and then registered in the detector.[159–161]

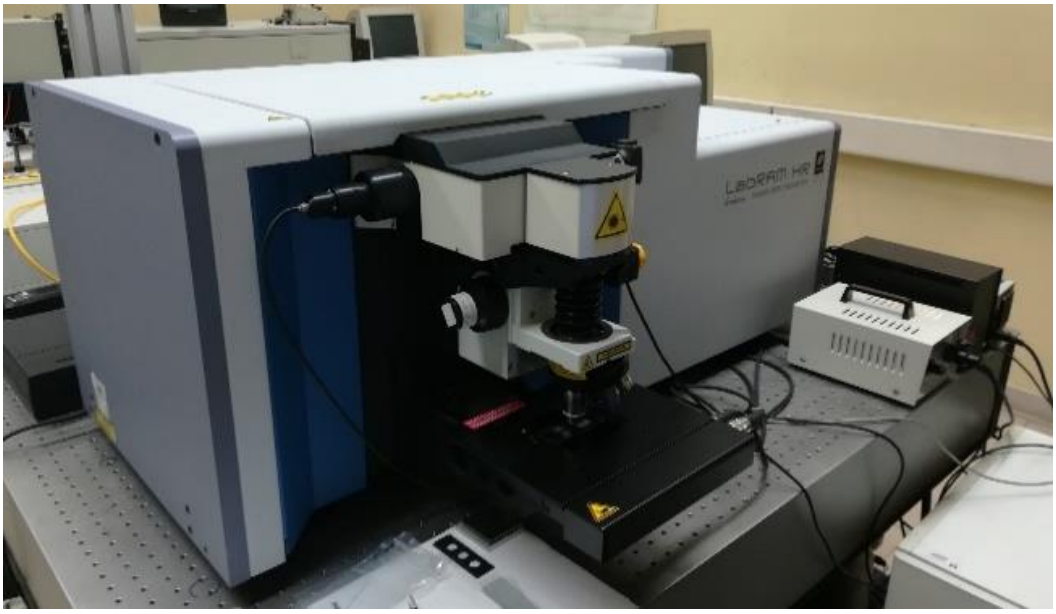

Fig. 23 Setup of the Horiba LabRam HR Evolution Raman microspectrometer

For this work, a Horiba LabRam HR Evolution Raman microspectrometer was used, as seen in Fig.23, with a diode laser with 532 nm wavelength and 10mW power. All the samples were analysed in the 150-1400 cm^{-1} wavenumber range with a 100x objective. The spectra acquisition parameters were 5 scans of 30s duration each at 100% laser intensity for as-cast and annealed samples, and 5 scans of 300s duration each with 10-25% laser intensity for hot-pressed samples, this change in laser intensity was to minimize surface sample disintegration due to high laser intensity, while still obtaining an eligible spectra with minimized peaks related to material ejection.

2.3.3 Scanning Electron Microscopy- Energy Dispersive X-ray Spectroscopy

Scanning Electron Microscopy (SEM) is a technique to analyse the microstructure and identify the phases that exist in a sample. With this non-destructive technique, it is possible to study the surface of materials, by focusing an electron beam and performing multiple scans over a specific area of the sample surface. This results in a SEM image with three-dimensional appearance with large depth-of-field.

When high-energy electrons hit the sample surface, they suffer elastic and inelastic scattering. Elastic scattered electrons also called Back Scattered Electrons (BSE) are scattered by the atoms of the sample, generally have between 60 to 80 % of the energy of incident electrons and are deflected at high angles. On the other hand, inelastic scattered electrons also called Secondary Electrons (SE), are emitted at low angles from the electron shell of the atom after interaction with the electron beam and generally have significantly lower energy. Through the signal obtained with two different detectors (one for SE and other for BSE) it is possible to gather information about the topography contrast with the SE signal and the chemical composition contrast from BSE signal.

Fig. 24 Thermo Scientific Phenom ProX generation 6 desktop SEM with integrated EDS system.

In addition, when coupled with Energy Dispersive X-raySpectroscopy (EDS), it enables elemental analysis of the surface sample. As it happens, when the SE are ejected from the atom's electron shell, higher energy electrons move to fill the vacancy, resulting in relaxation

of the electron cloud and the emission of the excess energy in the form of X-rays. Because each element has a unique atom structure, they end up with a unique set of peaks on the electromagnetic emission spectrum. The energy of these peaks is predicted by the Moseley's law, where, simply put, it is stated that the square root of the frequency of the emitted X-ray is approximately proportional to the atomic number of the element. As such, by also comparing the intensity of the peaks, EDS allows the qualitative and semi-quantitative analysis of the chemical composition of a thin layer at the surface of the sample.[161]

The SEM-EDS equipment used was a Thermo Scientific Phenom ProX generation 6 desktop SEM with integrated EDS detector (Fig.24). This technique was used to identify the phases observed in as-cast, annealed and hot-pressed samples, and provide an estimated chemical composition of the tetrahedrite phases. All micrographs depicted wherein were captures with an applied voltage between 15-20 keV with BSE detector.

2.3.4 Low temperature transport properties measurement

To measure the Seebeck coefficient (*S*), a system based on the apparatus developed by Chaikin was used[162]. The original Chaikin's apparatus was originally designed to measure highly conducting organic single crystals, however, with some adjustments, it is possible to adapt to inorganic samples, like the presently studied tetrahedrite samples. The samples need to be shaped into a plate-like geometry with dimensions around 2x1.5x0.5 mm, then placed between two gold foils, glued directly with GE varnish to the quartz block to ensure good thermal contact. The gold foils are attached to a single crystal quartz block each, the blocks have copper wiring coiled around them that will enable heating the quartz blocks, thus functionally behaving like two independent heat sinks with separate temperature control. Two gold wires are then connected to the sample with silver paint to establish the electrical contact. For the voltage measurements, a low frequency AC technique was used with a maximum temperature gradient in the sample of 1 K. One differential pair of thermocouples are attached to the quartz blocks to measure the temperature difference between them, another thermocouple is attached in one end to one of the quartz blocks and the other junction is immersed in iced water at 0ºC that serves as a temperature reference, this thermocouple measures the quartz block temperature and gives the temperature of the measurement.

In the beginning of operations, the system is heated up to 310K and then slowly cooled to 20K. The closed cycle cryostat being cooled by successive cycles of compression and subsequent expansion of helium gas, like in a refrigerator, with the overall temperature within the chamber being controlled through a heater and a silicide diode thermometer situated in the cold finger of the cryostat with the help of a PID temperature controller.

Since the temperature gradient is being measured in the quartz blocks and not directly in the sample, an excellent thermal coupling of the system is required so that ΔT in the sample is as similar as possible to ΔT between the quartz blocks. However, thermal losses are inevitable, leading to a temperature gradient lower in the sample than in the quartz crystals, heavily dependent on the quality of the thermal contact. Consequently, the measured Seebeck coefficient is usually underestimated in comparison with the real Seebeck coefficient of the material, errors can be minimized assuring the best possible thermal contact combined with optimum sample's geometry. In the case of tetrahedrites, optimum geometry was long thin plates in order to have the highest gradient possible on the samples and thus minimize thermal losses.

Measurements of electrical resistivity (ρ) at low temperature were obtained through the four-point technique with an AC resistant bridge for high resolution in measurements of small resistances. This technique was chosen to avoid errors associated with contacts resistances. For these measurements, the sample needs to be shaped into a bar-like geometry with regular cross-section and dimensions around 2x0.5x0.5 mm. The setup of the wires and the samples are shown in Fig.25: the two outer wires pass current (I) through the ends of the bar, the inner wires kept at a distance (l') detect the voltage difference (ΔV) across the sample. The voltage measured can be converted into electrical resistivity through the equation:

$$\rho = \frac{\Delta V.w.h}{I.\,l'} \qquad (15)$$

Where w is the width of the bar and h the thickness. A 1mA current was injected in the sample while the temperature was controlled with thermocouples directly connected to the sample. Electrical transport properties were measured in the 20-300K temperature interval, at a rate of 0.3K/min for Seebeck coefficient and 0.5K/min for electrical resistivity, using a closed-cycle cryostat.

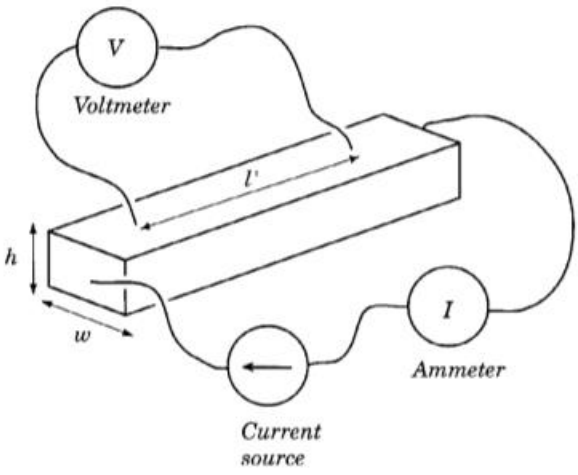

Fig. 25 Schematic of the position four wire connections used according to the 4-point method.[163]

3. COMPUTATIONAL RESULTS

3.1 WIEN2K

The simulated band diagram and corresponding density of states (DOS) for ternary tetrahedrite ($Cu_{12}Sb_4S_{13}$) were obtained from the Wien2K calculations and are presented in Fig. 26 and 27, respectively. The calculations converged into a non-magnetic solution, and since the Fermi level resides below the top of the valence band complex, tetrahedrite can be described as an almost metallic heavily doped p-type semiconductor.

Simulations of the DOS for tetrahedrite with different dopant contents were also calculated. The first observable difference in DOS of tetrahedrites due to containing Ni in their composition, is the increase of asymmetry between minority and majority spin, which pertains to the transition of the top of the valence band past the Fermi level, in the spin down condition. This transition results in an apparent energy band gap reduction, a sign that could be interpreted as increased conductivity. The asymmetric response to minority and majority spin, points to a change in magnetic properties, similar to what was reported by Suekuni et al.[164]: the magnetic momentum carried by Ni results in a magnetic susceptibility proportional to Ni content and postulate that Ni atoms adopt an antiferromagnetic interaction with each other. Also there is an increase in the density of states below Fermi level, which is connected to the electronic configuration of Ni^{2+}, [Ar]3d8, when compared to Cu^{2+}, [Ar]3d9. This means there is one less electron, and since tetrahedrite is a p-type semiconductor, where “holes“ are the charge carrier, after doping with Ni there are more charge carriers (holes) thus there is an increase in the density of states.[124]

Se content does not appear to contribute in the DOS, which would translates to an expecting limited impact in the thermoelectric performance of tetrahedrite. Thus, it is expected that Ni doping causes a greater variation in the thermoelectric properties than Se doping. However, it should be noted that while Se seemingly does not contribute directly to the density of states, doping with certain amounts of Se alters the contribution of Cu, S, Sb and Ni. Comparing DOS diagrams of composition with the same Ni stoichiometric content shows that there is very little difference in the DOS between a stoichiometric content of Se of 0.0 or 1.0, which can be attributed to the fact the Se and S belonging to the same column in the periodic table, so isovalent doping will result in the same number of valence electrons, thus it is not expected to alter the charge carrier concentration, which explains the no perceivable change to the DOS. However, for the compositions with a Se stoichiometric

content of 0.5, there is a significant increase in the intensity peaks. This odd nonmonotonic response to Se content, might be a result of lattice strain caused by the larger size of the Se atom comparatively to the S atom it replaces. Lattice strains and other defects in the crystal structure might create energy levels within the band gap or alter the density of states, with the latter being observed in the simulations containing Se= 0.5. these distortions can result in charge carrier traps resulting in localized energy levels or altering the mobility or reconfiguration speed of the charge carriers.[165]

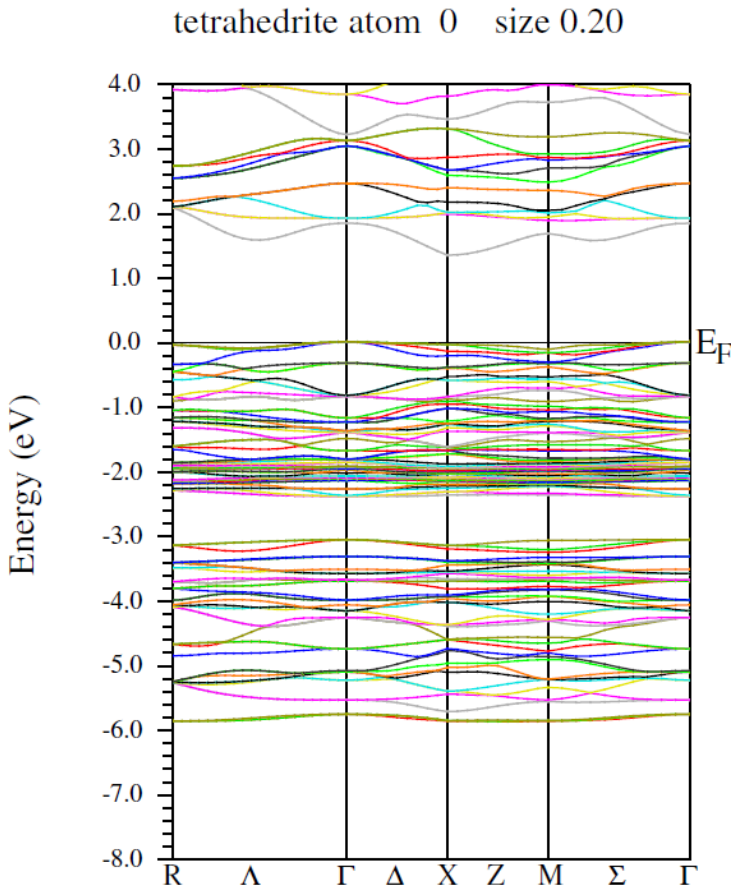

Fig. 26 Band diagram of undoped tetrahedrite simulated by the Wien2K software.

Unfortunately, due to limitations in the available computational capability, performing the simulations with stoichiometric dopant content x or y=1.5 became unreasonable, as it would require simulating extremely large and highly complex unit cells in the Wien2K, resulting in extremely morose computational cycles that often failed to converge due to the high level of complexity. Amongst the simulations carried out, the longest successful simulation took over a month the conclude calculations.

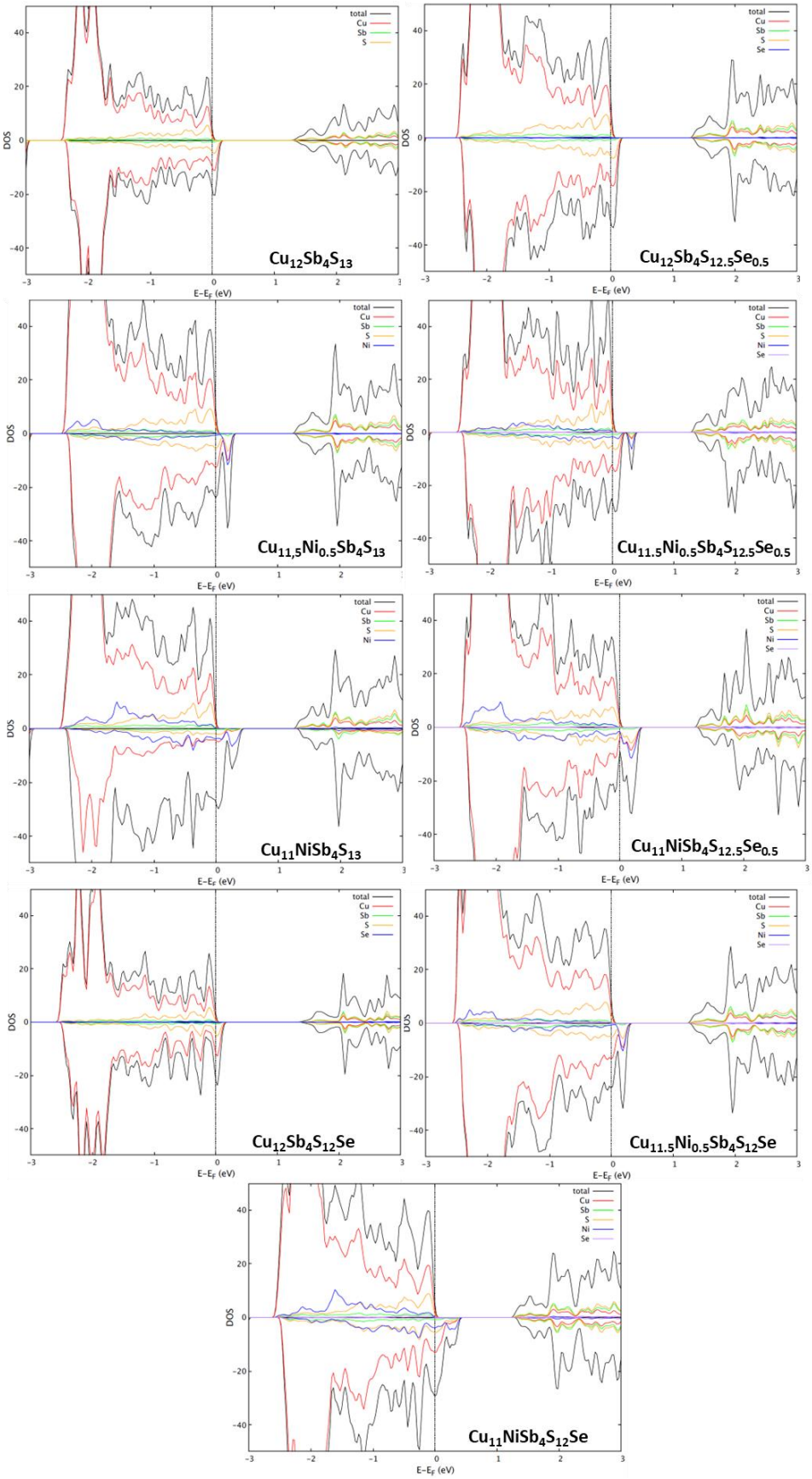

Fig. 27 Density of States calculated through the WIEN2k package of tetrahedrite with specific stoichiometric content of Ni and Se, in accordance with the formula $Cu_{12-x}Ni_xSb_4S_{13-y}Se_y$ ($0 \leq x \leq 1,0$; $0 \leq y \leq 1,0$)

3.2 BOLTZTRAP SIMULATIONS

To have a better framework to compare the experimental results, simulations of the thermoelectric properties were carried out by combining the Wien2K package for predicting the electronic structure of the crystalline structure of tetrahedrite, with the BoltzTraP software, to provide an estimation of the Seebeck coefficient, electrical resistivity, and thermal conductivity, which are represented in Fig. 28. Unfortunately, the composition $Cu_{11}NiSb_4S_{12.5}Se_{0.5}$ failed to converge even after numerous attempts, thus it is not presented.

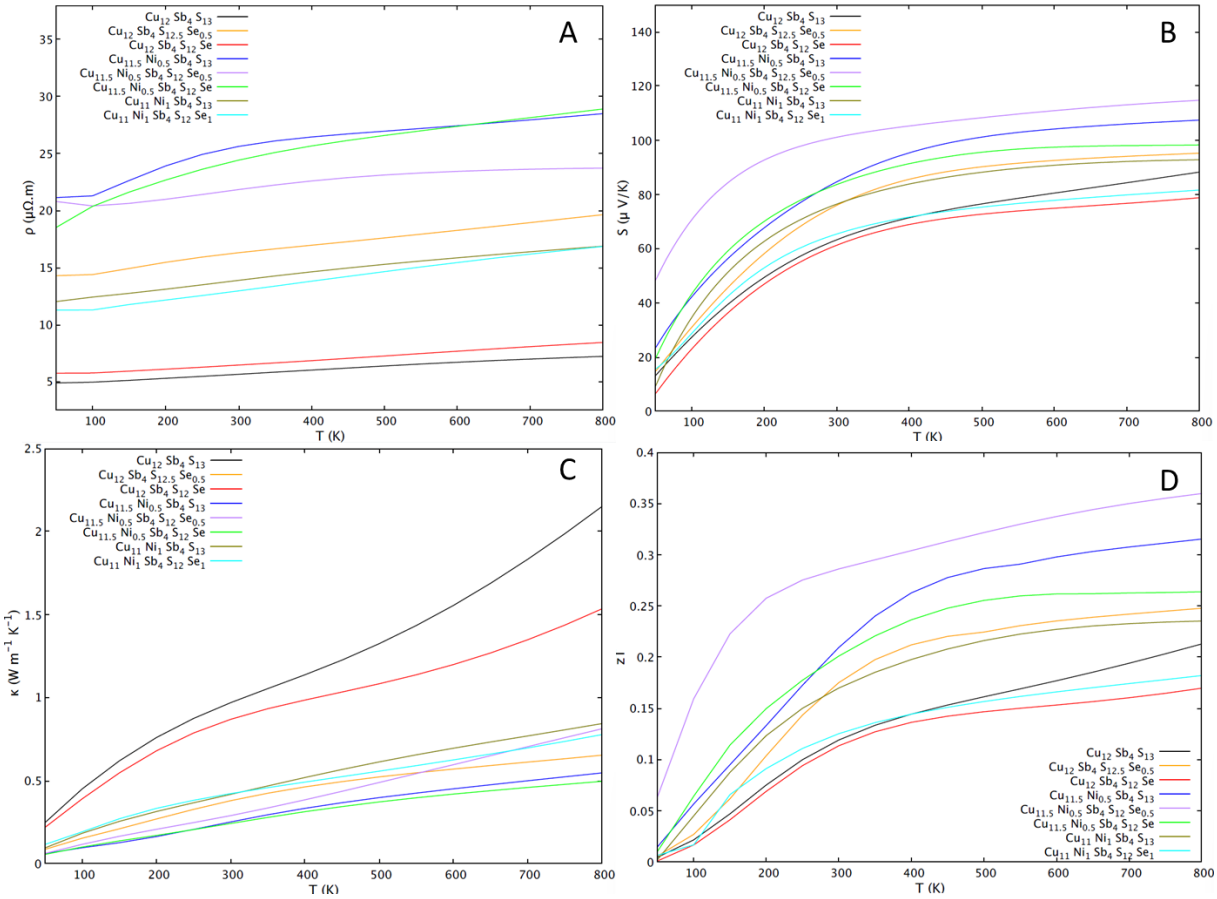

Fig. 28 BoltzTraP estimations of the temperature dependence of thermoelectric properties of tetrahedrite with different dopant contents following the formula $Cu_{12-x}Ni_xSb_4S_{13-y}Se_y$ ($0 \leq x \leq 1,0$; $0 \leq y \leq 1,0$): A) electrical resistivity; B) Seebeck coefficient; C) thermal conductivity; D) figure of merit, zT.

The BoltzTraP calculation show that Ni doping increases electrical resistivity and Seebeck coefficient, and decreases thermal conductivity, resulting in an overall improvement of the figure of merit. Noteworthy, is the fact that, contrary to what was expected, despite the increase in the number of "holes" due to Ni doping, the compositions ended up becoming more resistive. All compositions presented a positive Seebeck coefficient, which is an indication of the conductivity dependant on positive charge carriers, ergo "holes", and following this assumption, increasing "hole" concentration should have improved

conductivity, however, as explained by Suekuni et al.[76], where Ni doped tetrahedrites revealed a negative measurement for Hall coefficient, which contradict the assumption convened by the positive Seebeck coefficient, in other words, according to Hall coefficient negative measurement, conductivity is dependent on negative charge carriers, ergo, electrons. Combining both these arguments, only attests to tetrahedrite having a metallic-semiconductor behaviour, resulting in the conductivity being dependent on both "holes" and electrons, and the increase in electrical resistivity not for the added "hole" but for the missing electron. Nonetheless there was a significant narrowing of the band gap in the minority spin of compositions containing Ni, leaving the question whether Ni-doped tetrahedrite might have spin-dependent transport properties, which could significantly alter the overall thermoelectric performance.

In regard to Se doping, as expected, $Cu_{12-x}Ni_xSb_4S_{13}$ and $Cu_{12-x}Ni_xSb_4S_{12}Se$ compositions showed very similar properties between compositions with the same Ni content (x), and compositions with Se=0.5 showed a higher difference in the variation of their properties with temperature. This is best observed when comparing $Cu_{12}Sb_4S_{13}$ and $Cu_{12}Sb_4S_{12}Se$ compositions with the differentiated curve for $Cu_{12}Sb_4S_{12.5}Se_{0.5}$. Other studies have also reported a non-monotonic relation between Se content in tetrahedrite and thermoelectric properties, often suggesting that there is a specific optimum stoichiometric Se content for tetrahedrite. However, as different studies analysed different value intervals for both Se content and temperature, it resulted in different and, to some extent, seemingly contradicting conclusions. Lu et al[166], reports that when comparing tetrahedrite with Se stoichiometric content of 0.0, 0.5, 1.0, and 2.0, experimental results show that doping with Se reduced the electrical resistivity and thermal conductivity and provided a minor increase in the Seebeck coefficient. Despite the decrease over ternary tetrahedrite, electrical resistivity exhibited a non-monotonic response to Se content, achieving the lowest values Se content= 1.0 and increasing for Se content=2.0. The low resistivity with Se content=1.0, was attributed to a potential increase in hole mobility due to a modified electronic structure near the band edge caused by the Se substitution, which was corroborated, after performing some DFT calculations, by noticing a dispersion of the P and Γ bands, resulting in smaller average band effective mass, which in turn translates to higher charge carrier mobilities and higher electrical conduction. As for the increased resistivity for Se content=2.0, following similar calculations, was attributed to increased intervalley scattering. Zhu, et al.[140], on the other hand, studied experimentally smaller Se substitutions, varying the stoichiometric content

between 0.0 and 0.4 in 0.1 increments. They reported the same minor increase in Seebeck coefficient with Se content, but both electrical resistivity and thermal conductivity were non-monotonic with Se content, showing reducing results up to Se content=0.2 and 0.1, respectively, and increasing for higher contents, with the sample with Se content=0.4 having nearly the same electrical resistivity as ternary tetrahedrite but a higher thermal conductivity. They attributed this behaviour to the increased presence of Cu_3SbS_4 secondary phase, which resulted in a vacancy of S atoms of the tetrahedrite phase. This led to a smaller electron concentration (with a minimum in the Se content=0.2) which is translated in a higher concentration of holes that increased the mobility thus decreasing electrical resistivity. While this explanation is not suitable to the simulations results (which intrinsically assumes to be dealing only with a tetrahedrite phase), both these studies[140,166], present the conclusion that minute changes in Se content doped into the tetrahedrite may result in widely different thermoelectric properties, despite the fact that Se and S are isovalent and present very similar electronegativity (2.55 and 2.58, respectively, Pauling scale).

Overall, the simulations show that doping with both Ni and Se can induce significant changes to the thermoelectric properties, with most samples exhibiting higher electrical resistivity, higher Seebeck coefficient and lower thermal conductivity than un-doped tetrahedrite. This culminates in generally higher simulated figures of merit for most compositions, with the exception of the $Cu_{11}NiSb_4S_{12}Se$ (above ~400K) and $Cu_{12}Sb_4S_{12}Se$ ones.

The calculations also suggest that the potentially highest zT will be achieved with the sample $Cu_{11.5}Ni_{0.5}Sb_4S_{12.5}Se_{0.5}$, with an estimated $zT \approx 0.30$ at 300 K. This result, while promising, must be taken with a grain of salt, as various assumptions and approximations were taken in the calculation.

4. EXPERIMENTAL RESULTS

4.1 AS-CAST AND ANNEALED SAMPLES

4.1.1 X-ray Diffraction

Powder X-ray diffractograms of as-cast samples (Fig. 29) show that the most intense peaks are consistent with the tetrahedrite structure (COD 9004148), indicating that even with just the casting step, the samples are mainly composed of tetrahedrite. There are peaks related to secondary phases, namely, a chalcostibite phase with the presence of selenium ($CuSb(S,Se)_2$), which are evidenced by single wider peak in the 27-29º interval rather than the typical double peak in the 28.35 and 28.67º position. This is a result of the juxtaposition of the two peaks characteristic of the chalcostibite phase with 5 main peaks that are diffracted by a chalcostibite like crystal with Se replacing S ($CuSbSe_2$); the covellite (CuS) phase, with peaks around 31.76º, and copper sulphide, Cu_2S, with a peak at around 45.80º that does not coincide with tetrahedrite pattern.

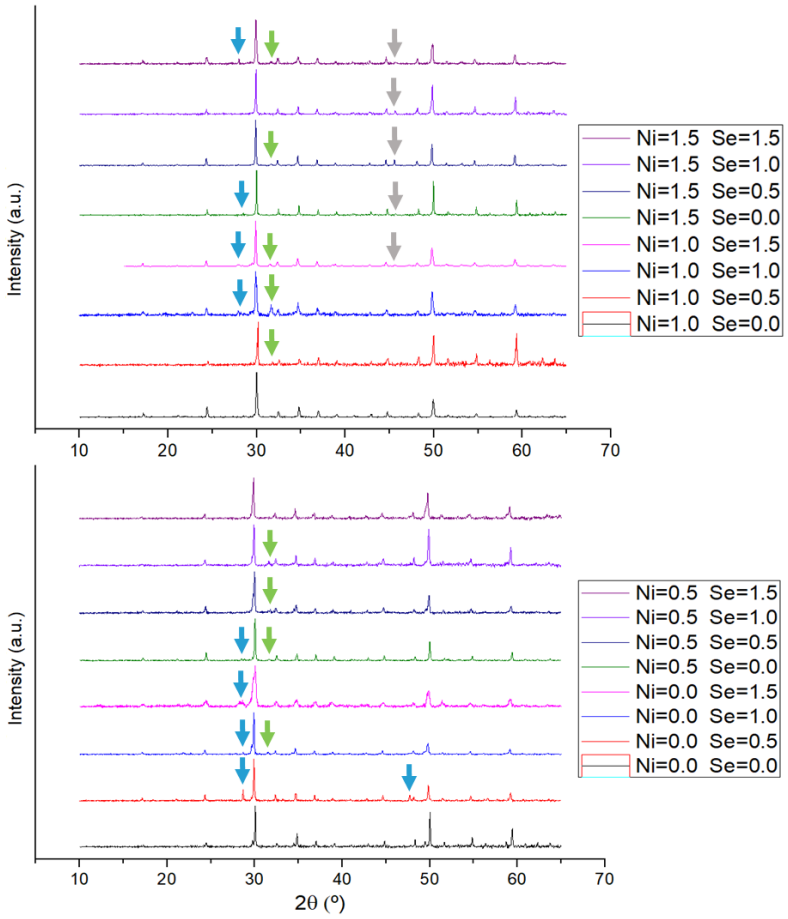

Fig. 29 Powder X-ray diffractograms of as-cast $Cu_{12-x}Ni_xSb_4S_{13-y}Se_y$ samples. Peaks of secondary phases are indicated by arrows: green for Covellite (CuS); blue for Chalcostibite ($CuSb(S,Se)_2$); in grey Copper sulphide (Cu_2S).

At the as-cast stage, chalcostibite and covellite phase distribution in the samples does not appear to possess a particular relation with any composition of dopant. On the other hand, the Cu_2S phase only appears in samples with high Ni content ($x \geq 1.0$), which could be interpreted as the presence of Ni favouring the formation of this phase, possibly by replacing copper in the tetrahedrite phase. This, combined a non-homogenic solid solution, could create regions with higher concentration of copper which would in turn produce the Cu_2S phase.

After annealing, the presence of these extra peaks is less prevalent and less intense, with more samples not exhibiting any perceivable peaks from secondary phases (Fig. 30) and indicating that the annealing step plays a crucial role in the mitigation of these secondary phases. Interestingly enough, prior to annealing, samples would frequently display two or more secondary phases, and aside from the Cu_2S only appearing in samples with high Ni content, the distribution of secondary phases did not appear to have a particular correlation with Ni or Se content. However, after annealing, the appearance of secondary phases on top of becoming less intense and frequent, also appear to be related to specific Ni or Se contents.

The chalcostibite phase, for instance, only appears on the diffractograms of samples doped with Se exclusively. This, coupled with an increase of the intensity of chalcostibite peaks, implies that the introduction of selenium, induces the formation of this extra phase. The tendency to form chalcostibite, for this particular group of samples, became one of the major obstacles to the study of these compositions both after annealing and later, after hot-pressing, and forced us to change the annealing conditions to lower temperatures, specifically to mitigate the formation of chalcostibite phase. The reason behind the absence of chalcostibite in the other compositions may be connected to the presence of Ni, which has already been demonstrated to favours the formation of tetrahedrite and reduce degeneration.[106]

In regards to the Cu_2S phase, after annealing, it appears in only two samples with high Ni content ($x=1.5$) and high Se content ($y=1.0$ and 1.5), which lends more credibility to the previous assessment that the presence of Cu_2S phase is apparently connected to the Ni content, but also, given the presence on only high Se content, it appears that at the annealing stage the presence of high total dopant content is also a contributor to its appearance. Also, the absence of this phase on the two other samples with Ni content $x=1.5$, implies that after annealing the sample is more homogeneous, which also logically suggests that samples with high total dopant content may exhibit lower homogeneity than samples with lower dopant content, at least for the present annealing conditions.

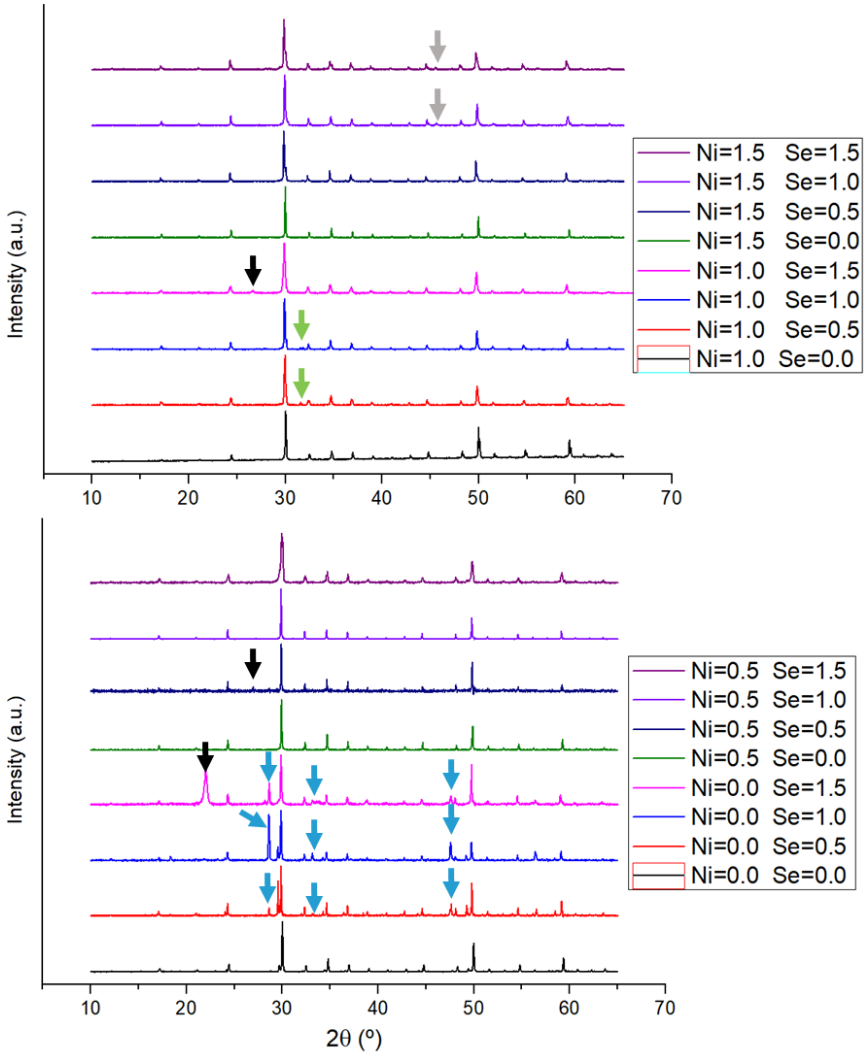

Fig. 30 Powder X-ray diffractograms of annealed $Cu_{12-x}Ni_xSb_4S_{13-y}Se_y$ samples. Peaks of secondary phases are indicated by arrows: green for Covellite (CuS); blue for Chalcostibite ($CuSb(S,Se)_2$); in grey Copper sulphide (Cu_2S); and in black- SiO_2 from a damaged sample holder.

As for the covellite phase, it only appears on $Cu_{11}NiSb_4S_{12.5}Se_{0.5}$ and $Cu_{11}NiSb_4S_{12}Se$ samples, which appears to be associated to those specific compositions, as both samples possess similarly close compositions.

Also of note, is that peaks of tetrahedrite are sometimes doubled, particularly in the undoped sample and the samples only doped with Se. This anomaly is characteristic of ternary tetrahedrite (without doping) and has been extensively studied even before their interest as a thermoelectric material. The splitting of the peaks in the X-ray diffraction pattern is a result of the exsolution of a single tetrahedrite phase into two tetrahedrites phases (a Cu-rich and a Cu-poor) when the solid solution is cooled below what is called the homogenization temperature, which is generally around 120ºC, but may vary depending on the composition.[90,92,93] This phenomenon has been attributed to the migration of copper

resulting in Cu-rich phases with partially vacated Cu12d sites and additional Cu ions present in the interstices of the lattice. The reason behind the anomaly becoming more visible in Se-only-doped samples after annealing, may be connected to the presence of a larger ion creating a bigger deformation of the crystal structure potentially creating bigger interstices that facilitate the Cu migration, or potentially, due to having to use a different annealing temperature, in order to mitigate secondary phase formation, which it might also have altered the cooling conditions, resulting in a more pronounced differentiation of both tetrahedrite phases.

It should also be noted that while not directly observable in the diffractograms, the main splitting peaks around 29.9 º and 49.8º (2θ) are often wider and/or present a irregular shape, which might imply that the exsolution is often occurring, but either the difference between compositions is small or that one phase is significantly more prevalent than the other, thus resulting in small peak differentiation. The exhaustive presentation of the powder X-ray diffractograms is shown in Attachment 1.

The position of the diffraction peaks (2θ) might yield some information regarding the doping condition of the samples, as the doping elements can have different ionic radius. These differences can lead to changes in the lattice cell parameters and, consequently, to small shifts in the position of the tetrahedrite phase peaks. The annealing process promotes the homogenization of the as-cast materials and a potential change in composition due to increased diffusion with higher temperatures.

A surface graph that represents the estimated lattice parameter as a function of composition is shown in Fig. 31. Overall, the lattice parameter of the as-cast materials ranges between 10.3224 to 10.3690(±0.0003) Å, denoting significant changes with the Se concentration, but being almost unaffected by the Nickel content. This is due to the small difference between the ionic radius of Cu^{2+} (73 pm) and Ni^{2+} (69 pm)[167] and to the appreciably larger ionic radius of Se^{2-} (198 pm), when compared with S^{2-} (184pm)[167]. After annealing, there is a tendency for the lattice parameter to increase, ranging now from 10.3215 to 10.3819 (±0.0003) Å, implying that more Selenium is integrating in the tetrahedrite phase. However, also in this case it is not possible to confirm the integration of Nickel in the tetrahedrite phase from X-ray diffraction data, since even after annealing the Nickel content seems to not affect the lattice parameter.

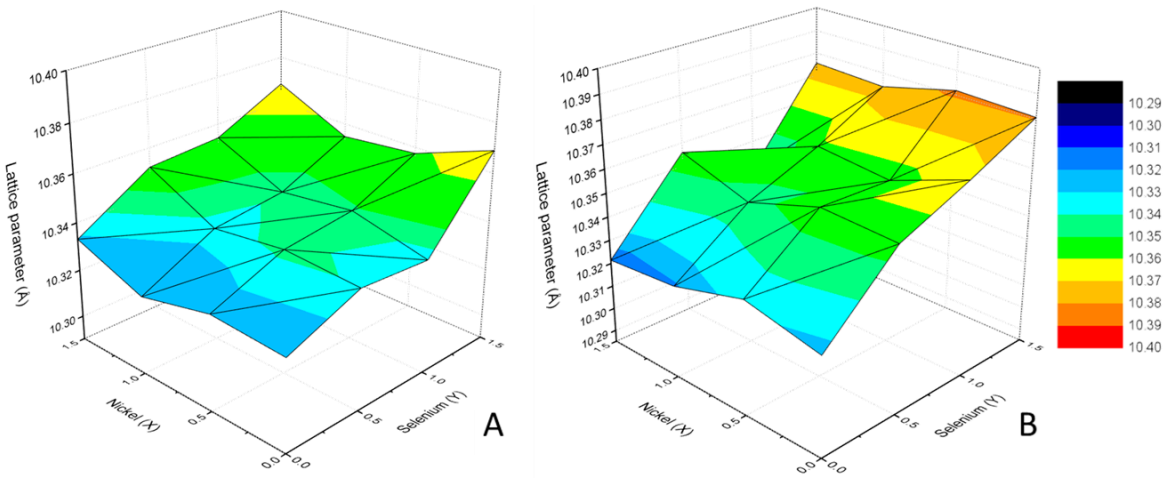

Fig. 31 Lattice parameter dependence on Nickel content (x) and Selenium content (y) in As-cast (A) and Annealed (B) $Cu_{12-x}Ni_xSb_4S_{13-y}Se_y$ samples.

4.1.2 Raman Spectroscopy

The Raman spectra, presented in Fig. 32, allowed the identification of different phases present in the samples, by comparing peak position to database references[168]. The first major constraint is proper identification of tetrahedrite and differentiation of famatinite (Cu_3SbS_4) (COD 9011133), which due to having a similar chemical composition and crystal structure also means a similar Raman signature, with both phases displaying two peaks with the same position (Raman shift) 315 and 348 cm^{-1}, and the only the major difference being which peak is the most intense. Since for tetrahedrite the most intense peak is the 348 cm^{-1}[169,170], it is possible to conclude that all samples exhibit a predominant tetrahedrite phase.

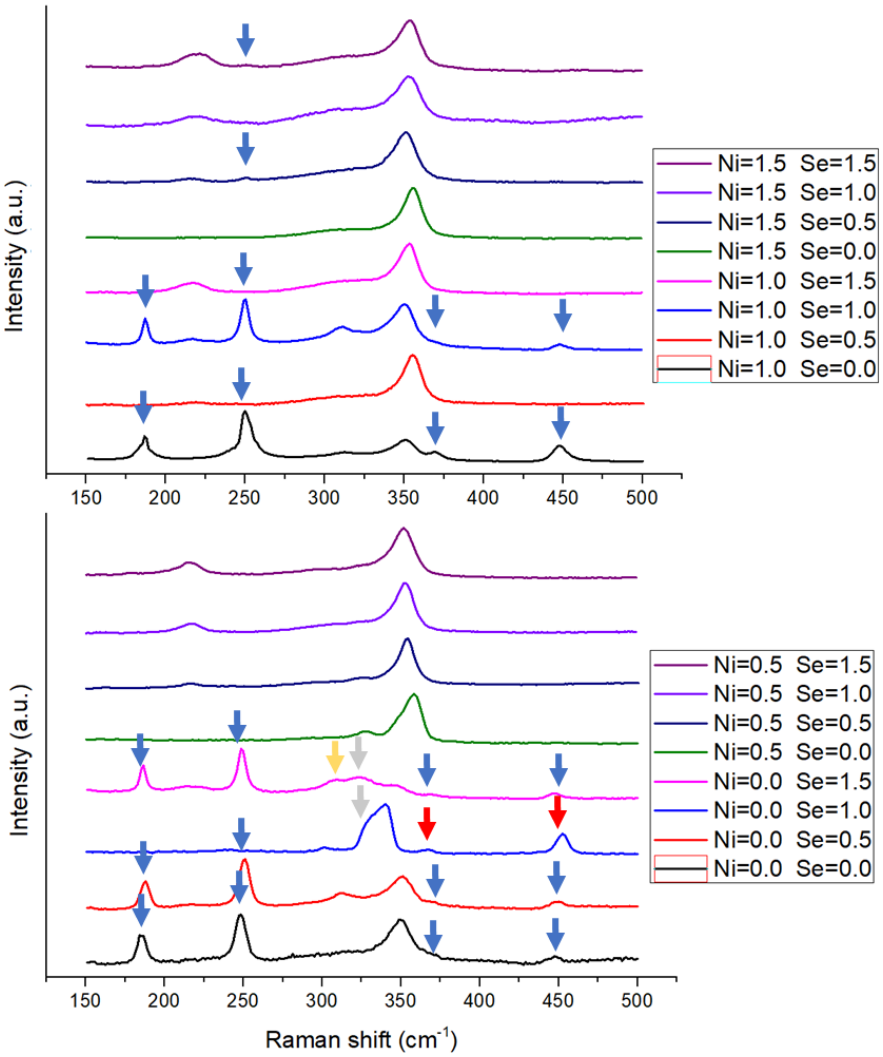

Fig. 32 Raman spectra of several $Cu_{12-x}Ni_xSb_4S_{13-y}Se_y$ samples after casting. The peaks pertaining to the tetrahedrite phase are located in the 315 and 348 cm^{-1} shifts[169,170]. Peaks not related to tetrahedrite phase are indicated with arrows: blue arrows for Cu-S chemical bond of ejected material which are also in common with chalcostibite and copper sulphides; red arrows representing copper sulphide (Cu_xS_y) secondary phase; yellow arrows represent famatinite (Cu_3SbS_4); and grey arrows- chalcostibite ($CuSbS_2$).

Pertaining to other phases, occasionally some samples display a small peak around the ~450 cm^{-1} position, which considering the elements present in the samples (Cu, Sb, S), was identified as a copper sulphide (Cu_xS_y) phase, most likely a combination of covellite (CuS) and anilite (Cu_7S_4); and a widening of the 348 cm^{-1} in some samples that are potentially connected to a chalcostibite phase which has a peak around 335 cm^{-1}, but due to this position being so close to that of the main peak of tetrahedrite (348 cm^{-1}), only in samples with excessive chalcostibite formation it is possible to observe this phase in the Raman spectra.

There are also some additional peaks observed, with the main ones around the 180 cm^{-1} and 250 cm^{-1} positions, which pertain to the Cu-S bond signature. These peaks are also common in the spectrums of chalcostibite and copper sulphide phases, however, because these peaks disappeared, exclusively, when reducing the laser beam intensity, it was determined that they are caused by material ejection of the sample surface due to high laser beam intensity. Unfortunately, the samples produced in this study proved to be highly susceptible to being "burned off" by laser beam, most likely connected to the low melting point of sulphur at 445ºC[71,72], thus proper analysis through Raman spectroscopy proved to be difficult, as it required balancing sample integrity and signal detection for spectra acquisition through adjusting laser intensity.

After annealing (Fig.33 and 34), samples present fewer peaks of secondary phases, and while the main tetrahedrite peak shifts position in the 338-355 cm^{-1}, there appears to be no clear correlation with Ni or Se content. However, when comparing sets of samples either with the same Ni or Se content, it is visible in most of sets, that samples without the Ni or Se have deviated peaks from the others. In other words, the presence of Ni or Se in the sample clearly changes the peak position.

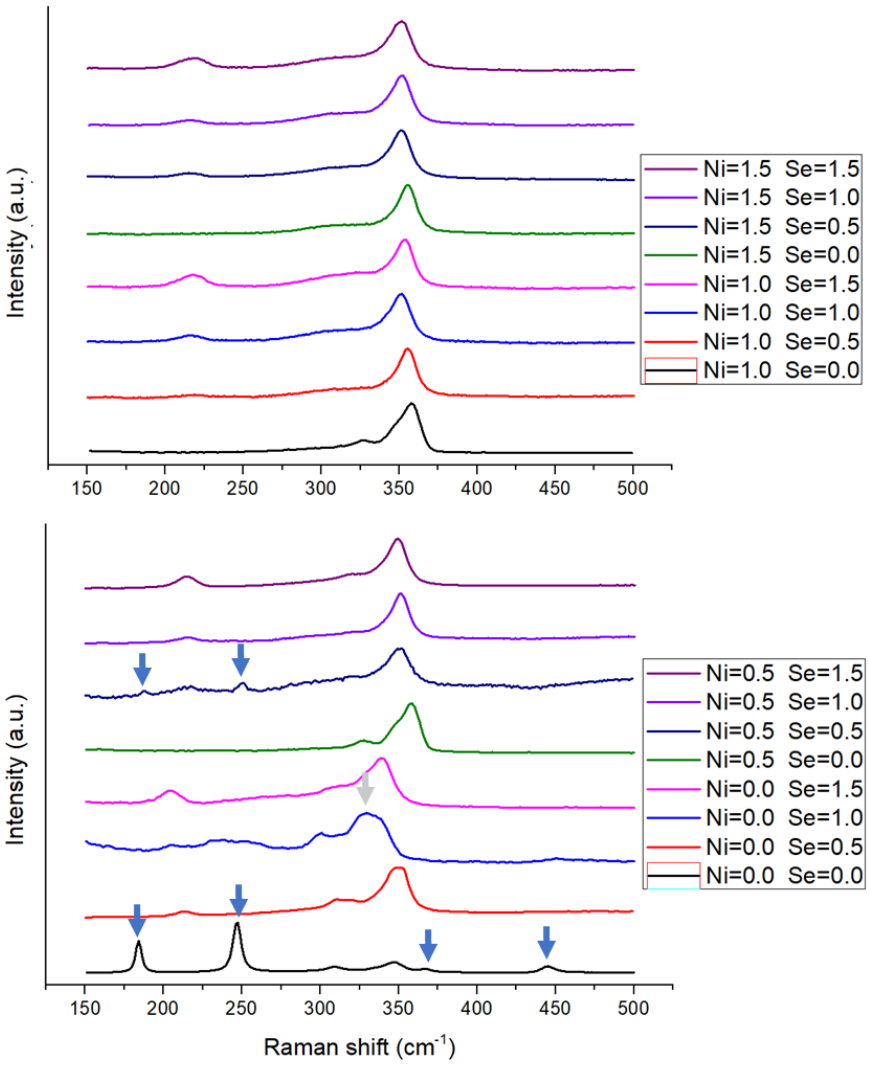

Fig. 33 Raman spectra of several $Cu_{12-x}Ni_xSb_4S_{13-y}Se_y$ samples after annealing grouped by equal Ni content and ordered by increasing Se content The peaks pertaining to the tetrahedrite phase are located in the 315 and 348 cm^{-1} shifts. With arrows, are indicated the peaks not related to the tetrahedrite phase: blue arrows-the Cu-S chemical bond of ejected material and gray arrows - chalcostibite ($CuSbS_2$).

To understand what these deviations in peak positions mean, it is necessary to refer back to the previous 2.3.2 chapter, where is stated that Raman shift or wavenumber ($\Delta\nu$, cm^{-1}) is calculated through the formula (eq.14). With this formula, and assuming a constant λ_0, it can be reasoned that a peak with a lower $\Delta\nu$ (shifted to the left), is a product of a Raman scattered emission with lower λ_1, which can be interpreted as an increase in the chemical bond strength, because a photon with smaller wavelength is, by definition, of higher energy. Conversely meaning that a higher $\Delta\nu$ (shifted to the right) would imply a larger λ_1 and thus a weaker chemical bond because the resulting photon would have less energy.

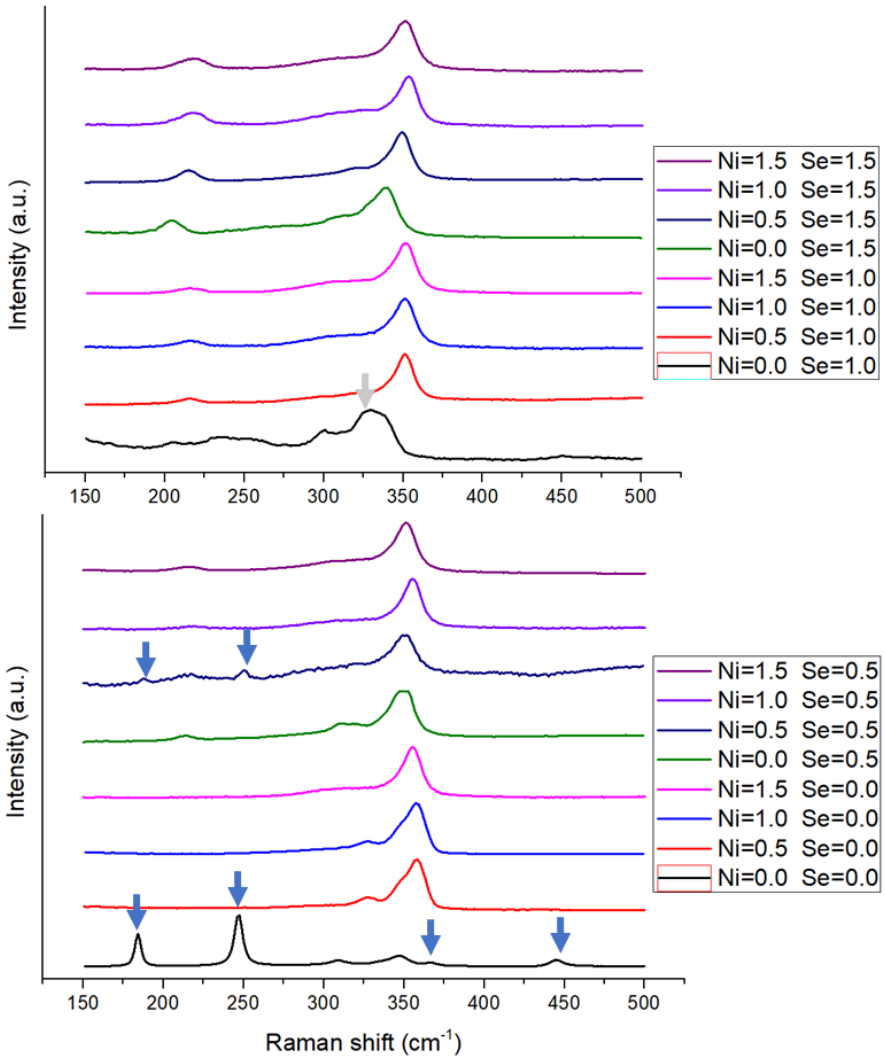

Fig. 34 Raman spectra of several $Cu_{12-x}Ni_xSb_4S_{13-y}Se_y$ samples after annealing grouped by equal Se content and ordered by increasing Ni content. The peaks pertaining to the tetrahedrite phase are located in the 315 and 348 cm^{-1} shifts. With arrows, are indicated the peaks not related to the tetrahedrite phase: blue arrows- the Cu-S chemical bond of ejected material and gray arrows - chalcostibite ($CuSbS_2$).

Interestingly, introducing Ni in the tetrahedrite results in a shift of the main peak to the right, a higher wavenumber, and introducing Se results in a shift to the left, a lower wavenumber. Which both confirms that both Ni and Se are integrating the tetrahedrite phase and that Ni doping results in weaker bonds and Se doping results on stronger bonds. However, both these results are equally puzzling. In the Ni case, in principle, with the same oxidation state of Cu, Ni atoms should be less electronegative than Cu due to having one less electron, which would result in a larger electronegativity difference between Ni and S than Cu and S, thus in theory the bond should be stronger between Ni and S, and not weaker. On the Se case, due to Se having a higher atomic number than S and despite having the same electronic configuration, Se will be less electronegative than S and have significantly higher

ionic radius, both factors should result in a weaker bond, not a stronger bond as presented by the experimental results, which leaves us to conclude that there are other factors affecting the average bond energy in tetrahedrite.

One potential justification to these deviations lies on the size difference between the original atoms and the dopants. While small in the Ni-Cu case, with 73 pm for Cu^{2+} and 69 pm for Ni^{2+}[167], it should be noted that these particular Cu atoms are the ones located in the "rattler" configuration, does possessing a high degree of vibrational freedom, a smaller atom would garner a higher degree of freedom to vibrate, which would supposedly result in less stiff bond and ultimately weaker bonds. Conversely due to the larger ionic radius difference between Se^{-2} and S^{-2}, 198 pm and 184pm, respectively[167], which would result in a significantly distorted and strained crystal structure with the introduction of Se, which would imply stiffer bonds and thus bonds that would require more energy to be broken. While most of this justification are plain suppositions, it would explain the deviations that occurred due to merely introducing one dopant or the other and emphasize the idea that the size of the dopant element can potentially play a bigger role in phase formation and properties than expected.

The exhaustive presentation of the Raman spectra is shown in Attachment 2.

4.1.3 SEM-EDS analysis

SEM observations show that the as-cast samples are dotted with pores and fractures (Fig.35), and, aside from the matrix phase, there are two other visually different phases observed: a darker, often star-shaped phase, and a lighter intergranular phase. Semi-quantitative EDS analysis (Table 1) indicates that the chemical composition of the matrix is approximate to that of tetrahedrite, as the analysed composition is similar to the nominal one, including both Ni and Se in the composition, thus corroborating the X-ray diffraction and Raman spectroscopy assessment of a main tetrahedrite phase and that doping of both elements is occurring.

Fig. 35 SEM (BSE) micrography of the $Cu_{12}Sb_4S_{11.5}Se$ as-cast sample

The dark star-shaped phase has a composition that is similar to copper/nickel sulphides ($(Cu,Ni)_xS_y$) with varying ratios of (Cu, Ni) to S, with a small content of Se (generally less than 5.0 at%), when this element is present in the sample. This sulphide phase is the most commonly observed, being present in 14 out of 16 samples, and generally tending to either have a composition similar to the NiS_2 and NiS, with sole exception of the $Cu_{12}Sb_4S_{12.5}Se_{0.5}$ nominal composition sample presenting a Cu_2S phase. It should be noted that the formation of each these phases is heavily dependent on the the Ni content: the Cu_2S phase appeared in a phase with Ni content, x=0.0, the NiS_2 appears in samples with small Ni content (x=0.5) and in the $Cu_{11}NiSb_4S_{13}$ sample, while NiS appears on nearly all samples with x=1.0 and 1.5.

The lighter phase has a composition similar to a mixture of chalcostibite and příbramite ($CuSbS_{2-x}Se_x$) and is only observed in two samples, $Cu_{12}Sb_4S_{11.5}Se_{1.5}$ and $Cu_{10.5}Ni_{1.5}Sb_4S_{11.5}Se_{1.5}$, with the latter exhibiting both copper/nickel sulphides and

chalcostibite- příbramite phase as observed in Fig.36. The appearance of this phase seems to be associated with high Se content, as both samples that presented this phase had y=1.5.

As for coherence with the X-ray diffractograms, the three previously identified phases are present in the samples, albeit with Ni and Se. Both the covellite and Cu_2S phase are observed in the form of the dark phase mixture of copper and nickel sulphides with different (Cu, Ni):S ratios; and the chalcostibite observed on the diffractograms being more accurately a mixture of chalcostibite and příbramite that manifests in the lighter phase. However, compared with the X-ray diffractograms which identified the chalcostibite phase in half of the samples, SEM is not detecting as much differentiated chalcostibite- příbramite phase. Either this intergranular phase is more prevalent inside the samples, in other sections, than it is observed with SEM in the current studied surfaces, or it is finely distributed in the matrix (as seen in Fig. 36A).

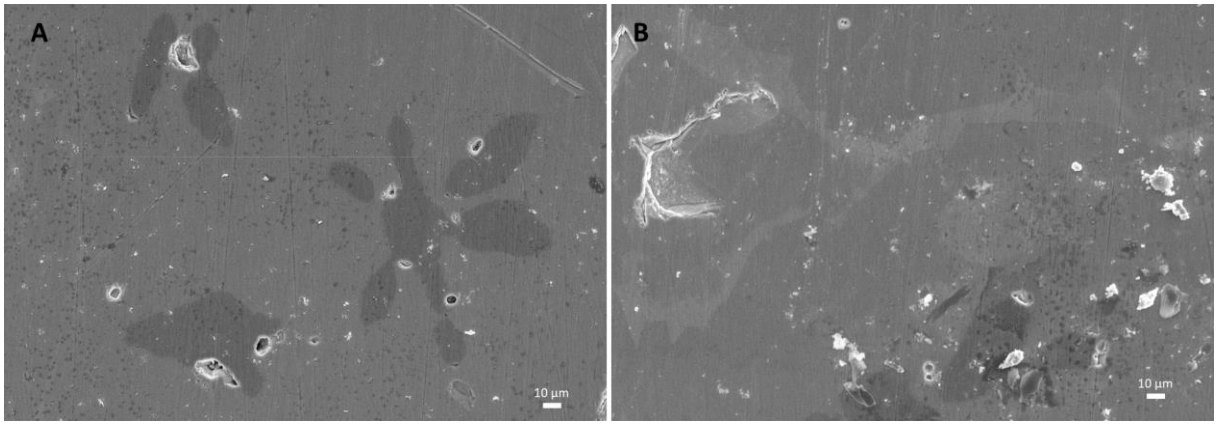

Fig. 36 SEM (BSE) micrography of the $Cu_{10.5}Ni_{1.5}Sb_4S_{11.5}Se_{1.5}$ as-cast sample: in (A) the dark grey phase visible has a composition pointing to Nickel Sulphide (Ni_xS_y); and in (B) the light grey phase has a composition similar to doped-chalcostibite ($CuSb(S,Se)_2$).

Table 1 SEM-EDS semi-quantitative analysis of the matrix of as-cast samples. The matrix chemical formula was calculated based on the composition and assuming a 29 atoms molecule like tetrahedrite.

Expected formula of the sample	Cu(at%)	Ni(at%)	Sb(at%)	S(at%)	Se(at%)	Matrix chemical formula
$Cu_{12}Sb_4S_{13}$	48.1±1.6		12.9±0.5	39.0±1.7		$Cu_{13.9\pm0.5}Sb_{3.8\pm0.1}S_{11.3\pm0.5}$
$Cu_{11.5}Ni_{0.5}Sb_4S_{13}$	44.4±1.2	2.1±0.1	12.1±0.3	41.3±1.3		$Cu_{12.88\pm0.3}Ni_{0.6\pm0.1}Sb_{3.5\pm0.1}S_{12.0\pm0.4}$
$Cu_{12}Sb_4S_{12.5}Se_{0.5}$	42.0±0.4		13.9±0.2	43.0±0.4	1.1±0.2	$Cu_{12.2\pm0.1}Sb_{4.0\pm0.1}S_{12.5\pm0.1}Se_{0.3\pm0.1}$
$Cu_{11.5}Ni_{0.5}Sb_4S_{12.5}Se_{0.5}$	39.6±1.3	1.2±0.1	13.0±0.5	44.7±1.8	1.5±0.3	$Cu_{11.5\pm0.4}Ni_{0.4\pm0.1}Sb_{3.8\pm0.1}S_{13.0\pm0.5}Se_{0.4\pm0.1}$
$Cu_{11}NiSb_4S_{13}$	47.4±2.4	4.2±0.4	13.2±0.7	35.2±2.2		$Cu_{13.7\pm0.7}Ni_{1.2\pm0.1}Sb_{3.8\pm0.2}S_{10.2\pm0.6}$
$Cu_{11}NiSb_4S_{12.5}Se_{0.5}$	43.5±1.5	4.2±0.3	12.8±0.5	38.2±1.6	1.3±0.3	$Cu_{12.6\pm0.4}Ni_{1.2\pm0.1}Sb_{3.7\pm0.1}S_{11.1\pm0.5}Se_{0.4\pm0.1}$
$Cu_{12}Sb_4S_{12}Se$	47.3±1.8		12.6±0.5	35.6±1.7	4.6±0.5	$Cu_{13.7\pm0.5}Sb_{4.0\pm0.1}S_{10.3\pm0.5}Se_{1.3\pm0.2}$
$Cu_{11.5}Ni_{0.5}Sb_4S_{12}Se$	47.0±1.9	1.9±0.2	13.2±0.6	34.8±1.7	3.2±0.5	$Cu_{13.6\pm0.5}Ni_{0.5\pm0.1}Sb_{3.8\pm0.2}S_{10.1\pm0.5}Se_{0.9\pm0.1}$
$Cu_{12}NiSb_4S_{12}Se$	46.8±1.5	1.6±0.2	14.0±0.5	35.4±1.4	2.3±0.3	$Cu_{13.6\pm0.4}Ni_{0.5\pm0.1}Sb_{4.1\pm0.1}S_{10.3\pm0.4}Se_{0.7\pm0.1}$
$Cu_{10.5}Ni_{1.5}Sb_4S_{13}$	44.6±1.6	5.4±0.3	12.5±0.5	37.5±1.6		$Cu_{12.9\pm0.5}Ni_{1.6\pm0.1}Sb_{3.6\pm0.1}S_{10.9\pm0.5}$
$Cu_{10.5}Ni_{1.5}Sb_4S_{12.5}Se_{0.5}$	44.1±1.4	4.8±0.3	12.8±0.4	38.3±1.5		$Cu_{12.8\pm0.4}Ni_{1.4\pm0.1}Sb_{3.7\pm0.1}S_{11.1\pm0.4}$
$Cu_{10.5}Ni_{1.5}Sb_4S_{12}Se$	44.2±1.7	4.5±0.3	12.4±0.5	33.9±1.6	5.0±0.6	$Cu_{12.8\pm0.5}Ni_{1.3\pm0.1}Sb_{3.6\pm0.1}S_{9.8\pm0.5}Se_{1.5\pm0.2}$
$Cu_{12}Sb_4S_{11.5}Se_{1.5}$	44.2±1.7		13.3±0.5	35.8±1.7	6.8±0.6	$Cu_{12.8\pm0.5}Sb_{3.9\pm0.2}S_{10.4\pm0.5}Se_{2.0\pm0.2}$
$Cu_{11.5}Ni_{0.5}Sb_4S_{11.5}Se_{1.5}$	42.0±1.3	1.2±0.1	12.1±0.4	38.3±1.5	6.4±0.5	$Cu_{12.2\pm0.4}Ni_{0.4\pm0.1}Sb_{3.5\pm0.1}S_{11.1\pm0.4}Se_{1.9\pm0.1}$
$Cu_{11}NiSb_4S_{11.5}Se_{1.5}$	41.2±1.4	3.3±0.2	11.9±0.4	40.0±1.6	3.7±0.4	$Cu_{11.9\pm0.4}Ni_{0.9\pm0.1}Sb_{3.5\pm0.1}S_{11.6\pm0.5}Se_{1.1\pm0.1}$
$Cu_{10.5}Ni_{1.5}Sb_4S_{11.5}Se_{1.5}$	44.2±1.9	5.6±0.4	14.2±0.6	29.2±1.5	6.9±0.7	$Cu_{12.8\pm0.5}Ni_{1.6\pm0.1}Sb_{4.1\pm0.2}S_{8.5\pm0.5}Se_{2.0\pm0.2}$

Aside from these phases, 6 out of 16 samples also exhibited two intertwined phases with roughly the same distribution and coloration of the matrix (Fig.37), EDS point analysis showed that both phases had highly similar chemical compositions identified as tetrahedrite with small differences in composition. It should be added that multiple tetrahedrite phases are common occurrence, with even the observation of double tetrahedrite signature peaks in powder X- ray diffraction in nearly all the samples, even if the differentiation of phases is not observed by SEM-EDS. Overall, the matrixes of as-cast samples had an atomic composition containing Ni and Se, in compositions that while off the expected values, were similar enough to be identified as doped tetrahedrite, which served to verify the chemical substitution with both dopants.

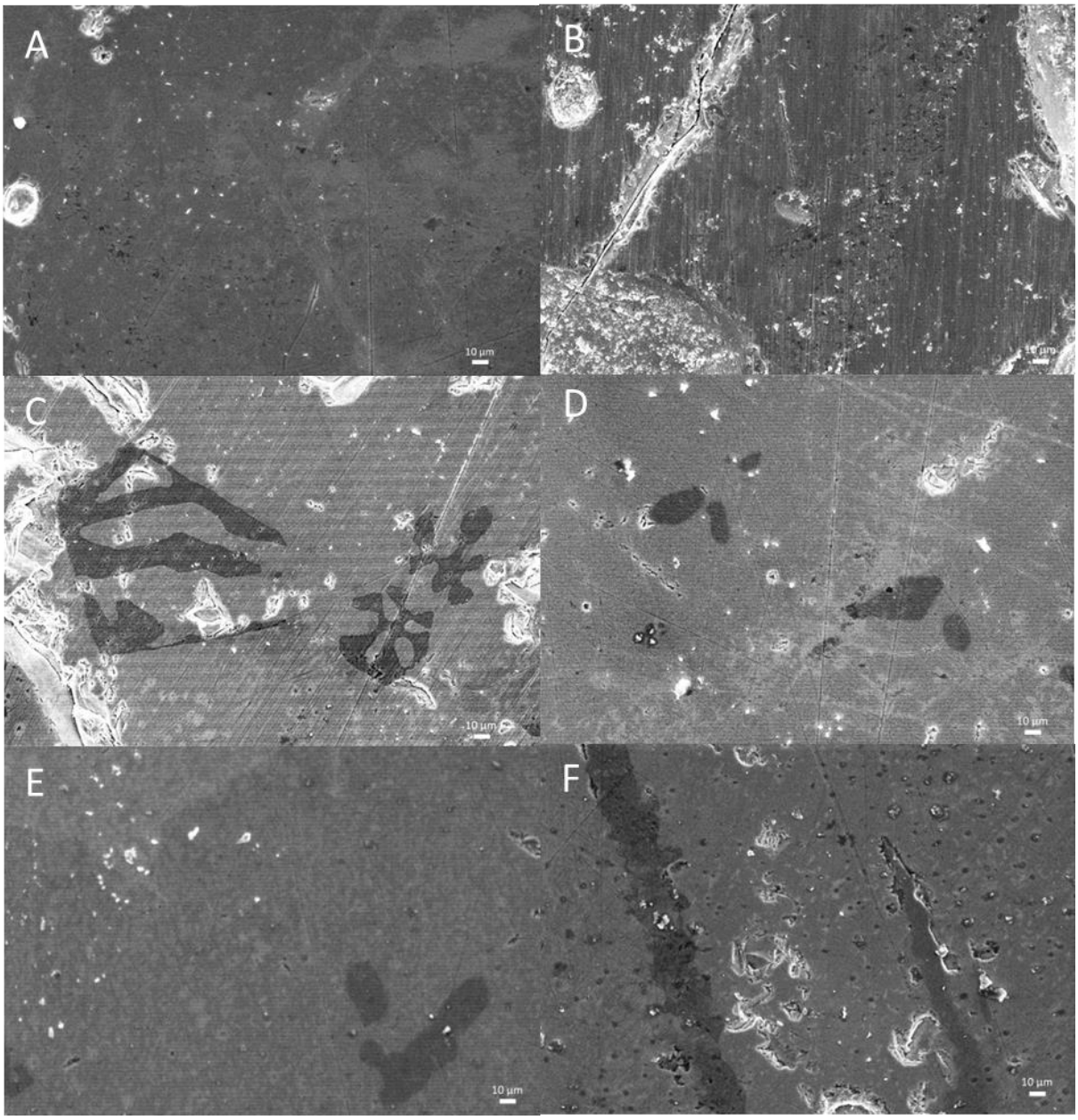

Fig. 37 SEM micrographies of (A) $Cu_{12}Sb_4S_{13}$; (B) $Cu_{12}Sb_4S_{12}Se$; (C) $Cu_{11.5}Ni_{0.5}Sb_4S_{12}Se$; (D) $Cu_{10.5}Ni_{1.5}Sb_4S_{13}$; (E) $Cu_{10.5}Ni_{1.5}Sb_4S_{12}Se$; and (F) $Cu_{11}NiSb_4S_{11.5}Se_{1.5}$ as-cast samples, to showcase the two tetrahedrite phases present in the matrix, with the black phases being composed of $(Cu,Ni)_xS_y$ phases

Semi-quantitative composition analysis (Table 1) also shows that samples tend to exhibit larger atomic percentage of Cu and the final stoichiometric dopant content severely fluctuates with a maximum stoichiometric difference of ±0.5 from the expected content, potentially implying that the tetrahedrite produced after casting is one of the Cu-rich forms of tetrahedrite previously discussed in chapter 1.5. The results displayed are merely indicative and may not be an accurate representation of the full matrix composition of each sample, as multiple measurements in the same matrix revealed lack of homogeneity.

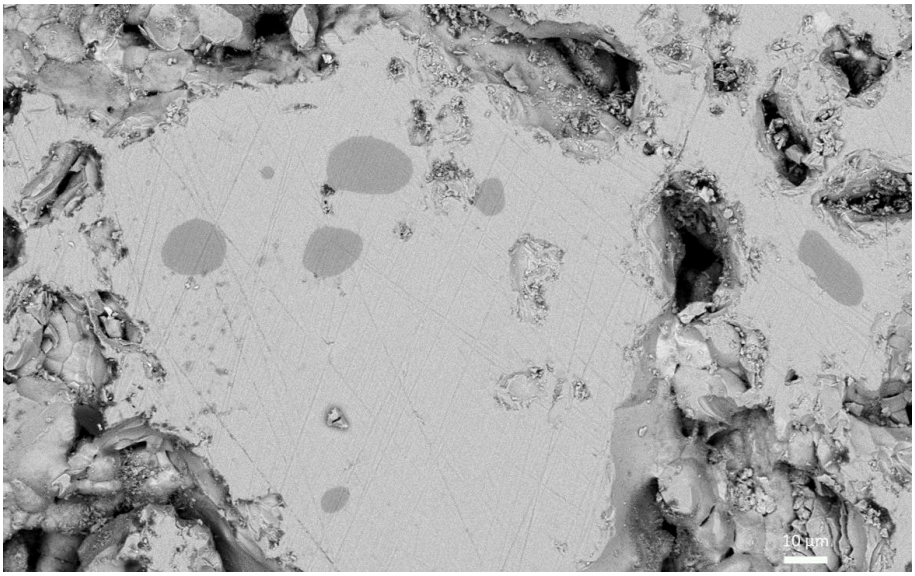

Fig. 38 Microstructures and pores observed in SEM imaging of annealed $Cu_{10.5}Ni_{1.5}Sb_4S_{11.5}Se_{1.5}$ sample with a dark toned NiS phase.

Compared to as-cast samples, it is immediately noticeable that after annealing there is a substantial reduction in the distribution and size of observable secondary phases (Fig. 38), with now more samples not exhibiting any secondary phase (6 out of 16). Also, no annealed sample exhibited two distinct tetrahedrite phases, which correlates to a more homogeneous chemical composition throughout the matrix. On the other hand, a new phase is observed in the $Cu_{11}NiSb_4S_{12}Se$ sample (Fig.39), a light-coloured vaguely square-shaped microstructure of ullmannite (NiSbS).

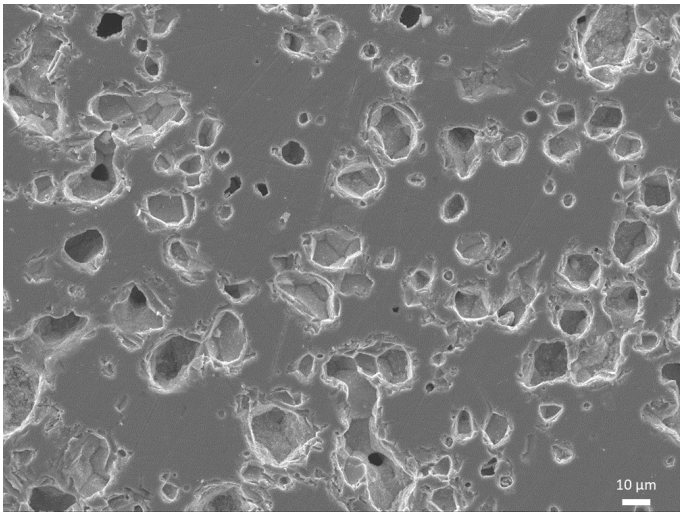

Fig. 39 Microstructures and pores observed in SEM imaging of the $Cu_{11}NiSb_4S_{12}Se$ annealed. The light phases are composed of ullmannite (NiSbS).

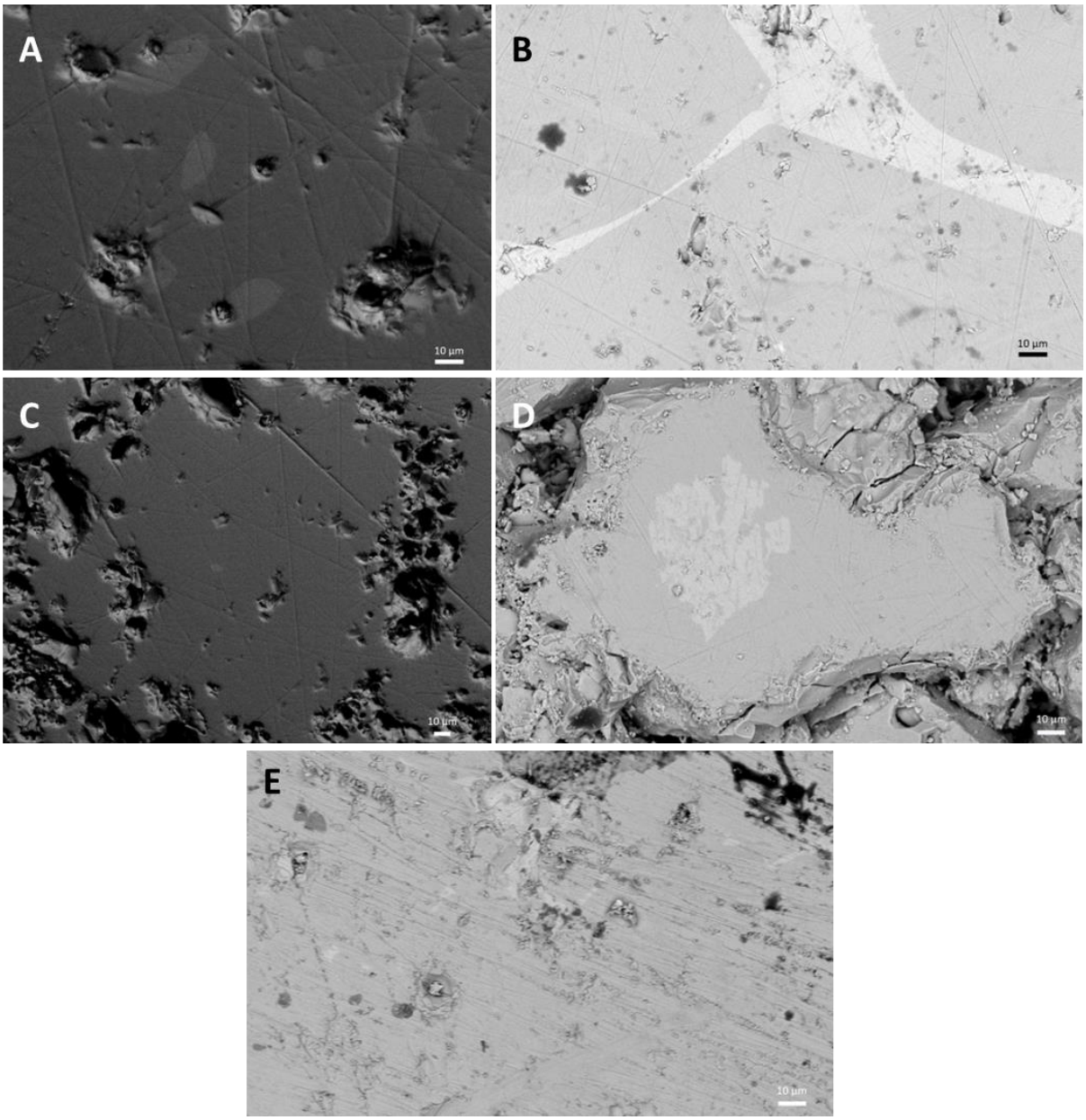

Fig. 40 SEM micrographies of (A) $Cu_{12}Sb_4 S_{12.5}Se_{0.5}$; (B) $Cu_{12}Sb_4 S_{11.5}Se_{1.5}$; (C) $Cu_{11.5}Ni_{0.5}Sb_4 S_{12.5}Se_{0.5}$; (D) $Cu_{11}NiSb_4S_{13}$; and (E) $Cu_{10.5}Ni_{1.5}Sb_4S_{13}$; annealed samples, to showcase the chalcostibite ($CuSbS_2$) phase indicted by the lighter coloration.

In regards to the distribution of the secondary phases: Cu_2S only appeared on the $Cu_{12}Sb_4S_{12}Se$ sample and NiS on two samples with high Ni content (x=1.5), $Cu_{10.5}Ni_{1.5}Sb_4S_{12.5}Se_{0.5}$ and $Cu_{10.5}Ni_{1.5}Sb_4S_{11.5}Se_{1.5}$, which maintain the previous tendency observed on as-cast samples; NiS_2 appeared on two samples, $Cu_{11.5}Ni_{0.5}Sb_4S_{11.5}Se_{1.5}$ $Cu_{10.5}Ni_{1.5}Sb_4S_{13}$, thus now appearing on both a sample with low Ni content (x=0.5) and high Ni content (x=1.5) rather than just low Ni content; and lastly, the chalcostibite- příbramite phase, which now becomes the most commonly observed phase on the SEM micrographs, appearing in 5 out of the 16 samples, namely $Cu_{12}Sb_4S_{12.5}Se_{0.5}$, $Cu_{12}Sb_4S_{11.5}Se_{1.5}$, $Cu_{11.5}Ni_{0.5}Sb_4S_{12.5}Se_{0.5}$, $Cu_{11}NiSb_4S_{13}$ and $Cu_{10.5}Ni_{1.5}Sb_4S_{13}$ (Fig.40). This disparity in

theoretical compositions forming chalcostibite phase is clear indication that at this stage, chalcostibite formation is non-dopant specific and quite likely a sign of minor tetrahedrite degeneration, in fact looking into the semi-quantitative compositions of the chalcostibite phase microstructures of all samples that previously did not form the chalcostibite phase, revealed only a small Se at% (1.8 and 5.0 at% for the $Cu_{12}Sb_4S_{12.5}Se_{0.5}$ and $Cu_{11.5}Ni_{0.5}Sb_4S_{12.5}Se_{0.5}$, respectively) when this dopant is present, this plus the other two samples that did not contain Se ($Cu_{11}NiSb_4S_{13}$ and $Cu_{10.5}Ni_{1.5}Sb_4S_{13}$) which nonetheless formed chalcostibite clearly points to a non Se-dependant or příbramite-dependant chalcostibite formation. Interestingly enough, the remaining annealed sample that presented chalcostibite, $Cu_{12}Sb_4S_{11.5}Se_{1.5}$, also previously exhibited the same phase after casting, and comparing the before and after annealing SEM micrographs (Fig. 41) reveals a clear evolution of the chalcostibite phase and clear depiction of the intergranular growth of this phase with clearly straight boundary lines.

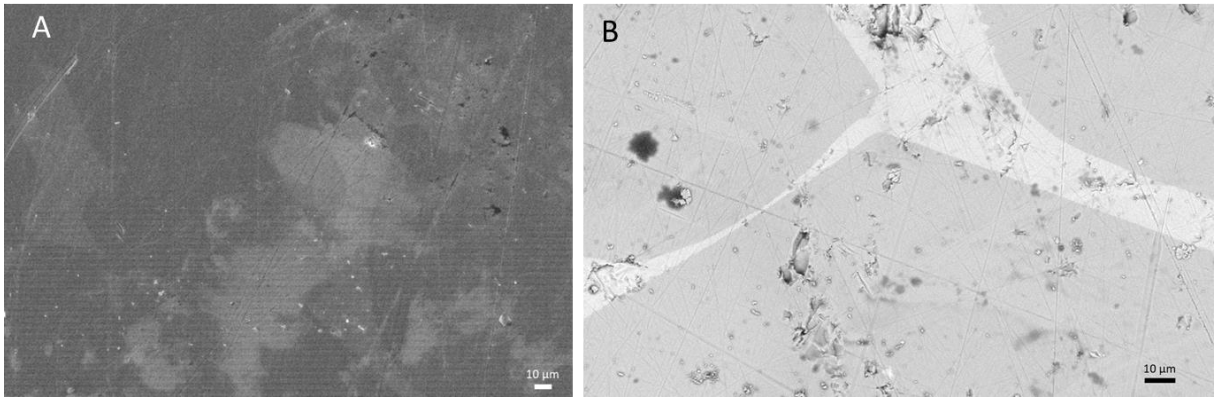

Fig. 41 SEM micrography of the $Cu_{12}Sb_4S_{11.5}Se_{1.5}$ sample after casting (A) and after annealing (B). The light grey phase has a composition similar to doped-chalcostibite ($CuSbS_2$).

Compared to the X-ray diffraction results, while it previously suggested that there was a clear correlation between specific compositions and the appearance of specific phases, SEM analysis does not yield the previously observed correlation or any coherent correlation between composition and phase formation, further implying that the prepared surfaces of the samples, even after polishing, are not complete absolute representations of the entire sample or that these secondary phases are potentially hidden in deeper inside the samples.

While taking these results with a grain of salt, the semi-quantitative analysis of the matrix (Table 2) shows that it maintains a composition similar to tetrahedrite, but the percentage of Se is consistently lower than what is expected in 11 out of the 12 Se-containing samples, with an average deficit of approximately 17.3%, which might suggest that Se has

higher difficulty for integrating in the tetrahedrite crystal structure, most likely rooted on the larger ionic radius of the element.

Ultimately despite this consistent deficit in Se content, the estimated composition is closer to what is expected when first weighting each element prior to casting. This fact coupled with the reduction in the number and size of secondary phase microstructures as well as pores and other observable imperfections, further justifies the need of the annealing step to produce samples with ultimately better thermoelectric properties, as it was previously discussed in the introduction that secondary phases, fractures, pores, and other structural defects may have a negative impact in the overall thermoelectric properties.

The exhaustive presentation of the SEM-EDS analysis is shown in Attachment 3.

Table 2 SEM-EDS semi-quantitative analysis of the matrix of annealed samples. The matrix chemical formula was calculated based on the composition and assuming a 29 atoms molecule like tetrahedrite.

Expected formula of the sample	Cu(at%)	Ni(at%)	Sb(at%)	S(at%)	Se(at%)	Matrix chemical formula
$Cu_{12}Sb_4S_{13}$	42.0±0.5		14.4±0.2	43.6±0.6		$Cu_{12.2\pm0.1}Sb_{4.2\pm0.1}S_{12.6\pm0.2}$
$Cu_{11.5}Ni_{0.5}Sb_4S_{12}$	40.1±0.5	1.9±0.3	14.2±0.3	43.9±0.7		$Cu_{11.6\pm0.2}Ni_{0.6\pm0.1}Sb_{4.1\pm0.1}S_{12.7\pm0.2}$
$Cu_{12}Sb_4S_{12.5}Se_{0.5}$	40.6±0.3		14.1±0.2	44.1±0.5	1.2±0.2	$Cu_{11.8\pm0.1}Sb_{4.1\pm0.1}S_{12.8\pm0.1}Se_{0.4\pm0.1}$
$Cu_{11.5}Ni_{0.5}Sb_4S_{12.5}Se_{0.5}$	41.5±0.4	1.4±0.3	11.1±0.2	45.0±0.6	1.0±0.2	$Cu_{11.7\pm0.1}Ni_{0.4\pm0.1}Sb_{4.0\pm0.1}S_{12.6\pm0.2}Se_{0.4\pm0.1}$
$Cu_{11}NiSb_4S_{13}$	39.0±0.4	2.6±0.2	13.8±0.2	44.7±0.6		$Cu_{11.3\pm0.1}Ni_{0.8\pm0.1}Sb_{4.0\pm0.1}S_{13.0\pm0.2}$
$Cu_{11}NiSb_4S_{12.5}Se_{0.5}$	38.4±0.5	3.8±0.3	14.4±0.2	41.9±0.6	1.6±0.2	$Cu_{11.1\pm0.1}Ni_{1.1\pm0.1}Sb_{4.2\pm0.1}S_{12.2\pm0.2}Se_{0.5\pm0.1}$
$Cu_{12}Sb_4S_{12}Se$	38.9±0.5		12.7±0.3	44.7±0.7	3.7±0.3	$Cu_{11.3\pm0.2}Sb_{3.7\pm0.1}S_{13.0\pm0.2}Se_{1.1\pm0.1}$
$Cu_{11.5}Ni_{0.5}Sb_4S_{12}Se$	39.4±0.4	2.1±0.2	13.7±0.2	42.0±0.5	2.8±0.2	$Cu_{11.4\pm0.1}Ni_{0.6\pm0.1}Sb_{4.0\pm0.1}S_{12.2\pm0.2}Se_{0.8\pm0.1}$
$Cu_{12}NiSb_4S_{12}Se$	37.3±0.5	4.7±0.3	13.9±0.2	41.6±0.6	2.5±0.2	$Cu_{10.8\pm0.1}Ni_{1.4\pm0.1}Sb_{4.0\pm0.1}S_{12.1\pm0.2}Se_{0.7\pm0.1}$
$Cu_{10.5}Ni_{1.5}Sb_4S_{13}$	37.7±0.5	4.5±0.3	14.3±0.2	43.6±0.6		$Cu_{10.9\pm0.2}Ni_{1.3\pm0.1}Sb_{4.1\pm0.1}S_{12.6\pm0.2}$
$Cu_{10.5}Ni_{1.5}Sb_4S_{12.5}Se_{0.5}$	38.3±0.5	4.0±0.3	14.1±0.2	42.5±0.6	1.2±0.2	$Cu_{11.1\pm0.2}Ni_{1.2\pm0.1}Sb_{4.1\pm0.1}S_{12.3\pm0.2}Se_{0.3\pm0.1}$
$Cu_{10.5}Ni_{1.5}Sb_4S_{12}Se$	37.3±0.5	4.8±0.3	14.2±0.3	41.2±0.6	2.6±0.2	$Cu_{10.8\pm0.2}Ni_{1.4\pm0.1}Sb_{4.1\pm0.1}S_{11.9\pm0.2}Se_{0.7\pm0.1}$
$Cu_{12}Sb_4S_{11.5}Se_{1.5}$	44.2±0.4		14.5±0.2	37.1±0.5	4.2±0.3	$Cu_{12.8\pm0.1}Sb_{4.2\pm0.1}S_{10.8\pm0.1}Se_{1.2\pm0.1}$
$Cu_{11.5}Ni_{0.5}Sb_4S_{11.5}Se_{1.5}$	39.8±0.5	1.4±0.3	14.7±0.2	40.5±0.6	3.6±0.2	$Cu_{11.6\pm0.2}Ni_{0.4\pm0.1}Sb_{4.3\pm0.1}S_{11.7\pm0.2}Se_{1.1\pm0.1}$
$Cu_{11}NiSb_4S_{11.5}Se_{1.5}$	38.4±0.5	3.6±0.3	14.0±0.2	40.1±0.6	3.9±0.3	$Cu_{11.1\pm0.1}Ni_{1.1\pm0.1}Sb_{4.1\pm0.1}S_{11.6\pm0.2}Se_{1.1\pm0.1}$
$Cu_{10.5}Ni_{1.5}Sb_4S_{11.5}Se_{1.5}$	37.5±0.5	4.5±0.3	13.9±0.2	40.3±0.6	3.8±0.3	$Cu_{10.9\pm0.1}Ni_{1.3\pm0.1}Sb_{4.0\pm0.1}S_{11.7\pm0.2}Se_{1.1\pm0.1}$

4.1.4 Thermoelectric Properties of Annealed samples

The measurements of the thermoelectric properties of annealed samples are presented in Fig. 42, as well as the calculated PF. The electrical resistivity of the materials tends to increase as the temperature decreases, which is a characteristic of semiconducting behaviour, and the Seebeck coefficient is always positive indicating that "holes" are the main charge carriers making tetrahedrite a p-type semiconductor. The fact that the Seebeck coefficient decreases as temperature decreases, indicative of metallic behaviour, points to tetrahedrites as highly degenerate semiconductors. It should be noted that undoped tetrahedrite (x=0.0 and y=0.0) exhibit an additional jump in both Seebeck coefficient and electrical resistivity around the 80K, that reflects a metallic-semiconductor transition associated to a structural transition, which was previously discussed in chapter 1.5. The absence of the metal-semiconductor transition on the other samples could be attributed to changes in the band structure and band filling, which arise from the introduction of dopants that supress the conditions that constitute the driving force for this structural transition.

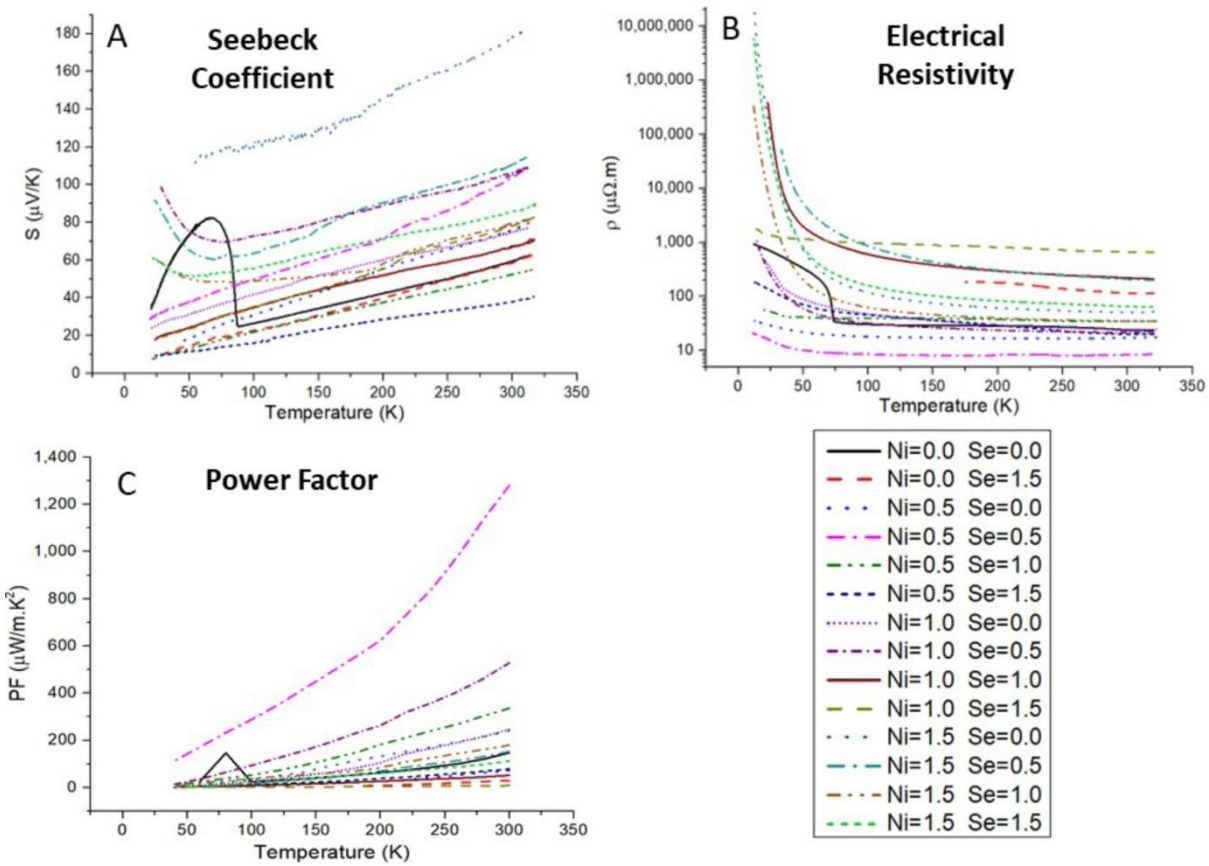

Fig. 42 Measured temperature dependence of electrical resistivity (A) and Seebeck coefficient (B); and resulting PF as a function of temperature (C) calculated for annealed samples following the formula $Cu_{12-x}Ni_xSb_4S_{13-y}$.

It is also noted that for the samples whose compositions have been previously reported in this temperature range ($Cu_{12-x}Ni_xSb_4S_{13}$ and $Cu_{12}Sb_4S_{13-y}Se_y$), the temperature dependence of electrical resistivity and Seebeck coefficient are very similar to the described in those works, albeit the overall Seebeck coefficient values are slightly lower than those previously reported[76,101,112,113,117,123,124,134,139,140,164,166]. This difference is most likely attributed to the presence of secondary phases in annealed samples, which may alter the composition of the matrix resulting in sufficient variation in charge carriers concentration that leads to lower Seebeck coefficients that those reported by the aforementioned studies. It should be also noted that these results come from annealed samples, while the results published in these studies were obtained in samples that underwent both annealing and a hot-pressing/spark plasma sintering step, which might exhibit a smaller presence of secondary phases due to the additional treatment step. Wherein, for the sake of simplicity, the stoichiometric content of Ni and Se shall be referred to x and y, respectively in accordance with the expected chemical formula of the samples ($Cu_{12-x}Ni_xSb_4S_{13-y}Se_y$).

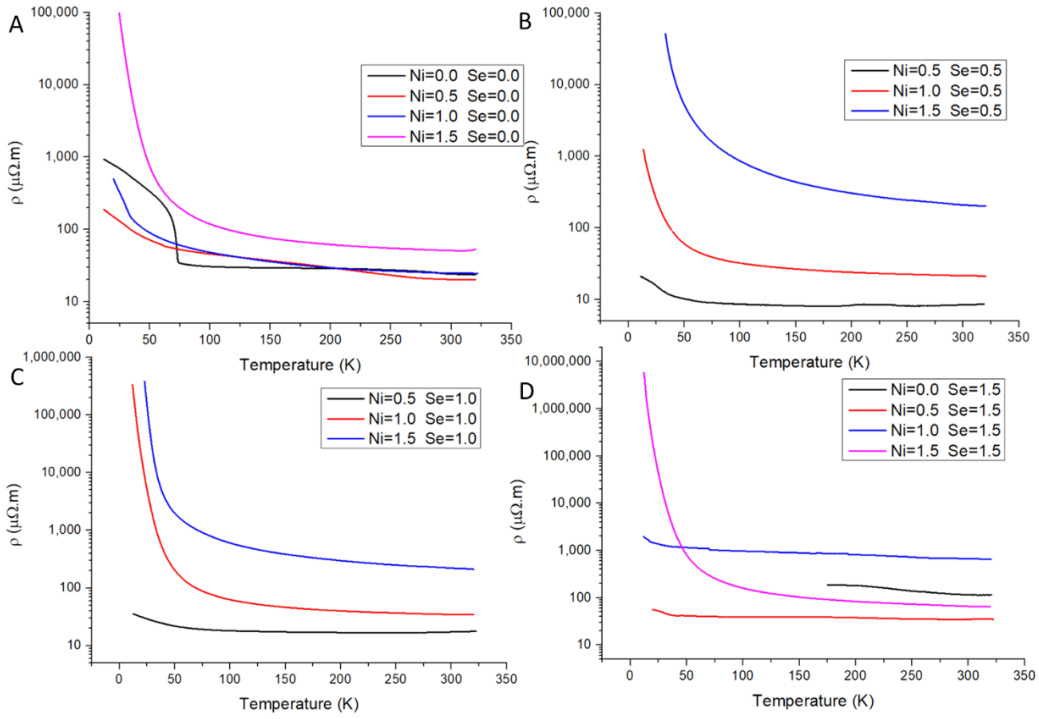

Fig. 43 Comparison of the temperature and Ni stoichiometric dependence of measured electrical resistivity of annealed samples with fixed Se stoichiometric content following the expected formulas: (A) $Cu_{12-x}Ni_xSb_4S_{13}$; (B) $Cu_{12-x}Ni_xSb_4S_{12.5}Se_{0.5}$; (C) $Cu_{12-x}Ni_xSb_4S_{12}Se$; (D) $Cu_{12-x}Ni_xSb_4S_{11.5}Se_{1.5}$.

When comparing the variation of both the electrical resistivity and Seebeck coefficient with a varying content of a single dopant while keeping the other dopant content fixed, it becomes clear that both Ni and Se play a significant role in the final thermoelectric properties of the sample, as it is difficult to observe the same tendencies across the different graphs. The

exhaustive presentation of the Seebeck coefficient and electrical resistivity measurement results is located in Attachments 4 and 5.

Looking into Fig. 43, a potential pattern can be observed when analysing the impact of Ni doping on electrical resistivity, where it is clear, for most samples (y=0.0-1.0), that electrical resistivity, after decreasing from x=0.0 to x=0.5, increases with x, but for samples with y=1.5, the previous pattern is not observed, as electrical resistivity decreases from x=0.0 to x=0.5, then increases with x=1.0 and decreases again with x=1.5.

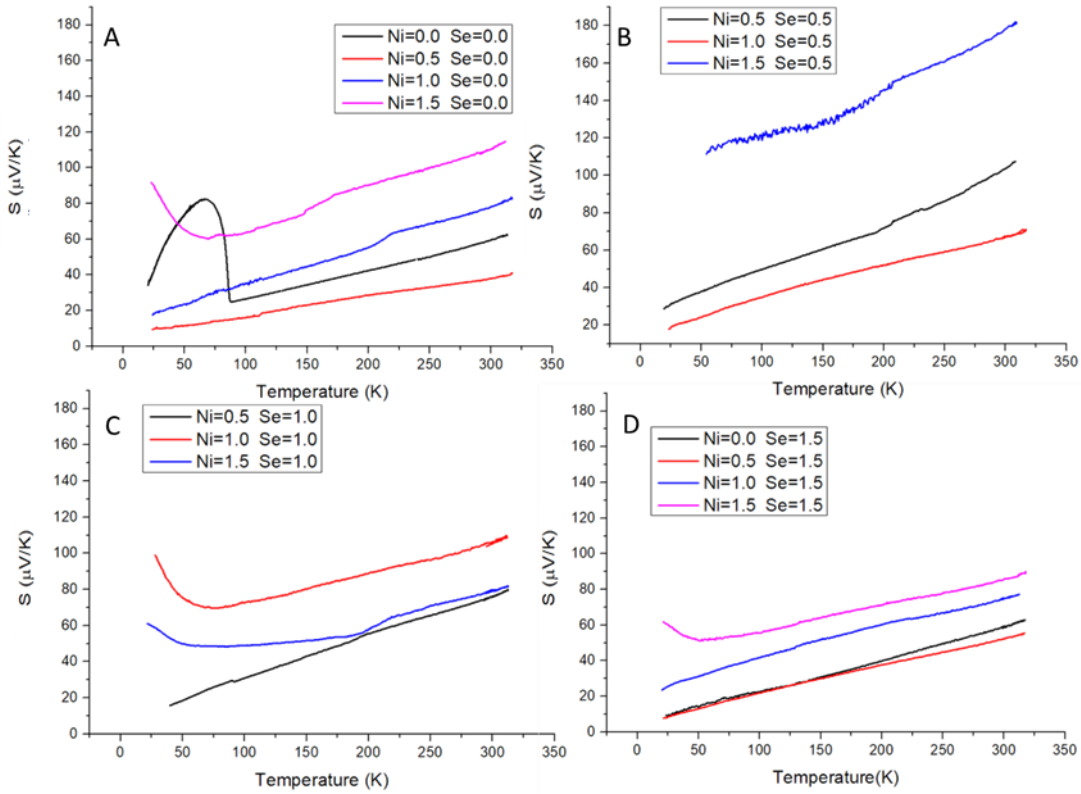

Fig. 44 Comparison of the temperature and Ni stoichiometric dependence of measured Seebeck coefficient of annealed samples with fixed Se stoichiometric content following the expected formulas: (A) $Cu_{12-x}Ni_xSb_4S_{13}$; (B) $Cu_{12-x}Ni_xSb_4S_{12.5}Se_{0.5}$; (C) $Cu_{12-x}Ni_xSb_4S_{12}Se$; (D) $Cu_{12-x}Ni_xSb_4S_{11.5}Se_{1.5}$.

As for the Seebeck coefficient (Fig.44), while it is clear that Seebeck coefficient tends to be higher with high Ni content ($x \geq 1.0$), the response to varying x is both non-monotonic and inconsistent across different sets of samples with fixed y. Nonetheless, one can argue that clearly electrical resistivity and Seebeck coefficient tend to increase with Ni content, which goes into conformity with what has been described by studies regarding Ni-doping of tetrahedrite[76,117]. This has been associated with the shift of the Fermi level to the top of the valence band, which causes a decrease in carrier concentration, thus increasing Seebeck coefficient and electrical resistivity. While this shift is not perceived in the DOS diagrams from the study simulations, the BoltzTraP calculation of electrical resistivity and Seebeck

coefficient show an increase in both of these properties after introducing Ni, which strangely is not consistent with the experimental measurements of the electrical resistivity, as it not account the dip in electrical resistivity from x=0.0 to x=0.5, which might indicate that the assumptions and simplifications taken into consideration during the simulations may not depict a fully reliable variation on thermoelectric properties with temperature, particularly at lower ones.

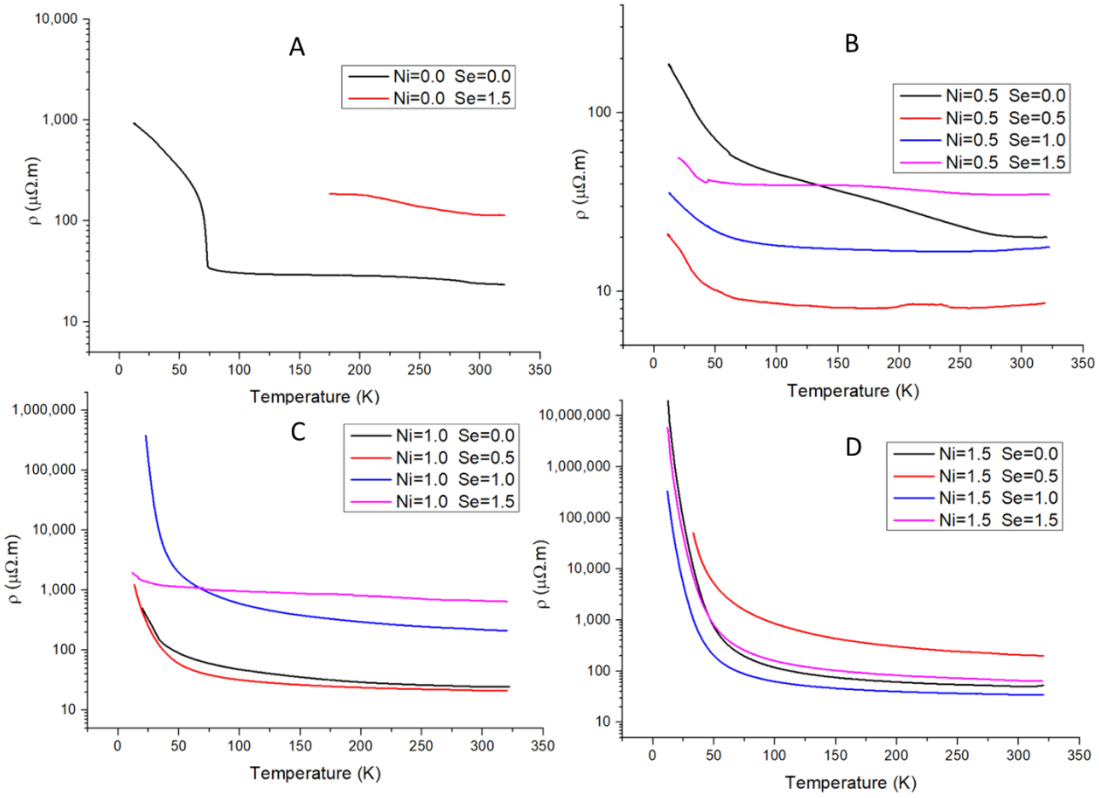

Fig. 45 Comparison of the temperature and Se stoichiometric dependence of measured electrical resistivity of annealed samples with fixed Ni stoichiometric content following the expected formulas: (A) $Cu_{12}Sb_4S_{13-y}Se_y$; (B) $Cu_{11.5}Ni_{0.5}Sb_4S_{13-y}Se_y$; (C) $Cu_{11}NiSb_4S_{13-y}Se_y$; (D) $Cu_{10.5}Ni_{1.5}Sb_4S_{13-y}Se_y$.

Regarding Se doping, studies have shown that there is a decrease of electrical resistivity with Se content in tetrahedrite up to y=1.0, followed by an increase of electrical resistivity as Se content increases with y=2.0, but remaining below undoped tetrahedrite. Also Se content is not expected to significantly alter the Seebeck coefficient, although to some small extent, Lu et al.[139] reports minor increase of Seebeck coefficient almost linearly proportional with Se-content.[112] However, in the current measurements (Fig.45), both these relations between Se-content and thermoelectric properties are not readily discernible, which in part is related to inability of produce solely Se-doped samples without an excessive presence of secondary phases (namely chalcostibite), which prevented the appropriate comparison between the

findings and the reported data. Despite the absence of a concrete relation between electrical resistivity and y, for all x values, the lowest electrical resistivity was achieved for y=0.5 or y=1.0, regardless of x value.

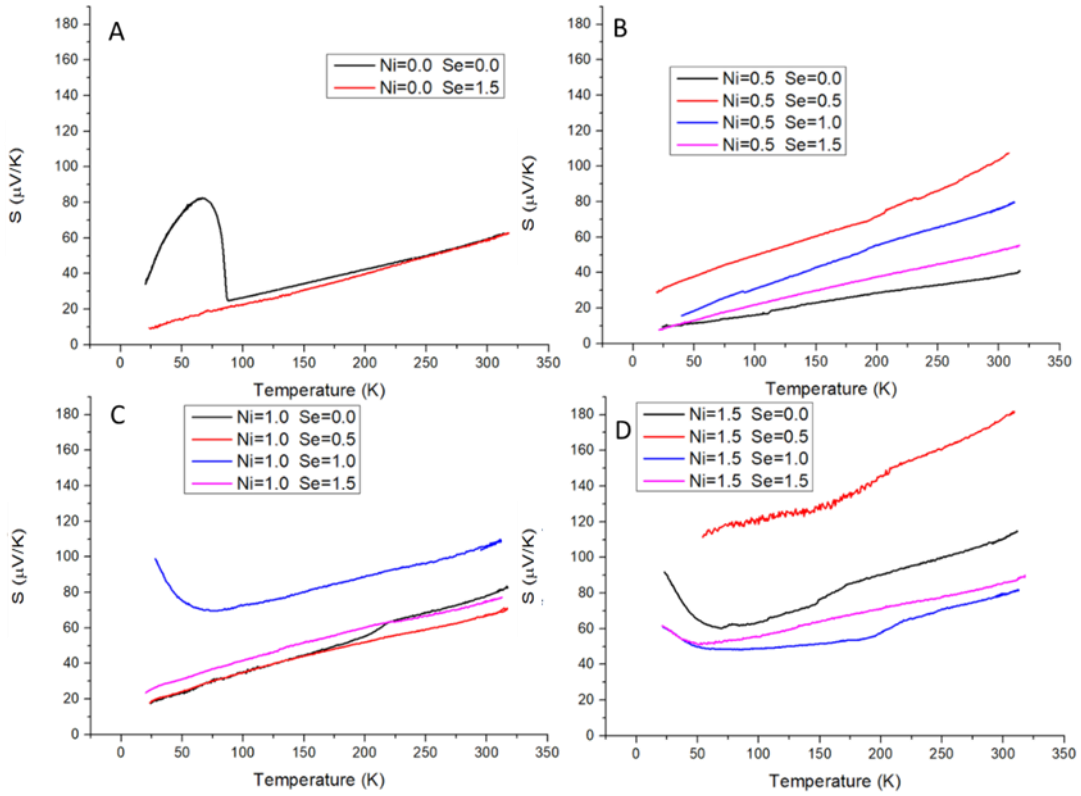

Fig. 46 Comparison of the temperature and Se stoichiometric dependence of measured Seebeck coefficient of annealed samples with fixed Ni stoichiometric content following the expected formulas: (A) $Cu_{12}Sb_4S_{13-y}Se_y$; (B) $Cu_{11.5}Ni_{0.5}Sb_4S_{13-y}Se_y$; (C) $Cu_{11}NiSb_4S_{13-y}Se_y$; (D) $Cu_{10.5}Ni_{1.5}Sb_4S_{13-y}Se_y$.

Similarly, the dependence of Seebeck coefficient with temperature (Fig.46) also ended up varying widely without a hint of a specific tendency. Interestingly enough while Seebeck coefficient changes with Se for the sets of samples containing Ni, the two samples not containing Ni that were successfully analysed ($Cu_{12}Sb_4S_{13}$ and $Cu_{12}Sb_4S_{11.5}Se_{1.5}$), presented nearly the same Seebeck coefficient in the entire temperature interval, except for the disappearance of the peak at around 80K characteristic of the undoped tetrahedrite metal-semiconductor transition. Obtaining similar Seebeck coefficient strongly implies that doping with only Se is not altering charge carrier concentration of tetrahedrite, which considering $Se^{2-}$and S^{2-} possess the same number of valence electrons is not particularly surprising. The large variations observed in the Seebeck coefficient of the $Cu_{11.5}Ni_{0.5}Sb_4S_{13-y}Se_y$ family of samples are especially peculiar, with a sharp increase in the Seebeck coefficient between y=0.0 (S_{300K} =37.93 μV/K) and y=0.5 (S_{300K} =103.6 μV/K) followed by a significant decrease in Seebeck coefficient with increasing y (S_{300K} =76.17 μV/K and S_{300K} =52.30 μV/K, for

y=1.0 and 1.5 respectively). The behaviour of the $Cu_{11.5}Ni_{0.5}Sb_4S_{13-y}Se_y$ set of samples becomes even more aberrant after analysing the two other sets of samples ($Cu_{11}NiSb_4S_{13-y}Se_y$ and $Cu_{10.5}Ni_{1.5}Sb_4S_{13-y}Se_y$), which aside from an outlier sample in each set ($Cu_{11}NiSb_4S_{12}Se$ and $Cu_{10.5}Ni_{1.5}Sb_4S_{12.5}Se_{0.5}$, respectively), the Seebeck coefficient hardly changes or present significantly smaller changes, as was expected. Curiously, if the semiquantitative SEM-EDS analysis of the compositions (Table 2, chapter 4.1.3) serves as minimally reliable indication of the overall composition of the entire sample, the outlier samples of both sets of samples displayed a significantly different Ni content from the other samples and the expected composition, with the expected $Cu_{11}NiSb_4S_{12}Se$ sample having an estimated $Cu_{10.8\pm0.1}Ni_{1.4\pm0.1}Sb_{4.0\pm0.1}S_{12.1\pm0.2}Se_{0.7\pm0.1}$ and the expected $Cu_{10.5}Ni_{1.5}Sb_4S_{12.5}Se_{0.5}$ sample having an estimated $Cu_{11.1\pm0.2}Ni_{1.2\pm0.1}Sb_{4.1\pm0.1}S_{12.3\pm0.2}Se_{0.3\pm0.1}$. Thus, the outlier Seebeck coefficient values could be attributed to fairly significant deviations between the actual Ni content present in the sample and the expected Ni content.

Overall, even considering the difference between expected composition and composition reported by SEM-EDS, it appears that for all Ni-containing sets of samples, the ones with highest Seebeck coefficients were achieved with either y=0.5 or y=1.0. This heavily implies that there is an optimum y value between 0.5 and 1.0, which may differ depending on x value. But considering that electrical resistivity also decreases at x=0.5, it might possibly indicate that the composition for optimized thermoelectric performance should be located in the x and y range values of 0.5-1.0 for both values.

Combining the two properties to calculate the PF, results in the graphs present in Fig.42C, which show that doping with various amounts of Ni and Se simultaneously can improve the thermoelectric properties of tetrahedrite, resulting in higher PFs than undoped tetrahedrite. The highest PF achieved with the current samples is for x=0.5 and y=0.5, which seems to validate the hypothesis that there might be an optimum composition in the $0.5\leq x\leq 1.0 \wedge 0.5\leq y\leq 1.0$ region. To properly verify this hypothesis, the properties and the resulting calculated PF at 300K were registered in Table 3 and a 3-coordinates bar graph was created to compare the PF of each sample at 300K (Fig. 47A). Curiously, the three highest values were indeed located in this region of composition with a clearly heavier tendency to be around x=0.5 and y=0.5, not only providing further confirmation to the hypothesis, but also corroborating the computational results obtained with Wien2K and BoltzTraP software, that also placed the optimum composition around x=0.5 and y=0.5. In the present results, the highest PF was achieved by the $Cu_{11.5}Ni_{0.5}Sb_4S_{12.5}Se_{0.5}$ sample, which achieved a PF of

1279.99 μW/m.K^2 at 300K, followed by the samples $Cu_{11}NiSb_4S_{12.5}Se_{0.5}$ with a PF=527.96 μW/m.K^2 and $Cu_{11.5}Ni_{0.5}Sb_4S_{12}Se$ with PF=335.56 μW/m.K^2 at 300K. It's important to note that the measurements show that annealed samples with high Se content (y=1.5) display even worst PF than undoped tetrahedrite, which goes against the results obtained by Lu[112], but this can be attributed to the lack of the hot-pressing step (resulting in different preparation conditions), and as a consequence, the samples are less dense and exhibit more structural defects that in the end hinder their final thermoelectric properties.

Unfortunately, due to inaccessibility to means of measuring thermal conductivity, κ_T, this property was not measured. However, it is possible estimate κ_T through the Wiedmann-Franz law[165], in order to evaluate the potential zT of the samples at 300K. The calculation of the thermal conductivity was carried out through eq.9 and the formula:

$$L = 1.5 + e^{-S/116} \qquad (16)$$

to calculate the Lorenz number, L ($10^{-8}V^2/K^2$), and it is assumed that κ_L=0.5 W/m.K, which is the typical value for undoped tetrahedrite[38,76,170–172].

Table 3 Electrical resistivity, Seebeck coefficient, PF, estimated thermal resistivity and figure of merit of $Cu_{12-x}Ni_xSb_4S_{13-y}Se_y$ samples at 300K.

X	Y	ρ (μΩm)	S (μV/K)	PF (μW/m.K^2)	κ_T estimated (μW/m.K)	zT
0.0	**0.0**	24.02	59.48	147.27	0.76	**0.06**
0.5	**0.0**	20.20	37.93	71.22	0.83	**0.03**
0.5	**0.5**	8.39	103.62	1279.99	1.18	**0.33**
1.0	**0.0**	24.73	78.10	246.64	0.74	**0.10**
1.0	**0.5**	21.42	106.35	527.96	0.77	**0.21**
0.5	**1.0**	17.29	76.17	335.56	0.85	**0.12**
1.0	**1.0**	219.89	106.32	51.40	0.53	**0.03**
1.5	**0.0**	50.62	110.37	240.61	0.61	**0.12**
1.5	**0.5**	208.70	178.22	152.19	0.52	**0.09**
1.5	**1.0**	34.70	78.96	179.71	0.67	**0.08**
0.0	**1.5**	114.98	58.75	30.02	0.55	**0.01**
0.5	**1.5**	34.91	52.30	78.35	0.68	**0.03**
1.0	**1.5**	667.27	74.84	8.39	0.51	**0.01**
1.5	**1.5**	65.47	85.65	112.05	0.59	**0.06**

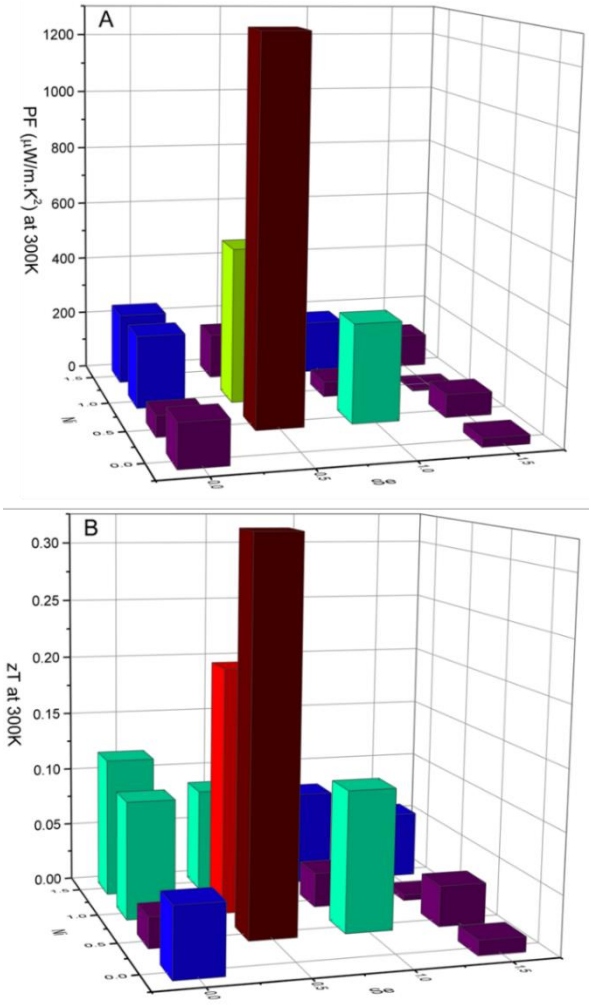

Fig. 47 Representation of PF (A) and estimated figure of merit (B) obtained for each sample following the formula $Cu_{12-x}Ni_xSb_4S_{13-y}$, with the x-axis representing Ni stoichiometric content and the y-axis representing Se stoichiometric content.

With this approximation, it was possible to create a similar 3-coordinates bar graph for figure of merit at 300K (Fig.47B), where a zT=0.33 at 300K was achieved for $Cu_{11.5}Ni_{0.5}Sb_4S_{12.5}Se_{0.5}$, which is a high figure of merit, with the previous highest zT for tetrahedrite doped with either Se and Ni being 0.22 at 300K with a $Cu_{10.5}Ni_{1.5}Sb_4S_{13}$.[(76)]

The exhaustive presentation of the measurements and calculations of electrical resistivity, Seebeck coefficient, PF and Figure of Merit analysis are presented in Attachments 4, 5, 6 and 7, respectively.

4.1.5 Weighted mobility

Weighted mobility analysis can provide an important information about the charge carrier mobility within the material. Typically, charge carrier mobility is obtained through the measurement of the Hall resistance (R_h) and electrical conductivity (σ) and subsequent calculation of Hall mobility (μ_h=σ. R_h). However due to the spread of Seebeck coefficient measuring systems, weighted mobility (μ_w) became an alternative approach to calculating the charge carrier mobility. By using this property in the calculations instead of the Hall resistance errors related to other magnetic effects are avoided, and permits the calculation of charge carrier mobility at high temperatures and low mobility bulk systems.

As such, using the measured electrical resistivity and Seebeck coefficient in the formula[173]:

$$\mu_w = \frac{331}{\rho}\left(\frac{T}{300}\right)^{-3/2}\left[\frac{exp\left[\frac{|S|}{k_B/e}-2\right]}{1+exp\left[-5\left(\frac{|S|}{k_B/e}-1\right)\right]}+\frac{\frac{3}{\pi^2}\frac{|S|}{k_B/e}}{1+exp\left[5\left(\frac{|S|}{k_B/e}-1\right)\right]}\right] \qquad (17)$$

with ρ representing with the electrical resistivity, S the Seebeck coefficient, k_B the Boltzmann constant and e the electronic charge. The reason behind studying this property after calculating PF and zT, is connected to the absence of the thermal conductivity measurements. With PF being the only factor that can be calculated with the current measured properties, to avoid falling into the typical pitfalls of assuming that the largest PF directly correlates to the best thermoelectric performance, which while not entirely untrue, often the influence of thermal conductivity will deviate the optimized zT from optimized PF. Weighted mobility provides another venue for confirming the optimum doping conditions, as zT is directly proportional to the thermoelectric quality factor, B,[26,174–176] which can be calculated through the formula:

$$B = \left(\frac{k_B}{e}\right)^2 \frac{8\pi e(2m_e k_B T)^{3/2}}{3\hbar^3}\frac{\mu_w}{k_L}T \qquad (18)$$

with m_e representing electron mass, κ_L the lattice thermal conductivity and $\hbar$ the Plank's constant. With zT being proportional to B through the re-expression of eq. 6 and the formulas:

$$zT = \frac{S'^2}{L'+\frac{1}{b}} \qquad (19)$$

$$b(E_F) = \frac{\sigma(E_F).T}{k_L}.\left(\frac{k_B}{q}\right)^2 = B.\boldsymbol{F}_{1/2}\left[\frac{E_F-E_C}{k_B.T}\right] \qquad (20)$$

where q represents electric charge, E_F Fermi energy, E_C the energy of a channel, $\boldsymbol{F}_{1/2}[x]$ Fermi-Dirac integral as defined by Blakemore[177] and S' and L' representing dimensionless Seebeck coefficient and Lorenz number respectively, calculated through the formulas:

$$S' = \frac{S}{k_B/q} \qquad (21)$$

$$L' = \frac{L}{k_B/q} \qquad (22)$$

As shown by the formula of B (eq.18), the thermoelectric quality factor is proportional to μ_w/κ_L, which in turn is proportional to zT. Thus, the improvement of overall thermoelectric performance can be achieved by increasing μ_w and reducing κ_L.

It is important to state if it is assumed there is only a single (or multiple overlapping) parabolic band structure, weighted mobility should remain unaffected by doping, as it should only alter the Fermi level without altering the density of states or the crystal structure, resulting in the same scattering times, charge carrier concentration and charge carrier mobility. However, this assumption cannot be made in the present case, as tetrahedrite has demonstrated to have multiple non-overlapping both parabolic and non-parabolic bands in their band structure, both in ternary tetrahedrite and doped with Ni and Se (Fig. 48 and 49)[115,124,164,166], as such, changes to the weighted mobility are to be expected.

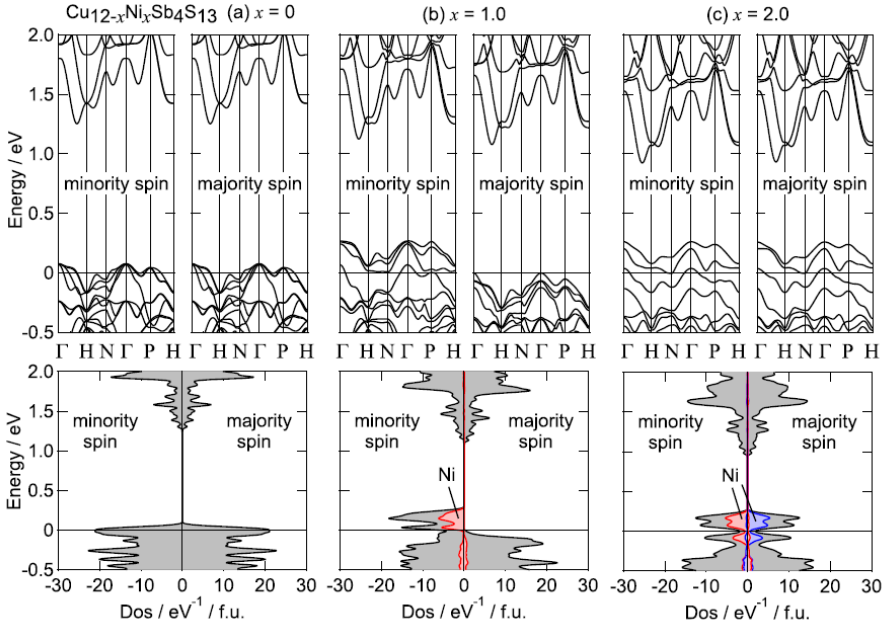

Fig. 48 Spin-resolved electronic band dispersion and DOS for U=0 of $Cu_{12-x}Ni_xSb_4S_{13}$ (x=0 (a), 1.0 (b), and 2.0 (c)). The red and blue areas describe partial DOS for Ni.[164]

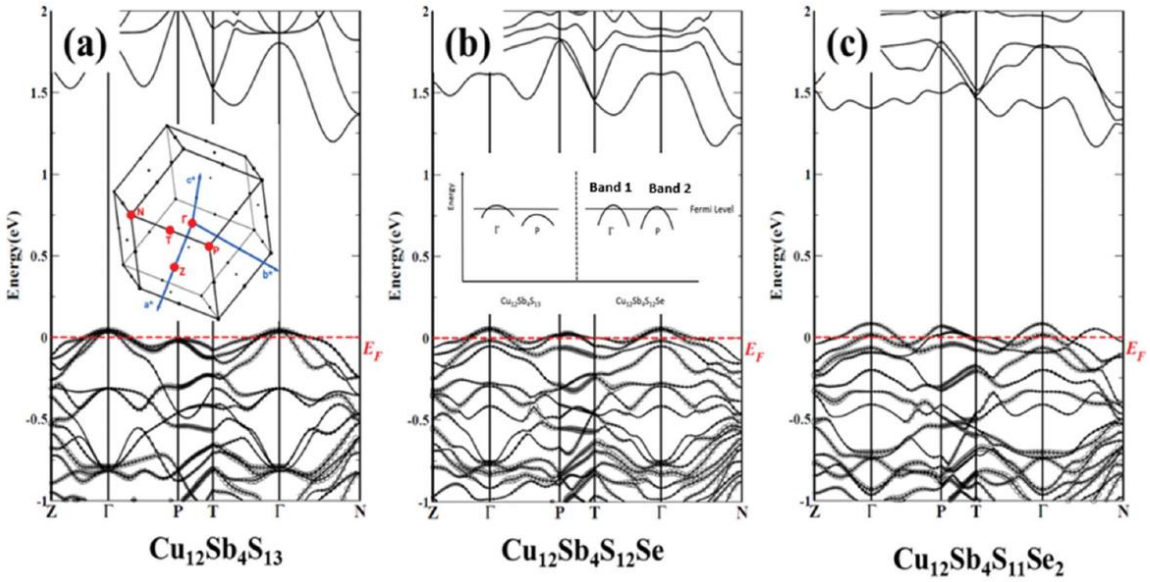

Fig. 49 Band structures of $Cu_{12}Sb_4S_{13-x}Se_x$ (x=0 (a), 1 (b), 2 (c)). The inset panel in (a) is the first Brillouin zone of $Cu_{12}Sb_4S_{13}$ with high symmetry points (red points). The inset panel in (b) illustrates the band degeneracy evolution when x=1.[166]

Also, as mentioned by Snyder et al.[173], assuming non-interacting charge carriers, perfect crystals of semiconductors will have $\mu_w(T)$ that follows the $T^{(-3/2)}$ progression. Deviations to this progression occur outside of these ideal conditions, which can be caused by: disorder and impurities in the crystal; non-parabolicity of band structures; carrier scattering due to carriers-phonons interaction and carrier-carrier interaction for high charge carrier concentration materials; and grain boundaries, interface roughness and other scattering mechanisms. As such, grain boundary resistance is identified as potentially the main contributor to the deviation mainly at lower temperatures, as illustrated in Fig.50.[178]

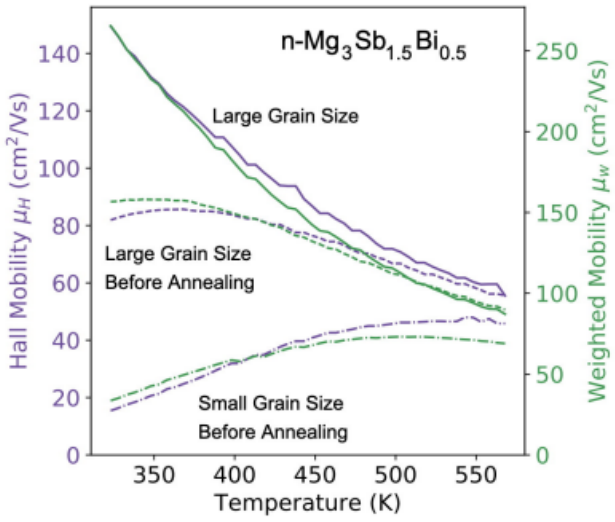

Fig. 50 Impact of heat treatment and grain size on the Weighted mobility (μ_w) and Hall mobility (μ_H) represented as functions of Temperature (K) for a polycrystalline n-type semiconductor $Mg_3Sb_{1.5}Bi_{0.5}$. [173]

The weighted mobility calculated using the experimental results obtained in this work is represented in Fig.51. The results show the existence of samples that exhibit a progression similar to $T^{(-3/2)}$, and some that show various degrees of deviation from that progression. These deviations were associated to high Ni content. In fact, as Ni content increases the greater is the divergence from $T^{(-3/2)}$ progression. This phenomenon is best observed when comparing weighted mobility of samples following the formulas $Cu_{12-x}Ni_xSb_4S_{12.5}Se_{0.5}$ and $Cu_{12-x}Ni_xSb_4S_{12}Se$ (Fig.52). There are two potential explanations to this Ni-induced mobility reduction at lower temperatures: a), grain boundary resistance, which would imply that Ni may have a hindering effect on crystal growth; or b) the introduction of antiferromagnetic interactions in the tetrahedrite, resulting in electron scattering by the Ni magnetic moment, as well as, potentially, induced magnetic moments of Cu and S, as demonstrated by Suekuni et al.[164]. The fact that at lower temperatures, magnetic interactions are stronger due to reduced thermal motion and consequently increased magnetic ordering, lends strength to the last hypothesis.

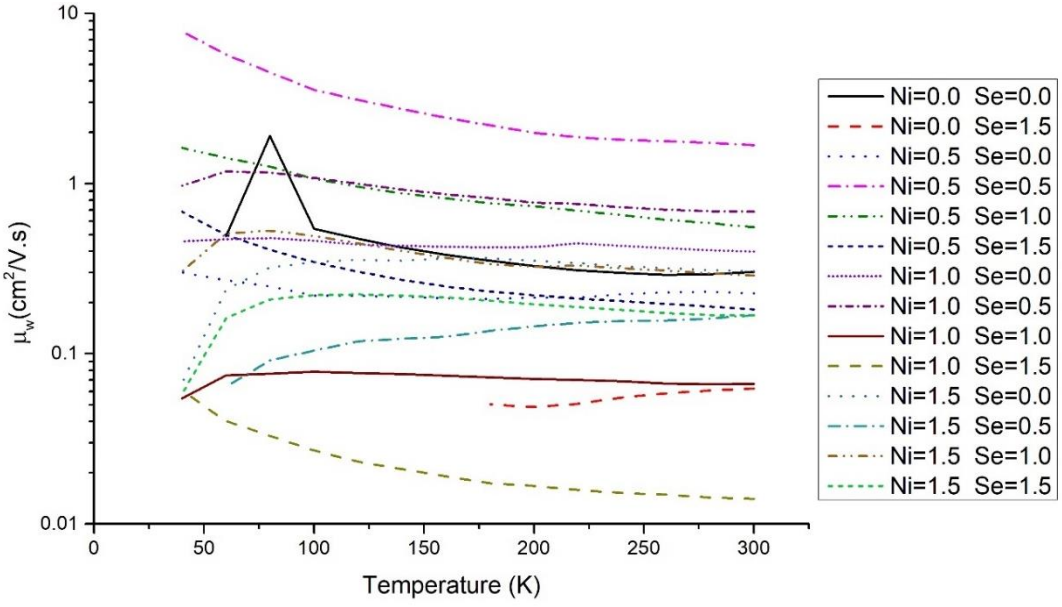

Fig. 51 Weighted mobility calculated from the measurements of the Seebeck coefficient and electrical resistivity of annealed samples following the formula $Cu_{12-x}Ni_xSb_4S_{13-y}Se_y$.

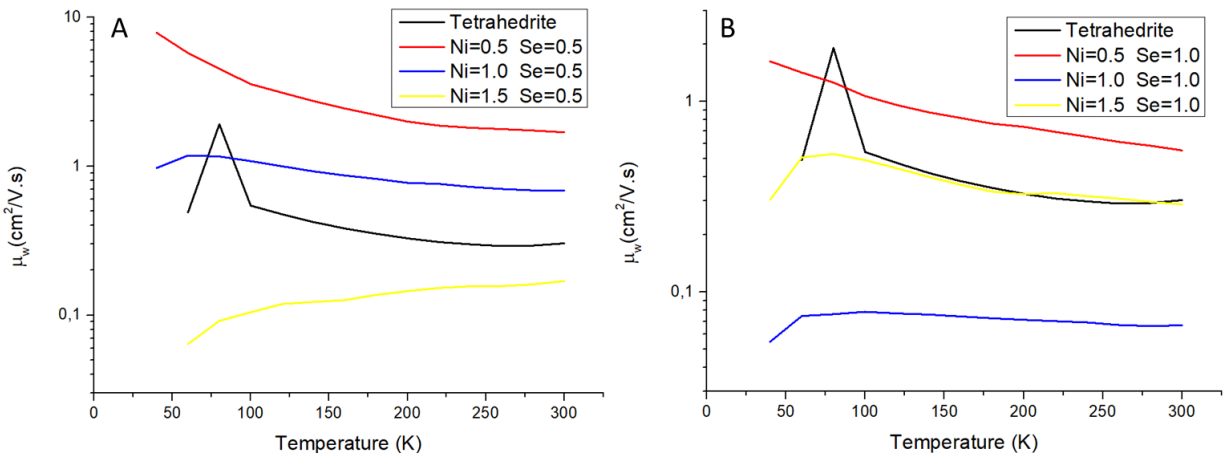

Fig. 52 Weighted mobility (cm^2/Vs) as a function of temperature (K) for annealed samples following the formulas $Cu_{12-x}Ni_xSb_4S_{12.5}Se_{0.5}$ (A) and $Cu_{12-x}Ni_xSb_4S_{12}Se$ (B). Showing the impact, the Ni content has on the Weighted mobility.

Despite the evident presence of high deviation from what would be considered ideal, the weighted mobility does corroborate the conclusions reached in previous chapters, namely the highest mobility being achieved by the $Cu_{11.5}Ni_{0.5}Sb_4S_{12.5}Se_{0.5}$ samples followed by $Cu_{11}NiSb_4S_{12.5}Se_{0.5}$ and $Cu_{11.5}Ni_{0.5}Sb_4S_{12}Se$ ones.

The exhaustive presentation of the calculated weighted mobility of annealed samples is shown in Attachment 8.

4.2 HOT-PRESSED SAMPLES

The main objective of applying the hot-pressing step, as mentioned in the previous chapter, is the reduction of microstructural and structural defects that increase electrical resistivity and reduce Seebeck coefficient, namely porosity, microstructures, cracks, and strain deformations, and potentially reduce the presence of secondary phases, by increasing elemental diffusion and increasing homogeneity of the samples.

4.2.1 X-ray Diffraction

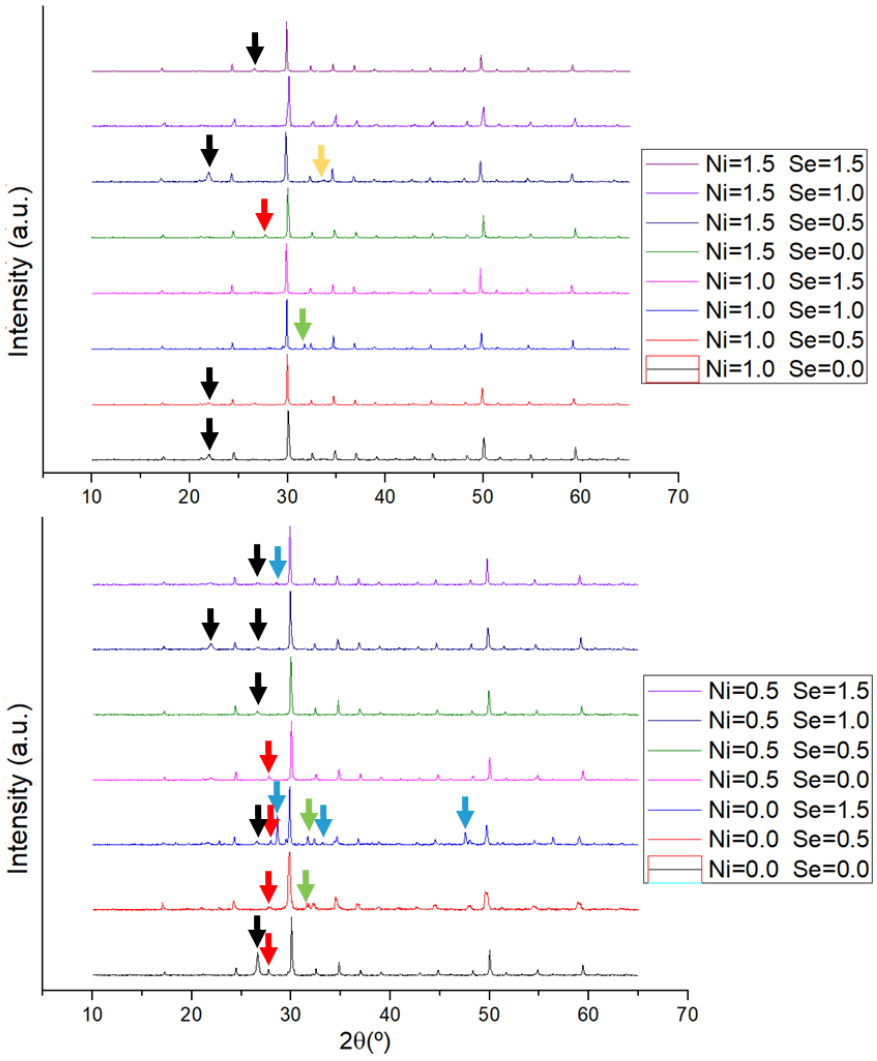

Fig. 53 Powder X-ray diffractograms of several hot-pressed $Cu_{12-x}Ni_xSb_4S_{13-y}Se_y$ samples. Identified with arrows are peaks not associated to tetrahedrite: in green- covellite (CuS); in blue - Chalcostibite ($CuSb(S,Se)_2$).; in red- antimony oxide (Sb_2O_3); in yellow- ullmannite (NiSbS) and in black-silicon dioxide from the sample holder.

Powder X-ray diffraction of the hot-pressed samples (Fig. 53) revealed that they still possess a main tetrahedrite phase, but some peaks of $CuSbS_2$ and CuS secondary phases are

observable. A new secondary phase is observed on the $Cu_{10.5}Ni_{1.5}Sb_4S_{12.5}Se_{0.5}$, a peak attributed to a ullmannite (NiSbS) phase. Some samples displayed a peak for antimony oxide (Sb_2O_3), which means that during hot-pressing the inert atmosphere was breached and contaminated with oxygen, resulting in the oxidation of the sample's surface. It should be added that prior to the hot-pressing step, producing the $Cu_{12}Sb_4S_{12}Se$ nominal composition sample with a main tetrahedrite phase was not possible to do, thus only 15 samples were studied past this point in the experimental procedure.

When comparing samples before and after hot-pressing, aside from the antimony oxide which resulted from an unfortunate breach of the inert gas atmosphere during this synthesis step, fewer samples presented secondary phases (5 out of 15), and those that presented in general showed a different set of secondary phases. For instance, the $Cu_{12}Sb_4S_{12.5}Se_{0.5}$ sample, which before hot-pressing exhibited chalcostibite peaks, afterwards, they disappeared and covellite peaks, which were not present in previous synthesis steps, were visible. Similarly, the $Cu_{12}Sb_4S_{11.5}Se_{1.5}$ sample after hot-pressing seemingly formed covellite in addition to the chalcostibite phase that was already present. Two other samples also formed new secondary phases after hot-pressing namely: the $Cu_{11.5}Ni_{0.5}Sb_4S_{11.5}Se_{1.5}$ forming chalcostibite; and $Cu_{10.5}Ni_{1.5}Sb_4S_{12.5}Se_{0.5}$ forming the new phase ullmannite. On the other hand, the $Cu_{11}NiSb_4S_{12.5}Se_{0.5}$ sample, which prior to hot-pressing exhibited covellite peaks, and the $Cu_{10.5}Ni_{1.5}Sb_4S_{12}Se$ and $Cu_{10.5}Ni_{1.5}Sb_4S_{11.5}Se_{1.5}$ samples, with Cu_2S peaks, all disappeared after this synthesis step.

This dichotomy in the results prior and after hot-pressing makes it impossible to clearly state, at this point, whether this synthesis step had an overall positive or negative effect on the production of samples with only a tetrahedrite phase. It should be added that the antimony oxide, while present in the powder X-ray diffractogram, is a phase exclusively formed on the surface of the samples, and due to their minor intensity in the diffractograms, will most likely be removed from the sample after polishing, a step necessary for both SEM-EDS analysis and measuring the thermoelectric properties, thus expected to have no impact later on.

The exhaustive presentation of the powder X-ray diffractograms of hot-pressed samples are shown in Attachment 1.

Estimations of the lattice parameter of the tetrahedrite phase in hot-pressed samples are shown in Fig.54B, with lattice parameter now ranging between 10.2979 to 10.3669(±0.0003) Å. The same relation between lattice parameter size and Se content is observed, with Ni

content continuing not presenting discernible impact on the unit cell size. However, there is an almost generalized decrease of the lattice parameter of the hot-pressed sample compared to their annealed counterparts. This decrease is most likely related to sulphur loss of the samples, because sulphur has a particularly high vapour pressure and low melting point at 445ºC[71,72], which ends up creating more vacancies and shrinks the unit cell of the tetrahedrite. The disappearance of sulphur can also be interpreted as a sign of degeneration of tetrahedrite and secondary phase formation.

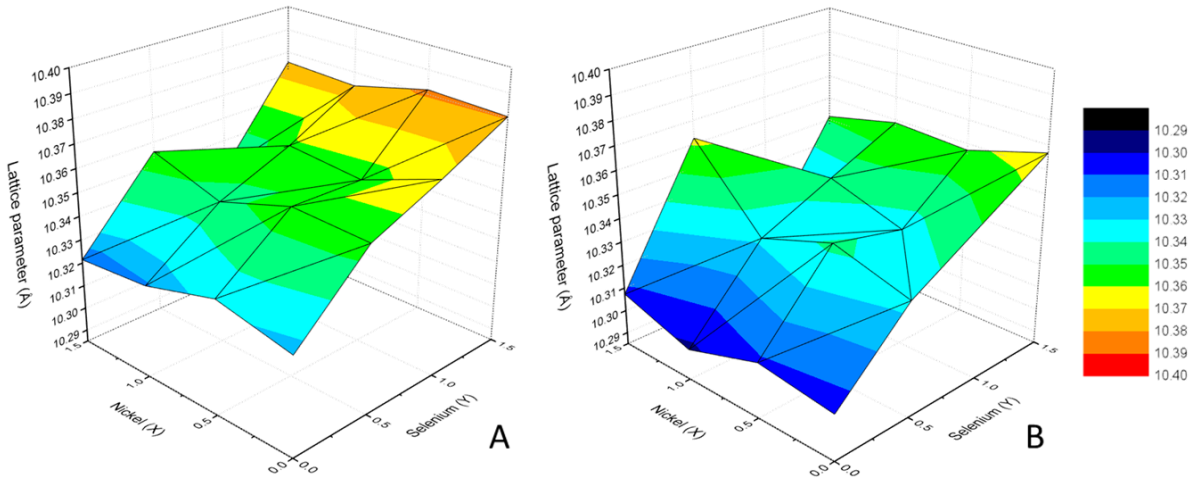

Fig. 54 Lattice parameter dependence on Nickel content (x) and Selenium content (y) in annealed (A) and hot-pressed (B) $Cu_{12-x}Ni_xSb_4S_{13-y}Se_y$ samples.

4.2.2 Raman Spectroscopy

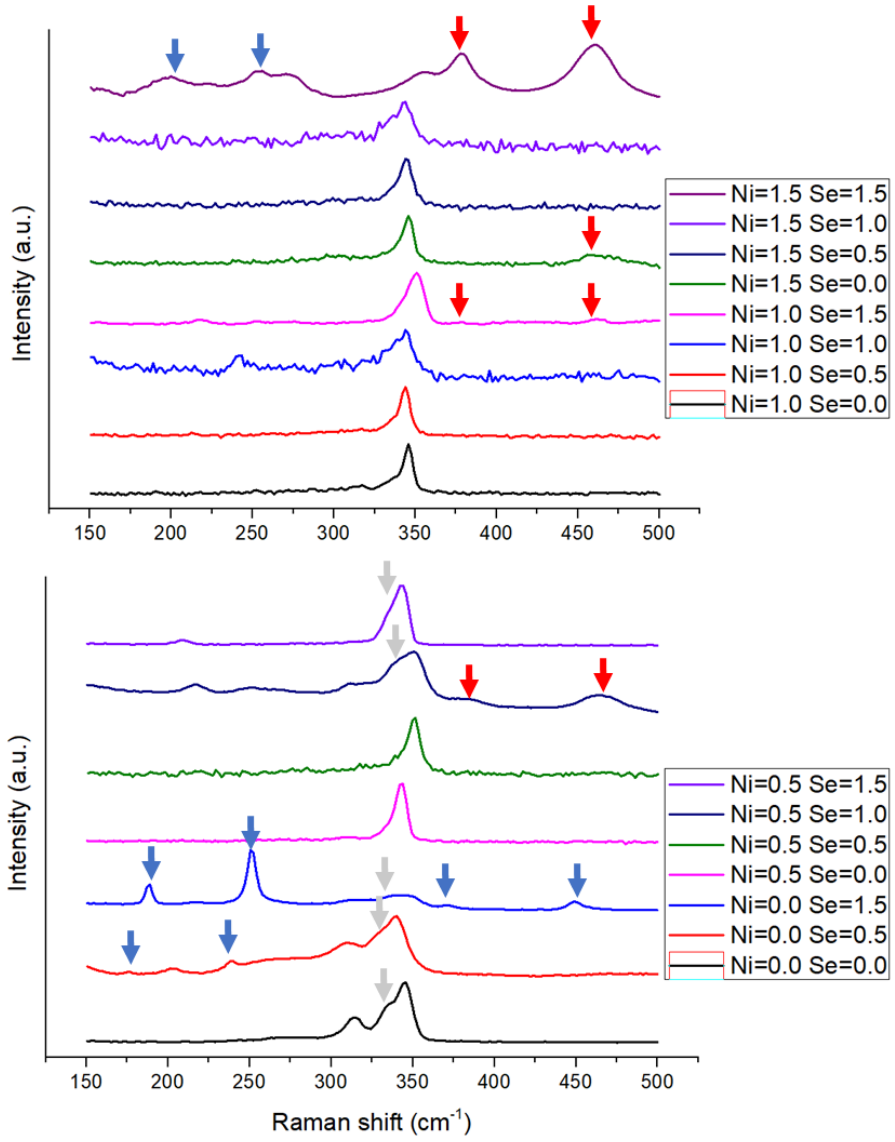

Fig. 55 Raman spectra of $Cu_{12-x}Ni_xSb_4S_{13-y}Se_y$ hot-pressed samples. Peaks not related to tetrahedrite phase are indicated with arrows: blue arrows for Cu-S chemical bond of ejected material which are also in common with chalcostibite and copper sulphides; red arrows representing copper sulphide (Cu_xS_y) secondary phase; and grey arrows- chalcostibite ($CuSbS_2$).[168,169]

Raman spectroscopy results indicate that after hot-pressing (Fig. 55) there is a significant increase in the presence of the secondary phases chalcostibite and copper sulphides, which lends more credibility to the previously made assessment from the X-ray diffraction analysis, that hot-pressing conditions, employed in this experimental procedure, favoured the degeneration of the tetrahedrite phase. It should also be noted that the peak position shifts for introducing either Ni or Se are no longer visible after hot-pressing and no visible difference between Raman spectra is visible that might be attributed to variation of Ni or Se content.

The presence of copper sulphide peaks only in samples containing nickel, coupled with the analysis provided by the SEM-EDS characterization, provides compelling evidence that these peaks correspond to nickel-based sulphides. This occurrence can be attributed to the close resemblance between copper and nickel in terms of electronic configuration and atomic size, as well as the same crystal structure (space group $P6_3/mmc$)[179,180], resulting in similar peak patterns for both groups of compounds. Notably, these peaks were not observed in the annealed samples, suggesting that the hot-pressing process led to the formation of additional Ni_xS_y phases.

Owing to the proximity of the chalcostibite phase to the primary peak of tetrahedrite, accurate identification of this phase in the Raman spectra poses challenges. However, the Raman spectra suggest that the chalcostibite phase tends to emerge in samples with minimal to no Ni content (x=0.0 and 0.5). This observation can be linked to the preventive effect of Ni doping on the degradation of the tetrahedrite phase, as elucidated in the studies conducted by Barbier et al.[106] and Pi et al.[114] concerning the thermal stability of ternary and doped tetrahedrite.

The exhaustive presentation of the Raman spectra is shown in Attachment 2.

4.2.3 SEM-EDS analysis

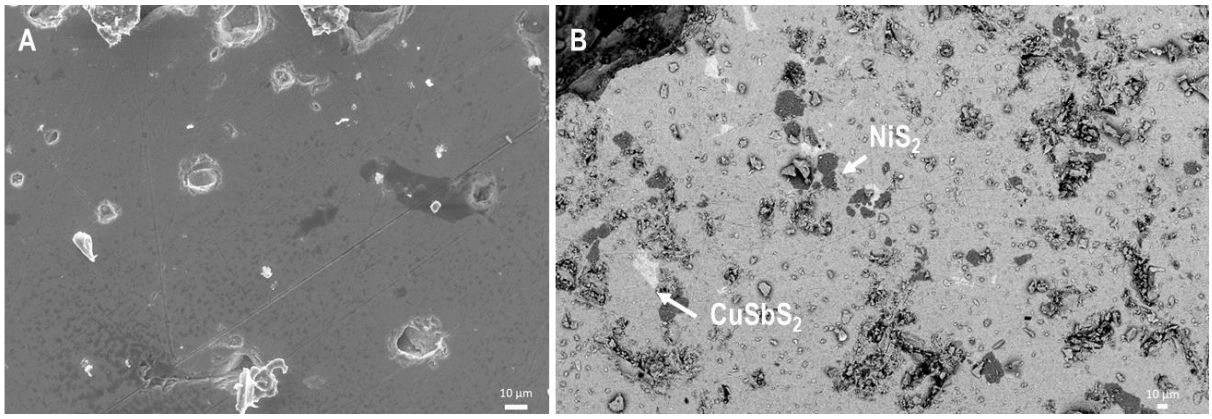

Fig. 56 Phases observed in the $Cu_{11.5}Ni_{0.5}Sb_4S_{12}Se$ after annealing and after hot-pressing sample during SEM-EDS analysis: light-grey phase has a composition similar to doped-chalcostibite ($CuSbS_2$) and dark-grey has a composition similar Nickel Sulphide (Ni_xS_y)

As hinted by the characterization with Raman spectroscopy and X-ray diffraction, SEM-EDS (Fig. 56) revealed, unsurprisingly, the degeneration of the tetrahedrite phase into the formation of $(Cu, Ni)_xS_y$ and $CuSb(S, Se)_2$ secondary phases in all but one sample ($Cu_{11}NiSb_4S_{12.5}Se_{0.5}$) after hot-pressing, in addition to the formation of ullmannite (NiSbS) in the $Cu_{10.5}Ni_{1.5}Sb_4S_{12.5}Se_{0.5}$ sample. In contrast with the samples after casting and after annealing, which only have one sample with two secondary phases ($Cu_{10.5}Ni_{1.5}Sb_4S_{11.5}Se_{1.5}$ and $Cu_{10.5}Ni_{1.5}Sb_4S_{13}$), after hot-pressing five samples presented two different phases, as seen in Fig. 57.

The deterioration of the tetrahedrite phase allows the confirmation of the connection between dopant content and phase formation. The NiS_2 phase (and also the Ni_2S_3 phase present on the $Cu_{11.5}Ni_{0.5}Sb_4S_{11.5}Se_{1.5}$ sample) are only observed on samples with low Ni content, namely samples with x=0.5 and the $Cu_{11}NiSb_4S_{13}$ sample. The Cu_2S is present in samples with no Ni content (x=0.0) and the $Cu_{11.5}Ni_{0.5}Sb_4S_{13}$ sample. The NiS sample is present in all samples with x=1.5 and the $Cu_{11}NiSb_4S_{11.5}Se_{1.5}$ sample. And the $CuSb(S, Se)_2$ phase is only present in samples with a high Se content (y=1.0 and 1.5). Clearly, the phases formation are dependent on the dopant content, with: Ni doping favouring the formation of nickel sulphides over copper sulphides, and the Ni:S ratio being highly dependent on the overall Ni content of the sample; high Se content also favouring the formation of chalcostibite-příbramite phase. Naturally, samples with high total dopant content ($x+y\geq2.0$) tended to form two secondary phases, with the sole exception being the $Cu_{11.5}Ni_{0.5}Sb_4S_{12}Se$

sample with a total dopant content x+y=1.5 and forming a chalcostibite and NiS_2 secondary phases.

It should also be mentioned that one of the analysed samples ($Cu_{11.5}Ni_{0.5}Sb_4S_{13}$) exhibited oxidation in the form of a light-coloured phase with the composition of an antimony oxide (Sb_2O_3), which had also been indicated by powder X-ray diffraction. However, the absence of antimony oxide on the other samples suggests that the polishing of the samples was effective in removing the oxidized portion of the surface of the sample, and that potentially, the oxidation of the $Cu_{11.5}Ni_{0.5}Sb_4S_{13}$ sample was more extensive than expected.

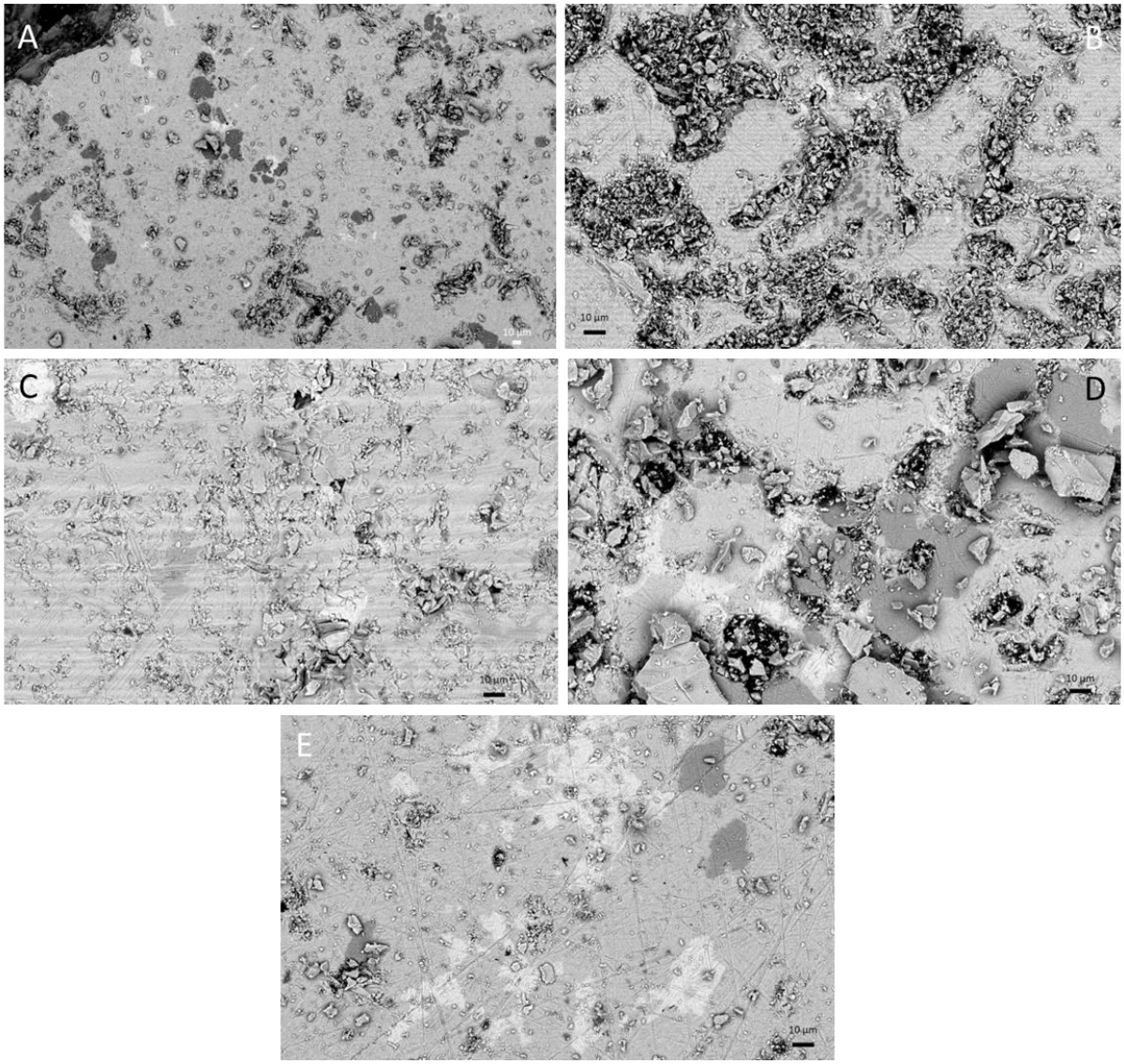

Fig. 57 SEM micrographs of hot-pressed samples with two distinct phases: (A) $Cu_{11.5}Ni_{0.5}Sb_4S_{12}Se$ sample with NiS_2 (dark) and $CuSb(S,Se)_2$ (light) phases; (B) $Cu_{11}NiSb_4S_{11.5}Se_{1.5}$ sample with NiS (dark) and $CuSb(S,Se)_2$ (light) phases; (C) $Cu_{10.5}Ni_{1.5}Sb_4S_{12.5}Se_{0.5}$ sample with NiS (dark) and NiSbS (light) phases; (D) $Cu_{10.5}Ni_{1.5}Sb_4S_{12}Se$ sample with NiS (dark) and $CuSb(S,Se)_2$ (light) phases; and (E) $Cu_{10.5}Ni_{1.5}Sb_4\ S_{11.5}Se_{1.5}$ sample with NiS (dark) and $CuSb(S,Se)_2$ (light) phases.

Despite a clear indication of denser samples, the prevalence of porosity, most likely evidence of incomplete densification of the powder during hot-pressing, is a clear indication of less than optimal hot-pressing conditions which warrant a future adjustment of these conditions, whether by increasing either temperature, pressure and/or duration of the procedure, with pressure being probably the most viable parameter to adjust given the lower chance of causing formation of secondary phases.

Semi-quantitative analysis (Table 4) also shows that, for a 29 atoms molecule, the estimated chemical formula is still similar to the theoretical composition. However, it differs more from the theoretical composition than the previous annealed samples, which is a sign of tetrahedrite degeneration altering the compositions, as well as the fact that sulphur loss seems to facilitate Se integration on the tetrahedrite thus resulting in samples with a significantly higher Se content than expected.

Therefore, it can be surmised that the applied hot-pressing conditions were not conducive to maintaining the tetrahedrite phase. In fact, it seems they had the opposite effect, and that, while successful in reducing the fragility of the samples, the final result was the formation of secondary phases, which ultimately defeats the purpose of studying the thermoelectric properties of Ni and Se doped tetrahedrites.

The exhaustive presentation of the SEM-EDS analysis of hot-pressed samples is shown in Attachment 3.

Table 4 SEM-EDS semi-quantitative analysis of the matrix of hot-pressed samples. The matrix chemical formula was calculated based on the composition and assuming a 29 atoms molecule like tetrahedrite.

Expected formula of the sample	Cu(at%)	Ni(at%)	Sb(at%)	S(at%)	Se(at%)	Matrix chemical formula
$Cu_{11.5}Ni_{0.5}Sb_4S_{13}$	38.2±0.4	3.0±0.2	14.4±0.2	44.5±0.6		$Cu_{11.1\pm0.1}Ni_{0.9\pm0.1}Sb_{4.2\pm0.1}S_{12.9\pm0.2}$
$Cu_{12}Sb_4S_{12.5}Se_{0.5}$	41.2±0.4		13.7±0.2	42.4±0.6	2.7±0.2	$Cu_{11.9\pm0.1}Sb_{4.0\pm0.1}S_{12.3\pm0.2}Se_{0.8\pm0.1}$
$Cu_{11.5}Ni_{0.5}Sb_4S_{12.5}Se_{0.5}$	38.7±0.4	1.2±0.3	13.8±0.2	42.2±0.6	4.1±0.2	$Cu_{11.2\pm0.1}Ni_{0.4\pm0.1}Sb_{4.0\pm0.1}S_{12.3\pm0.2}Se_{1.2\pm0.1}$
$Cu_{11}NiSb_4S_{13}$	40.5±0.4	2.0±0.2	14.2±0.2	43.3±0.6		$Cu_{11.7\pm0.1}Ni_{0.6\pm0.1}Sb_{4.1\pm0.1}S_{12.6\pm0.2}$
$Cu_{11}NiSb_4S_{12.5}Se_{0.5}$	37.5±0.4	2.5±0.3	13.9±0.2	42.3±0.6	3.8±0.2	$Cu_{110.9\pm0.1}Ni_{0.7\pm0.1}Sb_{4.0\pm0.1}S_{12.3\pm0.2}Se_{1.1\pm0.1}$
$Cu_{11.5}Ni_{0.5}Sb_4S_{12}Se$	39.2±0.4	1.6±0.3	14.3±0.2	41.0±0.6	3.9±0.2	$Cu_{11.4\pm0.1}Ni_{0.5\pm0.1}Sb_{4.2\pm0.1}S_{11.9\pm0.2}Se_{1.1\pm0.1}$
$Cu_{12}NiSb_4S_{12}Se$	37.1±0.4	3.3±0.3	13.8±0.2	41.2±0.6	4.7±0.2	$Cu_{10.8\pm0.1}Ni_{0.9\pm0.1}Sb_{4.0\pm0.1}S_{11.9\pm0.2}Se_{1.4\pm0.1}$
$Cu_{10.5}Ni_{1.5}Sb_4S_{13}$	36.9±0.4	3.9±0.2	14.2±0.2	45.0±0.6		$Cu_{10.7\pm0.1}Ni_{1.1\pm0.1}Sb_{4.1\pm0.1}S_{13.1\pm0.1}$
$Cu_{10.5}Ni_{1.5}Sb_4S_{12.5}Se_{0.5}$	37.4±0.4	4.0±0.3	13.6±0.2	41.3±0.6	3.8±0.2	$Cu_{10.8\pm0.1}Ni_{1.2\pm0.1}Sb_{3.9\pm0.1}S_{12.0\pm0.2}Se_{1.1\pm0.1}$
$Cu_{10.5}Ni_{1.5}Sb_4S_{12}Se$	36.1±0.4	3.5±0.3	13.9±0.2	42.0±0.6	4.5±0.2	$Cu_{10.5\pm0.1}Ni_{1.0\pm0.1}Sb_{4.0\pm0.1}S_{12.2\pm0.2}Se_{1.3\pm0.1}$
$Cu_{12}Sb_4S_{11.5}Se_{1.5}$	39.7±0.5		14.2±0.2	39.0±0.6	7.1±0.2	$Cu_{11.5\pm0.1}Sb_{4.1\pm0.1}S_{11.3\pm0.2}Se_{2.1\pm0.1}$
$Cu_{11.5}Ni_{0.5}Sb_4S_{11.5}Se_{1.5}$	44.1±0.5	0.8±0.3	12.6±0.2	37.2±0.6	5.4±0.2	$Cu_{12.8\pm0.1}Ni_{0.2\pm0.1}Sb_{3.7\pm0.1}S_{10.8\pm0.2}Se_{1.6\pm0.1}$
$Cu_{11}NiSb_4S_{11.5}Se_{1.5}$	37.3±0.5	2.9±0.2	14.0±0.2	39.5±0.6	6.2±0.2	$Cu_{10.8\pm0.1}Ni_{0.9\pm0.1}Sb_{4.1\pm0.1}S_{11.5\pm0.2}Se_{1.8\pm0.1}$
$Cu_{10.5}Ni_{1.5}Sb_4S_{11.5}Se_{1.5}$	35.6±0.5	4.0±0.3	14.3±0.2	39.2±0.6	6.9±0.2	$Cu_{10.3\pm0.1}Ni_{1.2\pm0.1}Sb_{4.2\pm0.1}S_{11.4\pm0.2}Se_{2.0\pm0.1}$

4.2.4 Thermoelectric Properties of Hot-pressed samples

The thermoelectric characterization of the hot-pressed samples suggest that the conditions used in the hot-pressing step have, in general, degraded the tetrahedrite phase and resulted in porous pellets and objectively more riddled with secondary phases. All these characteristics have a negative impact in the thermoelectric performance of the materials, as they increase electrical resistivity and lower Seebeck coefficient. Therefore, lower thermoelectric performances of the samples are expected after this hot-pressing step which translates into lower PFs and zTs.

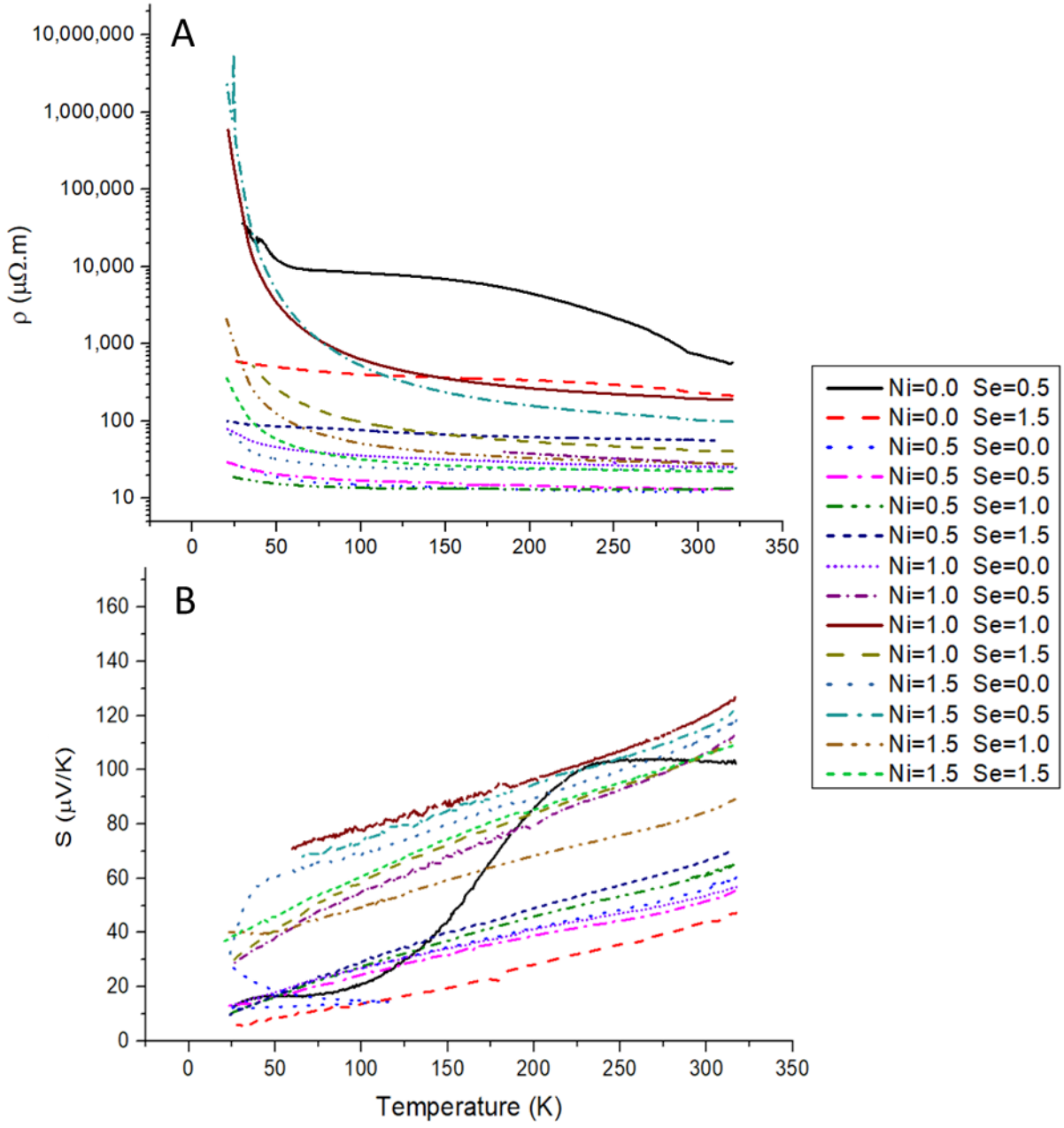

Fig. 58 Measured temperature dependence of electrical resistivity (A) and Seebeck coefficient (B) for samples following the formula $Cu_{12-x}Ni_xSb_4S_{13-y}Se_y$.

In Fig. 58, the results of electrical resistivity and Seebeck coefficient measurements of hot-pressed samples are shown. Comparing with annealed samples, they appear to be in general more resistant and have lower Seebeck coefficients.

Looking into the how varying the Ni content affects the electrical resistivity of hot-pressed samples (Fig.59), it is seen that for fixed Se content, y=0.0 and 1.0, electrical resistivity increases from x=0.5 to x=1.0 and decreases in x=1.5. This behaviour is not observed on the other y values. However, it is seen that samples without Ni (x=0.0) are more resistive than Ni-doped samples, which is in disagreement with Suekuni et al.[76] and our observations and the results obtained from samples prior to hot-pressing. This again corroborates that, instead of reducing detrimental factors in the samples, hot-pressing with these conditions actually increased them. In regard to Seebeck coefficient (Fig.60), it is clear that adding Ni normally results in its increase, and a high Ni content (y≥1.0) generally results in the highest values. However, while it was expected to also be proportional to Ni content, this relation is not observable for all fixed Se content, showcasing that there are other aspects at play altering the final thermoelectric properties of the samples.

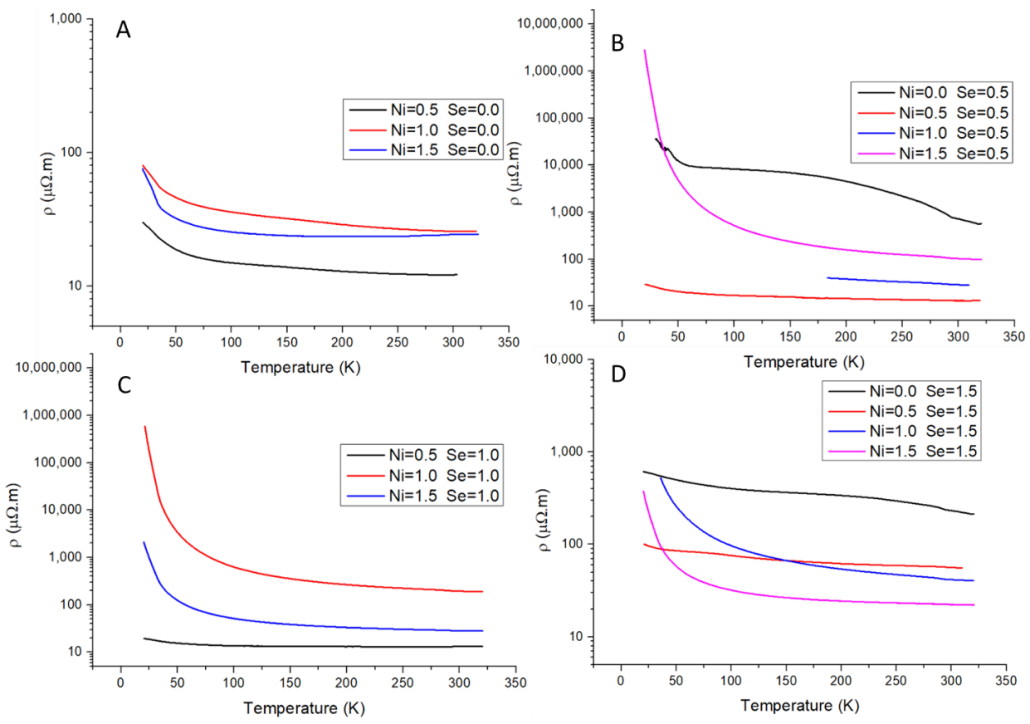

Fig. 59 Comparison of the temperature and Ni stoichiometric dependence of measured electrical resistivity of hot-pressed samples with fixed Se stoichiometric content following the expected formulas: (A) $Cu_{12-x}Ni_xSb_4S_{13}$; (B) $Cu_{12-x}Ni_xSb_4S_{12.5}Se_{0.5}$; (C) $Cu_{12-x}Ni_xSb_4S_{12}Se$; (D) $Cu_{12-x}Ni_xSb_4S_{11.5}Se_{1.5}$.

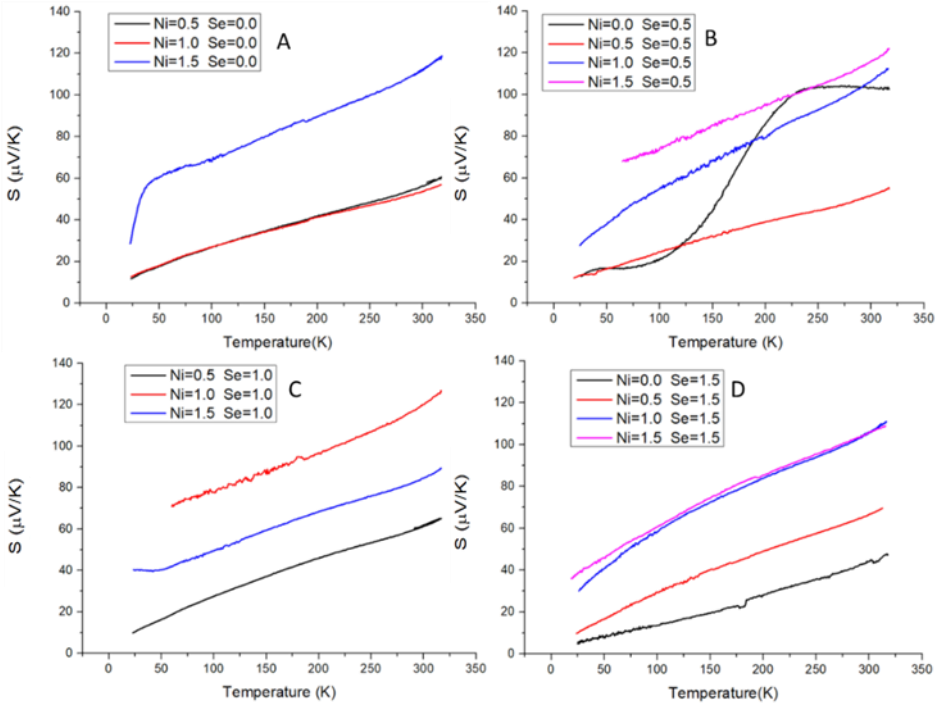

Fig. 60 Comparison of the temperature and Ni stoichiometric dependence of measured Seebeck coefficient of hot-pressed samples with fixed Se stoichiometric content following the expected formulas: (A) $Cu_{12-x}Ni_xSb_4S_{13}$; (B) $Cu_{12-x}Ni_xSb_4S_{12.5}Se_{0.5}$; (C) $Cu_{12-x}Ni_xSb_4S_{12}Se$; (D) $Cu_{12-x}Ni_xSb_4S_{11.5}Se_{1.5}$.

After hot-pressing, no clear correlation between Se content and electrical resistivity (Fig.61) is observed across all sets of samples with the same Ni content. Similarly, a proper clear correlation between Se content and Seebeck coefficient (Fig.62) is also hard to determine. However, the temperature dependence of both Seebeck coefficient and electrical resistivity appears to have a more uniform behavior across samples with the same Ni content. This level of uniformity in the temperature dependence of the properties of samples with the same Se content is not observed, implying that Ni content has a bigger role in determining the final properties than Se content. Looking into other studies and the present difficulty in producing Se-only doped tetrahedrites without excessive secondary phases, it becomes clear that tetrahedrite phase stability is a major factor into determining the final thermoelectric properties. Thermal Gravimetric analysis of Ni-doped tetrahedrite (x=1.5 and x=1.0) made by Barbier et al.[106] and Pi et al.[114], respectively, indicate a remarkable reduction of phase degeneration, when compared with the ternary tetrahedrite. This can be the reason behind the greater degree of uniformity for Seebeck coefficient and electrical resistivity dependence on temperature for samples with the same Ni content, has they would experience similar levels of tetrahedrite degeneration. Further confirmation of these results would require additional thermal stability studies of these samples, particularly those doped with Se only.

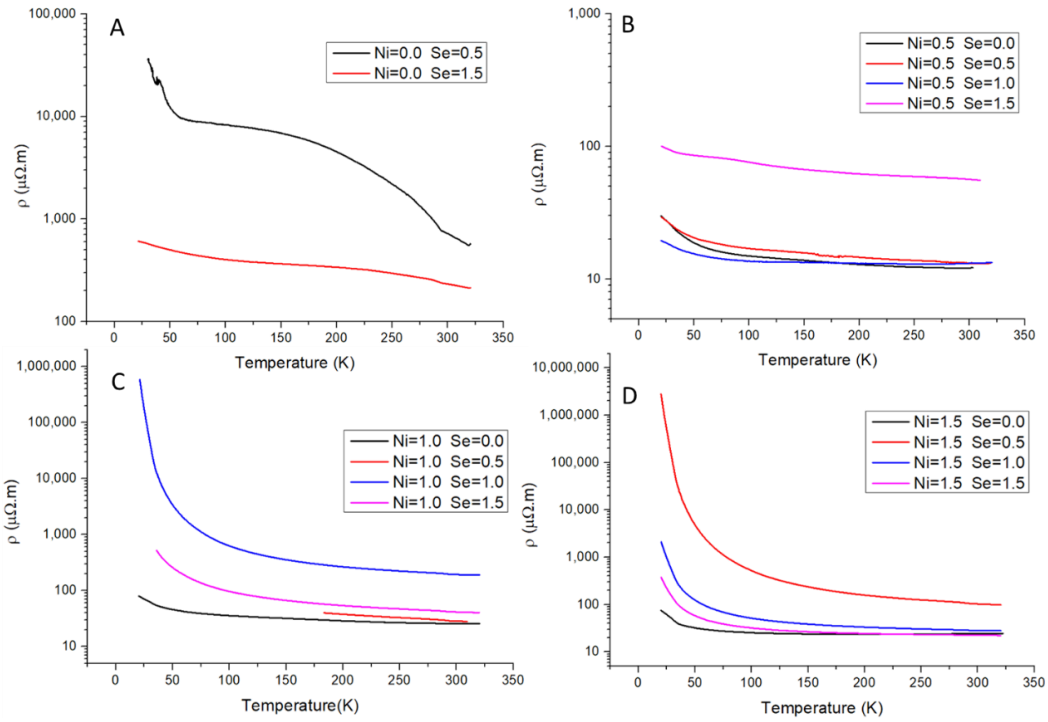

Fig. 61 Comparison of the temperature and Se stoichiometric dependence of measured electrical resistivity of hot-pressed samples with fixed Ni stoichiometric content following the expected formulas: (A) $Cu_{12}Sb_4S_{13-y}Se_y$; (B) $Cu_{11.5}Ni_{0.5}Sb_4S_{13-y}Se_y$; (C) $Cu_{11}NiSb_4S_{13-y}Se_y$; (D) $Cu_{10.5}Ni_{1.5}Sb_4S_{13-y}Se_y$.

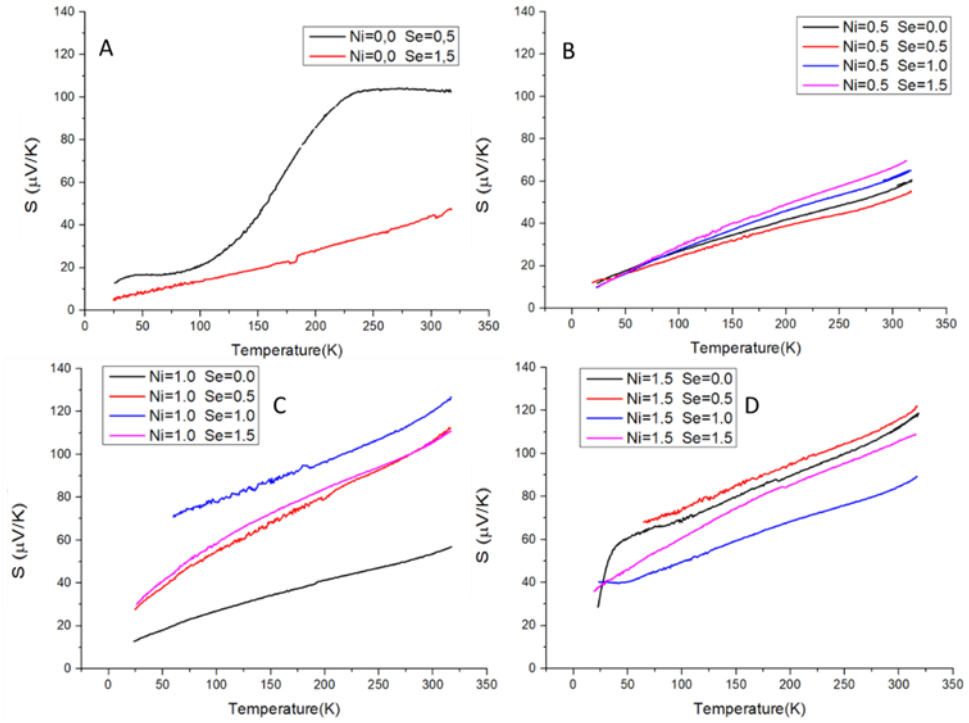

Fig. 62 Comparison of the temperature and Se stoichiometric dependence of measured Seebeck coefficient of hot-pressed samples with fixed Ni stoichiometric content following the expected formulas: (A) $Cu_{12}Sb_4S_{13-y}Se_y$; (B) $Cu_{11.5}Ni_{0.5}Sb_4S_{13-y}Se_y$; (C) $Cu_{11}NiSb_4S_{13-y}Se_y$; (D) $Cu_{10.5}Ni_{1.5}Sb_4S_{13-y}Se_y$.

After calculating the PF (Fig. 63B) and comparing the curves of annealed and hot-pressed samples, one could easily make an erroneous first observation that there seems to be general tendency for samples manifesting a lower PF after hot-pressing. However, individual comparison of each composition before and after hot-pressing for each property at 300K, as presented in Fig. 64, 65 and 66, reveals that not every hot-pressed sample presented worst thermoelectric properties. In fact, some samples benefited from the hot-pressing step, even in these clearly non-optimal conditions, being possible to observe that there is often a drastic improvement of thermoelectric properties, with one instance more than tripling their PF prior to hot-pressing ($Cu_{10.5}Ni_{1.5}Sb_4S_{11.5}Se_{1.5}$. with PF≈112.05 μW/m.K^2 before hot-pressing and PF≈499.56 μW/m.K^2 after hot-pressing at 300K).

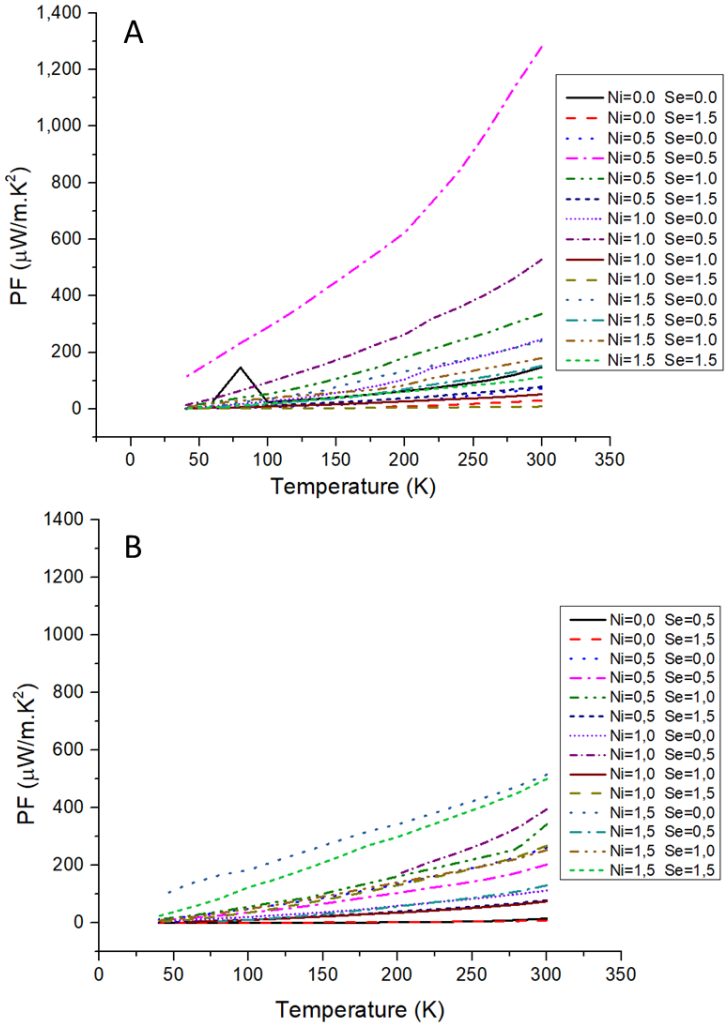

Fig. 63 Comparison of the PF between Annealed (A) and Hot-pressed (B) samples following the formula $Cu_{12-x}Ni_xSb_4S_{13-y}Se_y$.

Considering all observations made on this chapter, it is clear that there are multiple correlated factors at play that dictate the final thermoelectric performance of tetrahedrites,

namely: phase decomposition, sulphur loss and Ni content. Phase degeneracy is a most central factor: the presence of secondary phases is probably the biggest hindrance to the overall thermoelectric performance of the samples, as evidenced by a decrease in the PF at 300K between several annealed samples and hot-pressed samples. Sulphur loss, which is suggested by the overall decrease of lattice parameter of the tetrahedrite phase in all hot-pressed samples, can have both a detrimental and beneficial effect on the PF of the sample. On one hand, it promotes degeneration of tetrahedrite phase into secondary phases. However, the remaining tetrahedrite phase would end up having a higher Cu content (a Cu-rich tetrahedrite) that has higher charge carrier concentration, due to more Cu ions, thus becoming more conductive,[98]. Regarding the last factor, the Ni content, the samples that exhibited higher PFs, either were solely doped with Nickel or had high stoichiometric Ni content ($x \geq 1.0$), as was demonstrated by Barbier et al.[106]. Ni doping increases tetrahedrite thermal stability, reducing degeneration and the number of secondary phases formed when compared with undoped tetrahedrite. This means that Ni-doping preserved these Cu-rich tetrahedrites from degeneration, and after hot-pressing, these samples would have less defects like pores and fractures, resulting in samples with better thermoelectric properties than their annealed counterparts.

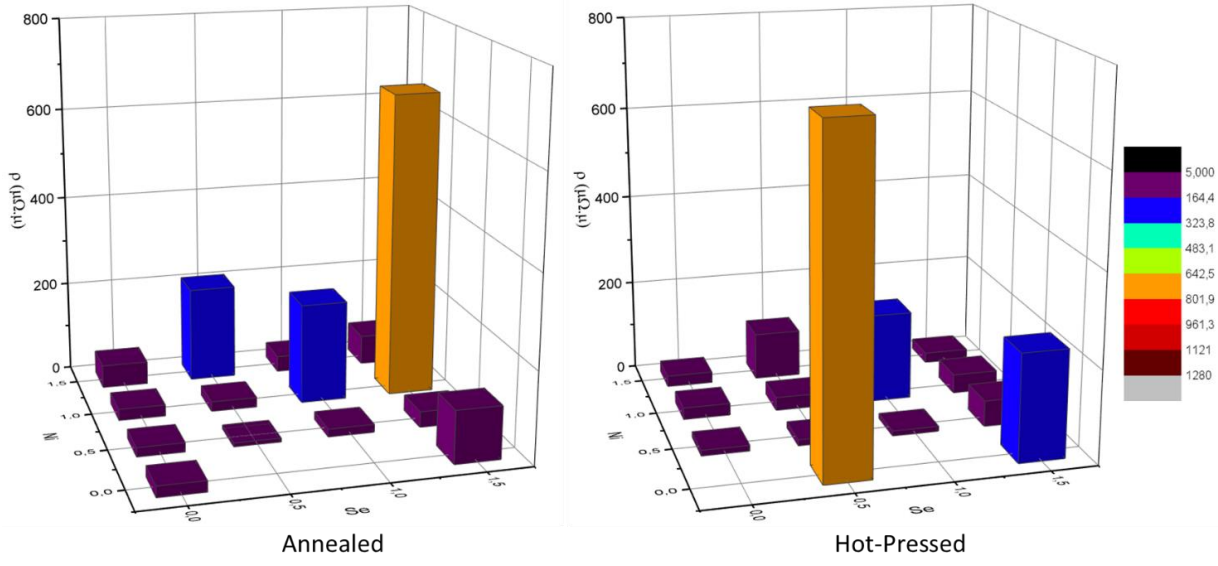

Fig. 64 Comparing Electrical resistivity of annealed and hot-pressed samples as a function of stoichiometric Nickel and Selenium content, following the formula $Cu_{12-x}Ni_xSb_4S_{13-y}Se_y$.

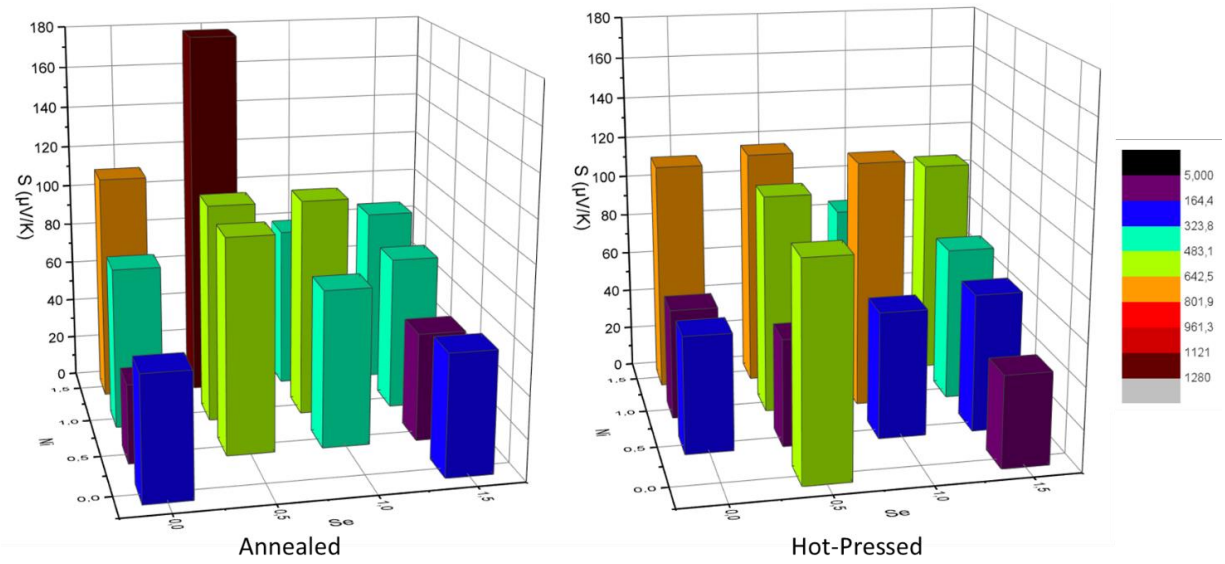

Fig. 65 Comparing Seebeck coefficient of annealed and hot-pressed samples as a function of stoichiometric Nickel and Selenium content, following the formula $Cu_{12-x}Ni_xSb_4S_{13-y}Se_y$.

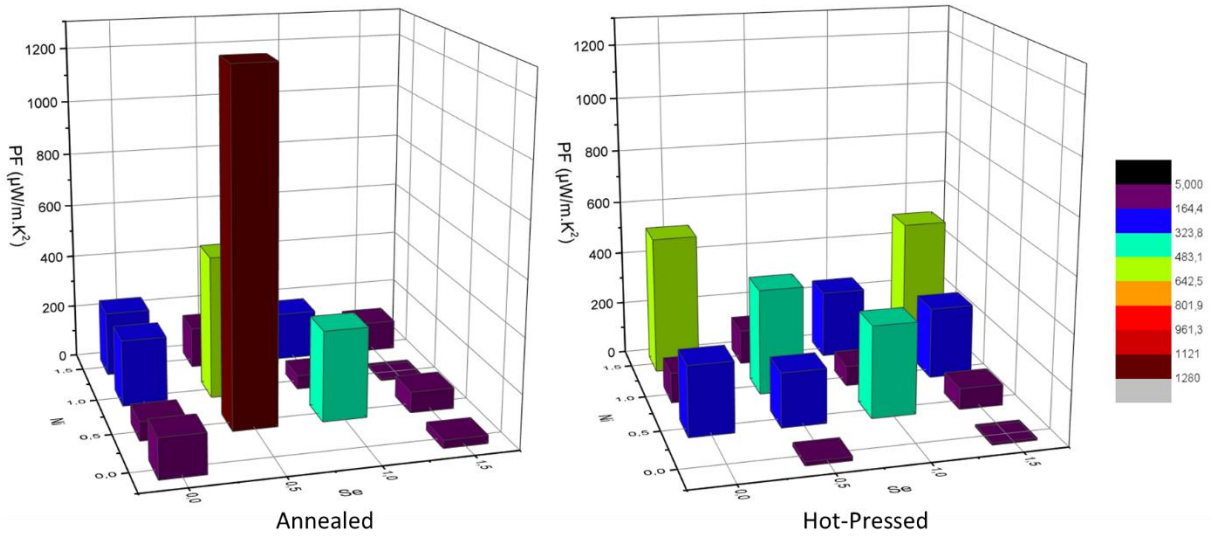

Fig. 66 Comparing PF of annealed and hot-pressed samples as a function of stoichiometric Nickel and Selenium content, following the formula $Cu_{12-x}Ni_xSb_4S_{13-y}Se_y$.

Following the same methodology presented in chapter 4.1.4, to estimate the thermal conductivity, the figure of merit for each sample at 300K was calculated, resulting in the graphs presented in Fig. 67 and Table 5.

Prior to hot-pressing, the sample with the best thermoelectric performance was the one with expected composition $Cu_{11.5}Ni_{0.5}Sb_4S_{12.5}Se_{0.5}$, which achieved an estimated zT of 0.33 at 300K. This result was corroborated by the Wien2K-BoltzTraP simulations, which also estimated a zT≈0.3 at 300K. After hot-pressing however, this sample presented a decrease in

their PF, which ultimately translated in a decrease in their zT to 0.06 at 300K. On the other hand, samples with high Ni content showed a general increase in PF and conversely, in estimated figure of merit, particularly the $Cu_{10.5}Ni_{1.5}Sb_4S_{13}$ sample, achieving a zT=0.21 at 300K, which is similar to what was achieved by Suekuni et al[76] for the same composition ,and the $Cu_{10.5}Ni_{1.5}Sb_4S_{11.5}Se_{1.5}$ sample with a zT_{300K}=0.20.

Nonetheless, overwhelming consensus of the data is that the hot-pressing conditions used in this study were not adequate to improve both thermoelectric and mechanical properties of the samples, given the porosity after the procedure, resulting in more fragile and brittle samples.

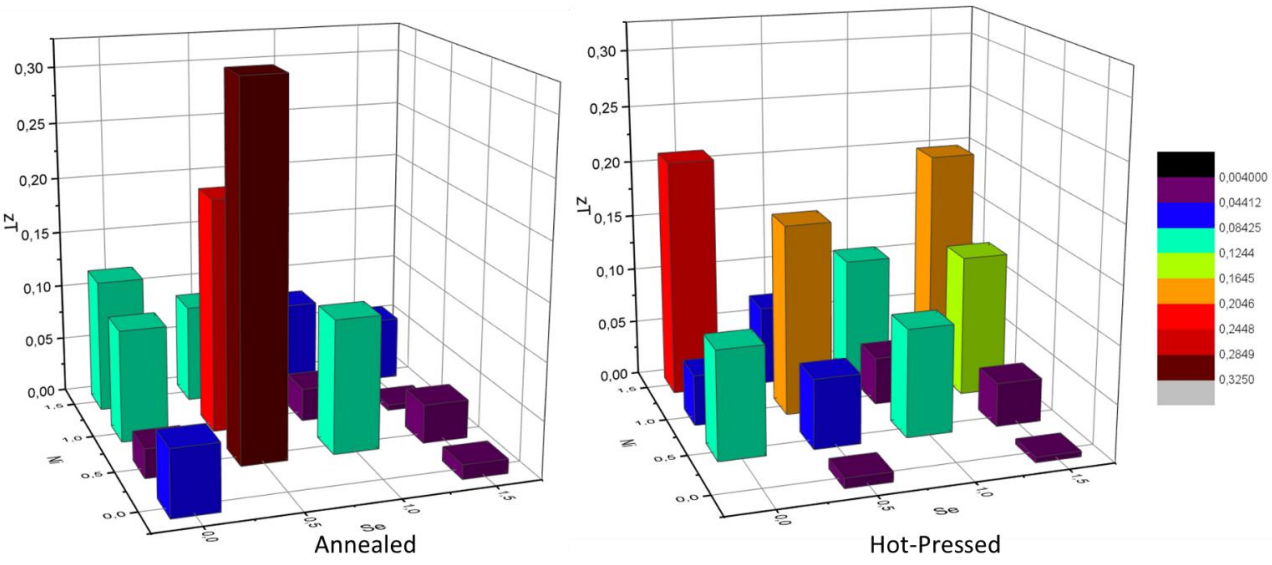

Fig. 67 Comparing zT of annealed and hot-pressed samples as a function of stoichiometric Nickel and Selenium content, following the formula $Cu_{12-x}Ni_xSb_4S_{13-y}Se_y$.

The exhaustive presentation of the measurements and calculations of electrical resistivity, Seebeck coefficient, PF and Figure of Merit analysis of hot-pressed samples are presented in Attachments 4, 5, 6 and 7, respectively.

Table 5 Electrical resistivity, Seebeck coefficient, PF, estimated thermal resistivity and figure of merit of hot-pressed $Cu_{12-x}Ni_xSb_4S_{13-y}Se_y$ samples at 300K.

X	Y	ρ (μΩm)	S (μV/K)	PF (μW/m.K^2)	κ estimated (μW/m.K)	zT
0.5	**0.0**	12.14	56.32	261.24	1.02	**0.10**
0.0	**0.5**	719.76	103.18	14.79	0.51	**0.01**
0.5	**0.5**	13.18	51.63	202.22	0.99	**0.06**
1.0	**0.0**	25.68	53.70	112.31	0.75	**0.05**
1.0	**0.5**	28.68	106.31	394.10	0.70	**0.17**
0.5	**1.0**	10.95	61.23	342.34	1.07	**0.10**
1.0	**1.0**	193.74	120.12	74.49	0.53	**0.04**
1.5	**0.0**	24.29	111.82	514.83	0.73	**0.21**
1.5	**0.5**	102.84	115.84	130.47	0.55	**0.07**
1.5	**1.0**	28.32	84.63	252.93	0.71	**0.11**
0.0	**1.5**	231.97	44.18	8.41	0.53	**0.01**
0.5	**1.5**	56.40	66.62	78.69	0.61	**0.04**
1.0	**1.5**	41.58	74.84	267.75	0.64	**0.13**
1.5	**1.5**	22.39	105.75	499.56	0.75	**0.20**

4.2.5 Weighted mobility

The variation of the weighted mobility with temperature of the annealed and hot-pressed samples is presented in Fig. 68. Their direct comparison shows that most samples maintained the values after the hot-press procedure, with only a few samples displaying important changes, associated with significant variations in their overall PF and zT.

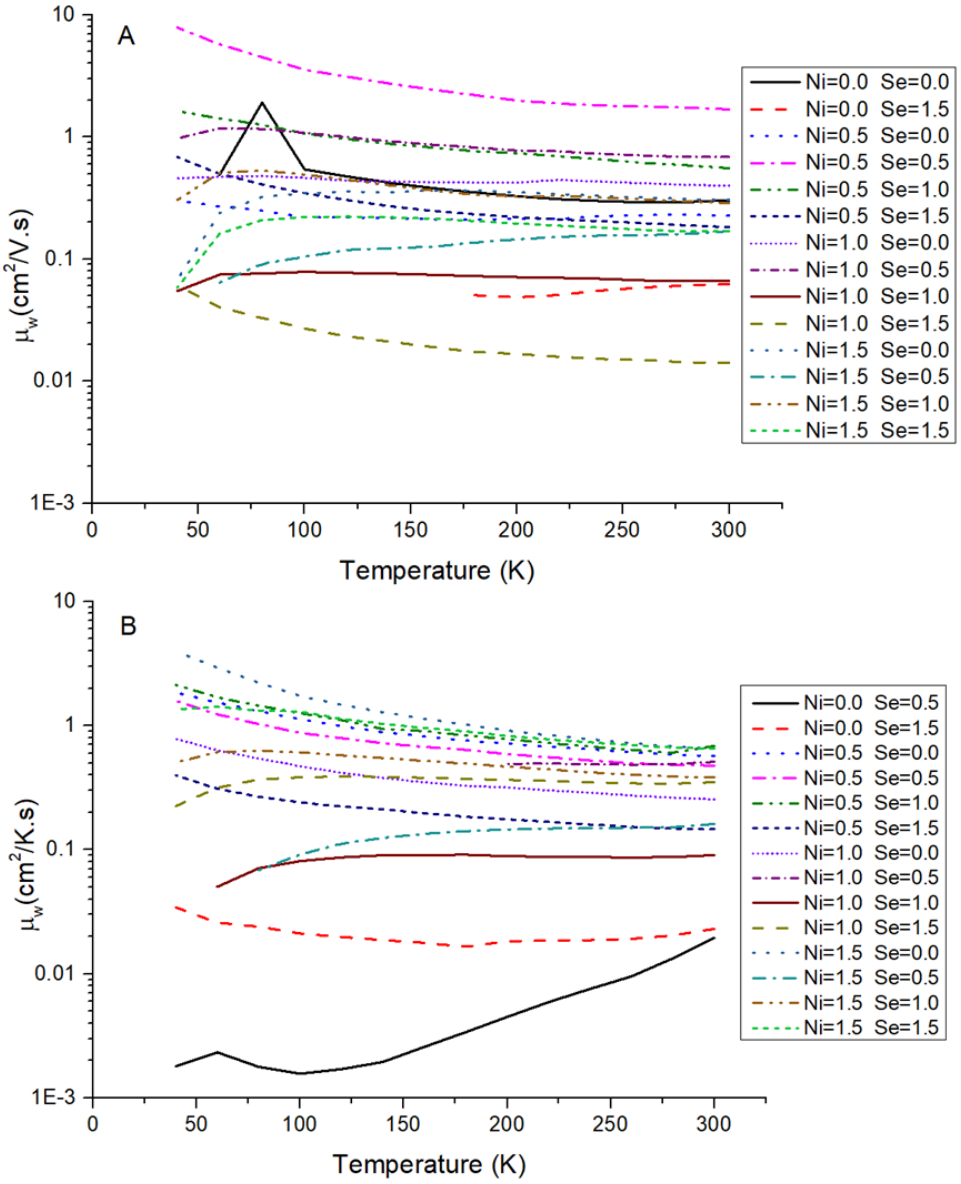

Fig. 68 Weighted mobility calculated from the measurements of the Seebeck coefficient and electrical resistivity of samples after annealing (A) and after hot-pressing (B)following the formula $Cu_{12-x}Ni_xSb_4S_{13-y}Se_y$.

Looking into the effect of Ni content (Fig.52), it was observed that in annealed samples Ni disrupted the $T^{(-3/2)}$ progression of the weighted mobility at low temperatures and that this disruption would appear to be proportional to Ni content. After hot-pressing, the same type of deviation from the $T^{(-3/2)}$ progression is observed at lower temperatures in several of the

samples containing high amounts of Ni (x≥1.0). However, hot-pressed samples exclusively doped with Ni did not exhibit this deviation, as seen in Fig. 69A. Only in samples containing both Ni and Se it is possible to observe the deviation at lower temperatures. Nonetheless, it is clear that Ni content still play a role in producing this deviation, but there are other factors contributing to it as well. This phenomenon is best observed when comparing samples with fixed Ni content x=1.0 and 1.5 (Fig. 70 C and D), where it appears that by introducing Se in the sample, the weighted mobility diverges from the $T^{(-3/2)}$ progression, but this divergence diminishes and overall μ_w increases as the Se content increases.

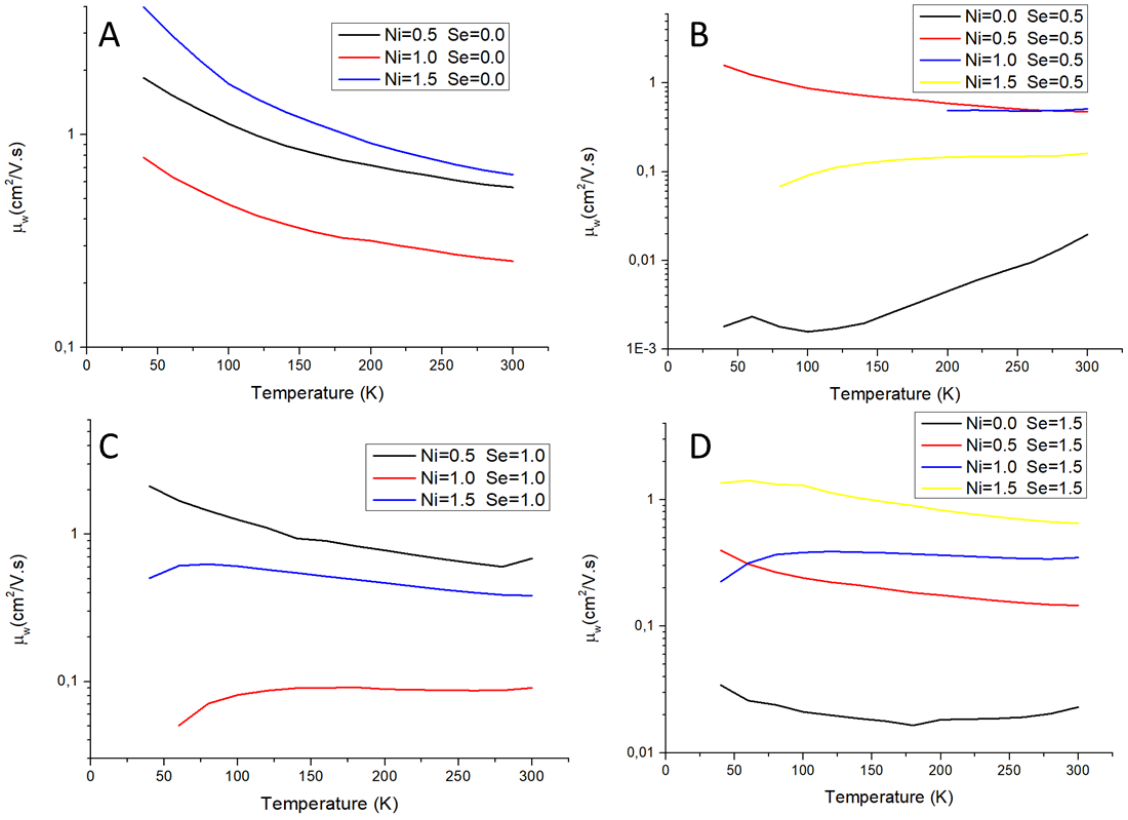

Fig. 69 Comparison of the temperature and Ni stoichiometric dependence of the calculated weighted mobility of hot-pressed samples with fixed Se stoichiometric content following the expected formulas: (A) $Cu_{12-x}Ni_xSb_4S_{13}$; (B) $Cu_{12-x}Ni_xSb_4S_{12.5}Se_{0.5}$; (C) $Cu_{12-x}Ni_xSb_4S_{12}Se$; (D) $Cu_{12-x}Ni_xSb_4S_{11.5}Se_{1.5}$.

It was previously considered two possible reasons for the origin of the lower temperature deviation, both associated to Ni content: increased grain boundary resistance or magnetism induced charge carrier scattering. After hot-pressing, it has become clear that Ni content is not the only factor contributing to this deviation, but it also appears that secondary phases formation might impact the weighted mobility, given the need of a high dopant content. In fact, comparing results for samples with the same Ni or Se content, a direct connection between a weighted mobility decrease of one or two orders of magnitude and the

presence of chalcostibite ($CuSb(S,Se)_2$), covellite (CuS) and ullmannite (NiSbS) can be inferred. The presence and quantity of these secondary phases negatively affect the weighted mobility, much probably in the same way as small grain sizes increase the grain boundary resistance, but also by introducing different mediums for electron transport, which ultimately results in increased mean-free-paths, thus decreased mobility. The presence of antimony oxide seems to not alter the weighted mobility, which is most like related to the fact that the oxidation is mainly localized at the sample surface. Moreover, these samples are also polished before SEM analysis and measurements of Seebeck coefficient and electrical resistivity.

It is important to note that many factors and mechanisms can affect the charge carrier's mobility and can cause this low temperature decrease in the weighted mobility, including, but not limited to, grain boundary resistance, intergranular secondary phases, impurity scattering, defect scattering and magnetic scattering. Moreover, it is quite likely that no factor alone is responsible for the deviation observed in weighted mobility, but all affect its simultaneously.

Nonetheless, as for the reason why $Cu_{11}NiSb_4S_{13}$ and $Cu_{10.5}Ni_{1.5}Sb_4S_{13}$ do not present the same decreasing weighted mobility with temperature decrease observed in other samples with x=1.0 or 1.5, both after annealing and hot-pressing, remains a puzzling question. While only samples with high Ni content ($x \geq 1.0$) present weighted mobility decrease, it appears to be stimulated by the presence of Se in hot-pressed samples. This line of thought conduces back into what changed with hot-pressing, namely the constriction of the unit cell and the S loss. However, assuming a relation between unit cell size and magnetic induced scattering would potentially imply a manifestation of a magnetovolume effect as described by Takahashi[181], where a crystal containing magnetostrictive elements, which include Ni, can change the size of the unit cell by applying a magnetic moment or when constricting the unit cell it is possible to mitigate magnetic moment. If this is the case, it could potentially explain why samples doped solely with Ni do not exhibit the decrease in weighted mobility at lower temperatures since they present a significant decrease in the unit cell size after hot-pressing. This would also explain why the weighted mobility decrease appears after doping with Se, the larger ionic radius of Se increases the lattice parameter, which then translates into the manifestation of antiferromagnetic moment of Ni and induced magnetic moment on Cu and S, resulting in the observation of the magnetic scattering at lower temperatures.

In regard to the impact of Se content in the weighted mobility (Fig.70), no discernible correlation can be inferred. However, it is interesting to notice that weighted mobility tends to be similar for samples with the same Ni content, which would imply that Se content is not

altering it. The existence of one sample with a significantly lower mobility in each set of samples (x=0.5, 1.0 and 1.5) (Fig. 70B, C and D) can be explained by comparing with the powder X-ray diffraction results, as the outlier samples correspond to the samples that exhibited secondary phases, namely $Cu_{11.5}Ni_{0.5}Sb_4S_{11.5}Se_{1.5}$, $Cu_{11}NiSb_4S_{12}Se$ and $Cu_{10.5}Ni_{1.5}Sb_4S_{12.5}Se_{0.5}$. This strengthens the argument that the presence of secondary phases has a detrimental impact in the weighted mobility. Since each of these samples present a different secondary phase (chalcostibite, covellite and ullmannite, respectively), it appears to be that this detriment is caused by the sheer presence of a secondary phase rather than being related to a specific phase, which shows the importance of producing single phased samples for the optimization of thermoelectric properties.

The exhaustive presentation of the weighted mobility results of the hot-pressed samples is shown in Attachment 8.

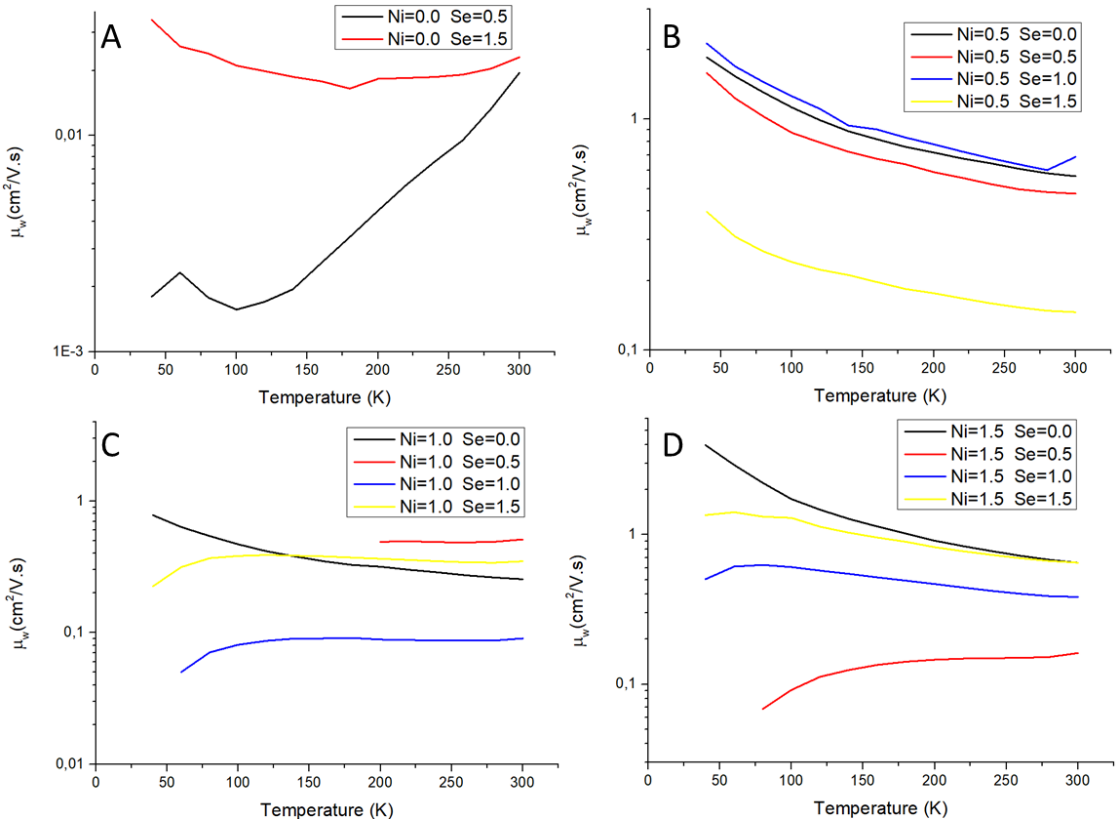

Fig. 70 Comparison of the temperature and Se stoichiometric dependence of the calculated weighted mobility of hot-pressed samples with fixed Ni stoichiometric content following the expected formulas: (A) $Cu_{12}Sb_4S_{13-y}Se_y$; (B) $Cu_{11.5}Ni_{0.5}Sb_4S_{13-y}Se_y$; (C) $Cu_{11}NiSb_4S_{13-y}Se_y$; (D) $Cu_{10.5}Ni_{1.5}Sb_4S_{13-y}Se_y$.

5. CONCLUSIONS

Throughout this work, samples were extensively studied throughout the synthesis process, to properly identify all the nuances, phenomena and changes occurring due to the introduction of not one but two dopants on tetrahedrite and how it affects not just the thermoelectric properties, but also the physical and chemical properties.

The computational analysis with Wien2k and BoltzTraP software packages allowed the preview of what potential changes to the band structure could be expected in the tetrahedrite after doping or substituting Cu and S with Ni and Se, which provided a basis of comparison to the experimental results obtained later in the project. The initial interpretation of the DOS graphs showed the decrease of the Fermi level and spin asymmetry introduced by Ni doping, clearly suggesting a potential change in magnetic behaviour of the tetrahedrite, as well as the nearly non-existent impact of Se on changes to the DOS of tetrahedrite at higher content, but an apparent increase in the overall DOS contributions of the other elements present. This culminated in estimations based on the Boltzmann transport theory of the electrical resistivity, Seebeck coefficient and thermal conductivity variation with temperature, pointing to that doping with both Ni and Se would generally significantly improve the thermoelectric performance of ternary tetrahedrite.

It is clear from the literature that, as single dopants, using Ni and Se have been effective in improving overall thermoelectric properties of tetrahedrite, yet combining both dopants seem to create a synergy that goes beyond the expected linear combination of the effect of both dopants per se. This is evident when we consider the results demonstrated by the present study but also taking into account what is known from the literature.[76,96–99,101,106,114–117,123–125,134,138–142,164,166]

It has been demonstrated that attaining Ni and Se doped tetrahedrite after a simple casting step is possible, however the presence of secondary phases namely chalcostibite and copper-nickel sulphides and low overall homogeneity, justifies the requirement of further refining steps to mitigate the formation of these phases. The annealing step, executed as described, has been effective in reducing secondary phase formation and improving homogeneity, however, tetrahedrite samples doped exclusively with Se, present a particular challenge as they favoured formation and growth of chalcostibite secondary phase, even after reducing the annealing temperature. Despite, otherwise, successfully producing tetrahedrite samples with negligible secondary phase formation, the porosity and brittleness of the

samples became the major hindrance to thermoelectric properties, which warranted further treatment. The hot-pressing, as described in the experimental methodology, has been successful in reducing brittleness and porosity on the samples, however, it led back to the formation of secondary phases and loss of sulphur in the tetrahedrite, which ultimately resulted in a mixed results between improvements and declines in the thermoelectric performance.

Both computational simulations and experimental analysis of the thermoelectric properties, shows that Ni-Se doped tetrahedrites maintain the highly degenerate semiconducting behaviour characteristic of ternary tetrahedrite. The impact that these dopants had on the thermoelectric properties indicate a potential improvement of the overall thermoelectric efficiency of tetrahedrite, even with just one annealing step. Particularly, the $Cu_{11.5}Ni_{0.5}Sb_4S_{12.5}Se_{0.5}$ sample shows a PF of 1279.99 $\mu W/m.K^2$ at 300K, much higher than the previously described regarding tetrahedrites with these dopants ($\approx$ 490 $\mu W/m.K^2$ at 300K).[76,101,109,112]

In terms of the thermoelectric performance, both computational simulations and estimations with experimental results after annealing concur that it is possible to significantly improve performance of tetrahedrite by introducing Ni and Se simultaneously, but they also seem to agree on the optimum composition to be around $Cu_{11.5}Ni_{0.5}Sb_4S_{12.5}Se_{0.5}$, predicting in simulations a $zT_{300K}\approx0.30$ and experimentally, an estimated $zT_{300K}\approx0.33$, through the Wiedmann-Franz law and assuming a κ_L=0.5 W/m.K, typical value of the lattice contribution for tetrahedrite.[76]

In what regards the performance after hot-pressing, unfortunately it confirms, comparing to the previous characterization assessment, that the conditions of the hot-pressing were not entirely adequate, as several samples display a decrease in performance, most likely associated with the formation of secondary phases and sulphur loss. That said, hot-pressing also showed the degeneration prevention effect of Ni content on tetrahedrite and showed also the beneficial potential of this step in improving thermoelectric performance, since samples with high Ni content ($x\geq1.0$) show overall improved thermoelectric performance, particularly samples $Cu_{10.5}Ni_{1.5}Sb_4S_{13}$ and $Cu_{10.5}Ni_{1.5}Sb_4S_{11.5}Se_{1.5}$ improving from a PF_{300K}=240.61 $\mu W/m.K^2$ to a PF_{300K}=514.83 $\mu W/m.K^2$ and a PF_{300K}=112.05 $\mu W/m.K^2$ to a PF_{300K}=499.56 $\mu W/m.K^2$, respectively. After estimating the electronic thermal conductivity with the Wiedmann-Franz law for hot-pressed samples, it was possible to estimate a zT_{300K}=0.21 and 0.20 for $Cu_{10.5}Ni_{1.5}Sb_4S_{13}$ and $Cu_{10.5}Ni_{1.5}Sb_4S_{11.5}Se_{1.5}$ samples, respectively, on par with a

$Cu_{10.5}Ni_{1.5}Sb_4S_{13}$ sample (zT_{300K}=0.22) synthesized with a similar procedure, reported by Suekuni, et al.[76]

Calculating weighted mobility can provide some insight into the charge carrier mobility in samples, revealing in our case that the presence of secondary phases can have a significant detrimental effect on the overall weighted mobility, as could be expected. Interestingly, it was noticed that the presence of Ni content appears to alter weighted mobility variation with temperature from the expected $T^{-3/2}$ progression at lower temperatures, most likely either by hindering crystal growth or by introducing an antiferromagnetic interaction which will alter electron transport and scattering, or by introducing some form of impurity scattering. After hot-pressing, there is also an apparent interaction between both Ni and Se content, altering weighted mobility variation with temperature at low temperatures, which might be associated with the sulphur loss, experienced by most samples after hot-pressing.

Overall, despite the non-optimum conditions applied in the hot-pressing step, it is clear that not only it is possible to significantly improve the thermoelectric performance of tetrahedrite through Ni and Se simultaneous doping even with just one annealing step and with clear indication that it is highly likely to be improved even more after a hot-pressing step or another sintering procedure that could reduce porosity and further strengthen the doped tetrahedrite mechanically.

Ultimately, should the $Cu_{11.5}Ni_{0.5}Sb_4S_{12.5}Se_{0.5}$ tetrahedrite or a similar composition maintain this increased thermoelectric performance at higher temperatures namely in 300-400 ^oC range as it is expected, and be successfully produced with minimum secondary phase formation, low porosity and with higher mechanical strength, it could very well become cheaper and less toxic alternative to current commercial thermoelectric materials, paving the way for more accessible and more widely applicable thermoelectric generators that can help lower the consumption of fossil fuels and other resources and became a green alternative for energy production. This objective would be further accomplished if, one day, it becomes possible to start with natural tetrahedrite minerals and change the chemical composition directly to the desired high performance optimum composition.

6. REFERENCES

1. Terasaki I. Introduction to thermoelectricity. In: Sorrel CC, Sugihara S, Nowotny J, editors. Materials for Energy Conversion Devices. First. Woodhead Publishing; 2005. p. 339–57.
2. Anatychuk LI. On the discovery of thermoelectricity by Volta. Journal of thermoelectricity. 2004;2:5–11.
3. Rowe DM. Handbook of Thermoelectrics. CRC Press; 1995. 666 p.
4. Goldsmid HJ. Introduction to Thermoelectricity. Hull R, Parisi J, Osgood Jr. RM, Warlimont H, editors. Springer; 2010. 240 p.
5. McCormick School of Engineering- Northwestern University. History of Thermoelectrics Brief History of Thermoelectrics [Internet]. 2023 [cited 2023 Jan 23]. p. 1–5. Available from: http://thermoelectrics.matsci.northwestern.edu/thermoelectrics/history.html
6. Joffe AF. The Revival of Thermoelectricity. Sci Am. 1958;199(5):31–7.
7. Rowe DM, editor. Thermolectrics Handbook-Macro to Nano. CRC Press; 2006.
8. Alimov R. Bellona. 2005 [cited 2022 Jun 20]. Radioisotope Thermoelectric Generators. Available from: https://bellona.org/news/nuclear-issues/radioactive-waste-and-spent-nuclear-fuel/2005-04-radioisotope-thermoelectric-generators-2
9. Emery G. Reuters. 2007 [cited 2022 Jun 25]. Nuclear pacemaker still energized after 34 years. Available from: https://uk.reuters.com/article/health-heart-pacemaker-dc/nuclear-pacemaker-still-energized-after-34-years-idUKN1960427320071219
10. U.S. Department of Energy's National Nuclear Security Administration. Nuclear-Powered Cardiac Pacemakers-Off-Site Source Recovery Program Fact Sheet. Los Alamos National Laboratory; 2018.
11. U.S. Congress- Office of Technology Assessment. Power Sources for Remote Arctic Applications June 1994. Washington, DC; 1994.
12. Bennett GL. Space nuclear power: Opening the final frontier. In: 4th International Energy Conversion Engineering Conference and Exhibit (IECEC). American Institute of Aeronautics and Astronautics; 2006. p. 1433–49.
13. Jacoby M. Chemical & Engineering News. 2015. Thermoelectrics Rise Again- Heating, cooling, power genenration technology makes a comeback thanks to material sciences discoveries. Available from: https://cen.acs.org/articles/93/i19/Thermoelectrics-Rise-Again.html
14. Forman C, Muritala IK, Pardemann R, Meyer B. Estimating the global waste heat potential. Renewable and Sustainable Energy Reviews. 2016;57:1568–79.
15. Firth A, Zhang B, Yang A. Quantification of global waste heat and its environmental effects. Appl Energy. 2019;235:1314–34.
16. European Comission. Clean Power for Transport: A European alternative fuels strategy. Brussels; 2013 p. 11.
17. Freer R, Powell A V. Realising the potential of thermoelectric technology: a Roadmap. J Mater Chem C Mater. 2020;8(2):441–63.

18. Wood C. Materials for thermoelectric energy conversion. Reports on Progress in Physics. 1988;51:459–539.

19. Gonçalves AP, Godart C. Alternative Strategies for Thermoelectric Materials Development. In: Zlatic V, Hewson A, editors. NATO Advanced Research Workshop on New Materials for Thermoelectric Applications: Theory and Experiment. Springer; 2013. p. 1–24.

20. Bardeen J. Conduction : Metals and Semiconductors. In: Condon EU, Odishaw H, editors. Handbook of Physics. 1st ed. McGraw-Hill Book Company; 1958. p. 4–73 to 4–102.

21. Ioffe AF, Stil'bans LS, Iordanishvili EK, Stavitskaya TS, Vineyard and AG. Semiconductor thermoelements and thermoelec. Phys Today. 1959;12(5):42.

22. Godart C, Gonçalves AP, Lopes EB, Villeroy B. Role of structures on thermal conductivity in thermoelectric materials. In: NATO Science for Peace and Security Series B: Physics and Biophysics. Springer, Dordrecht; 2009.

23. Vining CB. An inconvenient truth about thermoelectrics. Nature Materials. 2009;8:83–5.

24. Finn PA, Asker C, Wan K, Bilotti E, Fenwick O, Nielsen CB. Thermoelectric Materials: Current Status and Future Challenges. Frontiers in Electronic Materials. 2021;1(August):1–13.

25. Guruge AR. ARHSE- Chemical and Process Engineering Knowledge Bank. 2021 [cited 2023 Jun 6]. Rankine Cycle. Available from: https://www.arhse.com/rankine-cycle/

26. Mahan GD. Good Thermoelectrics. In: Solid State Physics. Academic Press; 1998. p. 81–157.

27. Chen Z gang, Han G, Yang L, Cheng L, Zou J. Nanostructured thermoelectric materials : Current research and future challenge. Progress in Natural Science: Materials International. 2012;22(6):535–49.

28. Karamitaheri H. Thermal and Thermoelectric Properties of Nanostructures. Technischen Universitat Wien Fakultat fur Elektrotechnik und Informationstechnik von; 2013.

29. Shi Y, Sturm C, Kleinke H. Chalcogenides as thermoelectric materials. J Solid State Chem. 2019;270:273–9.

30. Goupil C, Seifert W, Zabrocki K, Müller E, Snyder GJ. Thermodynamics of thermoelectric phenomena and applications. Entropy. 2011;13(8):1481–517.

31. Bux SK, Fleurial JP, Kaner RB. Nanostructured materials for thermoelectric applications. Chemical Communications. 2010;46(44):8311–24.

32. Szczech JR, Higgins JM, Jin S. Enhancement of the thermoelectric properties in nanoscale and nanostructured materials. J Mater Chem. 2011;21(12):4037–55.

33. Dresselhaus MS, Gang Chen, Ming Y. Tang, Ronggui Yang, Hohyun Lee, Dezhi Wang, Zhifeng Ren, Jean-Pierre Fleurial and PG. New Directions for Low-Dimensional Thermoelectric Materials. Advanced Materials. 2007;19:1043–53.

34. Piggott A. Applied Thermoelectric Solutions LLC. 2022 [cited 2022 Jun 21]. How Thermoelectric Generators Work. Available from: https://thermoelectricsolutions.com/how-thermoelectric-generators-work/

35. Faraji AY, Date A, Singh R, Akbarzadeh A. Base-load thermoelectric power generation using evacuated tube solar collector and water storage tank. Energy Procedia. 2014;57:2112–20.

36. Bouyrie Y, Ohta M, Suekuni K, Kikuchi Y, Jood P, Yamamoto A, et al. Enhancement in the thermoelectric performance of colusites Cu26A2E6S32 (A = Nb, Ta; E = Sn, Ge) using E-site non-stoichiometry. J Mater Chem C Mater. 2017;5(17):4174–84.

37. Dennler G, Chmielowski R, Jacob S, Capet F, Roussel P, Zastrow S, et al. Are binary copper sulfides/selenides really new and promising thermoelectric materials? Adv Energy Mater. 2014;4(1301581):1–12.

38. Mulla R, Rabinal MHK. Copper Sulfides: Earth-Abundant and Low Cost Thermoelectric Materials. Energy Technology. 2019;7(7):1–120.

39. Ohtaki M. Oxide Thermoelectric Materials for Heat-to-Electricity Direct Energy Conversion. Kyushu University Global COE Program Novel Carbon Resources Sciences Newsletter. 2010;3:8.

40. Gonçalves AP, Godart C. New promising bulk thermoelectrics: Intermetallics, pnictides and chalcogenides. Eur Phys J B. 2014;87(42):1–29.

41. Rowe DM. Thermoelectrics and its Energy Harvesting- Modules, Systems, and Applications in Thermoelectrics. Rowe DM, editor. CRC Press Taylor & Francis Group; 2012. 567 p.

42. Snyder GJ, Toberer ES. Complex thermoelectric materials. Nat Mater. 2008;7(February):105–14.

43. Tan G, Zhao LD, Kanatzidis MG. Rationally Designing High-Performance Bulk Thermoelectric Materials. Chem Rev. 2016;116(19):12123–49.

44. Poudel B, Hao Q, Ma Y, Lan Y, Minnich A, Yu B, et al. High-Thermoelectric Performance of Nanostructured Bismuth Antimony Telluride Bulk Alloys. Science (1979). 2008;320(5876):634–8.

45. Ge ZH, Zhao LD, Wu D, Liu X, Zhang BP, Li JF, et al. Low-cost, abundant binary sulfides as promising thermoelectric materials. Materials Today. 2016;19(4):227–39.

46. Zhou C, Lee YK, Yu Y, Byun S, Luo ZZ, Lee H, et al. Polycrystalline SnSe with a thermoelectric figure of merit greater than the single crystal. Nat Mater. 2021;20(10):1378–84.

47. Alashkar A, Alami AH. Energy Harvesting Materials: Overview of Thermoelectric Materials. Encyclopedia of Smart Materials. 2021;(March):319–25.

48. Hasan MN, Wahid H, Nayan N, Mohamed Ali MS. Inorganic thermoelectric materials: A review. Int J Energy Res. 2020;44(8):6170–222.

49. Ju H, Kim J. Chemically Exfoliated SnSe Nanosheets and Their SnSe/Poly(3,4-ethylenedioxythiophene):Poly(styrenesulfonate) Composite Films for Polymer Based Thermoelectric Applications. ACS Nano. 2016;10(6):5730–9.

50. Hinterleitner B, Knapp I, Poneder M, Shi Y, Müller H, Eguchi G, et al. Thermoelectric performance of a metastable thin-film Heusler alloy. Nature. 2019;576(7785):85–90.

51. Soleimani Z, Zoras S, Ceranic B, Shahzad S, Cui Y. A review on recent developments of thermoelectric materials for room-temperature applications. Sustainable Energy Technologies and Assessments. 2020;37:100604.

52. Ahn HJ, Kim S, Kim KH, Lee JY. Preparation and characterization of thermoelectric PEDOT/Te nanorod array composite films. Materials. 2022;15(148):1–14.

53. Prem Kumar DS, Chetty R, Rogl P, Rogl G, Bauer E, Malar P, et al. Thermoelectric properties of Cd doped tetrahedrite: Cu12−xCdxSb4S13. Intermetallics (Barking). 2016;78:21–9.

54. Zheng Z hao, Luo J ting, Li F, Liang G xing, Fan P. Enhanced thermoelectric performance of P-type Sb 2 Te 3 thin films through organic-inorganic hybridization on flexible substrate. Current Applied Physics. 2019;19(4):470–4.

55. Li C, Qin X, Li Y, Li D, Zhang J, Guo H, et al. Simultaneous increase in conductivity and phonon scattering in a graphene nanosheets/(Bi2Te3)0.2(Sb2Te3)0.8 thermoelectric nanocomposite. J Alloys Compd. 2016;661:389–95.

56. Patyk A. Thermoelectrics: Impacts on the Environment and Sustainability. J Electron Mater. 2010;39(9):2023–8.

57. Zheng XF, Liu CX, Yan YY, Wang Q. A review of thermoelectrics research - Recent developments and potentials for sustainable and renewable energy applications. Renewable and Sustainable Energy Reviews. 2014;32:486–503.

58. Lawrence Livermore National Laboratory. Energy Flow Charts: Charting the Complex Relationships among Energy, Water, and Carbon [Internet]. 2022 [cited 2022 Jun 20]. Available from: https://flowcharts.llnl.gov

59. Massaguer A, Pujol T, Comamala M, Massaguer E. Feasibility study on a vehicular thermoelectric generator coupled to an exhaust gas heater to improve aftertreatment's efficiency in cold-starts. Appl Therm Eng. 2020;167(February).

60. Coulibaly A, Zioui N, Bentouba S, Kelouwani S, Bourouis M. Use of thermoelectric generators to harvest energy from motor vehicle brake discs. Case Studies in Thermal Engineering. 2021;28(August):101379.

61. Brito FP, Peixoto JS, Martins J, Gonçalves AP, Louca L, Vlachos N, et al. Analysis and design of a silicide-tetrahedrite thermoelectric generator concept suitable for large-scale industrial waste heat recovery. Energies (Basel). 2021;14(5655):1–21.

62. Soleimani Z, Zoras S, Ceranic B, Cui Y, Shahzad S. A comprehensive review on the output voltage/power of wearable thermoelectric generators concerning their geometry and thermoelectric materials. Nano Energy. 2021;89:106325.

63. Hasan MN, Nafea M, Nayan N, Mohamed Ali MS. Thermoelectric Generator: Materials and Applications in Wearable Health Monitoring Sensors and Internet of Things Devices. Adv Mater Technol. 2022;7(5):1–32.

64. Kumar PM, Babu VJ, Subramanian A, Bandla A, Thakor N, Ramakrishna S, et al. The design of a thermoelectric generator and its medical applications. Designs (Basel). 2019;3(2):1–26.

65. Assawaworrarit S, Omair Z, Fan S. Nighttime electric power generation at a density of 50 mW/m2 via radiative cooling of a photovoltaic cell. Appl Phys Lett. 2022;120.

66. Jaziri N, Boughamoura A, Müller J, Mezghani B, Tounsi F, Ismail M. A comprehensive review of Thermoelectric Generators: Technologies and common applications. Energy Reports. 2020;6:264–87.

67. Tritt TM. Recent Trends in Thermoelectric Materials Research II. Tritt TM, Williardson RK, Weber ER, editors. Vol. 70, Semiconductors and Semimetals. Academic Press; 2001. 299 p.

68. US energy department. Thermoelectric Materials, Devices and Systems: Technology Assessment. 2015.

69. LeBlanc S. Thermoelectric generators: Linking material properties and systems engineering for waste heat recovery applications. Sustainable Materials and Technologies. 2014;1–2:26–35.

70. Powell A V. Recent developments in Earth-abundant copper-sulfide thermoelectric materials. J Appl Phys. 2019;126(10).

71. West, W. A.; Menzies AWC. The Vapor Pressures of Sulphur between 100° and 550° with related Thermal Data .pdf. J Phys Chem. 1928;(33(12)):1880–1892.

72. Haynes WM, Lide DR, Bruno TJ. Handbook of Chemistry and Physics. 95th ed. Haynes WM, Lide DR, Bruno TJ, editors. Journal of the American Pharmaceutical Association. CRC Press; 2014. 2665 p.

73. Sun FH, Li H, Tan J, Zhao L, Wang X, Hu H, et al. Review of current ZT > 1 thermoelectric sulfides. Journal of Materiomics. 2023;

74. Anthony JW, Bideaux RA, Bladh KW, Nichols MC. Handbook of Mineralogy. Mineralogical Society of America; 2010. 657 p.

75. Levinsky P, Vaney JB, Candolfi C, Dauscher A, Lenoir B, Hejtmánek J. Electrical, Thermal, and Magnetic Characterization of Natural Tetrahedrites–Tennantites of Different Origin. J Electron Mater. 2016 Mar 1;45(3):1351–7.

76. Suekuni K, Tsuruta K, Kunii M, Nishiate H, Nishibori E, Maki S, et al. High-performance thermoelectric mineral Cu12-xNi xSb4S13 tetrahedrite. J Appl Phys. 2013;113(4):043712.

77. Chetty R, Bali A, Mallik RC. Tetrahedrites as thermoelectric materials: An overview. J Mater Chem C Mater. 2015;3(48):12364–78.

78. Brito FP, Vieira R, Martins J, Goncalves LM, Goncalves AP, Coelho R, et al. Analysis of thermoelectric generator incorporating n-magnesium silicide and p-tetrahedrite materials. Energy Convers Manag. 2021;236(March):114003.

79. Chen WH, Lin YX, Wang XD, Lin YL. A comprehensive analysis of the performance of thermoelectric generators with constant and variable properties. Appl Energy. 2019;241:11–24.

80. Heo J, Ravichandran R, Reidy CF, Tate J, Wager JF, Keszler DA. Design meets nature: Tetrahedrite Solar Absorbers. Adv Energy Mater. 2015;5(7):1–7.

81. Kumar PDS, Ren M, Osipwicz T, Mallik RC, Malar P. Tetrahedrite (Cu12Sb4S13) thin films for photovoltaic and thermoelectric applications. Solar Energy. 2018;(174):422–730.

82. Korbel P, NovAK M. The Complete Encyclopedia of Minerals. Grange Books PLC; 2001. 299 p.

83. Baláž P, Guilmeau E, Daneu N, Dobrozhan O, Baláž M, Hegedus M, et al. Tetrahedrites synthesized via scalable mechanochemical process and spark plasma sintering. J Eur Ceram Soc. 2020;40(5):1922–30.

84. Baláž P. Extractive metallurgy of activated minerals. 1st ed. Baláž P, editor. Vol. 10, Minerals Engineering. Elsevier; 2000.

85. Ghassemi N, Lu X, Tian Y, Conant E, Yan Y, Zhou X, et al. Structure Change and Rattling Dynamics in Cu12Sb4S13 Tetrahedrite: an NMR Study. ACS Appl Mater Interfaces. 2018;10(42):36010–7.

86. Candolfi C, Bouyrie Y, Sassi S, Dauscher A, Lenoir B. Tetrahedrites: Prospective Novel Thermoelectric Materials. In: Thermoelectrics for Power Generation - A Look at Trends in the Technology. 2016. p. 71–89.

87. Lai W, Wang Y, Morelli DT, Lu X. From Bonding Asymmetry to Anharmonic Rattling in Cu 12 Sb 4 S 13 Tetrahedrites: When Lone-Pair Electrons Are Not So Lonely. Adv Funct Mater. 2015;25(24):3648–57.

88. Xia Y, Ozoliņš V, Wolverton C. Microscopic Mechanisms of Glass-Like Lattice Thermal Transport in Cubic Cu12Sb4S13 Tetrahedrites. Phys Rev Lett. 2020;125(8):1–7.

89. Uher C. Materials Aspect of Thermoelectricity. Uher C, editor. CRC Press Taylor & Francis Group; 2017. 597 p.

90. Weller DP, Morelli DT. Tetrahedrite Thermoelectrics: From Fundamental Science to Facile Synthesis. Frontiers in Electronic Materials. 2022;2(May):1–14.

91. Johnson ML, Jeanloz R. A Brillouin-zone model for compositional variation in tetrahedrite. American Mineralogist. 1983;68(1–2):220–6.

92. Tatsuka K, Morimoto N. Tetrahedrite Stability Relations in the Cu-Sb-S System. Economic Geology. 1977;72:258–70.

93. Tatsuka K, Morimoto N. Composition Variation and Polymorphism of Tetrahedrite in the Cu-Sb-S System below 400ºC. American Mineralogist. 1973;58:425–34.

94. Skinner BJ, Luce FD, Makovicky E. Studies of the Sulfosalts of Copper III. Phases and Phase relations in the System Cu-As-S. Economic Geology. 1972;67(6):924–38.

95. Johnson NE, Craig JR, Rimstidt JD. Crystal chemistry of tetrahedrite. American Mineralogist. 1988;73(3–4):389–97.

96. Makovicky E, Skinner BJ. Studies of the sulfosalts of copper. VI. Low-Temperature exsolution in synthetic tetrahedrite solid solution, Cu12+ xSB4+ yS13. Can Mineral. 1978;16:611–23.

97. Yan Y, Wu H, Wang G, Lu X, Zhou X. High thermoelectric performance balanced by electrical and thermal transport in tetrahedrites Cu12+xSb4S12Se. Energy Storage Mater. 2018;13:127–33.

98. Vaqueiro P, Guélou G, Kaltzoglou A, Smith RI, Barbier T, Guilmeau E, et al. The Influence of Mobile Copper Ions on the Glass-Like Thermal Conductivity of Copper-Rich Tetrahedrites. Chemistry of Materials. 2017;29(9):4080–90.

99. Zazakowny K, Kosonowski A, Lis A, Cherniushok O, Parashchuk T, Tobola J, et al. Phase Analysis and Thermoelectric Properties of Cu-Rich Tetrahedrite Prepared by Solvothermal Synthesis. Materials. 2022;15(849):1–16.

100. Yang H, Xing T, Song Q, Fan J, Li X. Influence of Sb self-doping on thermoelectric performance of Cu12Sb4S13. Mater Lett. 2021;288:129314.

101. Suekuni K, Tsuruta K, Ariga T, Koyano M. Thermoelectric Properties of Mineral Tetrahedrites Cu 10Tr 2Sb 4S 13 with Low Thermal Conductivity. Applied Physics Express. 2012;5(5):2–5.

102. Hathwar VR, Nakamura A, Kasai H, Suekuni K, Tanaka HI, Takabatake T, et al. Low-Temperature Structural Phase Transitions in Thermoelectric Tetrahedrite, Cu12Sb4S13, and Tennantite, Cu12As4S13. Cryst Growth Des. 2019;19(7):3979–88.

103. Long SO, Powell A V., Hull S, Orlandi F, Tang CC, Supka AR, et al. Jahn–Teller Driven Electronic Instability in Thermoelectric Tetrahedrite. Adv Funct Mater. 2020;30(12):1–9.

104. Chetty R, Bali A, Naik MH, Rogl G, Rogl P, Jain M, et al. Thermoelectric properties of Co substituted synthetic tetrahedrite. Acta Mater. 2015;100:266–74.

105. Chetty R, Prem Kumar DS, Rogl G, Rogl P, Bauer E, Michor H, et al. Thermoelectric properties of a Mn substituted synthetic tetrahedrite. Physical Chemistry Chemical Physics. 2015;17(3):1716–27.

106. Barbier T, Lemoine P, Gascoin S, Lebedev OI, Kaltzoglou A, Vaqueiro P, et al. Structural stability of the synthetic thermoelectric ternary and nickel-substituted tetrahedrite phases. J Alloys Compd. 2015;634:253–62.

107. Lara-Curzio E, May AF, Delaire O, McGuire MA, Lu X, Liu CY, et al. Low-temperature heat capacity and localized vibrational modes in natural and synthetic tetrahedrites. J Appl Phys. 2014;115(193515):1–7.

108. Kumar PDS, Tippireddy S, Ramakrishnan A, Chen KH, Malar P, Mallik RC. Thermoelectric and electronic properties of chromium substituted tetrahedrite. Semicond Sci Technol. 2019;34(3).

109. Heo J, Laurita G, Muir S, Subramanian MA, Keszler DA. Enhanced Thermoelectric Performance of Synthetic Tetrahedrites. Chemistry of Materials. 2014;26(6):2047–51.

110. Lu X, Morelli DT, Xia Y, Zhou F, Ozolins V, Chi H, et al. High Performance Thermoelectricity in Earth-Abundant Compounds Based on Natural Mineral Tetrahedrites. Adv Energy Mater. 2013;3(3):342–8.

111. Kim SY, Lee GE, Kim IH. Thermoelectric Properties of Mechanically-Alloyed and Hot-Pressed Cu 12−x Co x Sb 4 S 13 Tetrahedrites. Journal of the Korean Physical Society. 2019;74(10):967–71.

112. Lu X. Thermoelectric Properties of Natural Mineral Based Tetrahedrite Compounds. Michigan State University; 2014.

113. Lu X, Morelli DT. Rapid synthesis of high-performance thermoelectric materials directly from natural mineral tetrahedrite. MRS Commun. 2013;3(3):129–33.

114. Pi JH, Lee GE, Kim IH. Thermal Stability, Mechanical Properties and Thermoelectric Performance of Cu11TrSb4S13 (Tr = Mn, Fe, Co, Ni, Cu, and Zn). J Electron Mater. 2020;49(5):2710–8.

115. Tippireddy S, Chetty R, Naik MH, Jain M, Chattopadhyay K, Mallik RC. Electronic and Thermoelectric Properties of Transition Metal Substituted Tetrahedrites. The Journal of Physical Chemistry C. 2018;122(16):8735–49.

116. Battiston S, Fanciulli C, Fiameni S, Famengo A, Fasolin S, Fabrizio M. One step synthesis and sintering of Ni and Zn substituted tetrahedrite as thermoelectric material. J Alloys Compd. 2017;702:75–83.

117. Sun FH, Dong J, Dey S, Asfandiyar, Wu CF, Pan Y, et al. Enhanced thermoelectric performance of Cu12Sb4S13-δ tetrahedrite via nickel doping. Sci China Mater. 2018;61(9):1209–17.

118. Lv P, Yu Y, Li X. Quick Fabrication and Thermoelectric Properties of Doped Tetrahedrites. In: Han Y, editor. Advances in Energy and Environmental Materials -. Springer; 2018. p. 657–65.

119. Weller DP, Kunkel GE, Ochs AM, Morelli DT, Anderson ME. Observation of n-type behavior in Fe-doped tetrahedrite at low temperature. Materials Today Physics. 2018;7:1–6.

120. Huang LL, Wang YS, Zhu C, Xu R, Li JM, Zhang JH, et al. Preparation and enhanced thermoelectric performance of Pb-doped tetrahedrite Cu12-xPbxSb4S13. J Alloys Compd. 2018;769:478–83.

121. Tippireddy S, Ghosh S, Biswas R, Dasgupta T, Rogl G, Rogl P, et al. Thermoelectric properties of Al substituted tetrahedrite. J Appl Phys. 2020;127(035105):1–14.

122. Coelho R, Symeou E, Kyratsi T, Gonçalves AP. Tetrahedrite Sintering Conditions: The Cu11Mn1Sb4S13 Case. J Electron Mater. 2020;49(8):5077–83.

123. Lu X, Morelli DT. Natural mineral tetrahedrite as a direct source of thermoelectric materials. Physical Chemistry Chemical Physics. 2013;15(16):5762–6.

124. Lu X, Morelli DT, Xia Y, Ozolins V. Increasing the Thermoelectric Figure of Merit of Tetrahedrites by Co-Doping with Nickel and Zinc. Chemistry of Materials. 2015;27(2):408–13.

125. Barbier T, Rollin-Martinet S, Lemoine P, Gascoin F, Kaltzoglou A, Vaqueiro P, et al. Thermoelectric Materials: A New Rapid Synthesis Process for Nontoxic and High-Performance Tetrahedrite Compounds. Journal of the American Ceramic Society. 2016;99(1):51–6.

126. Hu H, Zhuang HL, Jiang Y, Shi J, Li JW, Cai B, et al. Thermoelectric Cu12Sb4S13-Based Synthetic Minerals with a Sublimation-Derived Porous Network. Advanced Materials. 2021;33(43):1–10.

127. Sun FH, Dong J, Tang H, Shang PP, Zhuang HL, Hu H, et al. Enhanced performance of thermoelectric nanocomposites based on Cu 12 Sb 4 S 13 tetrahedrite. Nano Energy. 2019;57:835–41.

128. Levinsky P, Candolfi C, Dauscher A, Tobola J, Hejtmánek J, Lenoir B. Thermoelectric properties of the tetrahedrite-tennantite solid solutions Cu12Sb4-: XAsxS13 and Cu10Co2Sb4-yAsyS13 ($0 \leq x, y \leq 4$). Physical Chemistry Chemical Physics. 2019;21(8):4547–55.

129. Kwon MC, Kim IH. Preparation and Thermoelectric Properties of Si-Doped Tetrahedrites Cu12Sb4-ySiyS13. Journal of Korean Institute of Metals and Materials. 2022;60(6):440–7.

130. Lu X, Morelli D. The effect of Te substitution for Sb on Thermoelectric Properties of Tetrahedrite. J Electron Mater. 2014;43(6):1983–7.

131. Kwak SG, Pi JH, Lee GE, Kim IH. Solid-State Synthesis and Thermoelectric Properties of Tetrahedrites Cu12Sb4-yBiyS13. Korean Journal of Metals and Materials. 2020;58(4):272–7.

132. Baláž P, Guilmeau E, Achimovičová M, Baláž M, Daneu N, Dobrozhan O, et al. Bismuth doping in nanostructured tetrahedrite: Scalable synthesis and thermoelectric performance. Nanomaterials. 2021;11(1386).

133. Bouyrie Y, Candolfi C, Ohorodniichuk V, Malaman B, Dauscher A, Tobola J, et al. Crystal structure, electronic band structure and high-temperature thermoelectric properties of Te-substituted tetrahedrites Cu12Sb4-xTexS13 ($0.5 \leq x \leq 2.0$). J Mater Chem C Mater. 2015;3(40):10476–87.

134. Bouyrie Y, Candolfi C, Vaney JB, Dauscher A, Lenoir B. High Temperature Transport Properties of Tetrahedrite Cu12−xMxSb4−yTeyS13 (M = Zn, Ni) Compounds. J Electron Mater. 2016;45(3):1601–5.

135. Bouyrie Y, Sassi S, Candolfi C, Vaney JB, Dauscher A, Lenoir B. Thermoelectric properties of double-substituted tetrahedrites Cu12-xCoxSb4- yTeyS13. Dalton Transactions. 2016;45(17):7294–302.

136. Prem Kumar DS, Chetty R, Femi OE, Chattopadhyay K, Malar P, Mallik RC. Thermoelectric Properties of Bi Doped Tetrahedrite. J Electron Mater. 2017;46(5):2616–22.

137. Gonçalves AP, Lopes EB, Villeroy B, Monnier J, Godart C, Lenoir B. Effect of Ni, Bi and Se on the tetrahedrite formation. RSC Adv. 2016;6(104):102359–67.

138. Kwak SG, Lee GE, Kim IH. Effects of Se Doping on Thermoelectric Properties of Tetrahedrite Cu12Sb4S13−zSez. Electronic Materials Letters. 2021;17(2):164–71.

139. Lu X, Morelli DT, Wang Y, Lai W, Xia Y, Ozolins V. Phase Stability, Crystal Structure, and Thermoelectric Properties of Cu12Sb4S13-xSex Solid Solutions. Chemistry of Materials. 2016;28(6):1781–6.

140. Zhu C, Ming H, Huang L, Zhang B, Lou X, Li D, et al. Achieving high power factor and thermoelectric performance through dual substitution of Zn and Se in tetrahedrites Cu12Sb4S13. Appl Phys Lett. 2019;115(18).

141. Alves TKC, Domingues G, Lopes EB, Gonçalves AP. Effect of Composition on Thermoelectric Properties of As-Cast Materials: The Cu 12−x Co x Sb 4 S 13−y Se y Case. J Electron Mater. 2019;48(4):2028–35.

142. Rout U, Tippireddy S, Werbach K, Pambannan P, Rogl G, Rogl P, et al. Simultaneous optimization of power factor and thermal conductivity via Te and Se double substitution in Cu12Sb4S13 tetrahedrite. Scr Mater. 2020;188:151–6.

143. Ravaji K, Ezzati R, Mohammadi AH, Abbas SA. Electric and Thermoelectric Properties of Cu12Sb4S13 Tetrahedrite with Impurities. Preprint. 2019;1(August):1–14.

144. Knížek K, Levinský P, Hejtmánek J. LDA + U Calculation of Electronic and Thermoelectric Properties of Doped Tetrahedrite Cu12Sb4S13. J Electron Mater. 2019;48(4):2018–21.

145. Blaha P, Schwarz K, Madsen GKH, Kvasnicka D, Luitz J, Laskowski R, et al. WIEN2k, An Augmented Plane Wave Plus Local Orbitals Program for Calculating Crystal Properties. Vienna University of Technology Institute of Materials Chemistry; 2021.

146. Madsen GKH, Singh DJ. BoltzTraP. A code for calculating band-structure dependent quantities. Vol. 175, Computer Physics Communications. Elsevier; 2006. p. 67–71.

147. Perdew JP, Burke K, Ernzerhof M. Generalized gradient approximation made simple. Phys Rev Lett. 1996;77(18):3865–8.

148. Allen PB, Schulz WW. Bloch-Boltzmann analysis of electrical transport in intermetallic compounds: ReO3, BaPbO3, CoSi2, and Pd2Si. Phys Rev B. 1993;47(21):14434–9.

149. Allen PB, Pickett WE, Krakauer H. Anisotropic normal-state transport properties predicted and analyzed for high-Tc oxide superconductors. Phys Rev B. 1988;37(13):7482–90.

150. Singh D, Mazin I. Calculated thermoelectric properties of La-filled skutterudites. Phys Rev B Condens Matter Mater Phys. 1997;56(4):R1650–3.

151. Yi Wang, Zi-Kui Liu and LQC. Theoretical Brief- BoltzTraP2Y 0.0 documentation [Internet]. 2021 [cited 2023 May 23]. Available from: https://boltztrap2y.readthedocs.io/en/latest/Theory.html

152. Grebenkemper J. Powder X-ray Diffraction [Internet]. 2022 [cited 2023 Jan 30]. p. 1–3. Available from: https://chem.libretexts.org/Bookshelves/Analytical_Chemistry/Supplemental_Modules_(Analytical_Chemistry)/Instrumentation_and_Analysis/Diffraction_Scattering_Techniques/Powder_X-ray_Diffraction

153. Dutrow BL, Clark CM. X-ray Powder Diffraction (XRD) [Internet]. 2023 [cited 2023 Jan 30]. p. 1–4. Available from: https://serc.carleton.edu/research_education/geochemsheets/techniques/XRD.html

154. Pirrie D, Power MR, Rollinson G, Hughes SH, Camm GS, Watkins DC. Camborne School of Mines-University of Exeter. 2023 [cited 2023 Jan 30]. X-ray Fluorescence. Available from: https://projects.exeter.ac.uk/geomincentre/estuary/Main/fluorescence.htm

155. Holland TJB, Redfern SAT. Unit cell refinement from powder diffraction data: the use of regression diagnostics. Mineral Mag. 1997;61(404):65–77.

156. Graulis S, Chateigner D, Downs RT, Yokochi AFT, Quirós M, Lutterotti L, et al. Crystallography Open Database - An open-access collection of crystal structures. J Appl Crystallogr. 2009;42(4):726–9.

157. Holland TJB, Redfern SAT. UNITCELL: A nonlinear least-squares program for cell-parameter refinement implementing regression and deletion diagnostics. Vol. 30, Journal of Applied Crystallography. 1997. p. 84.

158. Raman C V., Krishnan KS. A new type of secondary radiation. Nature. 1928;121(3048):501–2.

159. Raja PM V., Barron AR. LibreTexts project. 2022 [cited 2023 Jan 30]. p. 1–11 4.3: Raman Spectroscopy. Available from: https://chem.libretexts.org/Bookshelves/Analytical_Chemistry/Physical_Methods_in_Chemistry_and_Nano_Science_(Barron)/04%3A_Chemical_Speciation/4.03%3A_Raman_Spectroscopy

160. HORIBA. What is Raman Spectroscopy? - HORIBA [Internet]. 2020 [cited 2023 Jan 30]. p. 1–5. Available from: https://www.horiba.com/en_en/raman-imaging-and-spectroscopy/

161. Leng Y. Materials Characterization - Introduction to Microscopic and Spectroscopic Methods. Second. Wiley-VCH; 2013. 383 p.

162. Chaikin PM, Kwak JF. Apparatus for thermopower measurements on organic conductors. Review of Scientific Instruments. 1975;46(2):218–20.

163. Heaney MB. Electrical Conductivity and Resistivity. In: Webster JG, editor. Electrical Measurement, Signal Processing, and Displays. CRC Press LLC; 2004. p. 1–14.

164. Suekuni K, Tomizawa Y, Ozaki T, Koyano M. Systematic study of electronic and magnetic properties for Cu 12-xTMxSb4S13 (TM = Mn, Fe, Co, Ni, and Zn) tetrahedrite. J Appl Phys. 2014;115(14):12–7.

165. Kittel C. Introduction to Solid States Physics. John Wiley & Sons, Inc.; 1953. 396 p.

166. Lu X, Yao W, Wang G, Zhou X, Morelli D, Zhang Y, et al. Band structure engineering in highly degenerate tetrahedrites through isovalent doping. J Mater Chem A Mater. 2016;4(43):17096–103.

167. Shannon RD. Revised Effective Ionic Radii and Systematic Studies of Interatomie Distances in Halides and Chaleogenides. Acta Crystallogr. 1976;A(32):751–67.

168. Lafuente B, Downs RT, Yang H, Stone N. RRUFF^{TM} Project. The power of databases: the RRUFF project. Highlights in Mineralogical Crystallography, T Armbruster and R M Danisi, eds. 2015. p. 1–30.

169. Bouaniza N, Hosni N, Maghraoui-Meherzi H. Structural and optical properties of Cu3SbS3 thin film deposited by chemical bath deposition along with the degradation of methylene blue. Surf Coat Technol. 2018;333:195–200.

170. Rath T, MacLachlan AJ, Brown MD, Haque SA. Structural, optical and charge generation properties of chalcostibite and tetrahedrite copper antimony sulfide thin films prepared from metal xanthates. J Mater Chem A Mater. 2015;3(47):24155–62.

171. Kim HS, Gibbs ZM, Tang Y, Wang H, Snyder GJ. Characterization of Lorenz number with Seebeck coefficient measurement. APL Mater. 2015;3(4):1–6.

172. Thesberg M, Kosina H, Neophytou N. On the Lorenz number of multiband materials. Phys Rev B. 2017;95(12):1–14.

173. Snyder GJ, Snyder AH, Wood M, Gurunathan R, Snyder BH, Niu C. Weighted Mobility. Advanced Materials. 2020;32(25).

174. Witkoske E, Wang X, Lundstrom M, Askarpour V, Maassen J. Thermoelectric band engineering: The role of carrier scattering. J Appl Phys. 2017;122(17).

175. Witkoske E, Wang X, Maassen J, Lundstrom M, Lafayette W. Universal Behavior of the Thermoelectric Figure of Merit, zT, vs. Quality Factor. Materials Today Physics. 2019;8(March):43–8.

176. Zhang X, Bu Z, Shi X, Chen Z, Lin S, Shan B, et al. Electronic quality factor for thermoelectrics. Sci Adv. 2020;6(46):6–11.

177. Blakemore JS. Approximations for Fermi-Dirac integrals, especially the function F1 2(η) used to describe electron density in a semiconductor. Solid State Electronics. 1982;25(11):1067–76.

178. Kim M, Kim S il, Kim SW, Kim HS, Lee KH. Weighted Mobility Ratio Engineering for High-Performance Bi–Te-Based Thermoelectric Materials via Suppression of Minority Carrier Transport. Vol. 33, Advanced Materials. 2021.

179. Trahan and Goodrich. X-Ray Diffraction Measurements on Metallic and Semiconducting Hexagonal NiS. 1970.

180. Takéuchi Y, Kudoh Y, Sato G. The crystal structure of covellite CuS under high pressure Up to 33 kbar. Vol. 173, Zeitschrift für Kristallographie. 1985.

181. Takahashi Y. Magneto Volume Effect. In: Springer Tracts in Modern Physics. Springer; 2013. p. 131–77.

ATTACHMENTS

ATTACHMENT 1: POWDER X-RAY DIFFRACTION

As-cast samples

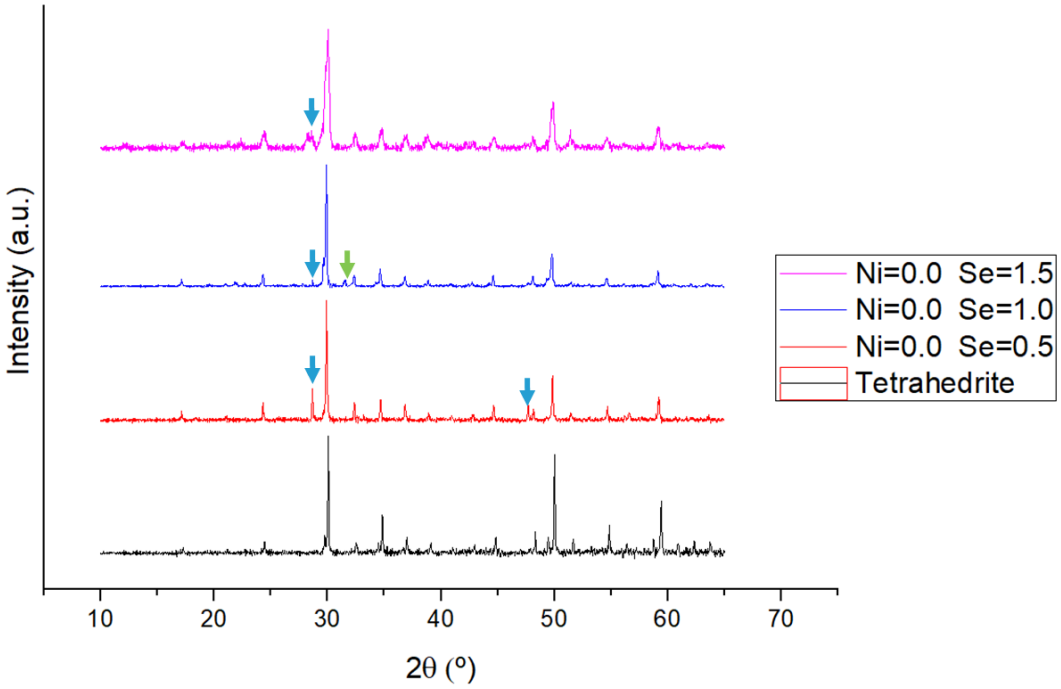

Fig. 71 Comparison of XRD of the as-cast $Cu_{12}Sb_4S_{13-x}Se_x$ samples. Identified with arrows are peaks not associated to tetrahedrite: in magenta- Chalcostibite ($CuSb(S,Se)_2$).; and in green- covellite (CuS).

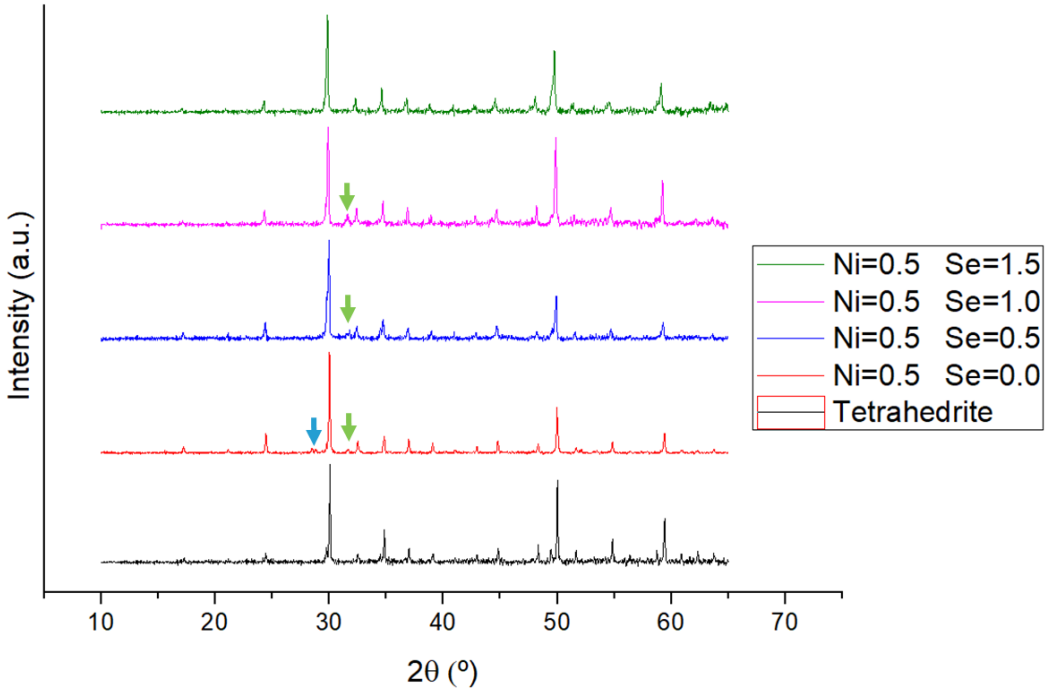

Fig. 72 Comparison of XRD of the as-cast $Cu_{11.5}Ni_{0.5}Sb_4S_{13-x}Se_x$ samples. Identified with arrows are peaks not associated to tetrahedrite: in green- covellite (CuS).

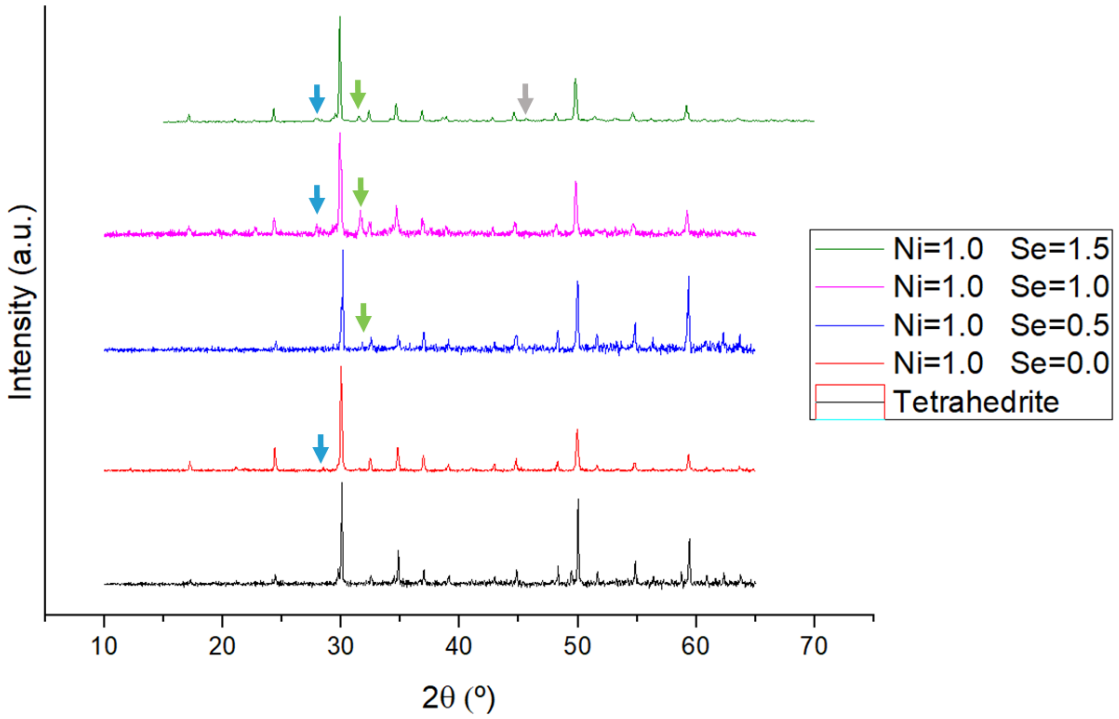

Fig. 73 Comparison of XRD of the as-cast $Cu_{11}NiSb_4S_{13-x}Se_x$ samples. Identified with arrows are peaks not associated to tetrahedrite: in magenta- Chalcostibite ($CuSb(S,Se)_2$).; in grey- copper sulphide (Cu_2S); and in green- covellite (CuS).

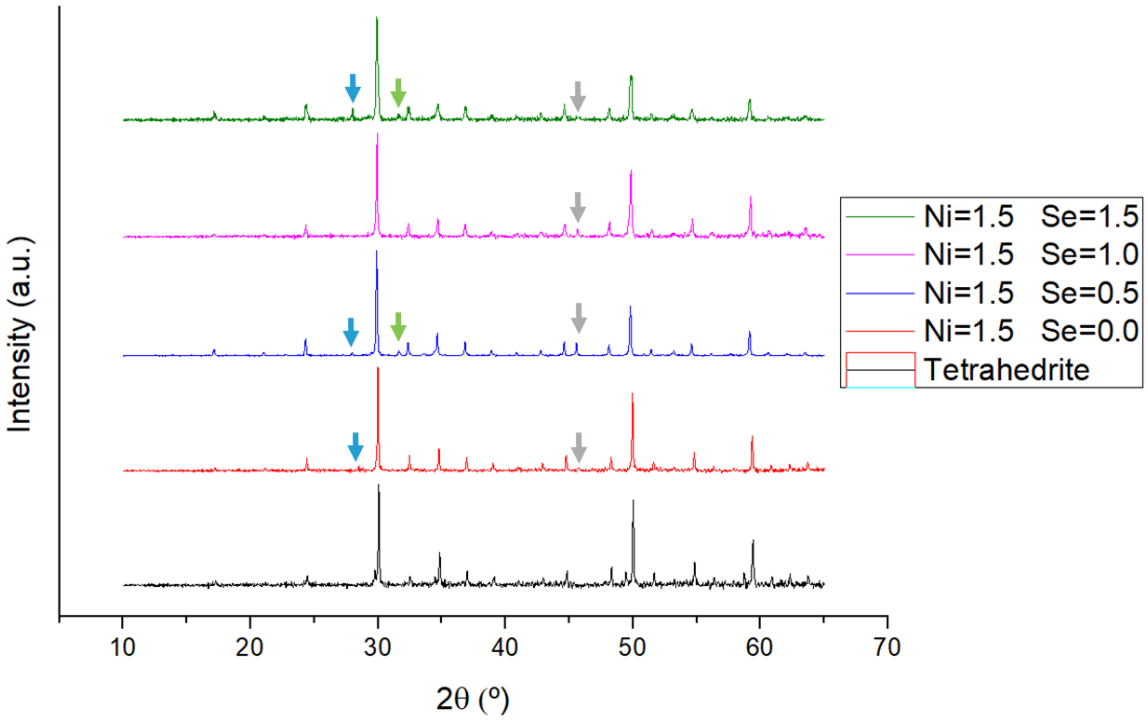

Fig. 74 Comparison of XRD of the as-cast $Cu_{10.5}Ni_{1.5}Sb_4S_{13-x}Se_x$ samples. Identified with arrows are peaks not associated to tetrahedrite: in magenta- Chalcostibite ($CuSb(S,Se)_2$); in grey- copper sulphide (Cu_2S); and in green- covellite (CuS).

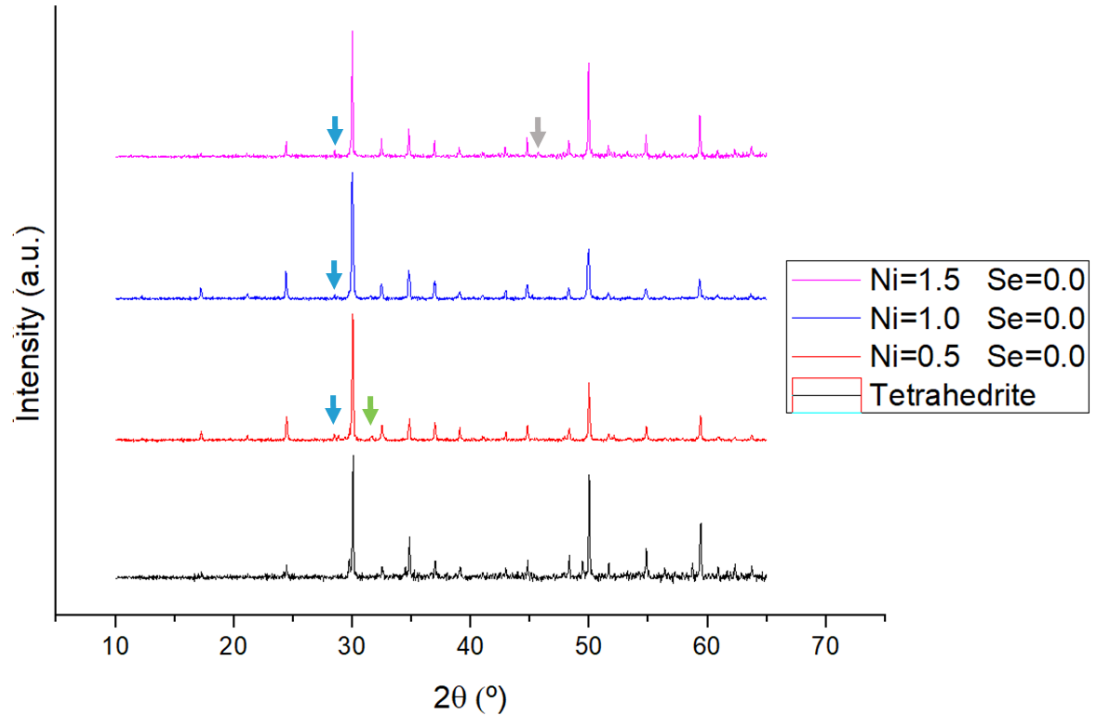

Fig. 75 Comparison of XRD of the as-cast $Cu_{12-x}Ni_xSb_4S_{13}$ samples. Identified with arrows are peaks not associated to tetrahedrite: in magenta- Chalcostibite ($CuSb(S,Se)_2$); in grey- copper sulphide (Cu_2S); and in green- covellite (CuS).

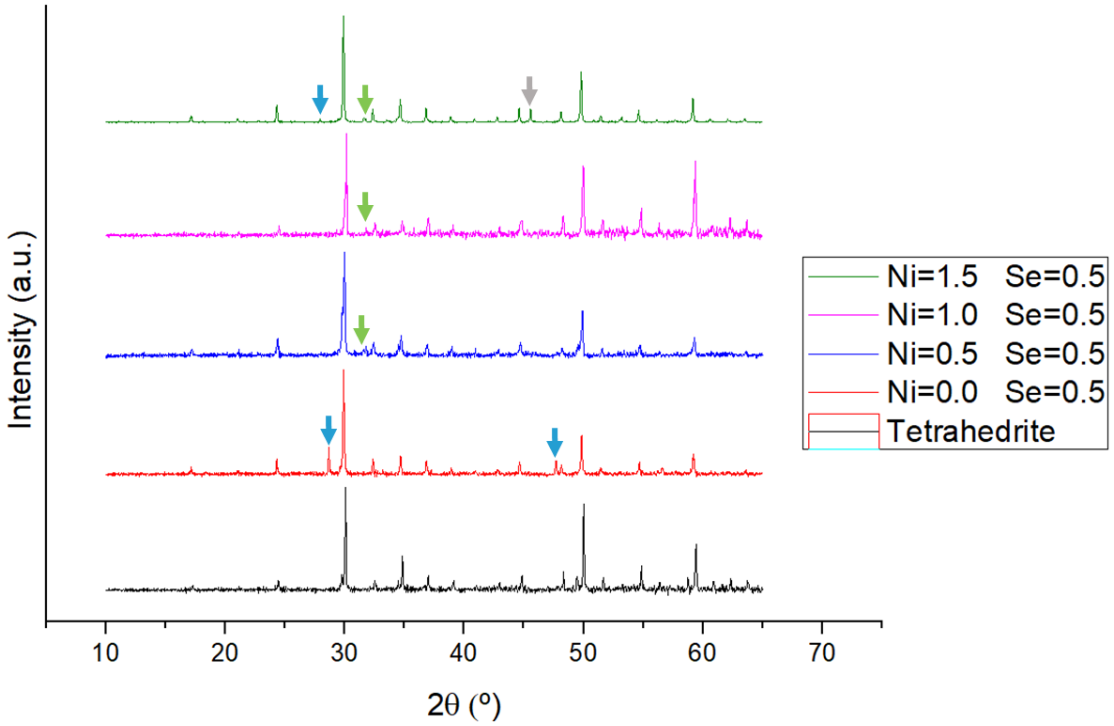

Fig. 76 Comparison of XRD of the as-cast $Cu_{12-x}Ni_xSb_4S_{12.5}Se_{0.5}$ samples. Identified with arrows are peaks not associated to tetrahedrite: in magenta- Chalcostibite ($CuSb(S,Se)_2$); in gray- copper sulphide (Cu_2S); and in green- covellite (CuS).

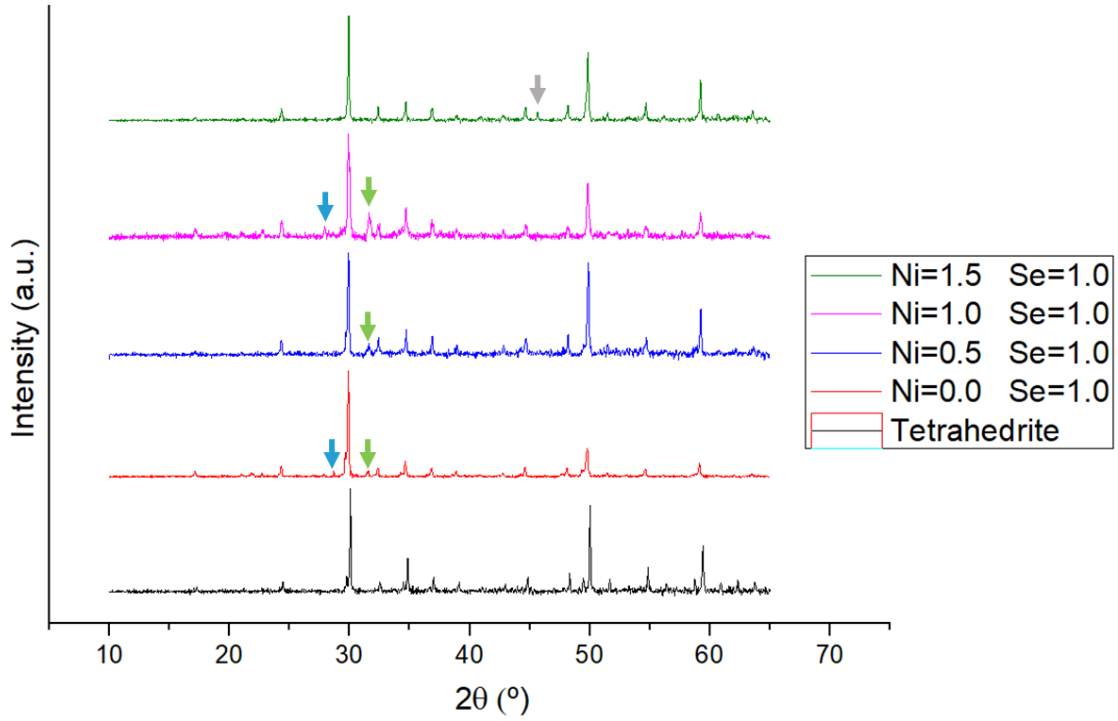

Fig. 77 Comparison of XRD of the as-cast $Cu_{12-x}Ni_xSb_4S_{12}Se$ samples. Identified with arrows are peaks not associated to tetrahedrite: in magenta- Chalcostibite ($CuSb(S,Se)_2$); in gray- copper sulphide (Cu_2S); and in green- covellite (CuS).

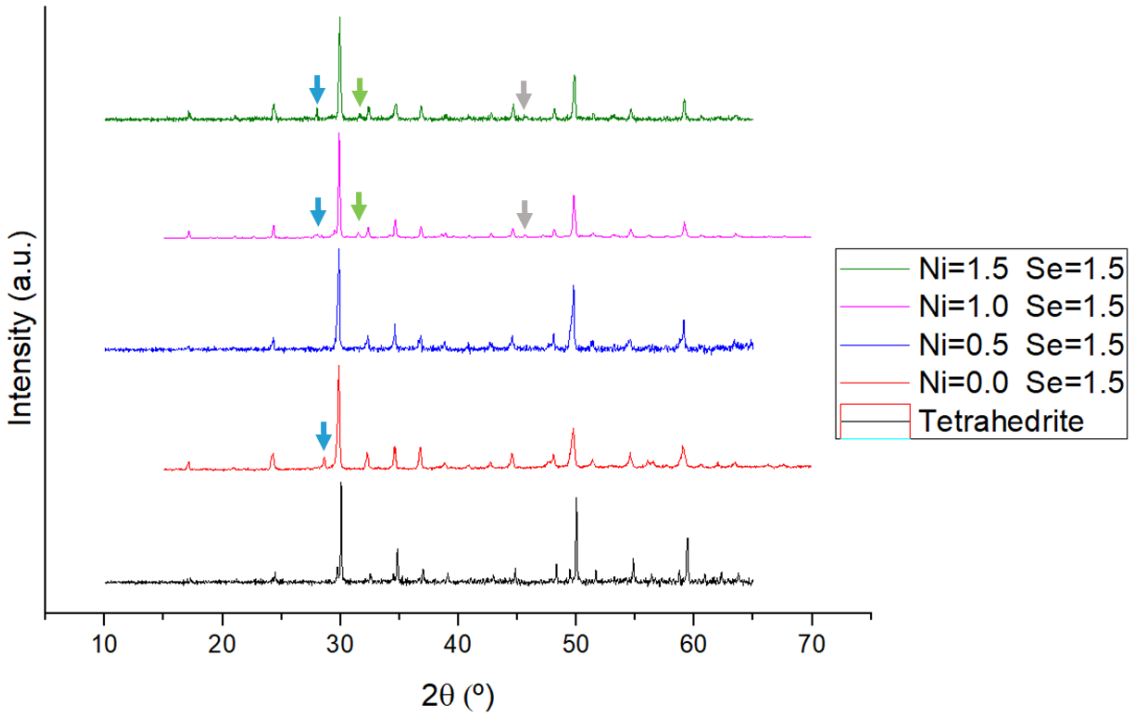

Fig. 78 Comparison of XRD of the as-cast $Cu_{12-x}Ni_xSb_4S_{11.5}Se_{1.5}$ samples. Identified with arrows are peaks not associated to tetrahedrite: in magenta- Chalcostibite ($CuSb(S,Se)_2$); in grey- copper sulphide (Cu_2S); and in green- covellite (CuS).

Annealed samples

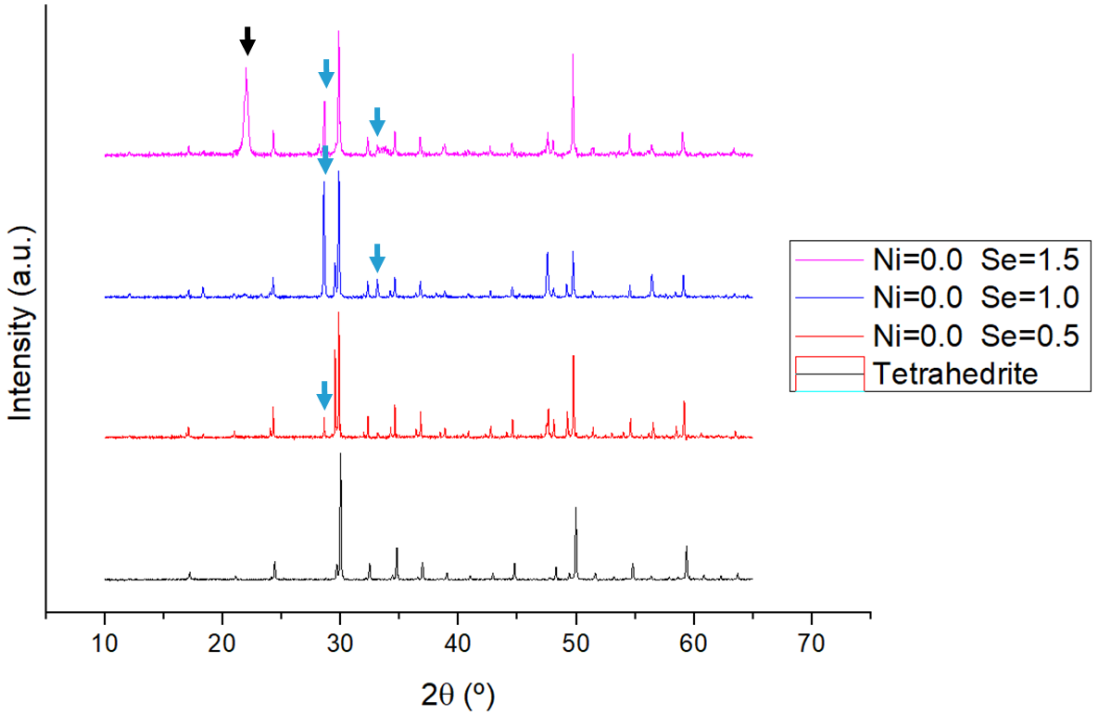

Fig. 79 Comparison of XRD of the annealed $Cu_{12}Sb_4S_{13-x}Se_x$ samples. Identified with arrows are peaks not associated to tetrahedrite: in magenta- Chalcostibite ($CuSb(S,Se)_2$); and in black-SiO_2 from a damaged sample holder.

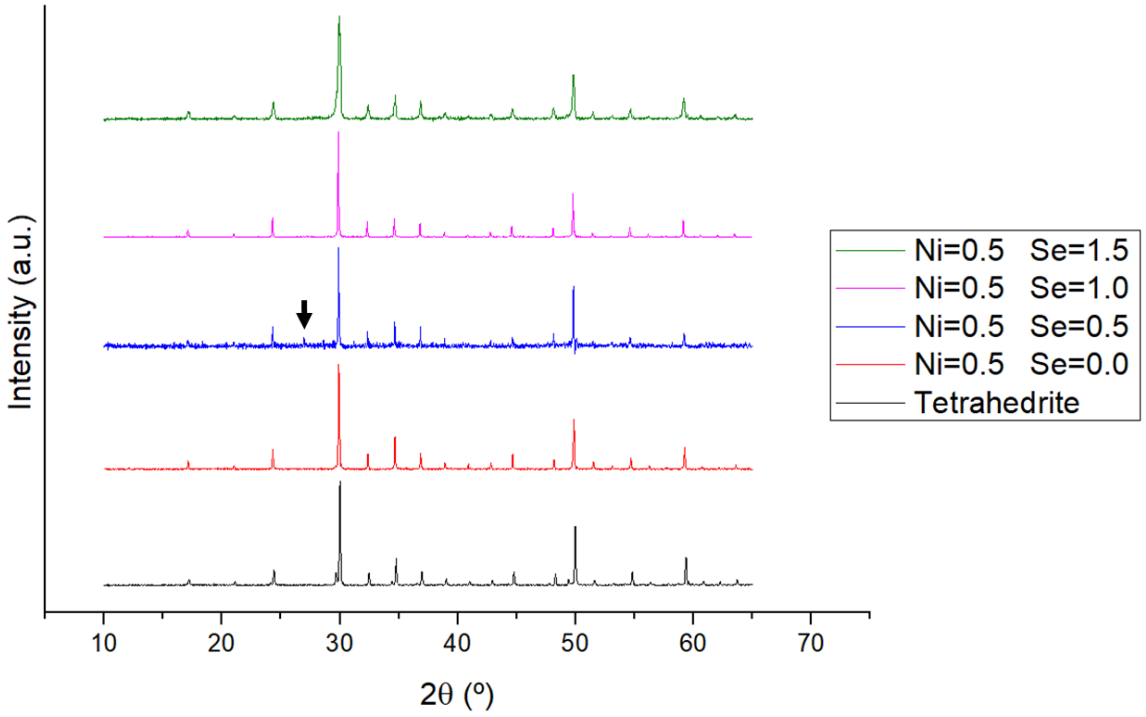

Fig. 80 Comparison of XRD of the annealed $Cu_{11.5}Ni_{0.5}Sb_4S_{13-x}Se_x$ samples. Identified with arrows are peaks not associated to tetrahedrite: in black-SiO_2 from a damaged sample holder.

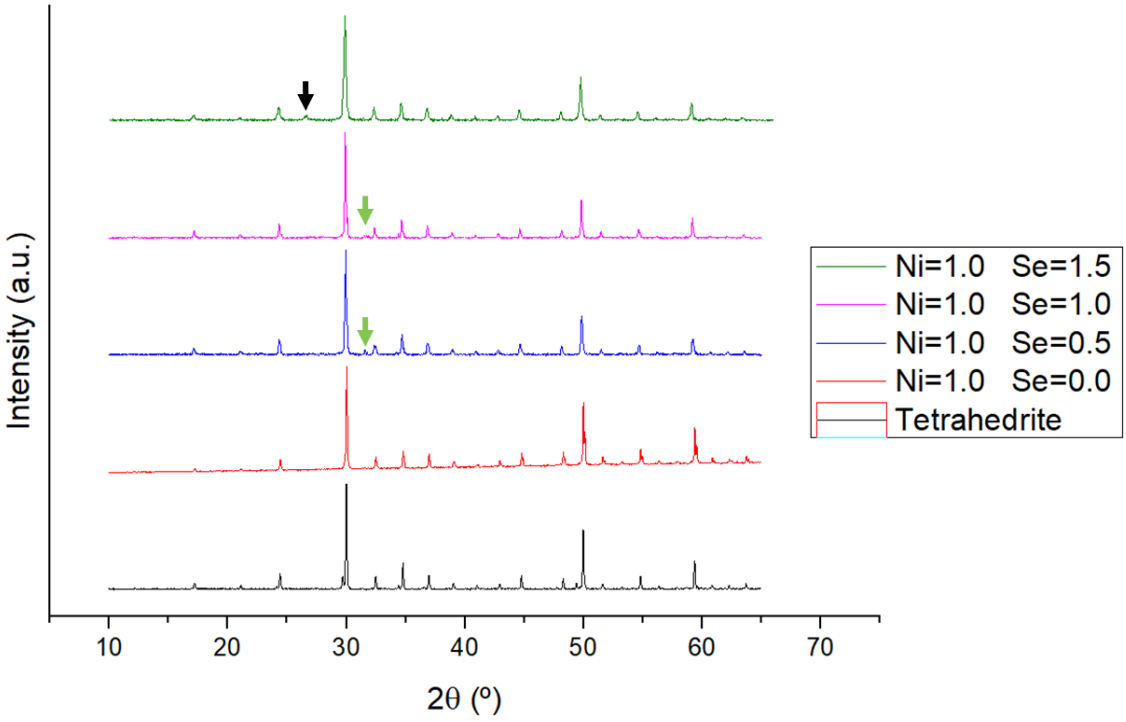

Fig. 81 Comparison of XRD of the annealed $Cu_{11}NiSb_4S_{13-x}Se_x$ samples. Identified with arrows are peaks not associated to tetrahedrite: in green- covellite (CuS); and in black- SiO_2 from a damaged sample holder.

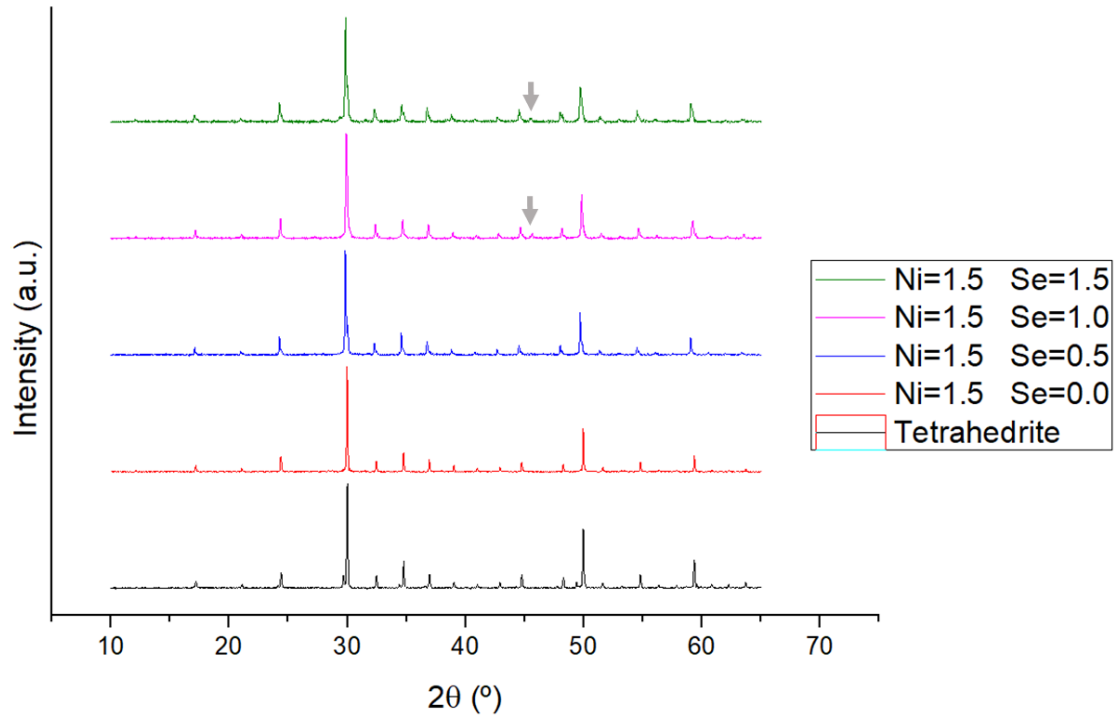

Fig. 82 Comparison of XRD of the annealed $Cu_{10.5}Ni_{1.5}Sb_4S_{13-x}Se_x$ samples. Identified with arrows are peaks not associated to tetrahedrite: in gray- copper sulphide (Cu_2S).

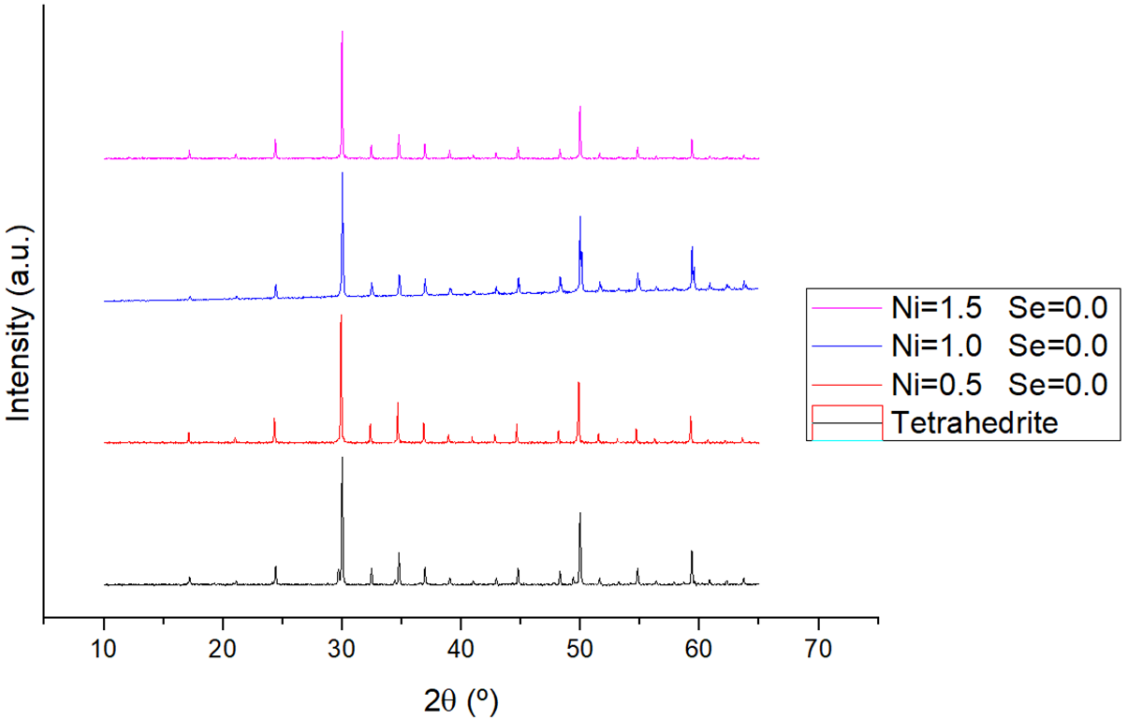

Fig. 83 Comparison of XRD of the annealed $Cu_{12-x}Ni_xSb_4S_{13}$ samples.

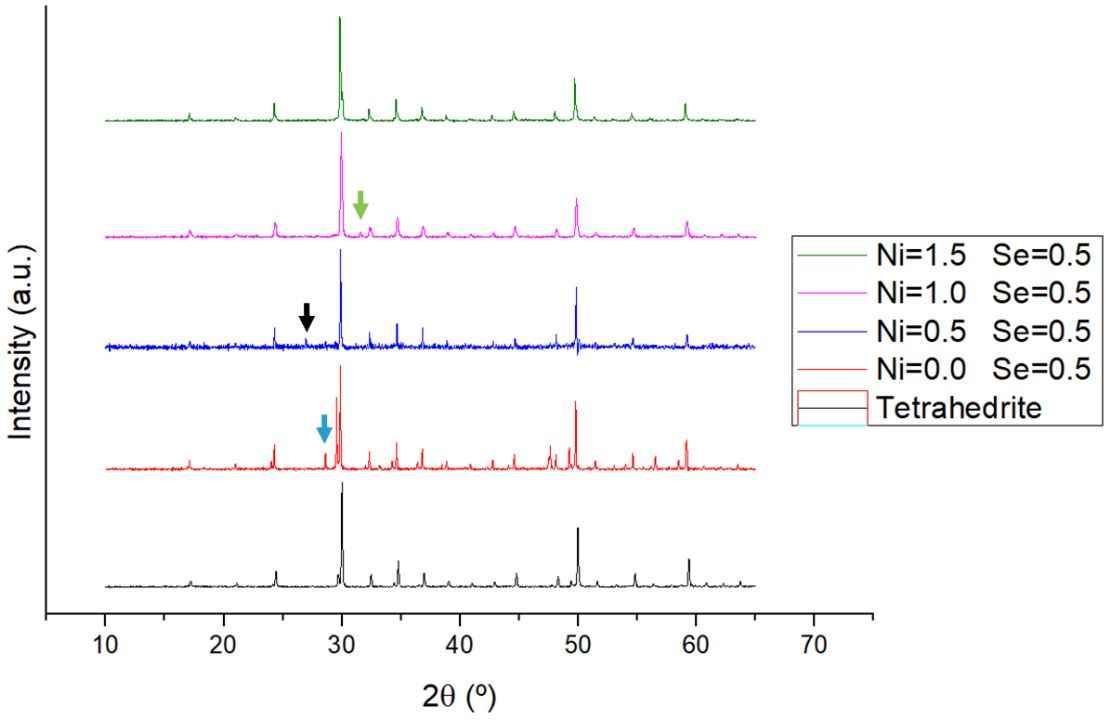

Fig. 84 Comparison of XRD of the annealed $Cu_{12-x}Ni_xSb_4S_{12.5}Se_{0.5}$ samples. Identified with arrows are peaks not associated to tetrahedrite: in magenta- Chalcostibite ($CuSb(S,Se)_2$); in green- covellite (CuS); and in black- SiO_2 from a damaged sample holder.

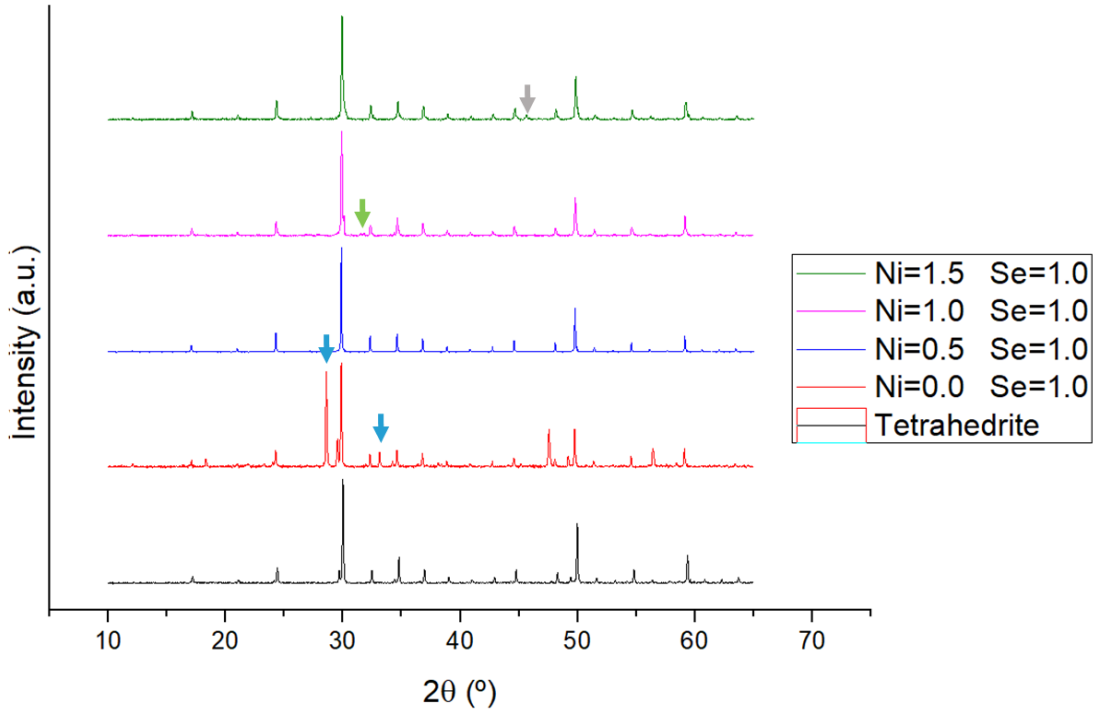

Fig. 85 Comparison of XRD of the annealed $Cu_{12-x}Ni_xSb_4S_{12}Se$ samples. Identified with arrows are peaks not associated to tetrahedrite: in magenta- Chalcostibite ($CuSb(S,Se)_2$); and in gray- copper sulphide (Cu_2S).

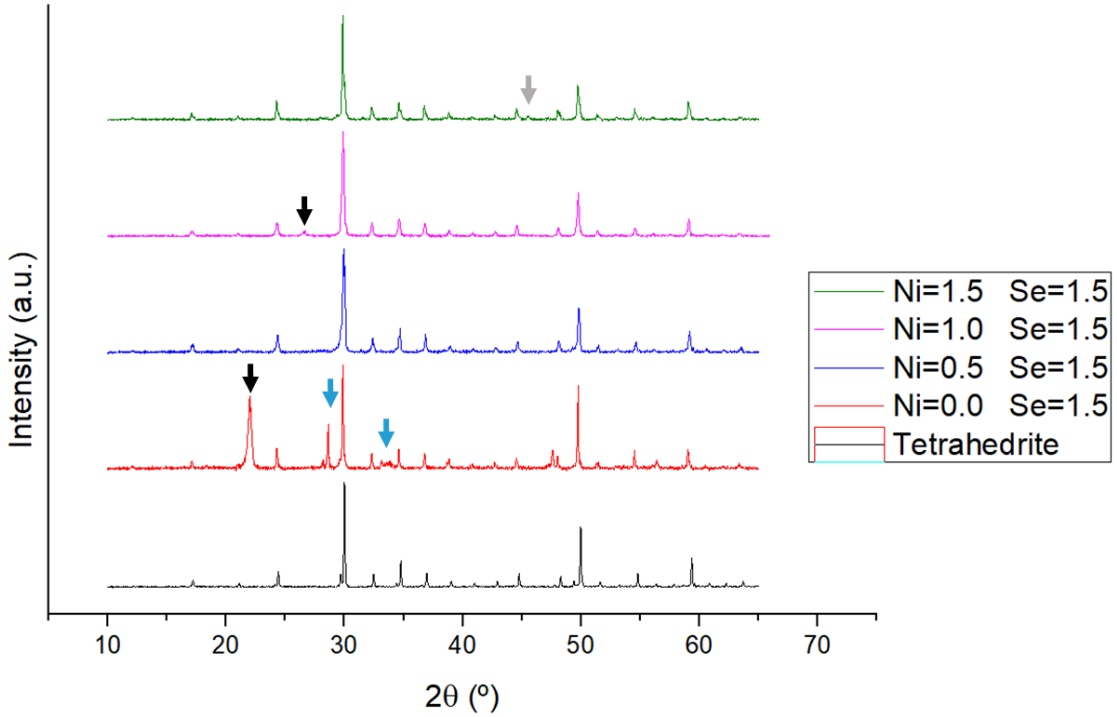

Fig. 86 Comparison of XRD of the annealed $Cu_{12-x}Ni_xSb_4S_{11.5}Se_{1.5}$ samples. Identified with arrows are peaks not associated to tetrahedrite: in magenta- Chalcostibite ($CuSb(S,Se)_2$); in green- covellite (CuS); in gray- copper sulphide (Cu_2S); and in black-silicon dioxide from the sample holder.

Hot-pressed samples

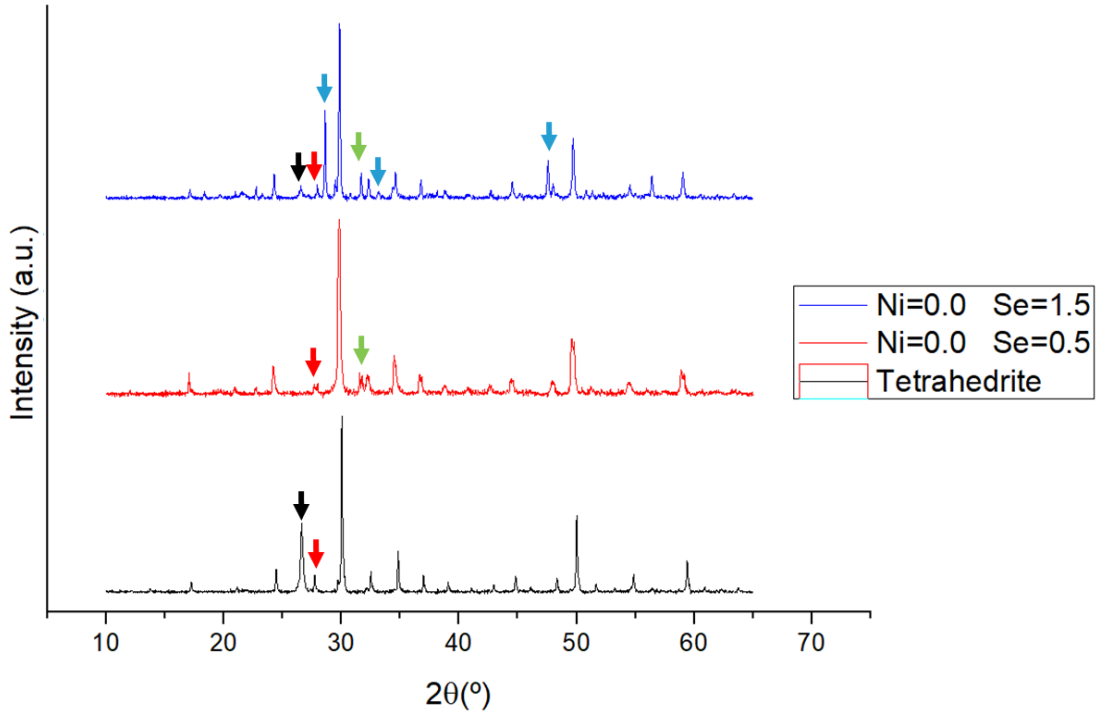

Fig. 87 Comparison of XRD of the hot-pressed $Cu_{12}Sb_4S_{13-x}Se_x$ samples. Identified with arrows are peaks not associated to tetrahedrite: in magenta- Chalcostibite ($CuSb(S,Se)_2$); in green- covellite (CuS); in red- antimony oxide (Sb_2O_3); and in black-silicon dioxide from the sample holder.

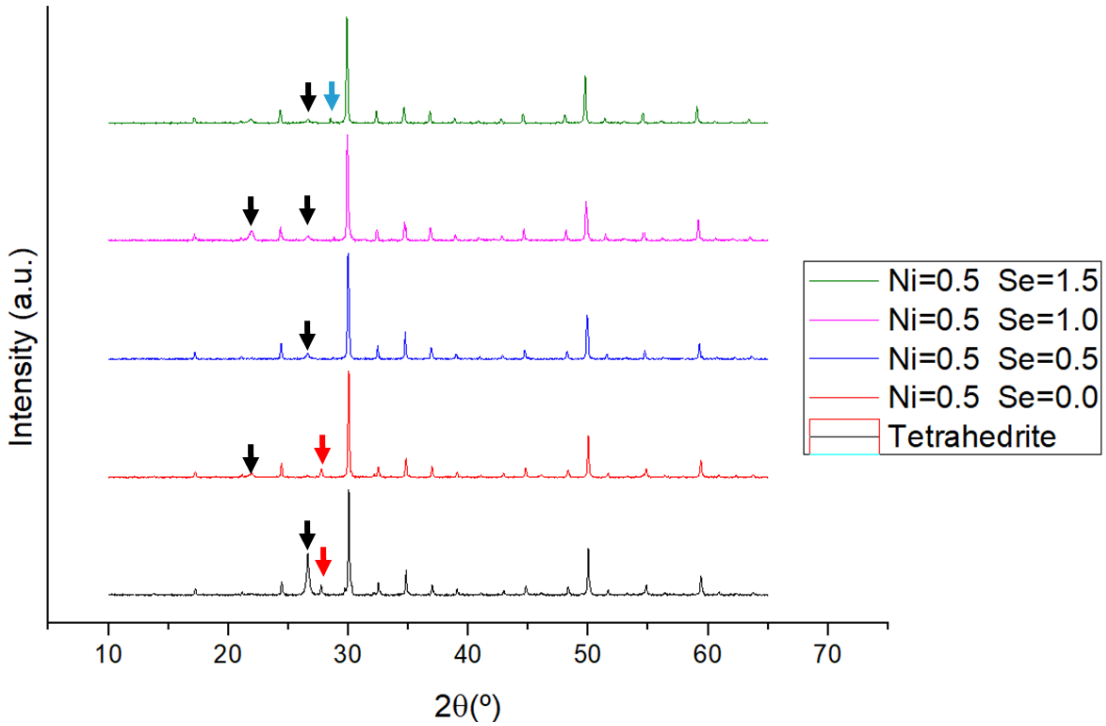

Fig. 88 Comparison of XRD of the hot-pressed $Cu_{11.5}Ni_{0.5}Sb_4S_{13-x}Se_x$ samples. Identified with arrows are peaks not associated to tetrahedrite: in magenta- Chalcostibite ($CuSb(S,Se)_2$); in red- antimony oxide (Sb_2O_3) and in black-silicon dioxide from the sample holder.

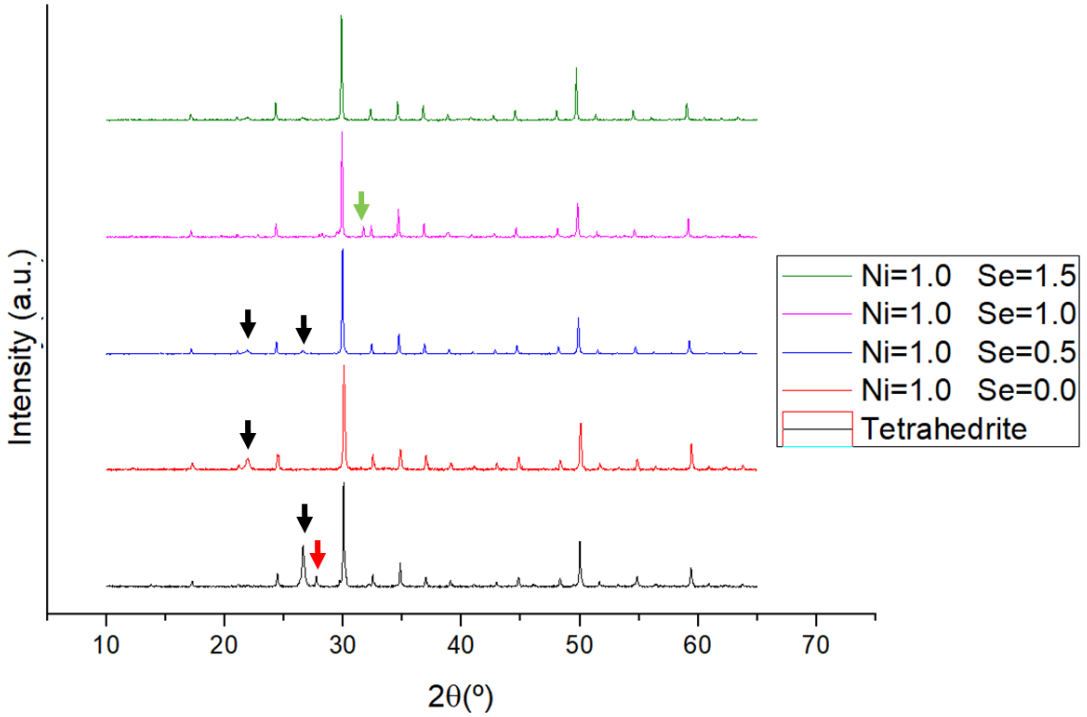

Fig. 89 Comparison of XRD of the hot-pressed $Cu_{11}NiSb_4S_{13-x}Se_x$ samples. Identified with arrows are peaks not associated to tetrahedrite: in green- covellite (CuS); in red- antimony oxide (Sb_2O_3) and in black-silicon dioxide from the sample holder.

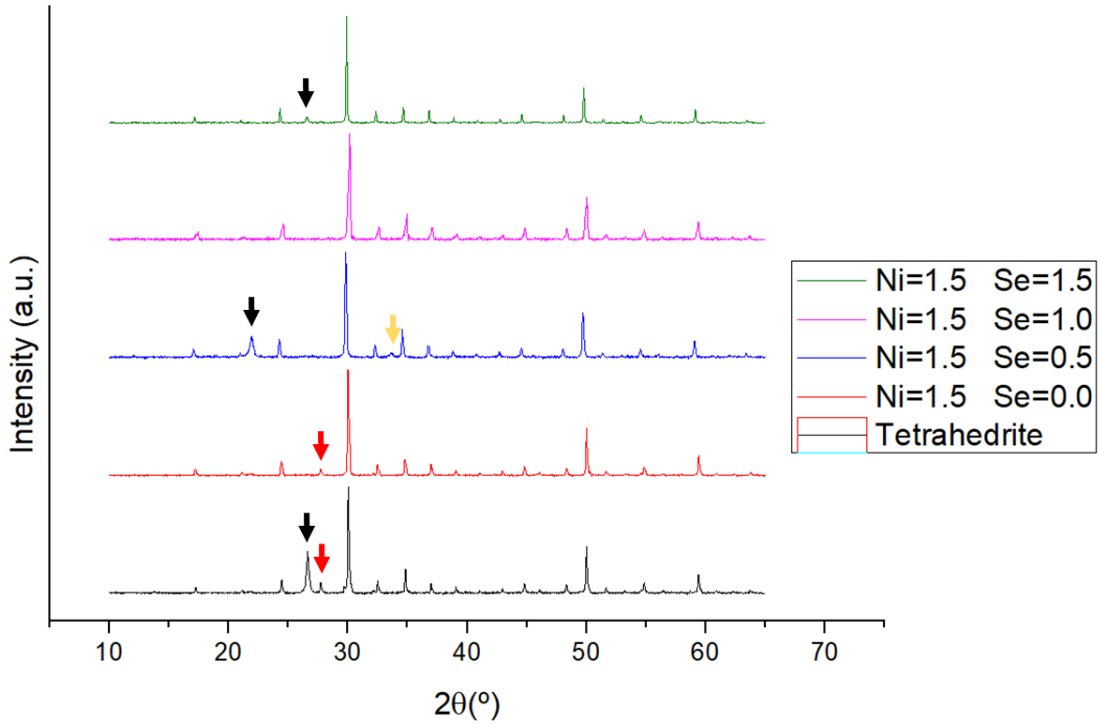

Fig. 90 Comparison of XRD of the hot-pressed $Cu_{10.5}Ni_{1.5}Sb_4S_{13-x}Se_x$ samples. Identified with arrows are peaks not associated to tetrahedrite: in red- antimony oxide (Sb_2O_3); in yellow- ullmannite (NiSbS); and in black-silicon dioxide from the sample holder.

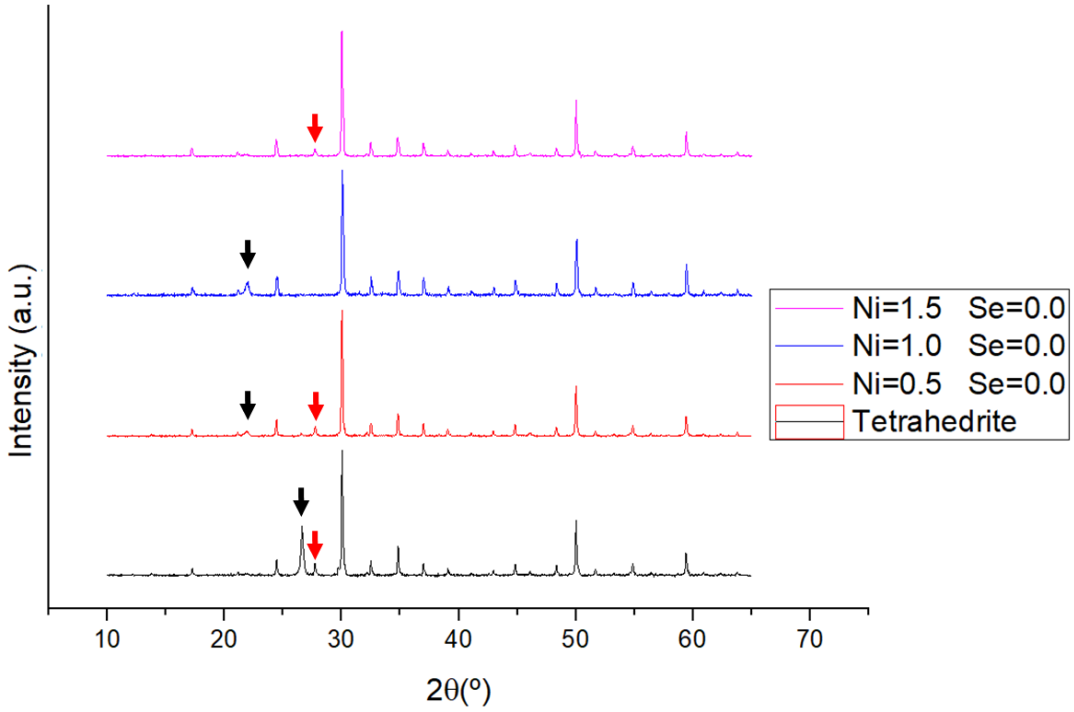

Fig. 91 Comparison of XRD of the hot-pressed $Cu_{12-x}Ni_xSb_4S_{13}$ samples. Identified with arrows are peaks not associated to tetrahedrite: in red- antimony oxide (Sb_2O_3) and in black-silicon dioxide from the sample holder.

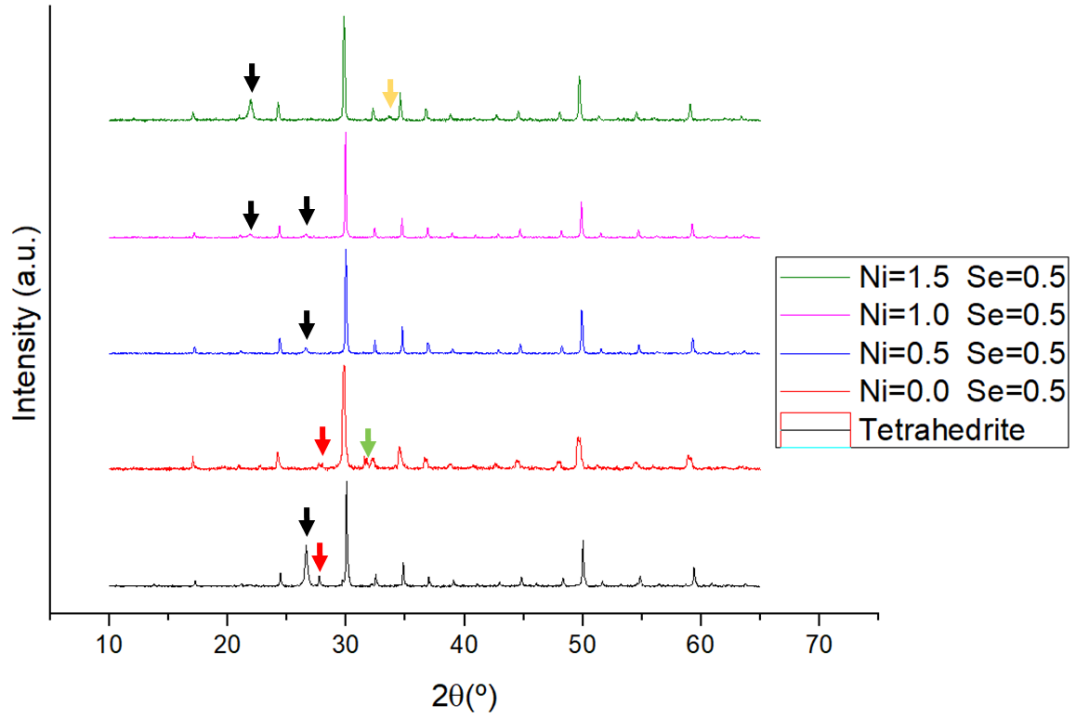

Fig. 92 Comparison of XRD of the hot-pressed $Cu_{12-x}Ni_xSb_4S_{12.5}Se_{0.5}$ samples. Identified with arrows are peaks not associated to tetrahedrite: in magenta- Chalcostibite ($CuSb(S,Se)_2$); in green- covellite (CuS); in red- antimony oxide (Sb_2O_3); in yellow- ullmannite (NiSbS); and in black-silicon dioxide from the sample holder.

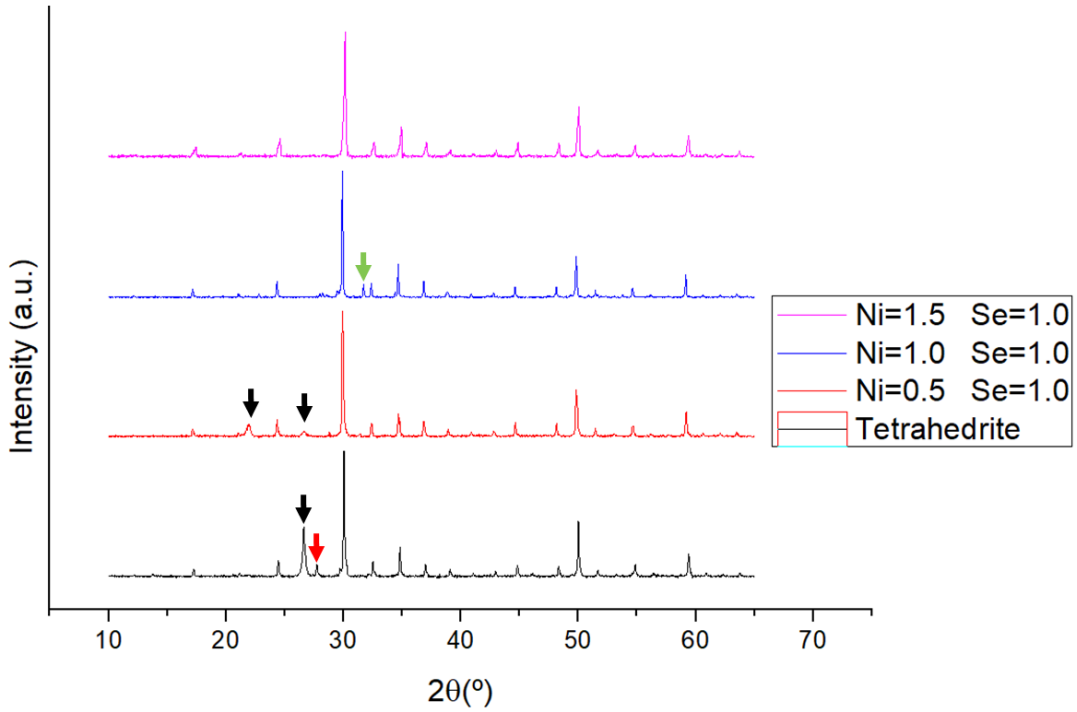

Fig. 93 Comparison of XRD of the hot-pressed $Cu_{12-x}Ni_xSb_4S_{12}Se$ samples. Identified with arrows are peaks not associated to tetrahedrite: in green- covellite (CuS); in red- antimony oxide (Sb_2O_3) and in black-silicon dioxide from the sample holder.

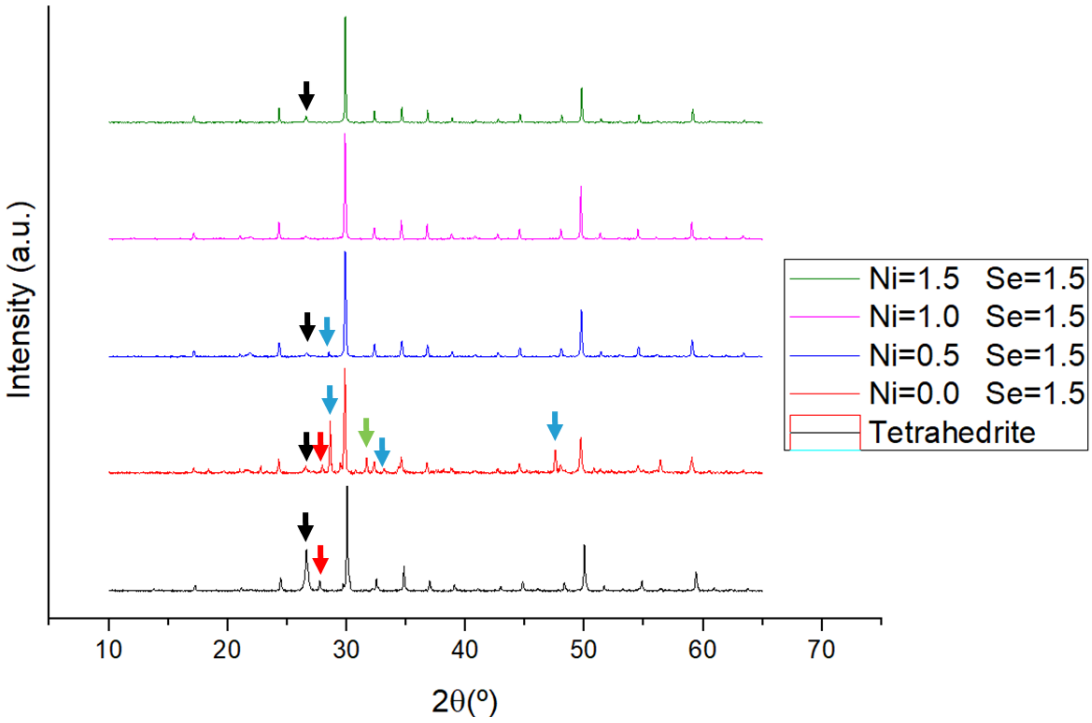

Fig. 94 Comparison of XRD of the hot-pressed $Cu_{12-x}Ni_xSb_4S_{11.5}Se_{1.5}$ samples. Identified with arrows are peaks not associated to tetrahedrite: in magenta- Chalcostibite ($CuSb(S,Se)_2$); in green- covellite (CuS); in red- antimony oxide (Sb_2O_3) and in black-silicon dioxide from the sample holder.

ATTACHMENT 2: RAMAN SPECTROSCOPY

As-cast samples

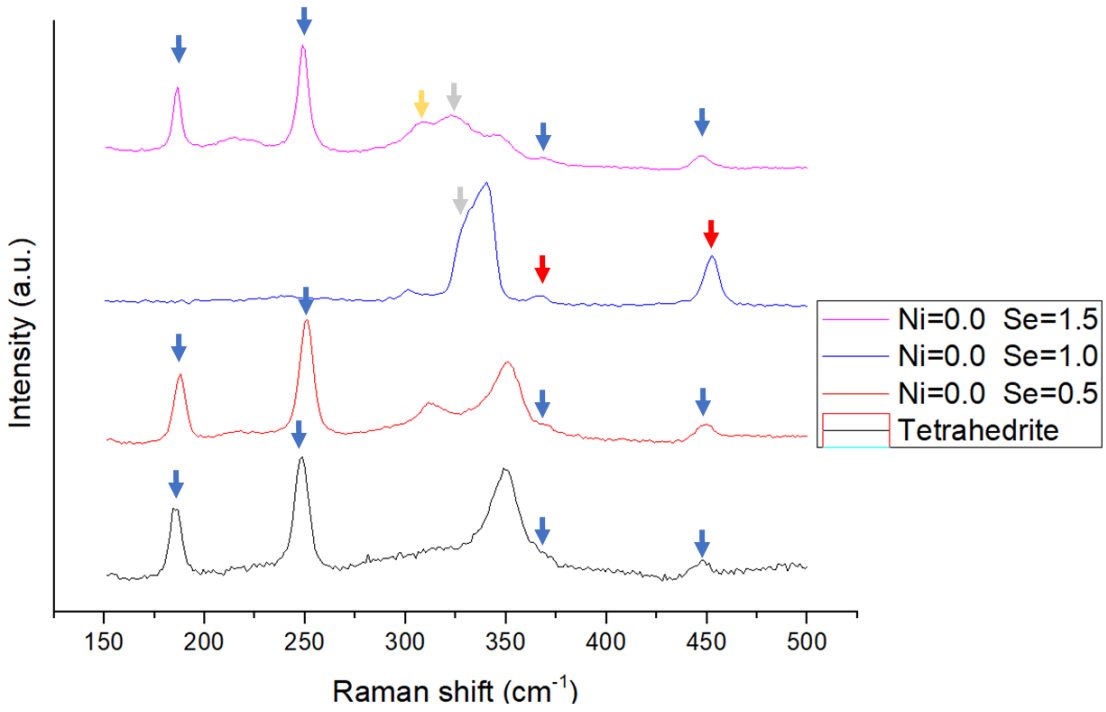

Fig. 95 Comparison of Raman spectra of the as-cast $Cu_{12}Sb_4S_{13-x}Se_x$ samples. Identified with arrows are peaks not associated to tetrahedrite: in blue- Cu-S chemical bond signal (ejected material); in gray- chalcostibite ($CuSbS_2$); in yellow- famatinite (Cu_3SbS_4); and in red- copper sulphide (Cu_xS_y).

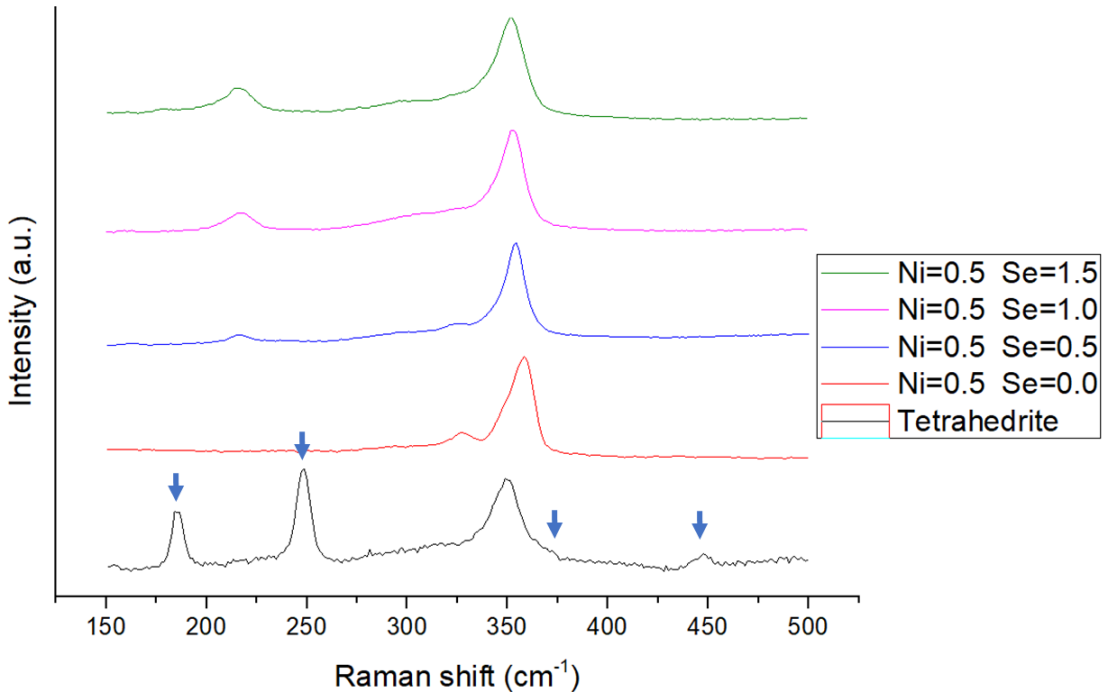

Fig. 96 Comparison of Raman spectra of the as-cast $Cu_{11.5}Ni_{0.5}Sb_4S_{13-x}Se_x$ samples. Identified with arrows are peaks not associated to tetrahedrite: in blue- Cu-S chemical bond signal (ejected material).

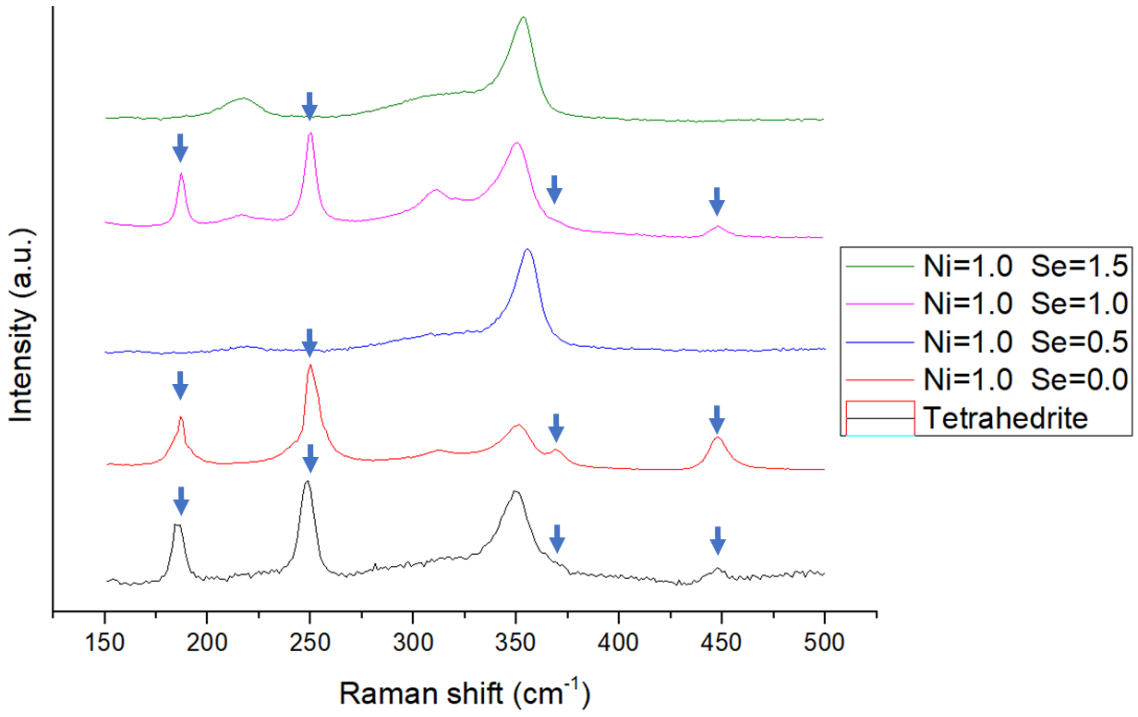

Fig. 97 Comparison of Raman spectra of the as-cast $Cu_{11}NiSb_4S_{13-x}Se_x$ samples. Identified with arrows are peaks not associated to tetrahedrite: in blue- Cu-S chemical bond signal (ejected material).

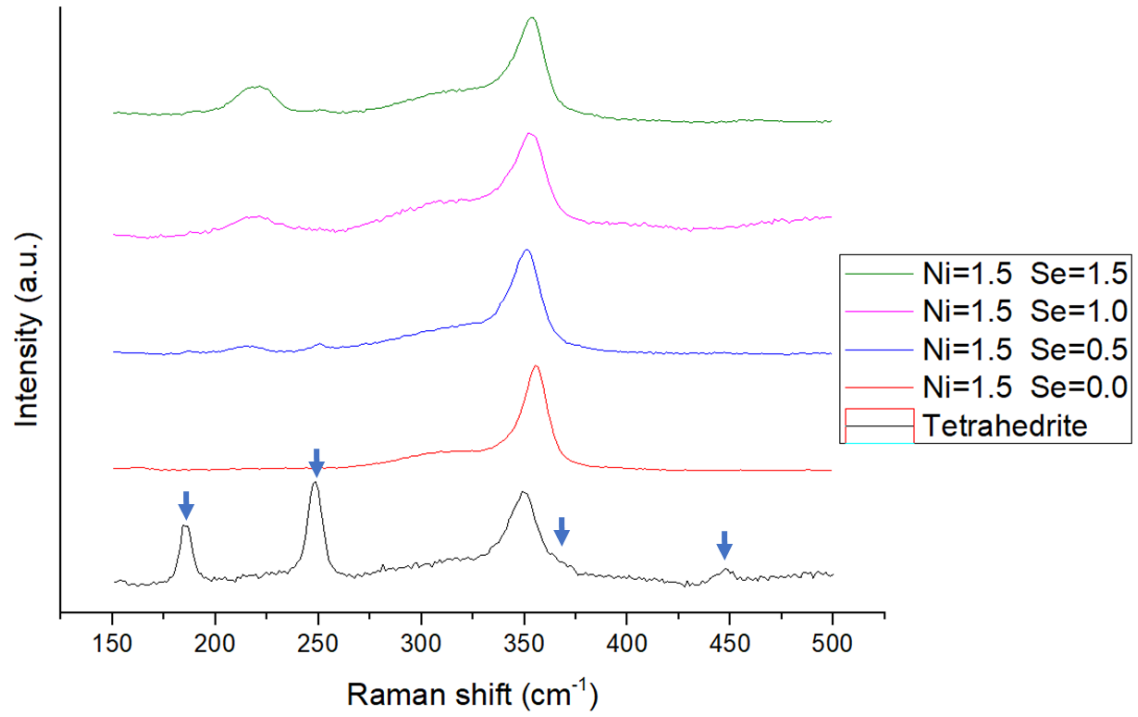

Fig. 98 Comparison of Raman spectra of the as-cast $Cu_{10.5}Ni_{1.5}Sb_4S_{13-x}Se_x$ samples. Identified with arrows are peaks not associated to tetrahedrite: in blue- Cu-S chemical bond signal (ejected material).

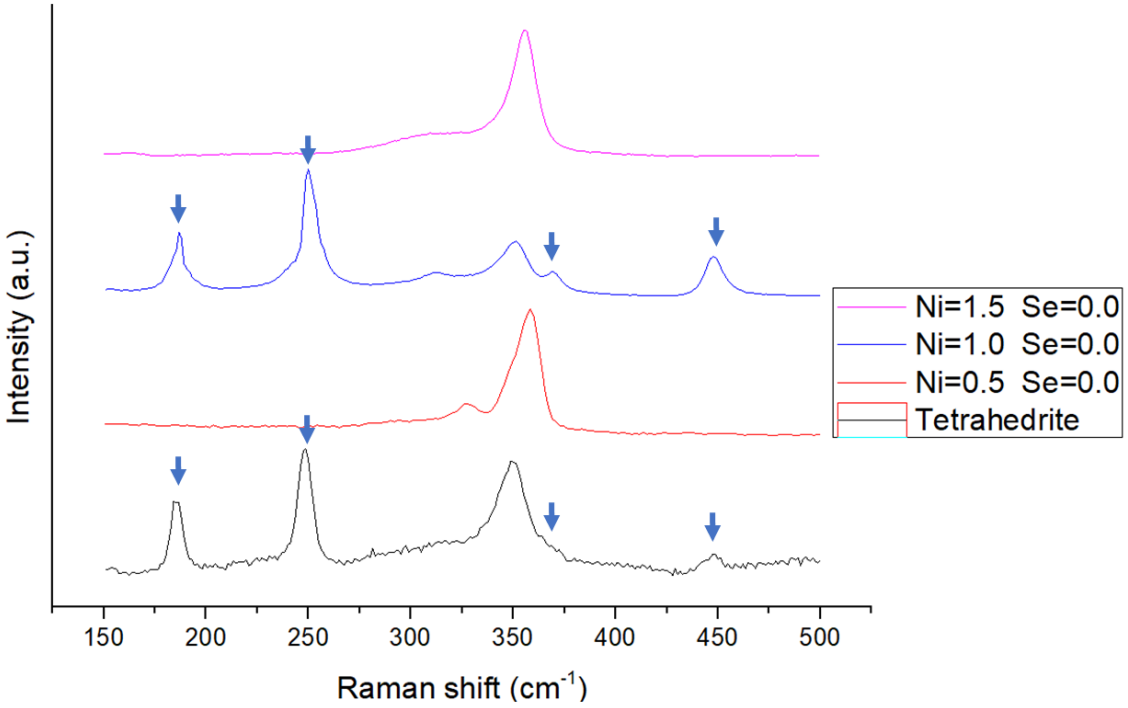

Fig. 99 Comparison of Raman spectra of the as-cast $Cu_{12-x}Ni_xSb_4S_{13}$ samples. Identified with arrows are peaks not associated to tetrahedrite: in blue- Cu-S chemical bond signal (ejected material).

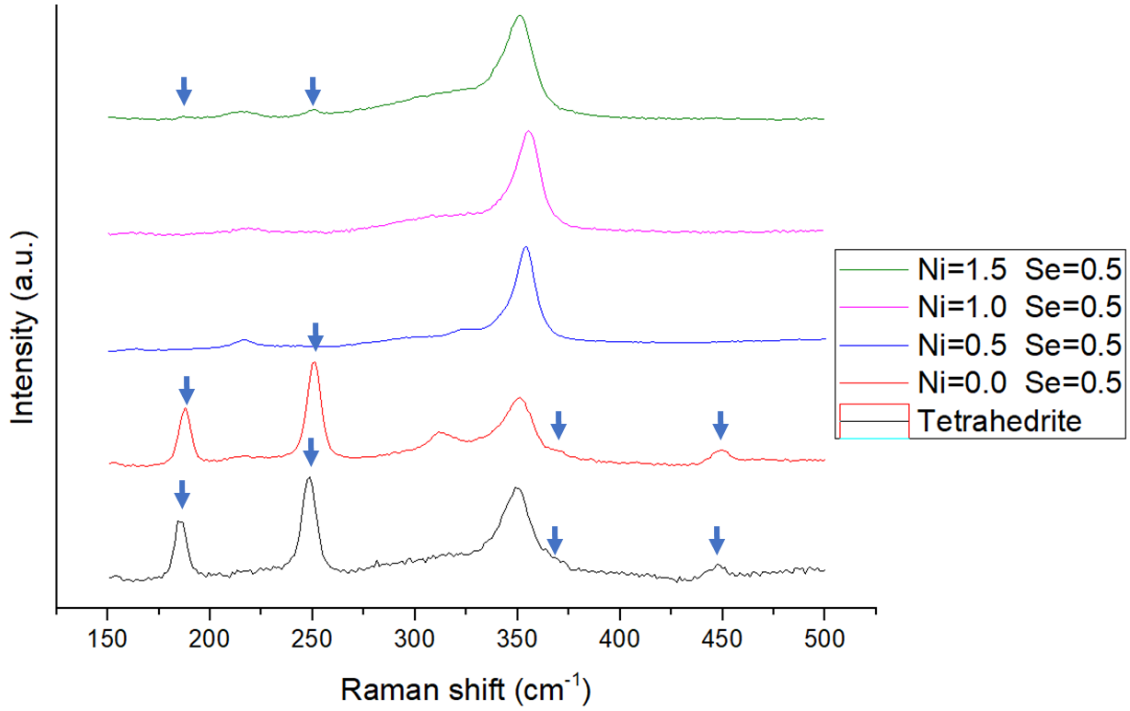

Fig. 100 Comparison of Raman spectra of the as-cast $Cu_{12-x}Ni_xSb_4S_{12.5}Se_{0.5}$ samples. Identified with arrows are peaks not associated to tetrahedrite: in blue- Cu-S chemical bond signal (ejected material).

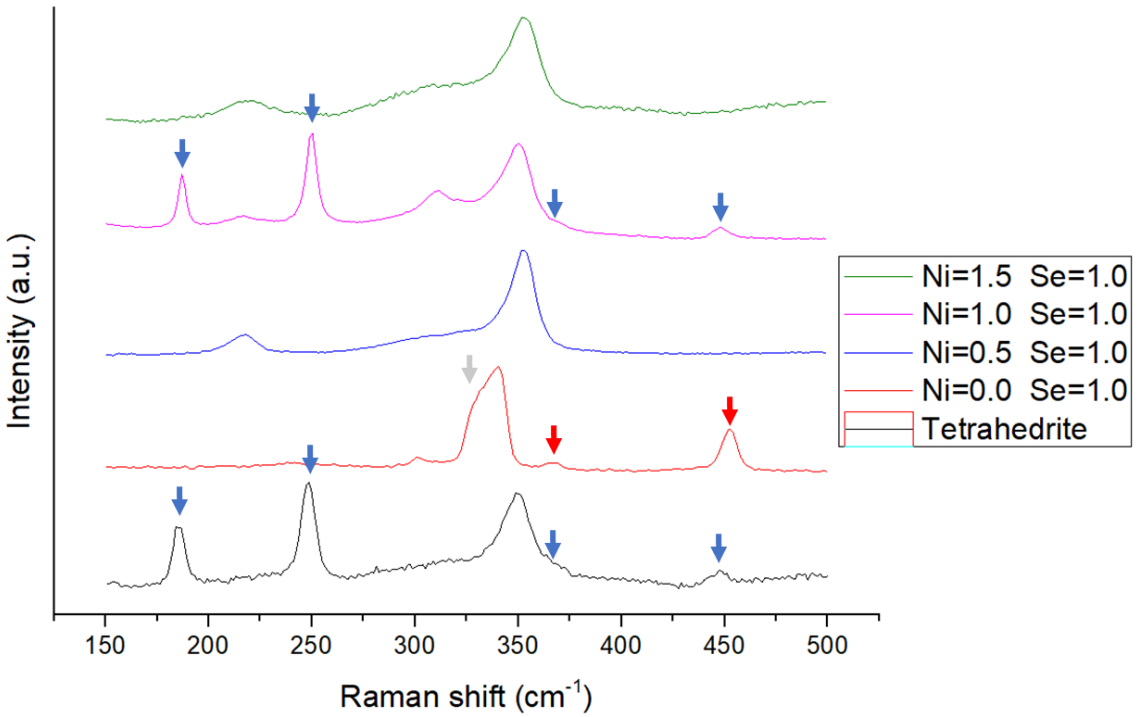

Fig. 101 Comparison of Raman spectra of the as-cast $Cu_{12-x}Ni_xSb_4S_{12}Se$ samples. Identified with arrows are peaks not associated to tetrahedrite: in blue- Cu-S chemical bond signal (ejected material); in gray- chalcostibite ($CuSbS_2$); and in red- copper sulphide (Cu_xS_y).

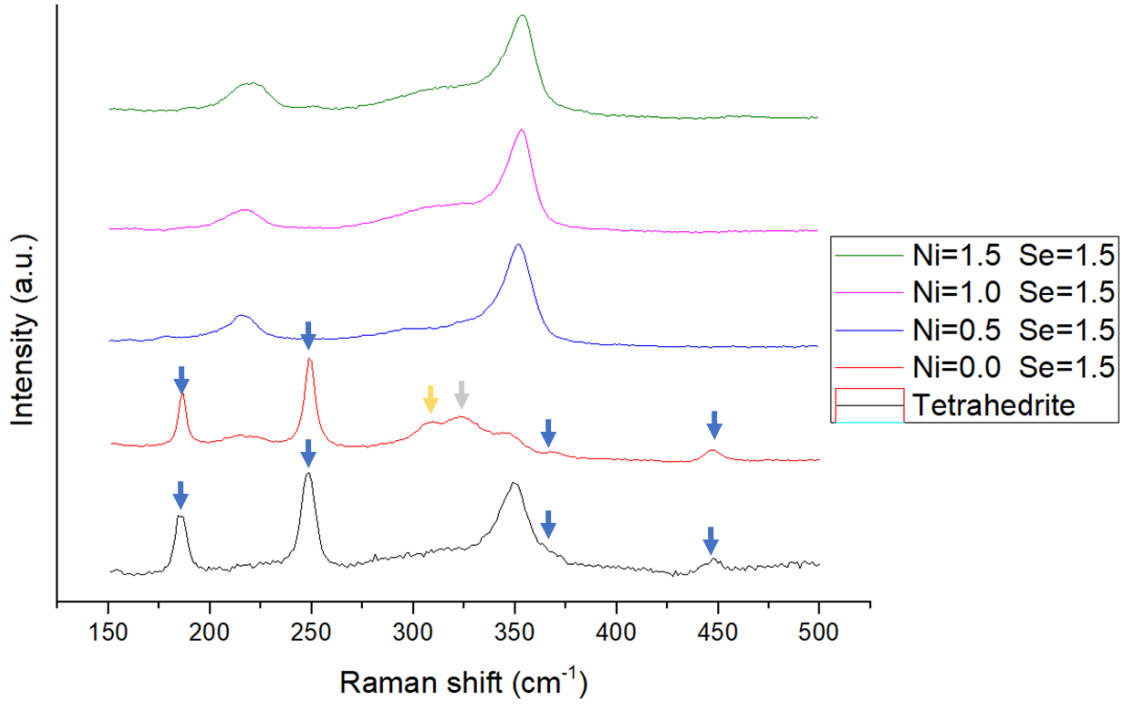

Fig. 102 Comparison of Raman spectra of the as-cast $Cu_{12-x}Ni_xSb_4S_{11.5}Se_{1.5}$ samples. Identified with arrows are peaks not associated to tetrahedrite: in blue- Cu-S chemical bond signal (ejected material); in gray- chalcostibite ($CuSbS_2$); in yellow- famatinite (Cu_3SbS_4); and in red- copper sulphide (Cu_xS_y).

Annealed samples

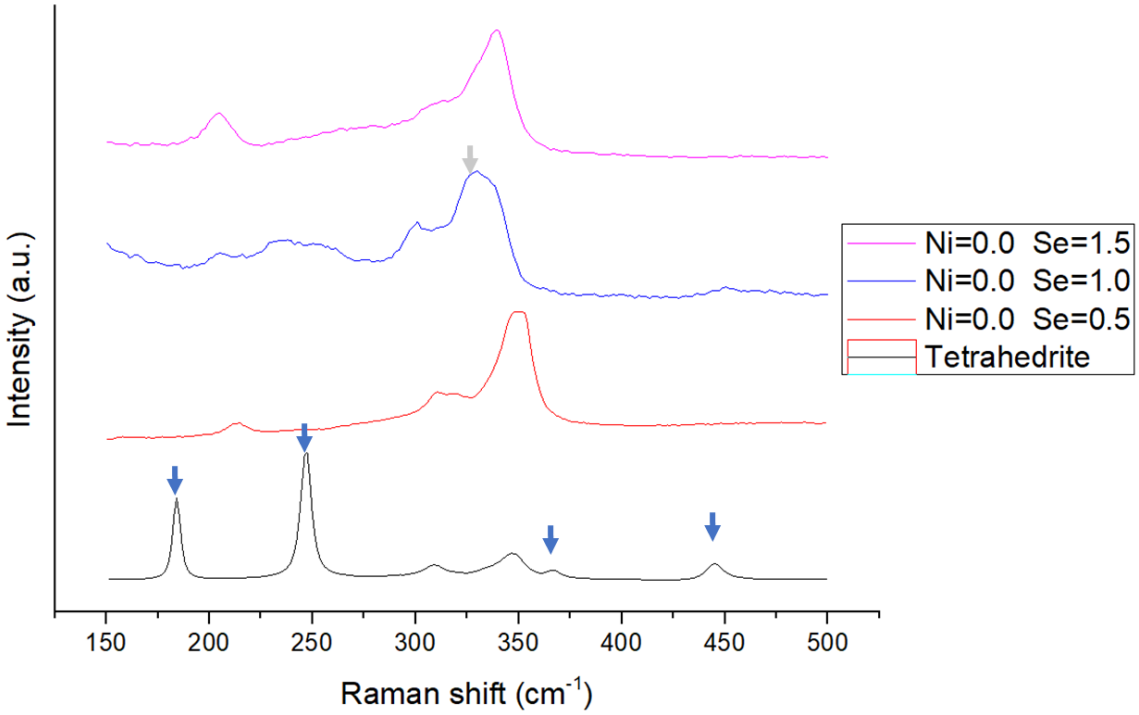

Fig. 103 Comparison of Raman spectra of the annealed $Cu_{12}Sb_4S_{13-x}Se_x$ samples. Identified with arrows are peaks not associated to tetrahedrite: in blue- Cu-S chemical bond signal (from ejected material); and in gray- chalcostibite ($CuSbS_2$).

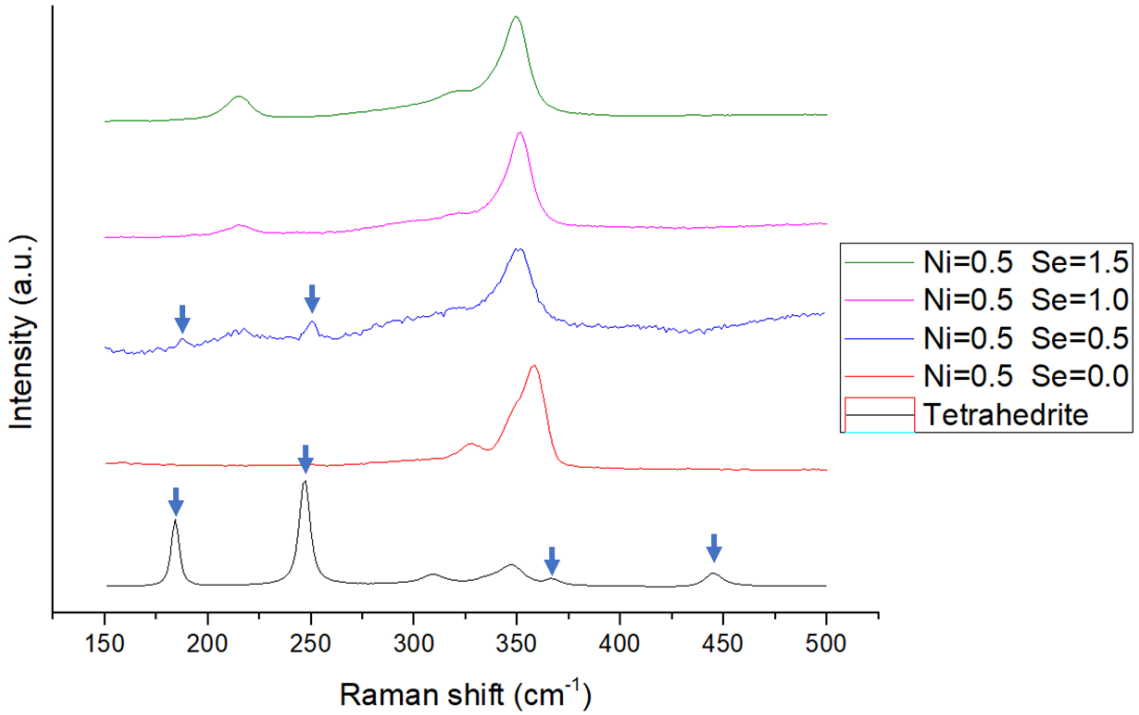

Fig. 104 Comparison of Raman spectra of the annealed $Cu_{11.5}Ni_{0.5}Sb_4S_{13-x}Se_x$ samples. Identified with arrows are peaks not associated to tetrahedrite: in blue- Cu-S chemical bond signal (from ejected material).

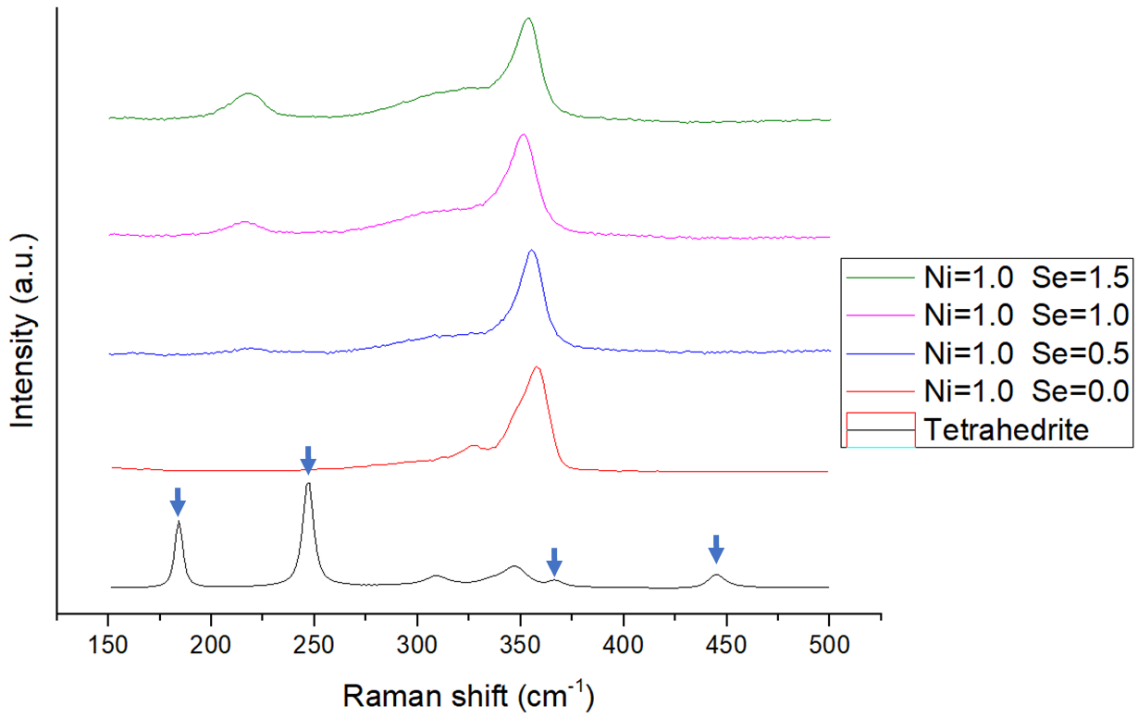

Fig. 105 Comparison of Raman spectra of the annealed $Cu_{11}NiSb_4S_{13-x}Se_x$ samples. Identified with arrows are peaks not associated to tetrahedrite: in blue- Cu-S chemical bond signal (from ejected material).

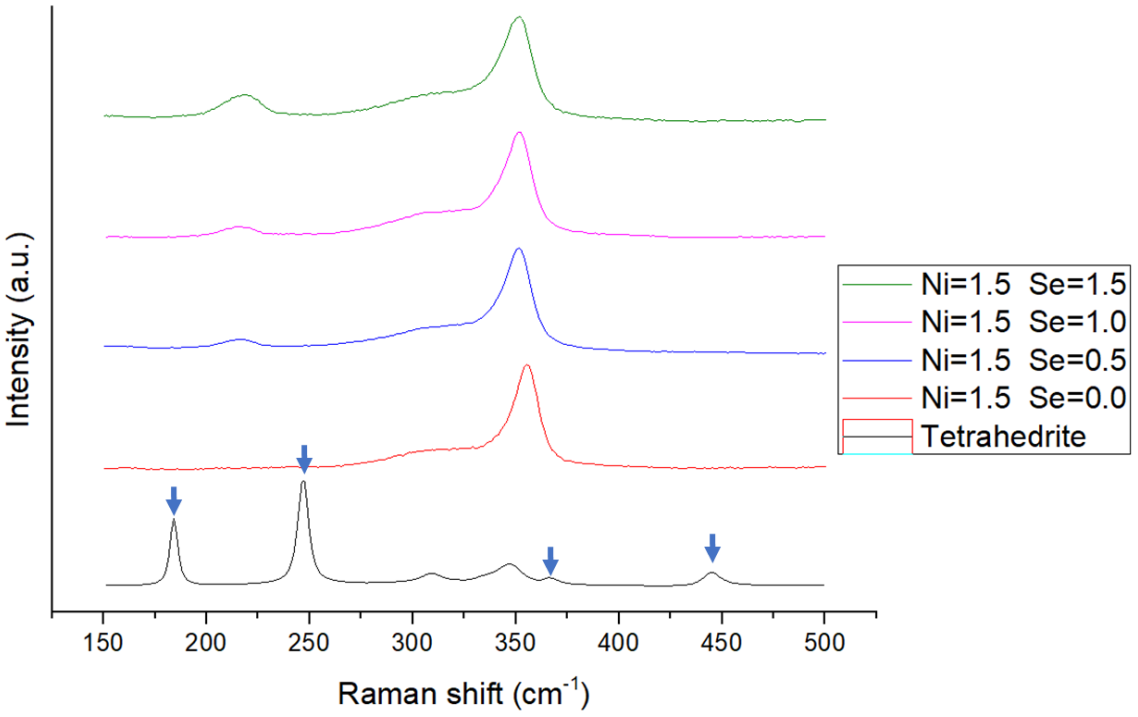

Fig. 106 Comparison of Raman spectra of the annealed $Cu_{10.5}Ni_{1.5}Sb_4S_{13-x}Se_x$ samples. Identified with arrows are peaks not associated to tetrahedrite: in blue- Cu-S chemical bond signal (from ejected material).

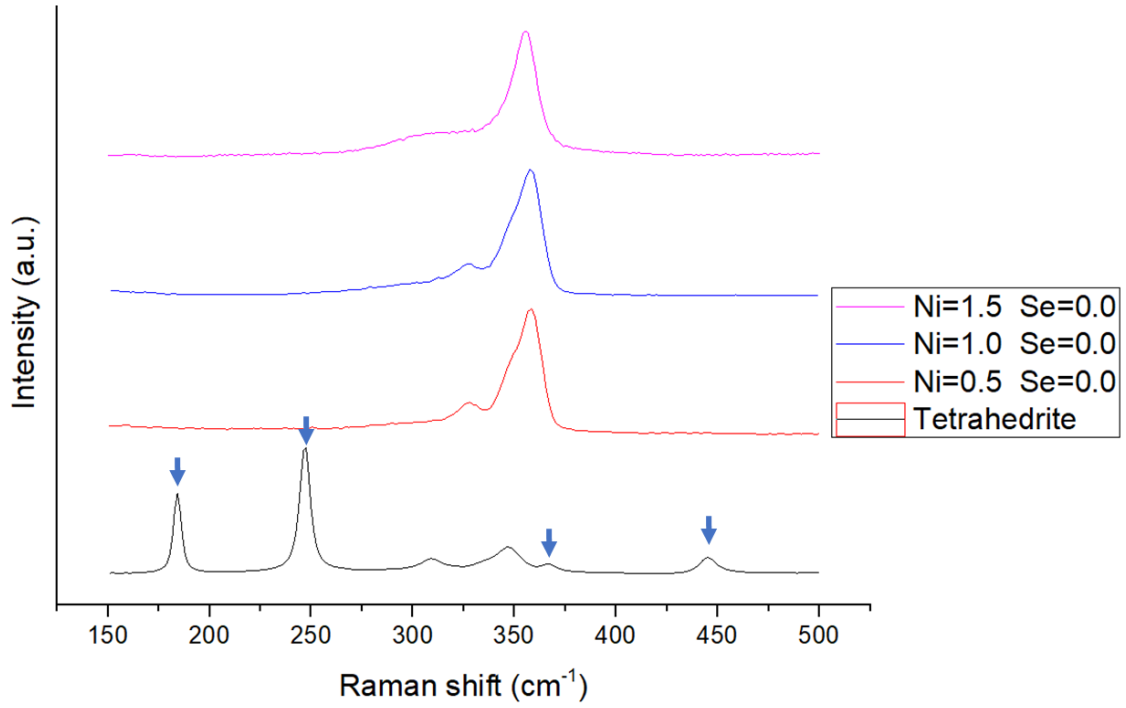

Fig. 107 Comparison of Raman spectra of the annealed $Cu_{12-x}Ni_xSb_4S_{13}$ samples. Identified with arrows are peaks not associated to tetrahedrite: in blue- Cu-S chemical bond signal (from ejected material).

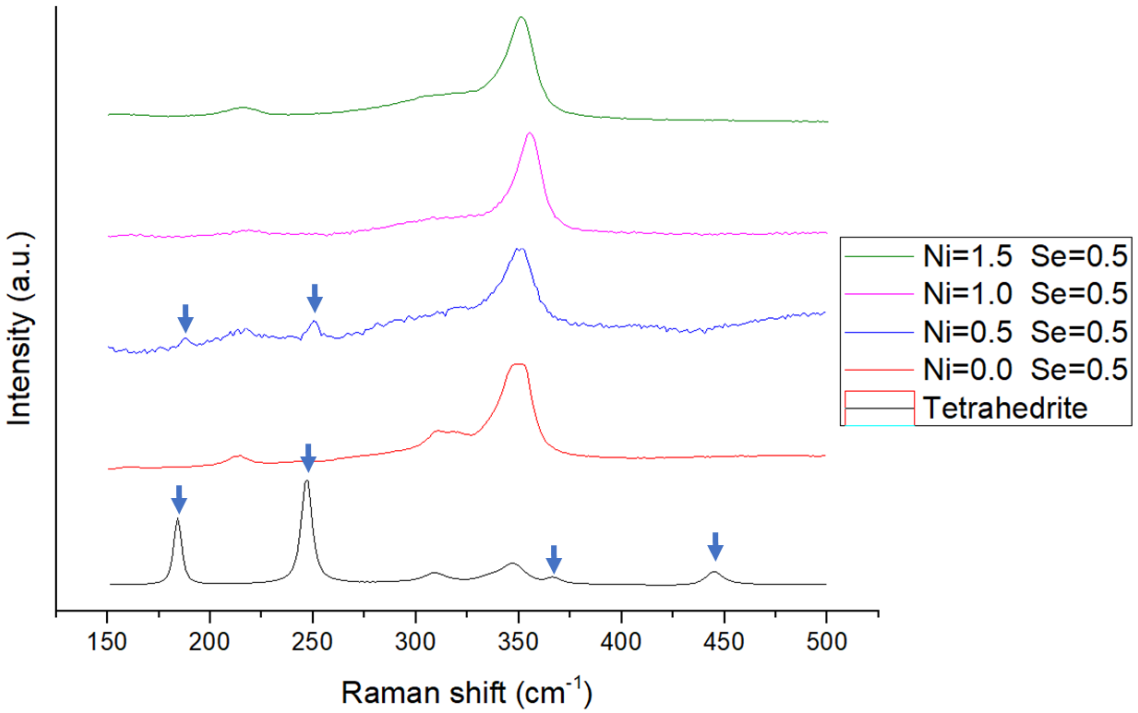

Fig. 108 Comparison of Raman spectra of the annealed $Cu_{12-x}Ni_xSb_4S_{12.5}Se_{0.5}$ samples. Identified with arrows are peaks not associated to tetrahedrite: in blue- Cu-S chemical bond signal (from ejected material).

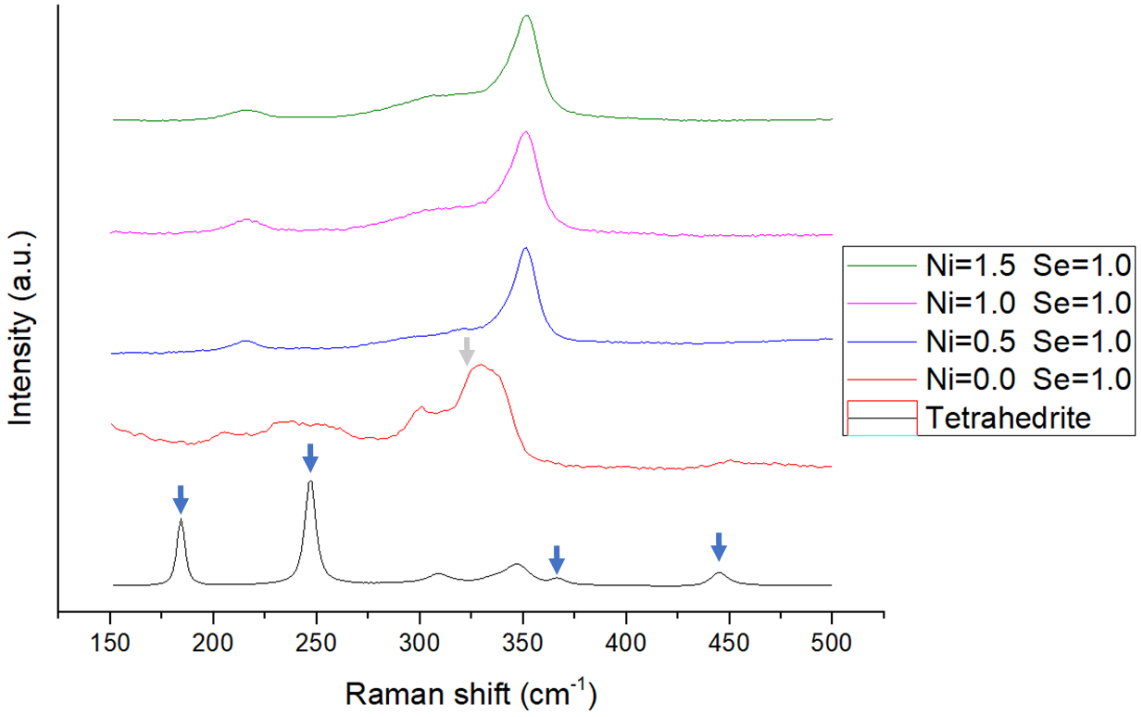

Fig. 109 Comparison of Raman spectra of the annealed $Cu_{12-x}Ni_xSb_4S_{12}Se$ samples. Identified with arrows are peaks not associated to tetrahedrite: in blue- Cu-S chemical bond signal (from ejected material); and in gray- chalcostibite ($CuSbS_2$).

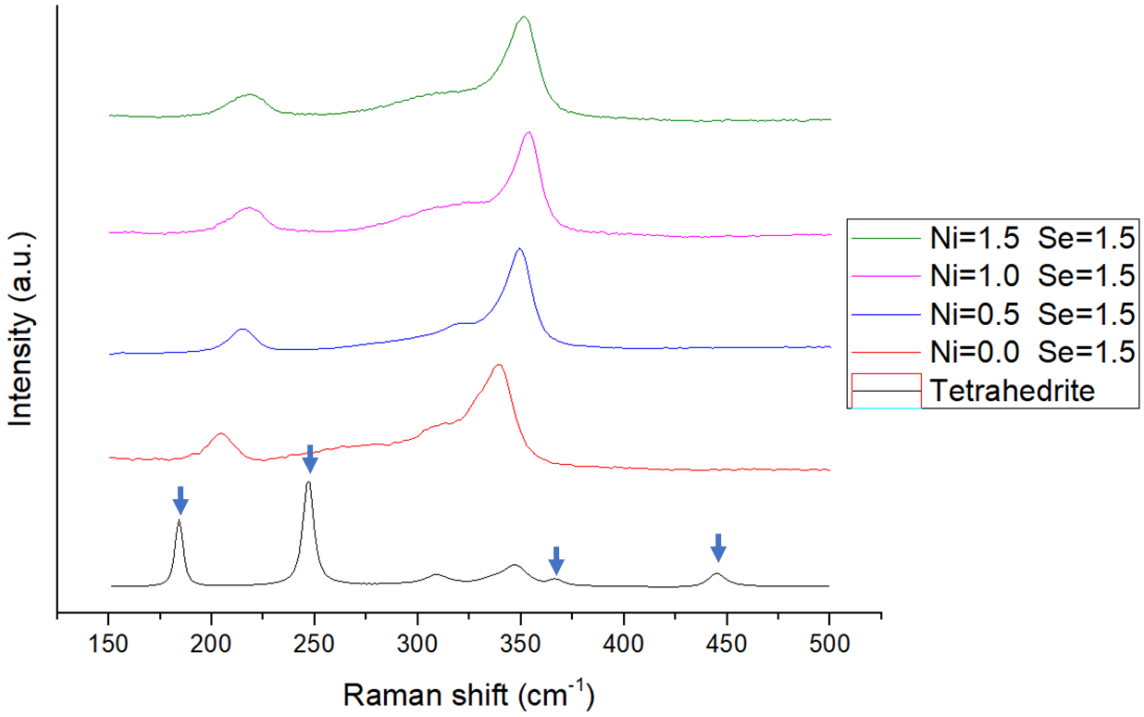

Fig. 110 Comparison of Raman spectra of the annealed $Cu_{12-x}Ni_xSb_4S_{11.5}Se_{1.5}$ samples. Identified with arrows are peaks not associated to tetrahedrite: in blue- Cu-S chemical bond signal (from ejected material).

Hot-pressed samples

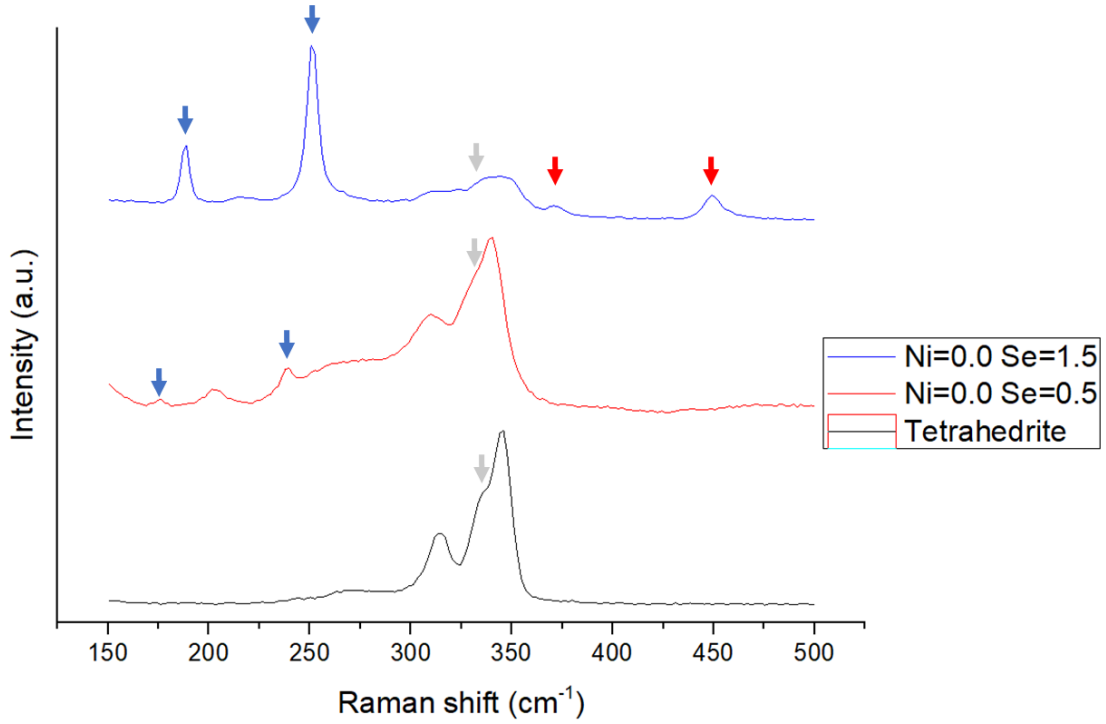

Fig. 111 Comparison of Raman spectra of the hot-pressed $Cu_{12}Sb_4S_{13-x}Se_x$ samples. Identified with arrows are peaks not associated to tetrahedrite: in blue- Cu-S chemical bond signal (from ejected material); in gray- chalcostibite ($CuSbS_2$); and in red- copper sulphide (Cu_xS_y).

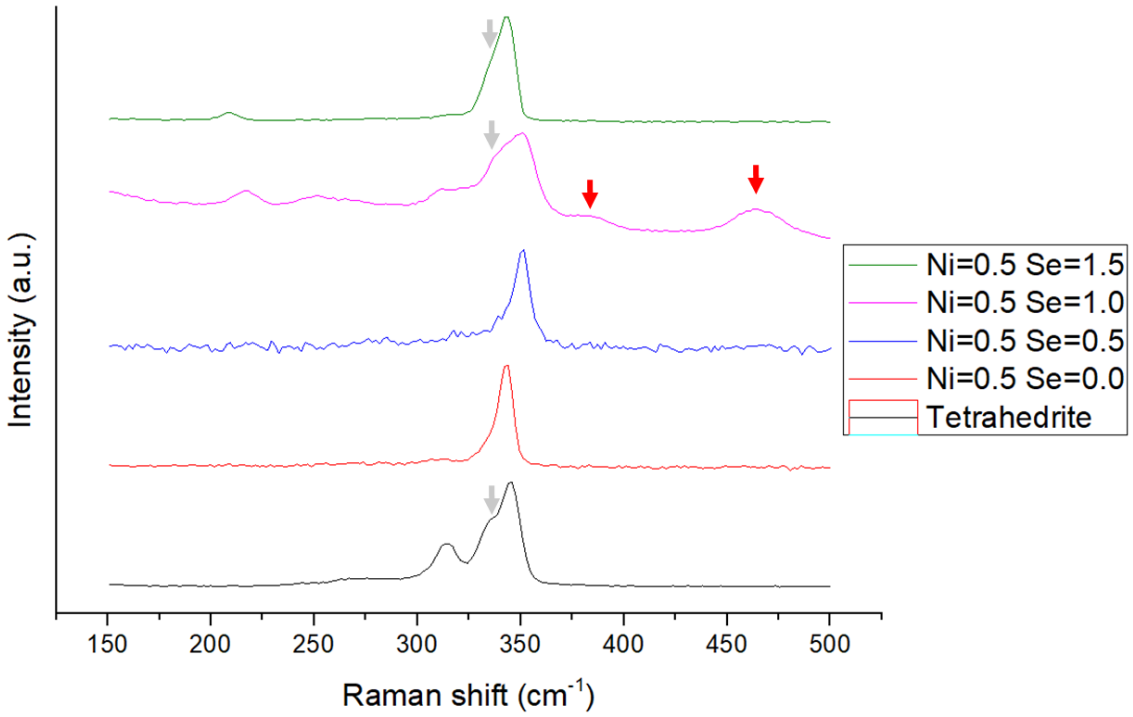

Fig. 112 Comparison of Raman spectra of the hot-pressed $Cu_{11.5}Ni_{0.5}Sb_4S_{13-x}Se_x$ samples. Identified with arrows are peaks not associated to tetrahedrite: in gray- chalcostibite ($CuSbS_2$); and in red- copper sulphide (Cu_xS_y).

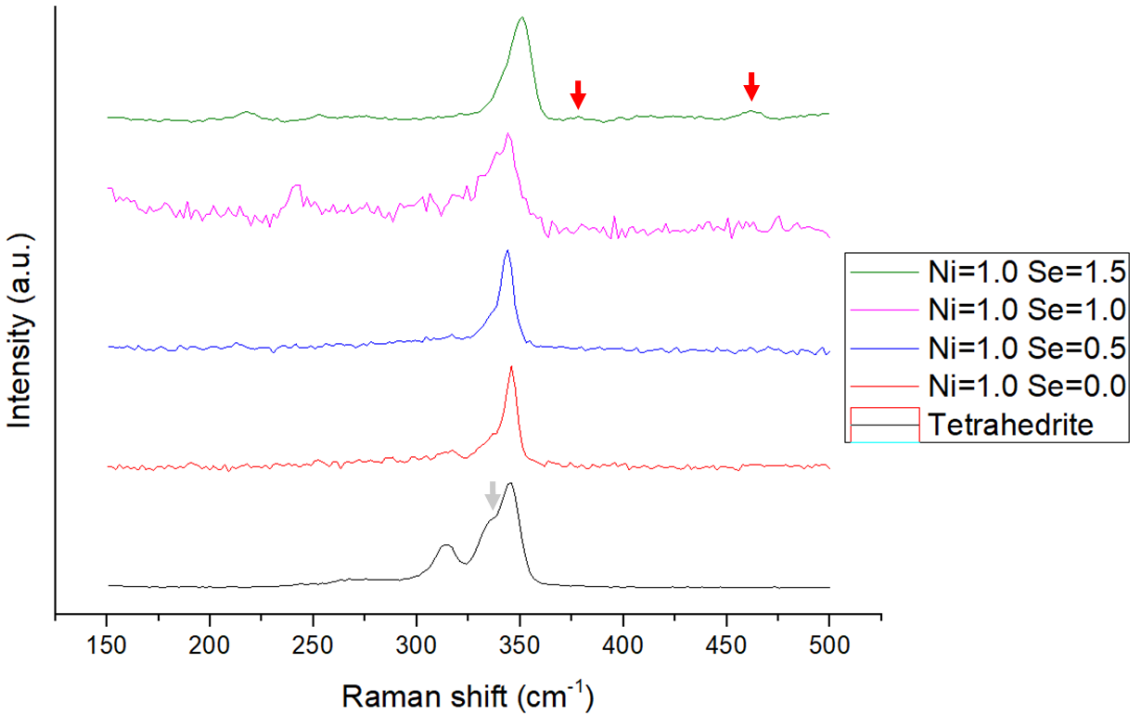

Fig. 113 Comparison of Raman spectra of the hot-pressed $Cu_{11}NiSb_4S_{13-x}Se_x$ samples. Identified with arrows are peaks not associated to tetrahedrite: in gray- chalcostibite ($CuSbS_2$); and in red- copper sulphide (Cu_xS_y).

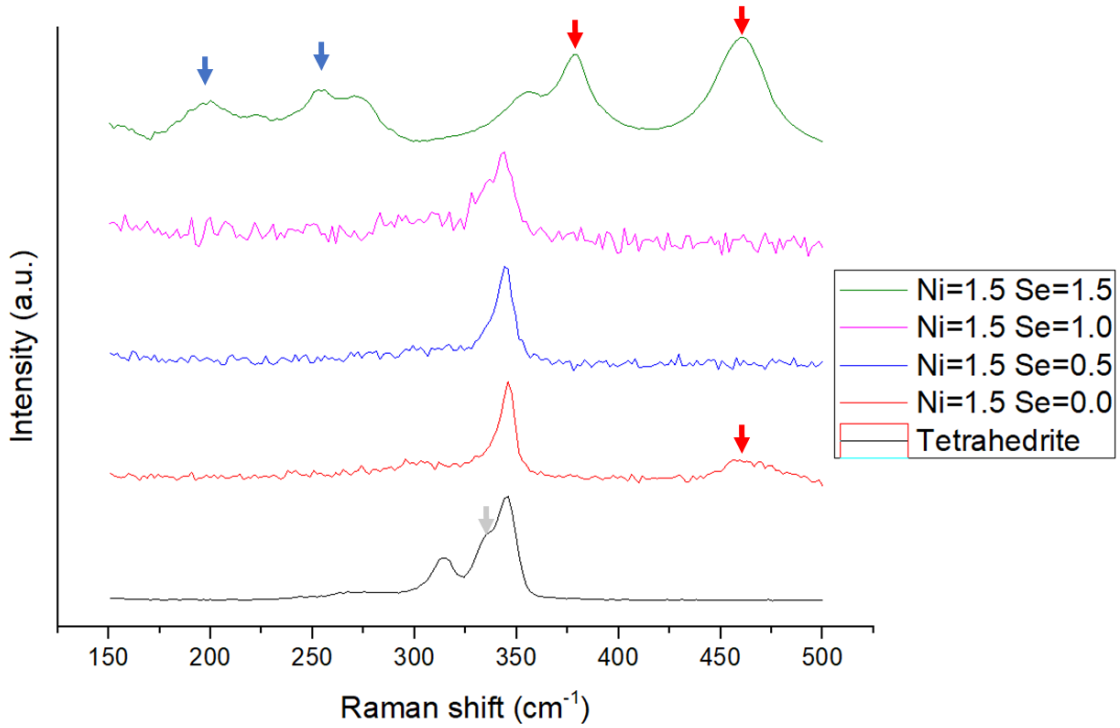

Fig. 114 Comparison of Raman spectra of the hot-pressed $Cu_{10.5}Ni_{1.5}Sb_4S_{13-x}Se_x$ samples. Identified with arrows are peaks not associated to tetrahedrite: in blue- Cu-S chemical bond signal (from ejected material); in gray- chalcostibite ($CuSbS_2$); and in red- copper sulphide (Cu_xS_y).

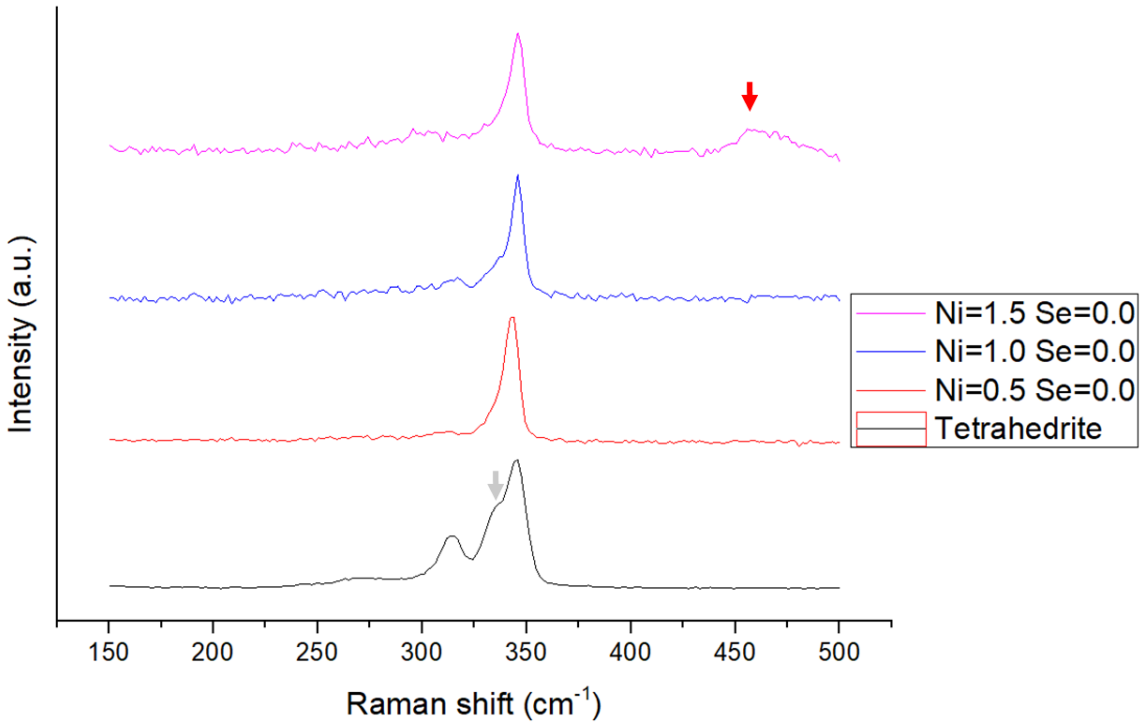

Fig. 115 Comparison of Raman spectra of the hot-pressed $Cu_{12-x}Ni_xSb_4S_{13}$ samples. Identified with arrows are peaks not associated to tetrahedrite: in gray- chalcostibite ($CuSbS_2$); and in red- copper sulphide (Cu_xS_y).

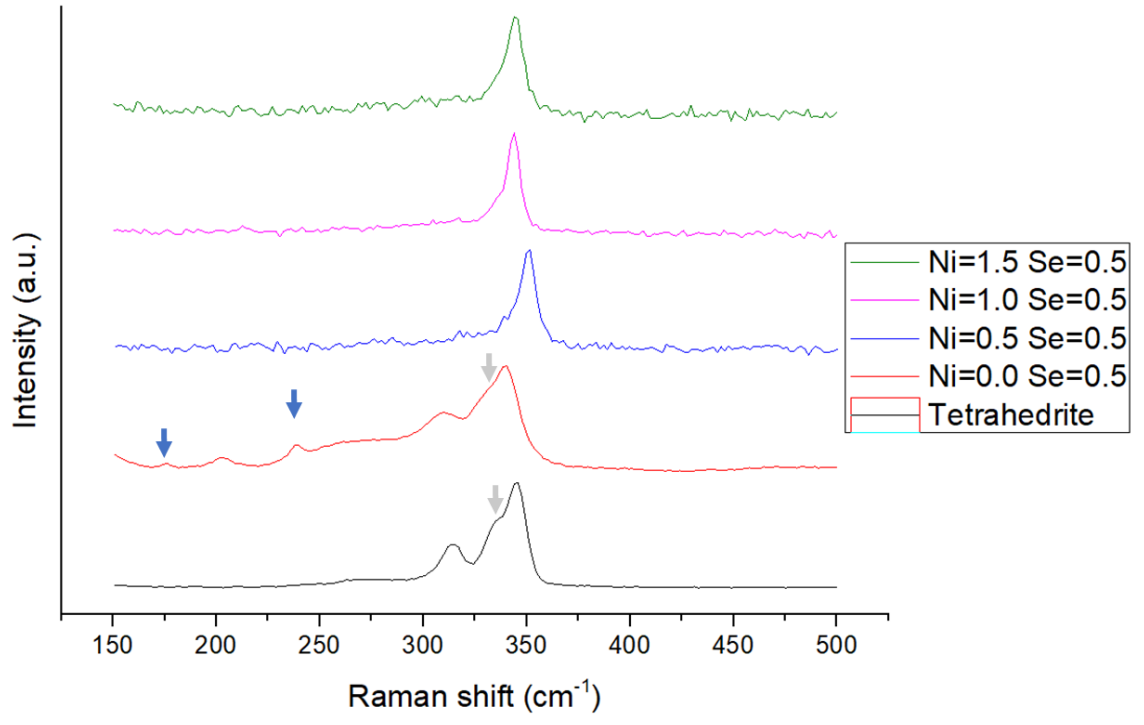

Fig. 116 Comparison of Raman spectra of the hot-pressed $Cu_{12-x}Ni_xSb_4S_{12.5}Se_{0.5}$ samples. Identified with arrows are peaks not associated to tetrahedrite: in blue- Cu-S chemical bond signal (from ejected material); and in gray- chalcostibite ($CuSbS_2$).

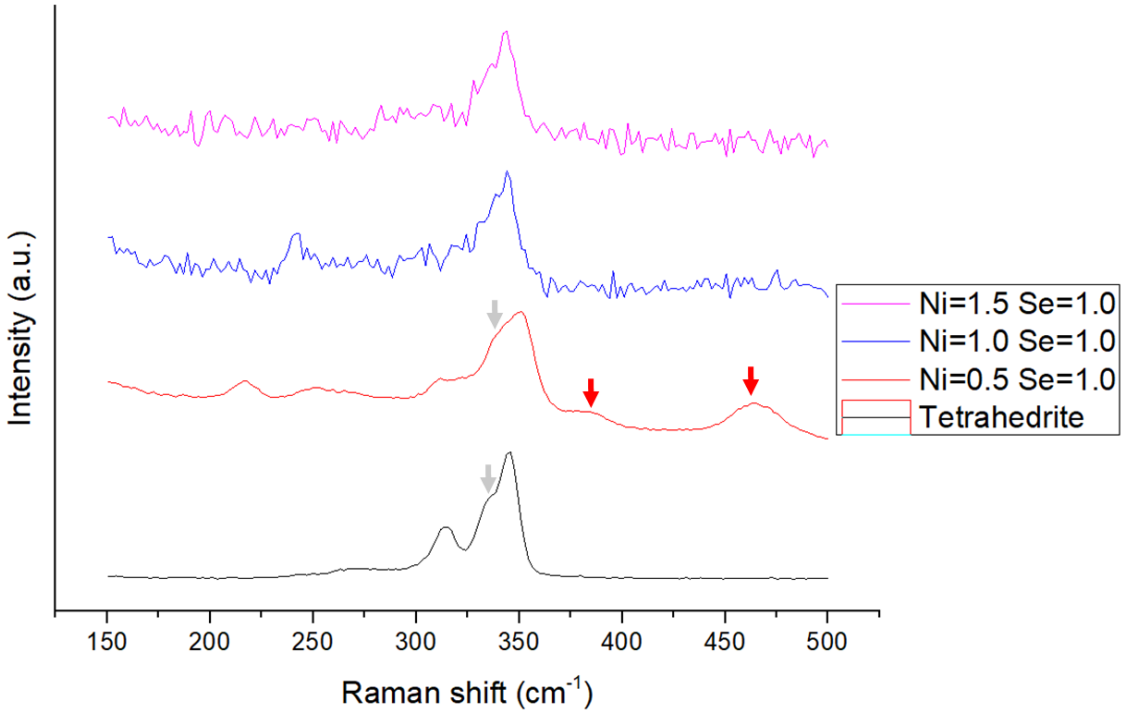

Fig. 117 Comparison of Raman spectra of the hot-pressed $Cu_{12-x}Ni_xSb_4S_{12}Se$ samples. Identified with arrows are peaks not associated to tetrahedrite: in gray- chalcostibite ($CuSbS_2$); and in red- copper sulphide (Cu_xS_y).

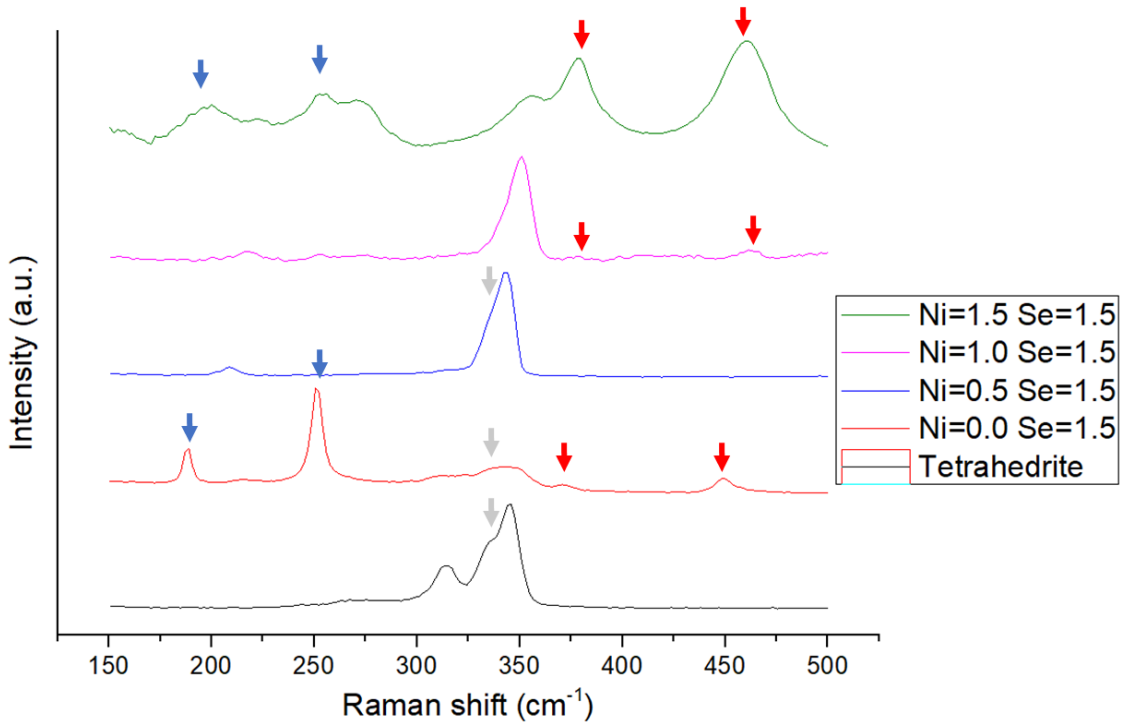

Fig. 118 Comparison of Raman spectra of the hot-pressed $Cu_{12-x}Ni_xSb_4S_{11.5}Se_{1.5}$ samples. Identified with arrows are peaks not associated to tetrahedrite: in blue- Cu-S chemical bond signal (from ejected material); in gray- chalcostibite ($CuSbS_2$); and in red- copper sulphide (Cu_xS_y).

ATTACHMENT 3: SEM-EDS ANALYSIS

As-cast samples

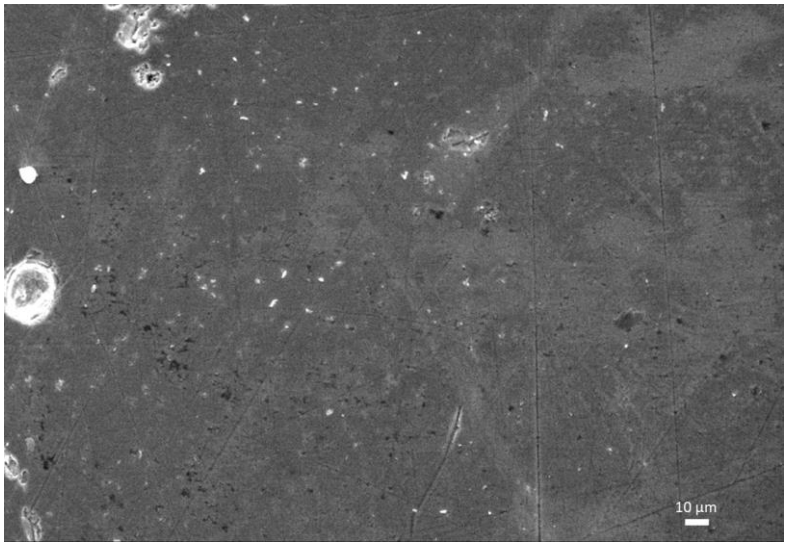

Fig. 119 Microstructures and pores observed in SEM imaging of the $Cu_{12}Sb_4S_{13}$ as-cast sample with 500x magnification. The matrix display regions of two different shades, both being a different tetrahedrite phase.

Phase	Cu(at%)	Ni(at%)	Sb(at%)	S(at%)	Se(at%)
Average Area Composition	48.1±1.6		12.9±0.5	39.0±1.7	

Table 6 Semi-quantitative analysis of the phases of $Cu_{12}Sb_4S_{13}$ as-cast sample.

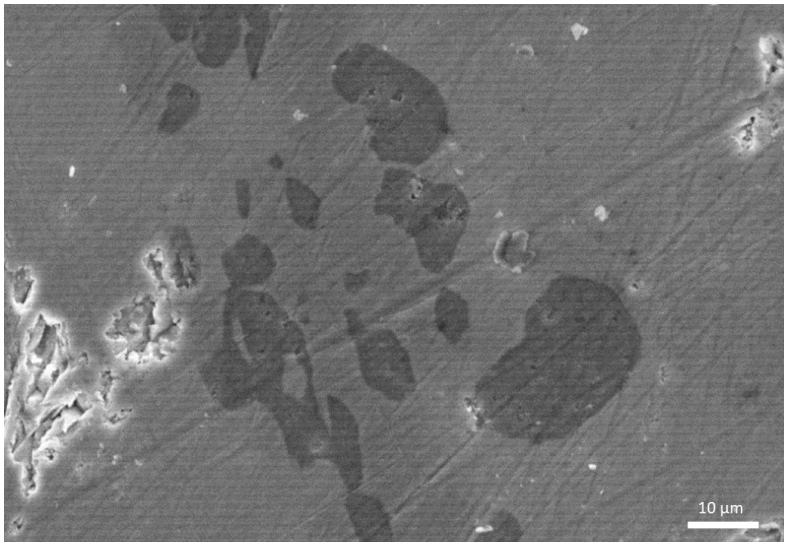

Fig. 120 Microstructures and pores observed in SEM imaging of the $Cu_{11.5}Ni_{0.5}Sb_4S_{13}$ as-cast sample with 1500x magnification. The dark phases are composed of nickel sulphides (Ni_xS_y).

Phase	Cu(at%)	Ni(at%)	Sb(at%)	S(at%)	Se(at%)
Matrix	44.4±1.2	2.1±0.1	12.1±0.3	41.3±1.3	
Dark	4.4±0.3	26.3±1.0		69.3±3.1	

Table 7 Semi-quantitative analysis of the phases of $Cu_{11.5}Ni_{0.5}Sb_4S_{13}$ as-cast sample.

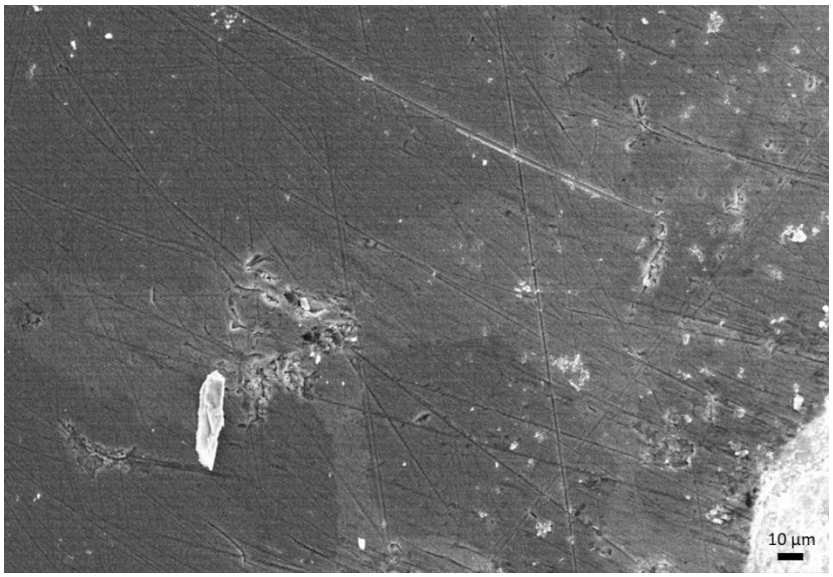

Fig. 121 Microstructures and pores observed in SEM imaging of the $Cu_{12}Sb_4S_{12.5}Se_{0.5}$ as-cast sample with 500x magnification. The darker phases are composed of copper sulphides (Cu_xS_y).

Phase	Cu(at%)	Ni(at%)	Sb(at%)	S(at%)	Se(at%)
Matrix	42.0±0.4		13.9±0.2	43.0±0.4	1.11±0.2
Dark	66.8±0.2			32.7±0.4	0.5±0.2

Table 8 Semi-quantitative analysis of the phases of $Cu_{12}Sb_4S_{12.5}Se_{0.5}$ as-cast sample.

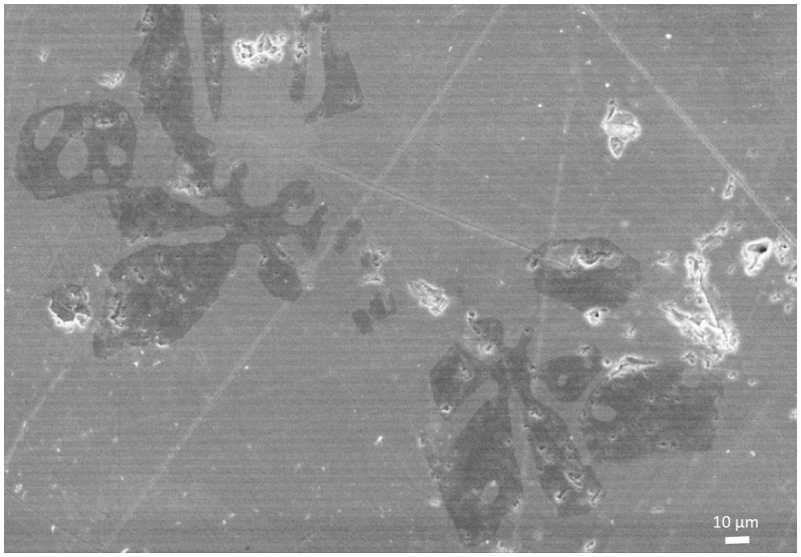

Fig. 122 Microstructures and pores observed in SEM imaging of the $Cu_{11.5}Ni_{0.5}Sb_4S_{12.5}Se_{0.5}$ as-cast sample with 500x magnification. The dark phases are composed of nickel sulphides (Ni_xS_y).

Phase	Cu(at%)	Ni(at%)	Sb(at%)	S(at%)	Se(at%)
Matrix	39.6±1.3	1.2±0.1	13.0±0.5	44.7±1.8	1.5±0.3
Dark	5.1±0.4	37.5±1.9		55.4±3.3	2.1±0.4

Table 9 Semi-quantitative analysis of the phases of $Cu_{11.5}Ni_{0.5}Sb_4S_{12.5}Se_{0.5}$ as-cast sample.

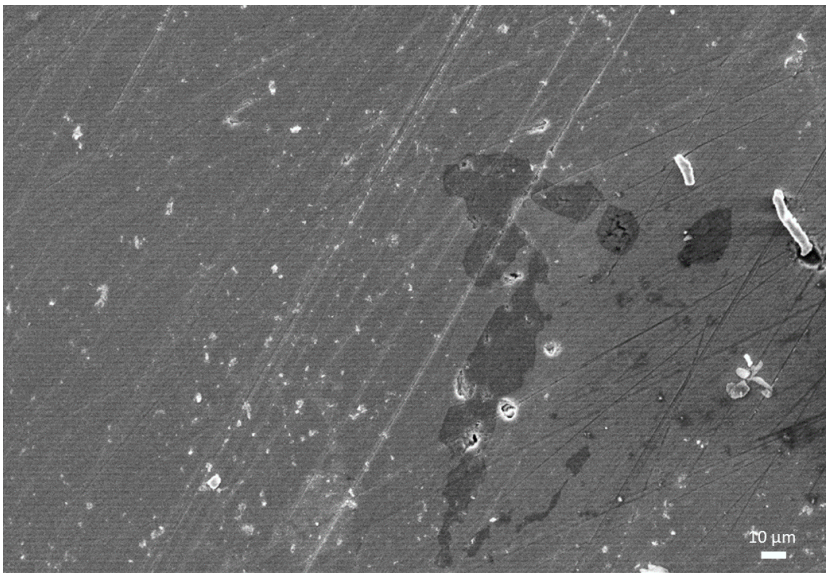

Fig. 123 Microstructures and pores observed in SEM imaging of the $Cu_{11}NiSb_4S_{13}$ as-cast sample with 500x magnification. The dark phases are composed of nickel sulphides (Ni_xS_y).

Phase	Cu(at%)	Ni(at%)	Sb(at%)	S(at%)	Se(at%)
Matrix	47.4±2.4	4.2±0.1	13.2±0.7	35.2±2.2	
Dark	2.9±0.3	34.8±1.4		62.3±3.0	

Table 10 Semi-quantitative analysis of the phases of $Cu_{11}NiSb_4S_{13}$ as-cast sample.

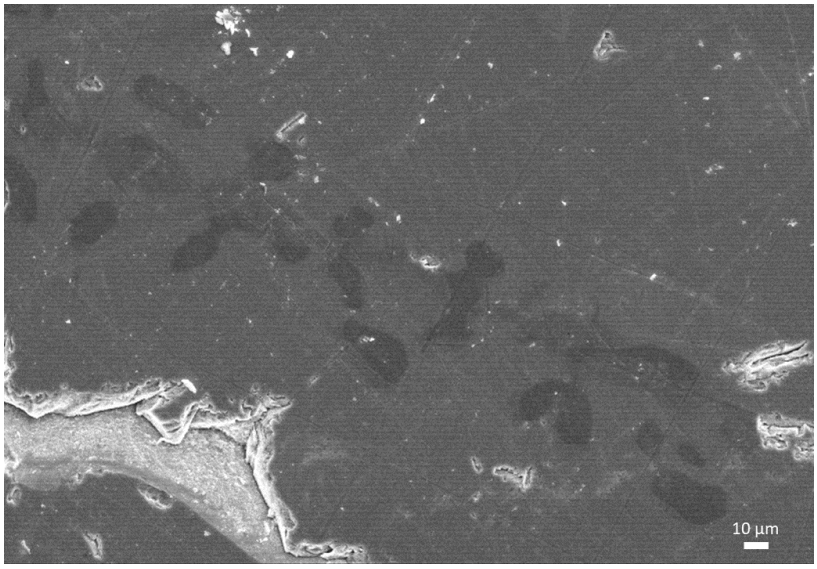

Fig. 124 Microstructures and pores observed in SEM imaging of the $Cu_{11}NiSb_4S_{12.5}Se_{0.5}$ as-cast sample with 500x magnification. The dark phases are composed of nickel sulphides (Ni_xS_y).

Phase	Cu(at%)	Ni(at%)	Sb(at%)	S(at%)	Se(at%)
Matrix	43.5±1.5	4.2±0.3	12.8±0.5	38.2±1.6	1.3±0.3
Dark	4.3±0.3	48.1±1.5		45.7±1.8	2.0±0.3

Table 11 Semi-quantitative analysis of the phases of $Cu_{11}NiSb_4S_{12.5}Se_{0.5}$ as-cast sample.

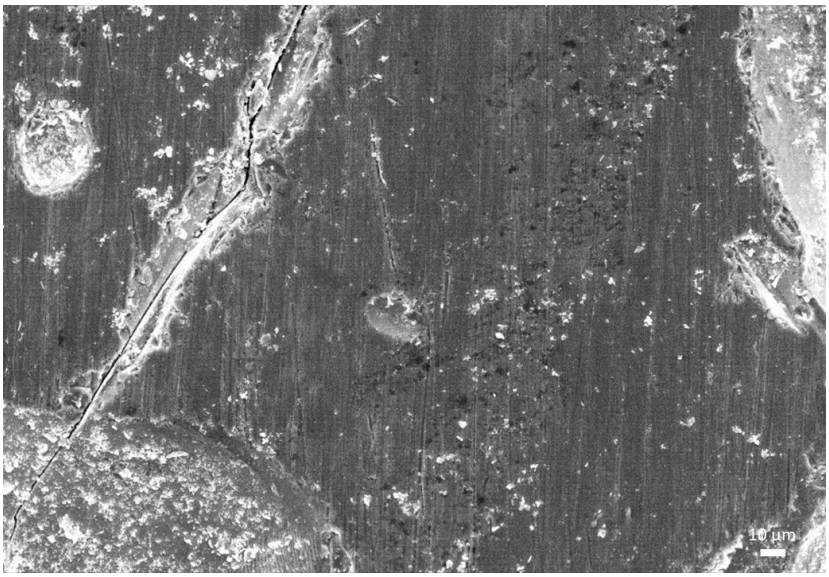

Fig. 125 Microstructures and pores observed in SEM imaging of the $Cu_{12}Sb_4S_{12}Se$ as-cast sample with 500x magnification.

Phase	Cu(at%)	Ni(at%)	Sb(at%)	S(at%)	Se(at%)
Average Area Composition	47.3±0.5		12.6±0.1	35.6±0.5	4.6±0.2

Table 12 Semi-quantitative analysis of the phases of $Cu_{12}Sb_4S_{12}Se$ as-cast sample.

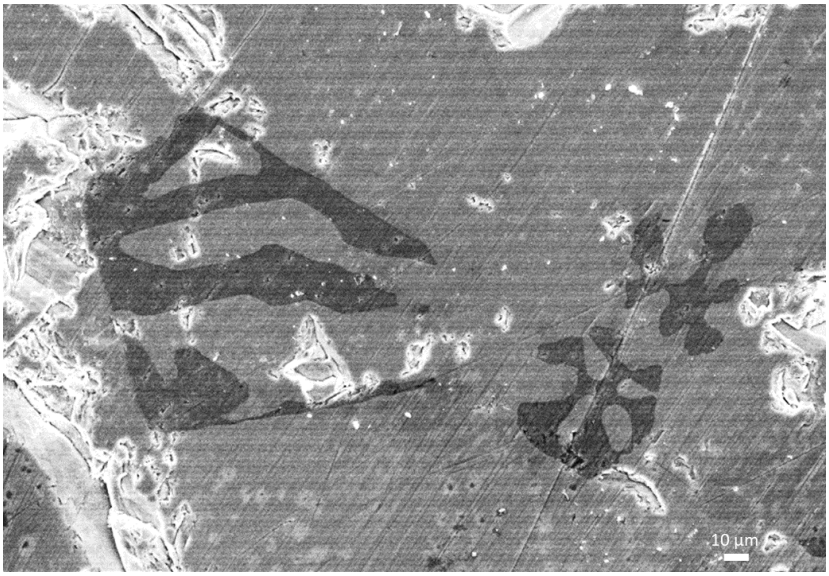

Fig. 126 Microstructures and pores observed in SEM imaging of the $Cu_{11.5}Ni_{0.5}Sb_4S_{12}Se$ as-cast sample with 500x magnification. The dark phases are composed of nickel sulphides (Ni_xS_y). The lighter-shade phase is another tetrahedrite phase richer in sulphur than the matrix-tetrahedrite.

Phase	Cu(at%)	Ni(at%)	Sb(at%)	S(at%)	Se(at%)
Matrix	47.0±1.9	1.9±0.2	13.2±0.6	34.8±1.7	3.2±0.5
Dark	4.5±0.4	33.9±1.6		58.8±3.2	2.9±0.5
Light	45.7±1.8	1.5±0.1	12.9±0.4	36.6±1.3	3.3±0.3

Table 13 Semi-quantitative analysis of the phases of $Cu_{12}Sb_4S_{12}Se$ as-cast sample.

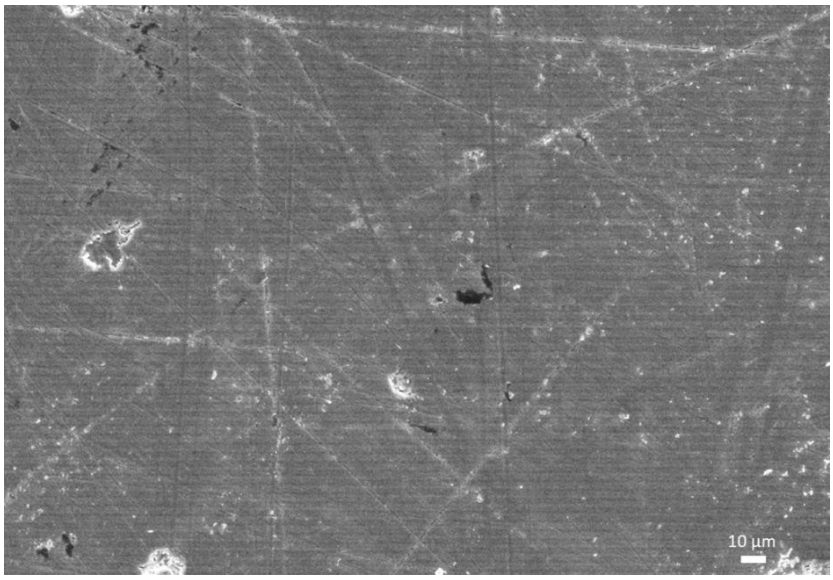

Fig. 127 Microstructures and pores observed in SEM imaging of the $Cu_{11}NiSb_4S_{12}Se$ as-cast sample with 500x magnification. The dark phases are composed of nickel sulphides (Ni_xS_y).

Phase	Cu(at%)	Ni(at%)	Sb(at%)	S(at%)	Se(at%)
Matrix	46.8±1.5	1.6±0.2	14.0±0.5	35.4±1.4	2.3±0.3
Dark	2.5±0.2	44.6±1.3		50.9±1.9	2.0±0.3

Table 14 Semi-quantitative analysis of the phases of $Cu_{12}Sb_4S_{12}Se$ as-cast sample.

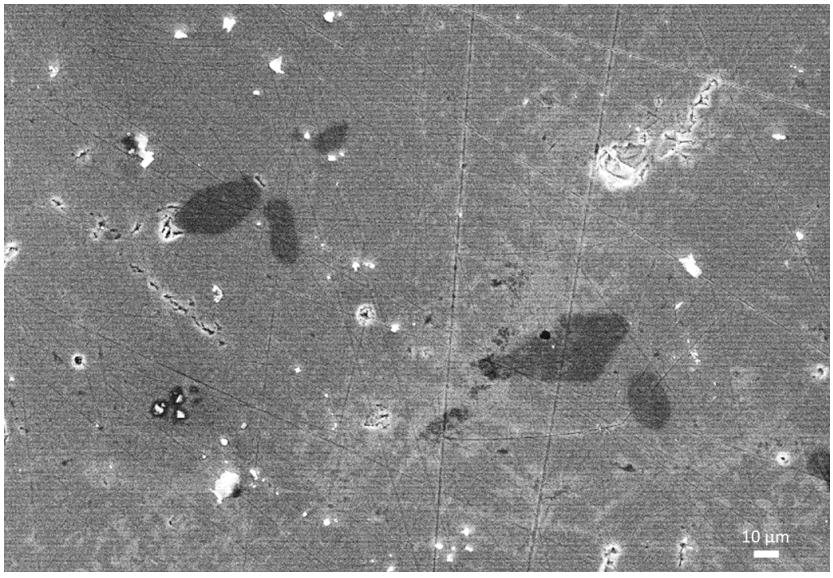

Fig. 128 Microstructures and pores observed in SEM imaging of the $Cu_{10.5}Ni_{1.5}Sb_4S_{13}$ as-cast sample with 500x magnification. The dark phases are composed of nickel sulphides (Ni_xS_y). The lighter shaded phase is another tetrahedrite phase

Phase	Cu(at%)	Ni(at%)	Sb(at%)	S(at%)	Se(at%)
Matrix	44.6±1.6	5.4±0.3	12.5±0.5	37.5±1.6	
Dark	5.1±0.4	52.3±1.9		42.6±1.9	
Light	45.1±1.4	5.3±0.2	12.5±0.3	37.2±1.2	

Table 15 Semi-quantitative analysis of the phases of $Cu_{10.5}Ni_{1.5}Sb_4S_{13}$ as-cast sample.

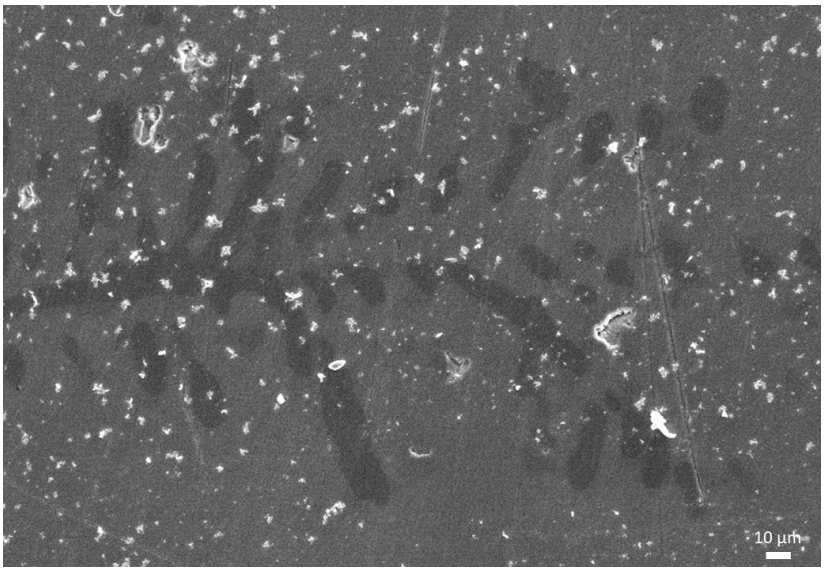

Fig. 129 Microstructures and pores observed in SEM imaging of the $Cu_{10.5}Ni_{1.5}Sb_4S_{12.5}Se_{0.5}$ as-cast sample with 500x magnification. The dark phases are composed of nickel sulphides (Ni_xS_y).

Phase	Cu(at%)	Ni(at%)	Sb(at%)	S(at%)	Se(at%)
Matrix	44.1±1.4	4.8±0.3	12.8±0.4	38.3±1.5	
Dark	4.4±0.3	48.5±1.5		45.0±1.8	2.1±0.3

Table 16 Semi-quantitative analysis of the phases of $Cu_{10.5}Ni_{1.5}Sb_4S_{12.5}Se_{0.5}$ as-cast sample.

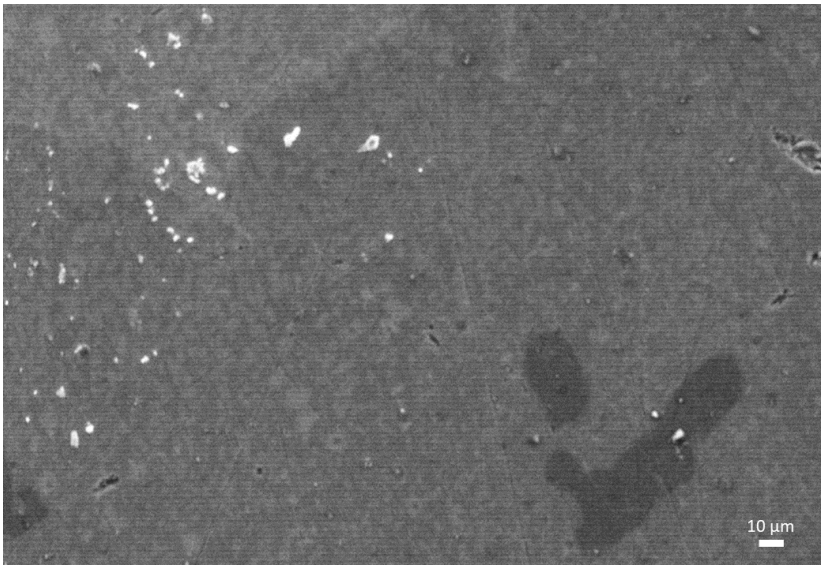

Fig. 130 Microstructures and pores observed in SEM imaging of the $Cu_{10.5}Ni_{1.5}Sb_4S_{12}Se$ as-cast sample with 500x magnification. The dark phases are composed of nickel sulphides (Ni_xS_y). The lighter shaded phase is another tetrahedrite phase.

Phase	Cu(at%)	Ni(at%)	Sb(at%)	S(at%)	Se(at%)
Matrix	44.2±1.7	4.5±0.3	12.4±0.5	33.9±1.6	5.0±0.6
Dark	4.5±0.4	49.8±2.0		42.0±2.1	3.8±0.6
Light	44.6±2.0	4.6±0.3	12.6±0.5	33.0±1.4	5.3±0.6

Table 17 Semi-quantitative analysis of the phases of $Cu_{10.5}Ni_{1.5}Sb_4S_{12}Se$ as-cast sample.

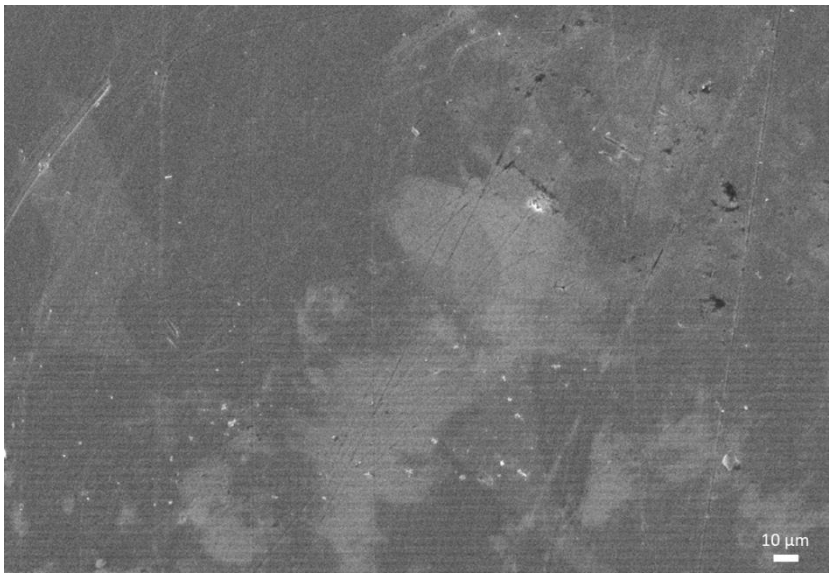

Fig. 131 Microstructures and pores observed in SEM imaging of the $Cu_{12}Sb_4S_{11.5}Se_{1.5}$ as-cast sample with 500x magnification. The lighter phases are composed of chalcostibite. ($CuSbS_2$)

Phase	Cu(at%)	Ni(at%)	Sb(at%)	S(at%)	Se(at%)
Matrix	44.2±1.7		13.3±0.5	35.8±1.7	6.8±0.6
Light	30.3±1.3		21.8±0.8	30.5±1.5	17.4±1.3

Table 18 Semi-quantitative e analysis of the phases of $Cu_{12}Sb_4S_{11.5}Se_{1.5}$ as-cast sample.

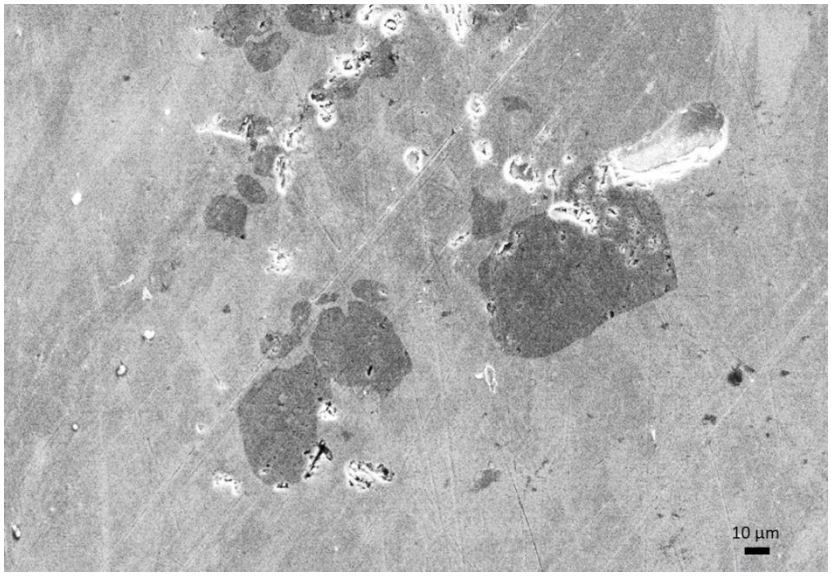

Fig. 132 Microstructures and pores observed in SEM imaging of the $Cu_{11.5}Ni_{0.5}Sb_4S_{11.5}Se_{1.5}$ as-cast sample with 500x magnification. The dark phases are composed of nickel sulphides (Ni_xS_y). The lighter shaded phase is another tetrahedrite phase.

Phase	Cu(at%)	Ni(at%)	Sb(at%)	S(at%)	Se(at%)
Average Area Composition	42.0±1.3	1.20±0.1	12.1±0.1	38.3±0.4	6.4±0.1
Dark	4.7±0.3	25.9±0.9		64.6±2.5	4.8±0.4

Table 19 Semi-quantitative analysis of the phases of $Cu_{11.5}Ni_{0.5}Sb_4S_{11.5}Se_{1.5}$ as-cast sample.

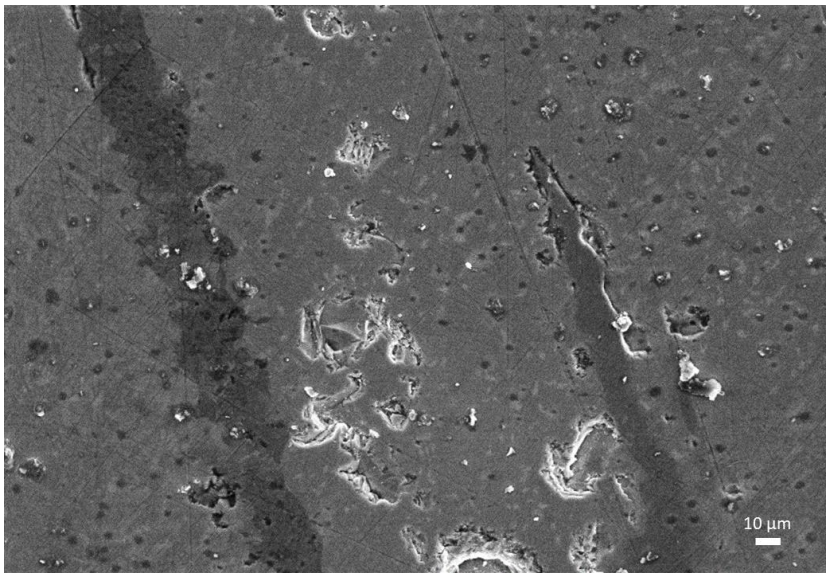

Fig. 133 Microstructures and pores observed in SEM imaging of the $Cu_{11}NiSb_4S_{11.5}Se_{1.5}$ as-cast sample with 500x magnification. The dark phases are composed of nickel sulphides (Ni_xS_y). The lighter shaded phase is another tetrahedrite phase.

Phase	Cu(at%)	Ni(at%)	Sb(at%)	S(at%)	Se(at%)
Matrix	41.2±1.4	3.3±0.2	11.9±0.4	40.0±1.6	3.7±0.4
Dark	4.4±0.3	47.2±1.6		44.1±1.9	4.2±0.4
Light	39.9±1.7	3.9±0.3	13.0±0.5	37.8±1.6	5.4±0.6

Table 20 Semi-quantitative analysis of the phases of $Cu_{10.5}Ni_{1.5}Sb_4S_{12}Se$ as-cast sample.

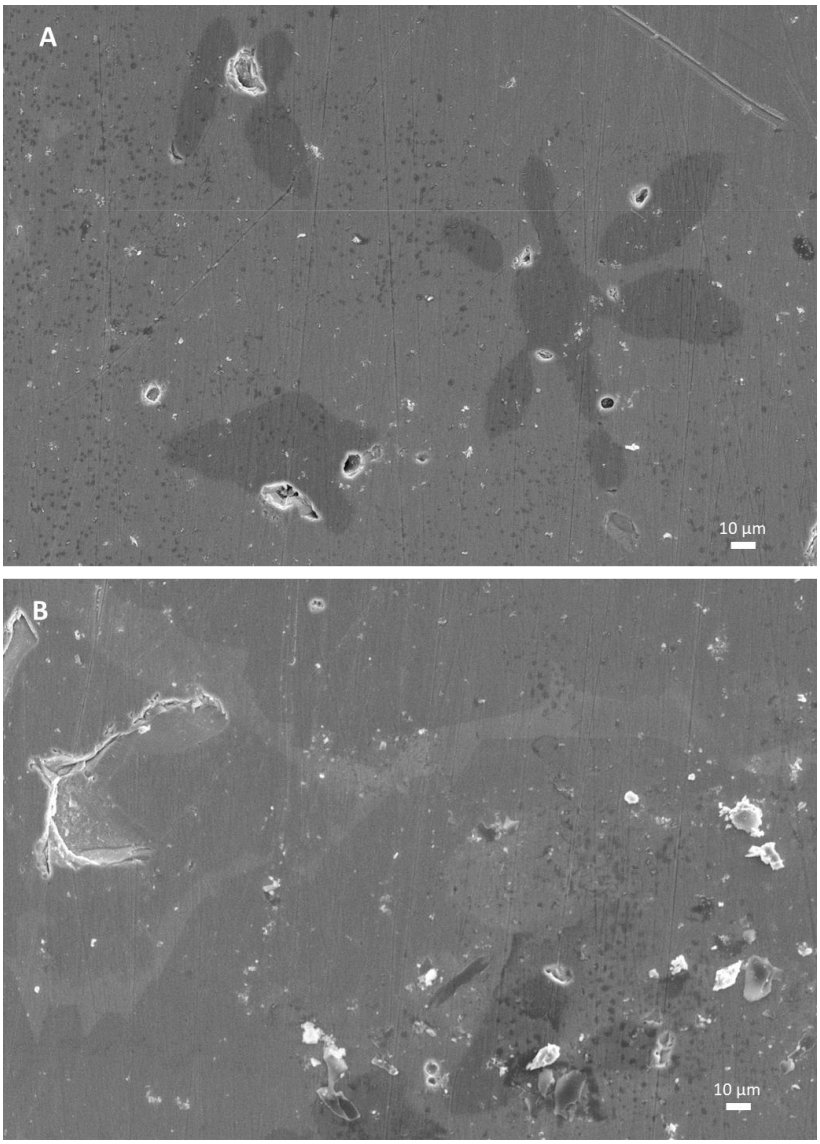

Fig. 134 Microstructures and pores observed in SEM imaging of the $Cu_{10.5}Ni_{1.5}Sb_4S_{11.5}Se_{1.5}$ as-cast sample with 500x magnification. The dark phases (A) are composed of nickel sulphides and lighter phases (B) are composed of chalcostibite ($CuSbS_2$).

Phase	Cu(at%)	Ni(at%)	Sb(at%)	S(at%)	Se(at%)
Matrix	44.2±1.9	5.6±0.4	14.2±0.6	29.2±1.5	6.9±0.7
Dark	3.4±0.3	51.5±2.0		39.2±2.0	5.9±0.5
Light	22.0±1.3		26.3±0.9	28.5±1.2	23.3±1.4

Table 21 Semi-quantitative analysis of the phases of $Cu_{10.5}Ni_{1.5}Sb_4S_{11.5}Se_{1.5}$ as-cast sample.

Expected formula of the sample	Cu(at%)	Ni(at%)	Sb(at%)	S(at%)	Se(at%)	Matrix chemical formula
$Cu_{12}Sb_4S_{13}$	48.1±1.6		12.9±0.5	39.0±1.7		$Cu_{13.9\pm0.5}Sb_{3.8\pm0.1}S_{11.3\pm0.5}$
$Cu_{11.5}Ni_{0.5}Sb_4S_{12}$	44.4±1.2	2.1±0.1	12.1±0.3	41.3±1.3		$Cu_{12.9\pm0.3}Ni_{0.6\pm0.1}Sb_{3.5\pm0.1}S_{12.0\pm0.4}$
$Cu_{12}Sb_4S_{12.5}Se_{0.5}$	42.0±0.4		13.9±0.2	43.0±0.4	1.1±0.2	$Cu_{12.2\pm0.1}Sb_{4.0\pm0.1}S_{12.5\pm0.1}Se_{0.3\pm0.1}$
$Cu_{11.5}Ni_{0.5}Sb_4S_{12.5}Se_{0.5}$	39.6±1.3	1.2±0.1	13.0±0.5	44.7±1.8	1.5±0.3	$Cu_{11.5\pm0.4}Ni_{0.4\pm0.1}Sb_{3.8\pm0.1}S_{13.0\pm0.5}Se_{0.4\pm0.1}$
$Cu_{11}NiSb_4S_{13}$	47.4±2.4	4.2±0.4	13.2±0.7	35.2±2.2		$Cu_{13.7\pm0.7}Ni_{1.2\pm0.1}Sb_{3.8\pm0.2}S_{10.2\pm0.6}$
$Cu_{11}NiSb_4S_{12.5}Se_{0.5}$	43.5±1.5	4.2±0.3	12.8±0.5	38.2±1.6	1.3±0.3	$Cu_{12.6\pm0.4}Ni_{1.2\pm0.1}Sb_{3.7\pm0.1}S_{11.1\pm0.5}Se_{0.4\pm0.1}$
$Cu_{12}Sb_4S_{12}Se$	47.3±1.8		12.6±0.5	35.6±1.7	4.6±0.5	$Cu_{13.7\pm0.5}Sb_{4.0\pm0.1}S_{10.3\pm0.5}Se_{1.3\pm0.2}$
$Cu_{11.5}Ni_{0.5}Sb_4S_{12}Se$	47.0±1.9	1.9±0.2	13.2±0.6	34.8±1.7	3.2±0.5	$Cu_{13.6\pm0.5}Ni_{0.5\pm0.1}Sb_{3.8\pm0.2}S_{10.1\pm0.5}Se_{0.9\pm0.1}$
$Cu_{12}NiSb_4S_{12}Se$	46.8±1.5	1.6±0.2	14.0±0.5	35.4±1.4	2.3±0.3	$Cu_{13.6\pm0.4}Ni_{0.5\pm0.1}Sb_{4.1\pm0.1}S_{10.3\pm0.4}Se_{0.7\pm0.1}$
$Cu_{10.5}Ni_{1.5}Sb_4S_{13}$	44.6±1.6	5.4±0.3	12.5±0.5	37.5±1.6		$Cu_{12.9\pm0.5}Ni_{1.6\pm0.1}Sb_{3.6\pm0.1}S_{10.9\pm0.5}$
$Cu_{10.5}Ni_{1.5}Sb_4S_{12.5}Se_{0.5}$	44.1±1.4	4.8±0.3	12.8±0.4	38.3±1.5		$Cu_{12.8\pm0.4}Ni_{1.4\pm0.1}Sb_{3.7\pm0.1}S_{11.1\pm0.4}$
$Cu_{10.5}Ni_{1.5}Sb_4S_{12}Se$	44.2±1.7	4.5±0.3	12.4±0.5	33.9±1.6	5.0±0.6	$Cu_{12.8\pm0.5}Ni_{1.3\pm0.1}Sb_{3.6\pm0.1}S_{9.8\pm0.5}Se_{1.5\pm0.2}$
$Cu_{12}Sb_4S_{11.5}Se_{1.5}$	44.2±1.7		13.3±0.5	35.8±1.7	6.8±0.6	$Cu_{12.8\pm0.5}Sb_{3.9\pm0.2}S_{10.4\pm0.5}Se_{2.0\pm0.2}$
$Cu_{11.5}Ni_{0.5}Sb_4S_{11.5}Se_{1.5}$	42.0±1.3	1.2±0.1	12.1±0.4	38.3±1.5	6.4±0.5	$Cu_{12.2\pm0.4}Ni_{0.4\pm0.1}Sb_{3.5\pm0.1}S_{11.1\pm0.4}Se_{1.9\pm0.1}$
$Cu_{11}NiSb_4S_{11.5}Se_{1.5}$	41.2±1.4	3.3±0.2	11.9±0.4	40.0±1.6	3.7±0.4	$Cu_{11.9\pm0.4}Ni_{0.9\pm0.1}Sb_{3.5\pm0.1}S_{11.6\pm0.5}Se_{1.1\pm0.1}$
$Cu_{10.5}Ni_{1.5}Sb_4S_{11.5}Se_{1.5}$	44.2±1.9	5.6±0.4	14.2±0.6	29.2±1.5	6.9±0.7	$Cu_{12.8\pm0.5}Ni_{1.6\pm0.1}Sb_{4.1\pm0.2}S_{8.5\pm0.5}Se_{2.0\pm0.2}$

Table 22 SEM-EDS semi-quantitative analysis of the matrix of as-cast samples. The matrix chemical formula was calculated based on the composition and assuming a 29 atoms molecule like tetrahedrite.

Annealed samples

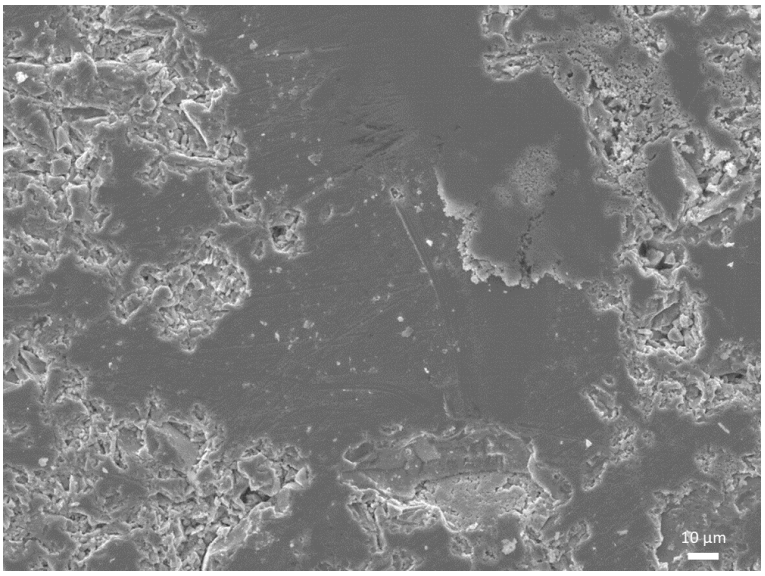

Fig. 135 SEM imaging of the $Cu_{12}Sb_4S_{13}$ annealed sample with 500x magnification. The matrix is composed of tetrahedrite phase.

Phase	Cu(at%)	Ni(at%)	Sb(at%)	S(at%)	Se(at%)
Matrix	42.0±0.5		14.4±0.2	43.6±0.6	

Table 23 Semi-quantitative analysis of the phases of $Cu_{12}Sb_4S_{13}$ annealed sample.

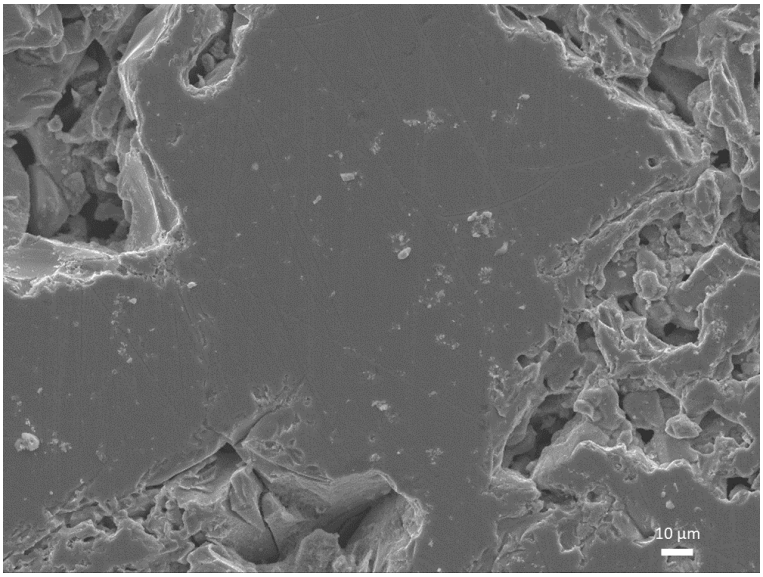

Fig. 136 Microstructures and pores observed in SEM imaging of the $Cu_{11.5}Ni_{0.5}Sb_4S_{13}$ annealed sample with 500x magnification.

Phase	Cu(at%)	Ni(at%)	Sb(at%)	S(at%)	Se(at%)
Matrix	40.1±0.5	1.9±0.3	14.2±0.3	43.9±0.7	

Table 24 Semi-quantitative analysis of the phases of $Cu_{11.5}Ni_{0.5}Sb_4S_{13}$ annealed sample.

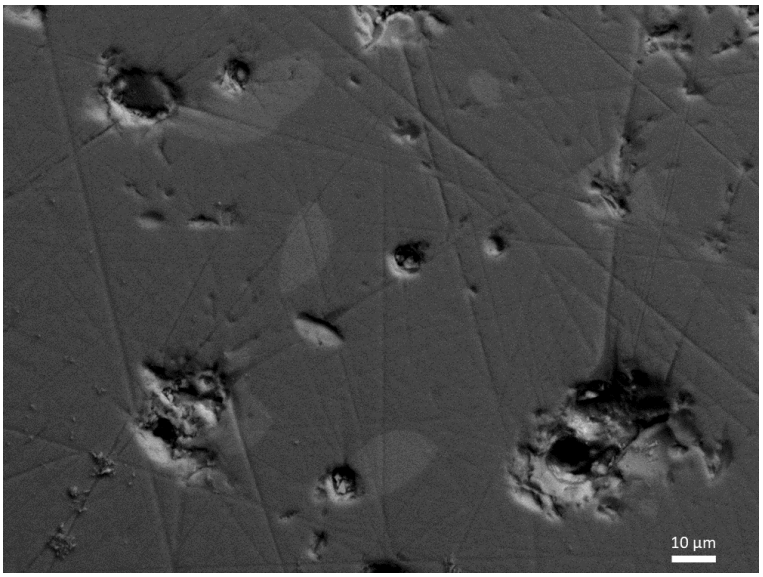

Fig. 137 Microstructures and pores observed in SEM imaging of the $Cu_{12}Sb_4S_{12.5}Se_{0.5}$ annealed sample with 700x magnification. The light phases are composed of chalcostibite ($CuSbS_2$).

Phase	Cu(at%)	Ni(at%)	Sb(at%)	S(at%)	Se(at%)
Matrix	40.6±0.3		14.1±0.2	44.1±0.5	1.2±0.2
Light	25.3±0.4		25.0±0.2	47.9±0.6	1.8±0.3

Table 25 Semi-quantitative analysis of the phases of $Cu_{12}Sb_4S_{12.5}Se_{0.5}$ annealed sample.

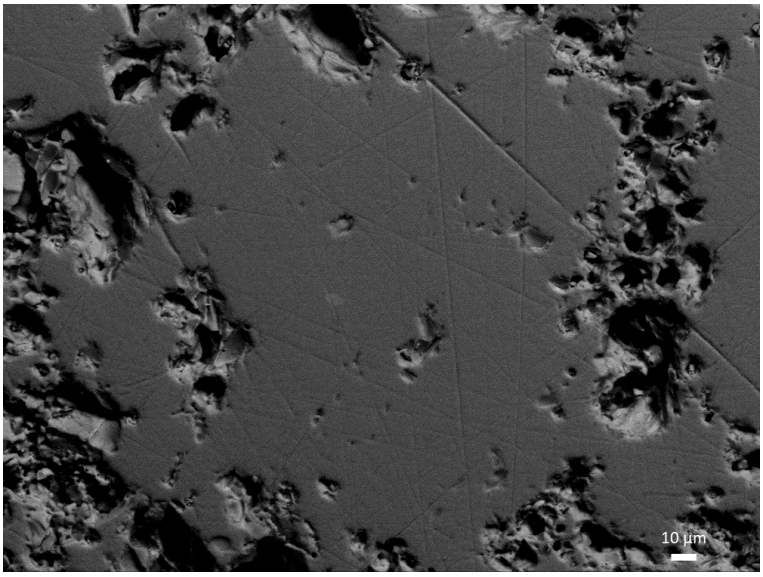

Fig. 138 Microstructures and pores observed in SEM imaging of the $Cu_{11.5}Ni_{0.5}Sb_4S_{12.5}Se_{0.5}$ annealed sample with 400x magnification. The light phases are composed of chalcostibite ($CuSbS_2$).

Phase	Cu(at%)	Ni(at%)	Sb(at%)	S(at%)	Se(at%)
Matrix	40.2±0.4	1.4±0.1	13.9±0.2	43.2±0.5	1.3±0.2
Light	26.2±0.4	0	24.6±0.2	44.1±0.6	5.0±0.3

Table 26 Semi-quantitative analysis of the phases of $Cu_{11.5}Ni_{0.5}Sb_4S_{12.5}Se_{0.5}$ annealed sample.

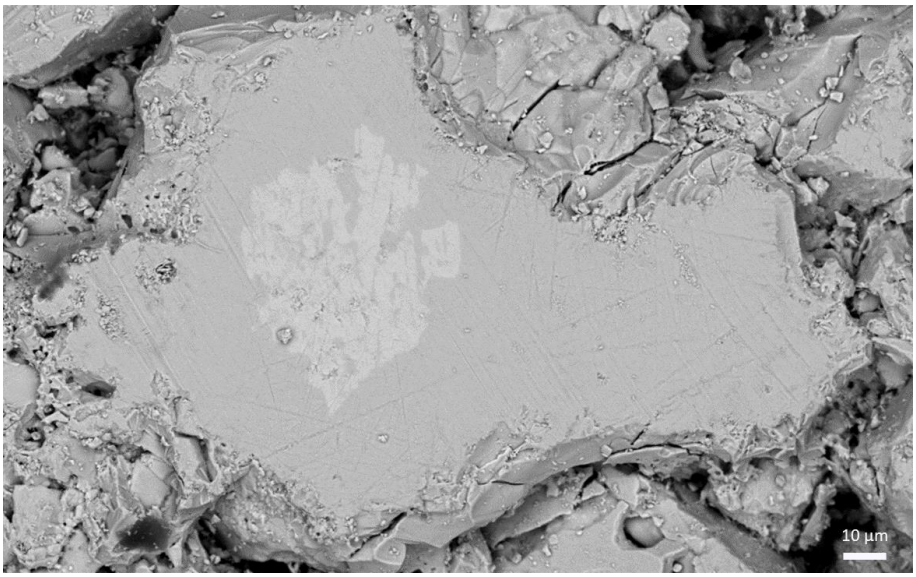

Fig. 139 Microstructures and pores observed in SEM imaging of the $Cu_{11}NiSb_4S_{13}$ annealed sample with 2450x magnification. The light phases are composed of chalcostibite ($CuSbS_2$).

Phase	Cu(at%)	Ni(at%)	Sb(at%)	S(at%)	Se(at%)
Matrix	39.0±0.4	2.6±0.2	13.8±0.2	44.7±0.6	
Light	25.7±0.4		24.9±0.2	49.4±0.6	

Table 27 Semi-quantitative analysis of the phases of $Cu_{11}NiSb_4S_{13}$ annealed sample.

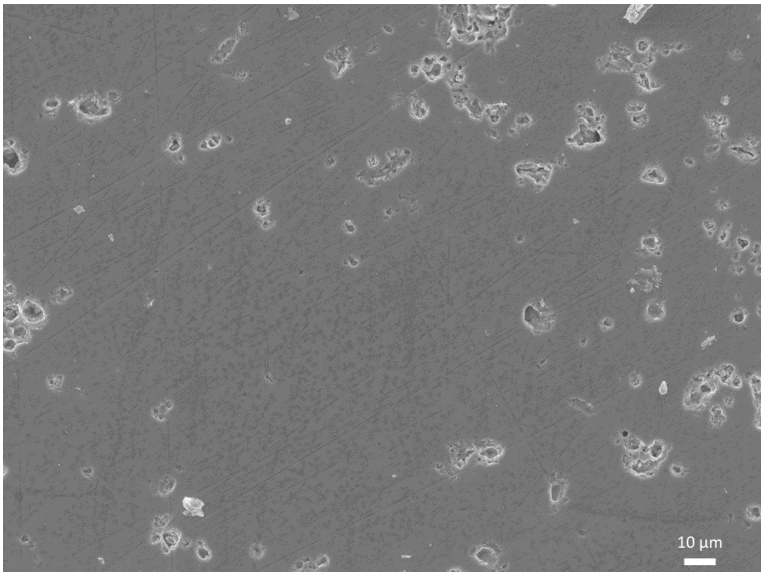

Fig. 140 Microstructures and pores observed in SEM imaging of the $Cu_{11}NiSb_4S_{12.5}Se_{0.5}$ annealed sample with 500x magnification.

Phase	Cu(at%)	Ni(at%)	Sb(at%)	S(at%)	Se(at%)
Matrix	38.4±0.5	3.8±0.3	14.4±0.2	41.9±0.6	1.6±0.2

Table 28 Semi-quantitative analysis of the phases of $Cu_{11}NiSb_4S_{12.5}Se_{0.5}$ annealed sample.

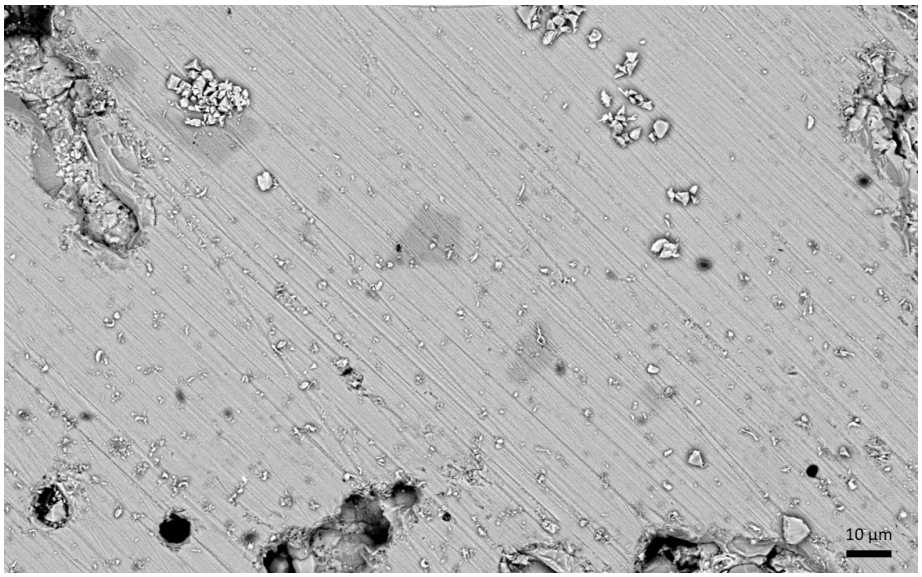

Fig. 141 Microstructures and pores observed in SEM imaging of the $Cu_{12}Sb_4S_{12}Se$ annealed sample with 2550x magnification. The dark phases are composed of copper sulphides (Cu_xS_y).

Phase	Cu(at%)	Ni(at%)	Sb(at%)	S(at%)	Se(at%)
Matrix	38.9±0.5		12.7±0.3	44.7±0.7	3.7±0.3
Dark	65.0±0.4			31.9±0.64	3.1±0.3

Table 29 Semi-quantitative analysis of the phases of $Cu_{12}Sb_4S_{12}Se$ annealed sample.

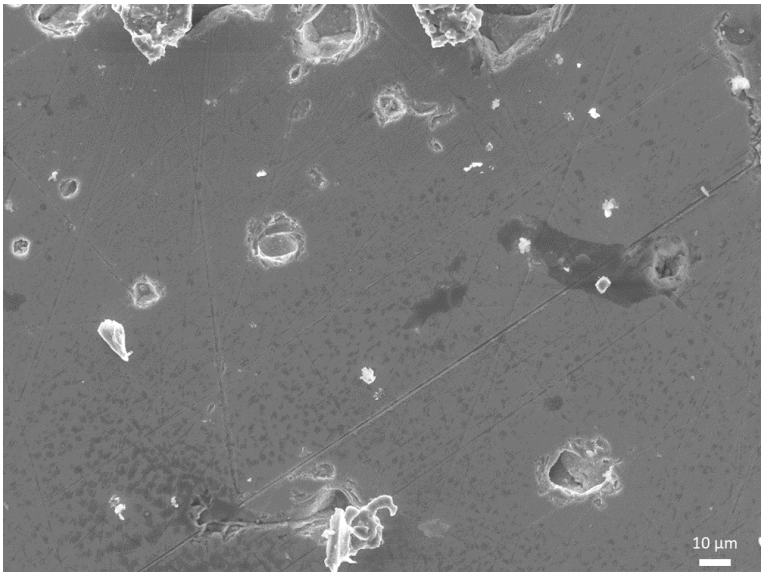

Fig. 142 Microstructures and pores observed in SEM imaging of the $Cu_{11.5}Ni_{0.5}Sb_4S_{12}Se$ annealed sample with 500x magnification. The dark regions are low depth pores.

Phase	Cu(at%)	Ni(at%)	Sb(at%)	S(at%)	Se(at%)
Matrix	39.4±0.4	2.1±0.2	13.7±0.2	42.0±0.5	2.8±0.2

Table 30 Semi-quantitative analysis of the phases of $Cu_{12}Sb_4S_{12}Se$ annealed sample.

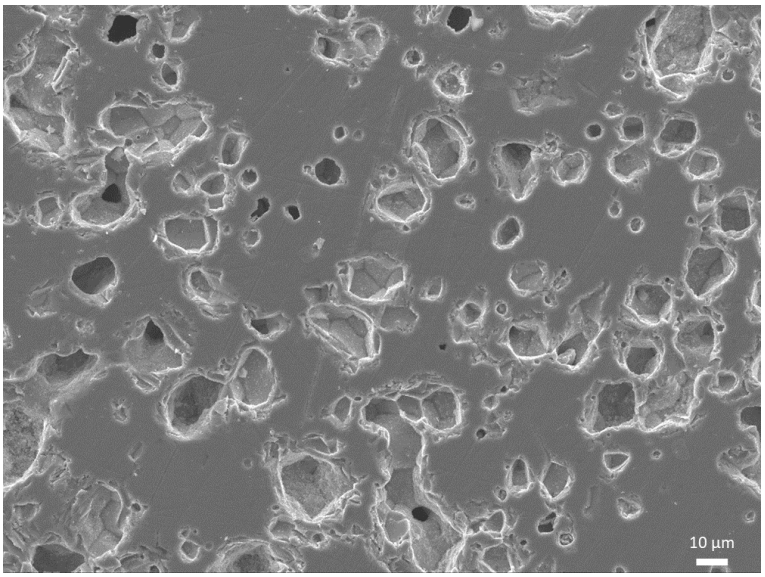

Fig. 143 Microstructures and pores observed in SEM imaging of the $Cu_{11}NiSb_4S_{12}Se$ annealed sample with 500x magnification. The light phases are composed of ullmannite (NiSbS).

Phase	Cu(at%)	Ni(at%)	Sb(at%)	S(at%)	Se(at%)
Matrix	37.3±0.5	4.7±0.3	13.9±0.2	41.6±0.6	2.5±0.2
Light	4.7±0.4	30.2±0.6	31.8±0.3	29.9±0.6	3.4±0.3

Table 31 Semi-quantitative analysis of the phases of $Cu_{12}Sb_4S_{12}Se$ annealed sample.

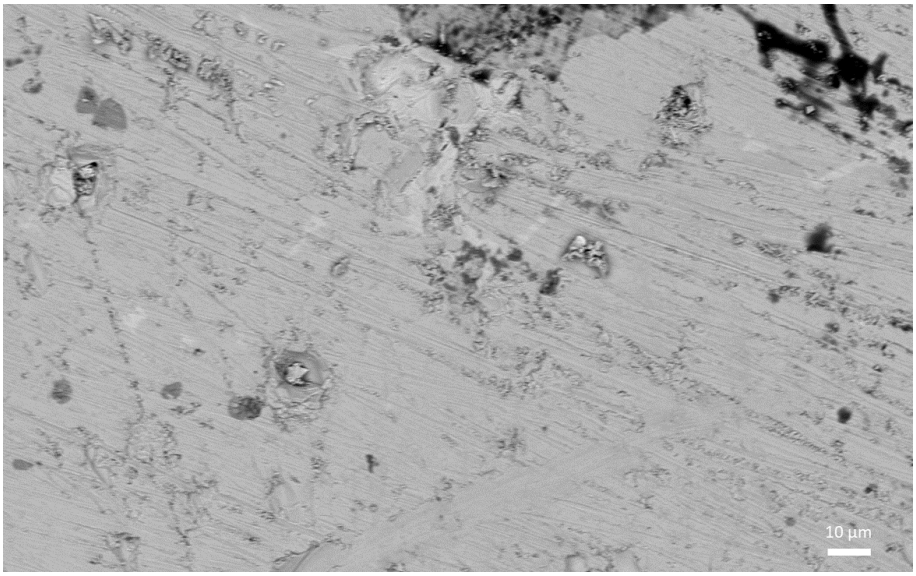

Fig. 144 Microstructures and pores observed in SEM imaging of the $Cu_{10.5}Ni_{1.5}Sb_4S_{13}$ annealed sample with 2450x magnification. The dark phases are composed of nickel sulphides (Ni_xS_y). The light phases are composed of chalcostibite ($CuSbS_2$).

Phase	Cu(at%)	Ni(at%)	Sb(at%)	S(at%)	Se(at%)
Matrix	37.7±0.5	4.5±0.3	14.3±0.2	43.6±0.6	
Dark		33.6±0.3		66.4±0.6	
Light	25.4±0.5		25.5±0.2	49.1±0.5	

Table 32 Semi-quantitative analysis of the phases of $Cu_{10.5}Ni_{1.5}Sb_4S_{13}$ annealed sample.

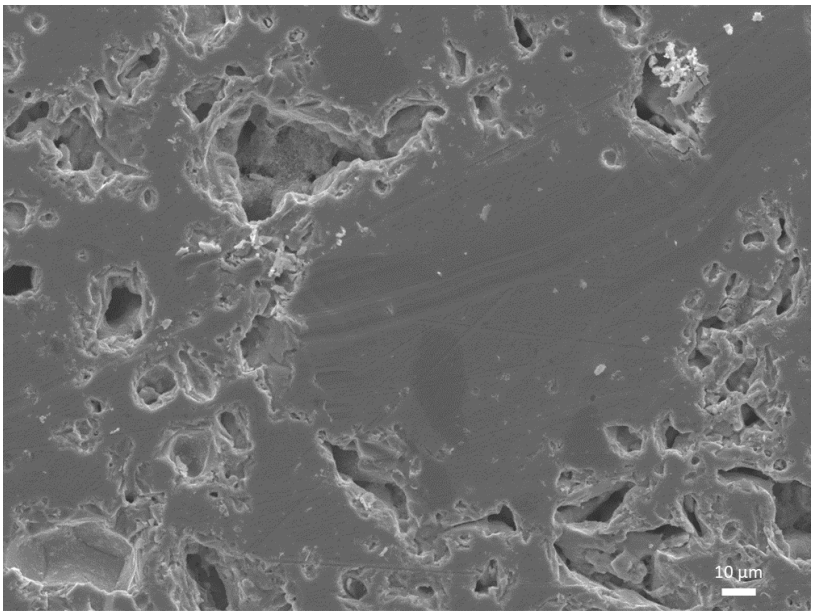

Fig. 145 Microstructures and pores observed in SEM imaging of the $Cu_{10.5}Ni_{1.5}Sb_4S_{12.5}Se_{0.5}$ annealed sample with 500x magnification. The dark phases are composed of nickel sulphides (Ni_xS_y).

Phase	Cu(at%)	Ni(at%)	Sb(at%)	S(at%)	Se(at%)
Matrix	38.3±0.5	4.0±0.3	14.05±0.2	42.47±0.6	1.2±0.2
Dark		49.5±0.4		49.6±0.6	0.8±0.2

Table 33 Semi-quantitative analysis of the phases of $Cu_{10.5}Ni_{1.5}Sb_4S_{12.5}Se_{0.5}$ annealed sample.

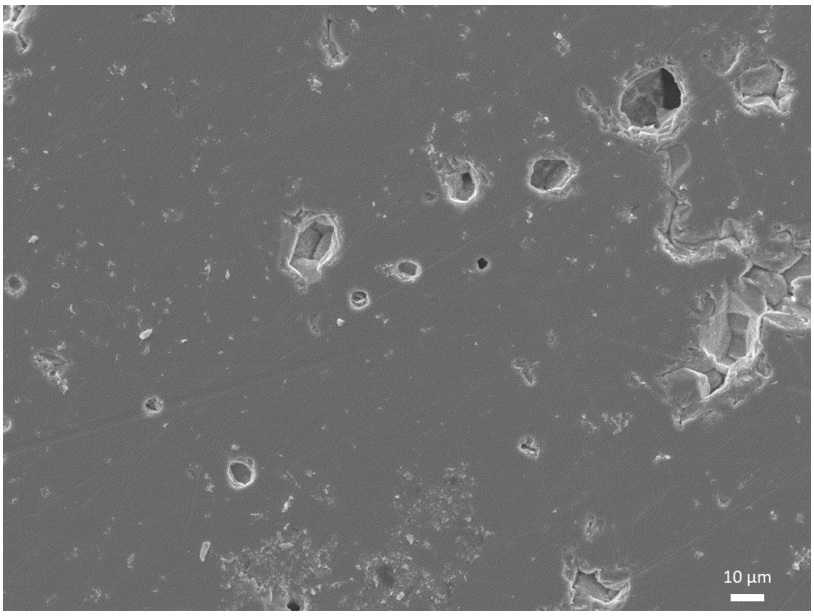

Fig. 146 Microstructures and pores observed in SEM imaging of the $Cu_{10.5}Ni_{1.5}Sb_4S_{12}Se$ annealed sample with 500x magnification.

Phase	Cu(at%)	Ni(at%)	Sb(at%)	S(at%)	Se(at%)
Matrix	37.3±0.5	4.8±0.3	14.2±0.3	41.2±0.6	2.6±0.2

Table 34 Semi-quantitative analysis of the phases of $Cu_{10.5}Ni_{1.5}Sb_4S_{12}Se$ annealed sample.

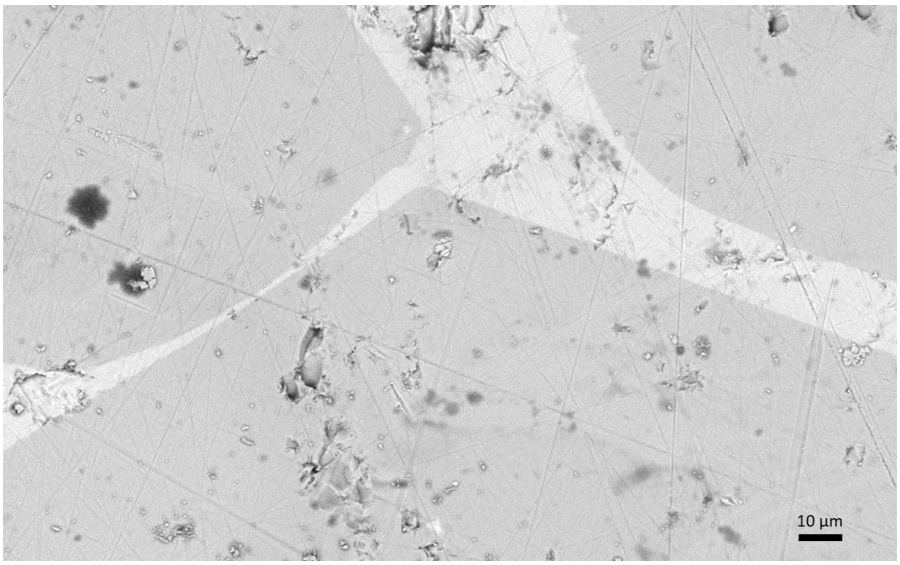

Fig. 147 Microstructures and pores observed in SEM imaging of the $Cu_{12}Sb_4S_{11.5}Se_{1.5}$ annealed sample with 2550x magnification. The light phases are composed of chalcostibite ($CuSbS_2$).

Phase	Cu(at%)	Ni(at%)	Sb(at%)	S(at%)	Se(at%)
Matrix	42.6±0.4		13.7±0.2	39.5±0.6	4.3±0.2
Light	27.2±0.4		25.0±0.2	36.6±0.6	13.1±0.3

Table 35 Semi-quantitative analysis of the phases of $Cu_{12}Sb_4S_{11.5}Se_{1.5}$ as-cast sample.

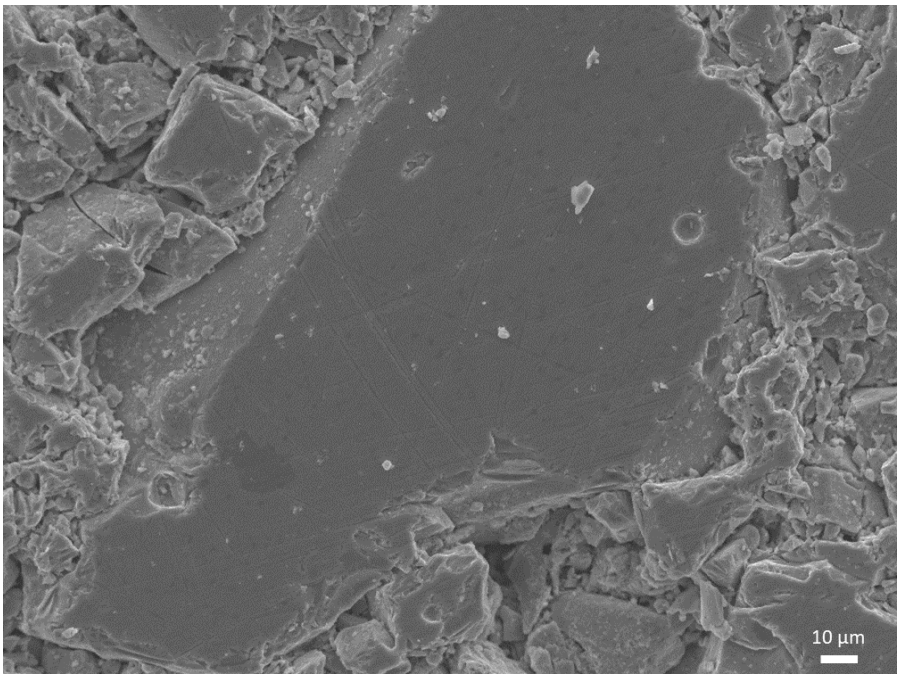

Fig. 148 Microstructures and pores observed in SEM imaging of the $Cu_{11.5}Ni_{0.5}Sb_4S_{11.5}Se_{1.5}$ annealed sample with 500x magnification. The dark phases are composed of nickel sulphides (Ni_xS_y).

Phase	Cu(at%)	Ni(at%)	Sb(at%)	S(at%)	Se(at%)
Matrix	39.8±0.5	1.4±0.3	14.7±0.2	40.5±0.6	3.6±0.2
Dark	2.3±0.2	31.6±0.3		63.1±0.6	3.0±0.2

Table 36 Semi-quantitative analysis of the phases of $Cu_{11.5}Ni_{0.5}Sb_4S_{11.5}Se_{1.5}$ as-cast sample.

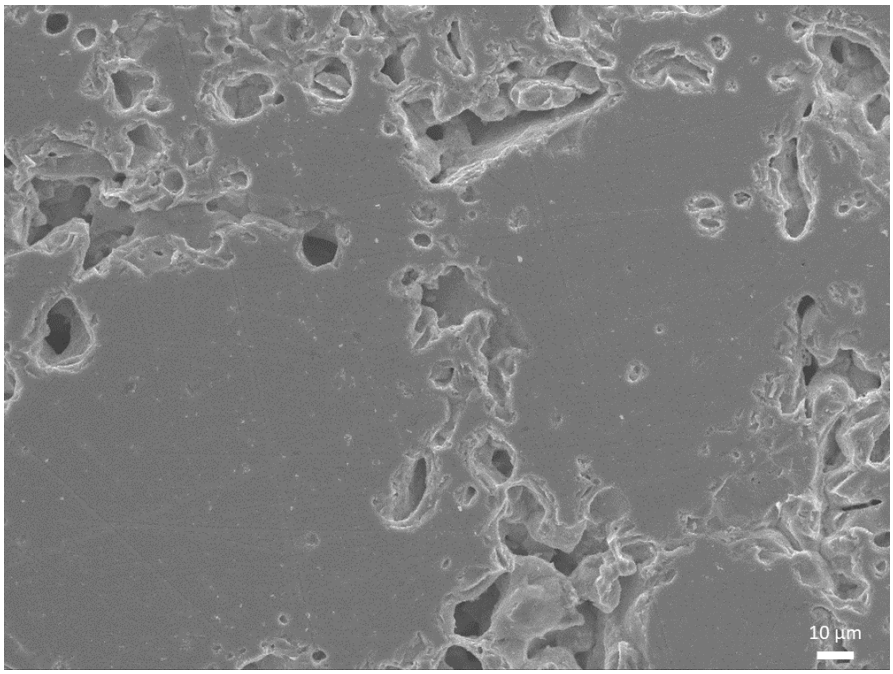

Fig. 149 Microstructures and pores observed in SEM imaging of the $Cu_{11}NiSb_4S_{11.5}Se_{1.5}$ annealed sample with 500x magnification.

Phase	Cu(at%)	Ni(at%)	Sb(at%)	S(at%)	Se(at%)
Matrix	38.4±0.5	3.6±0.3	14.0±0.2	40.1±0.6	3.9±0.3

Table 37 Semi-quantitative analysis of the phases of $Cu_{10.5}Ni_{1.5}Sb_4S_{12}Se$ as-cast sample.

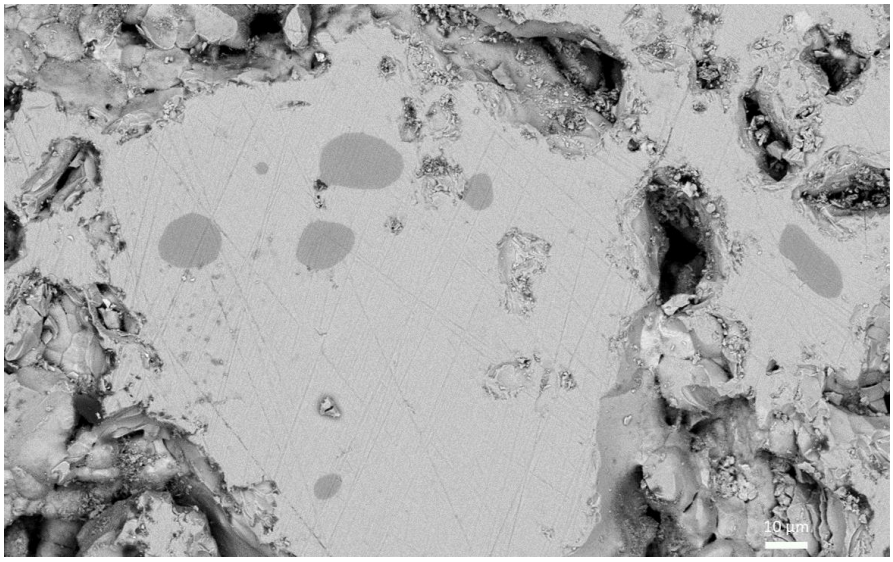

Fig. 150 Microstructures and pores observed in SEM imaging of the $Cu_{10.5}Ni_{1.5}Sb_4S_{11.5}Se_{1.5}$ annealed sample with 2450x magnification. The dark phases are composed of nickel sulphides (Ni_xS_y).

Phase	Cu(at%)	Ni(at%)	Sb(at%)	S(at%)	Se(at%)
Matrix	37.5±0.5	4.5±0.3	13.9±0.2	40.3±0.6	3.8±0.3
Dark		47.9±0.3		48.4±0.5	3.7±0.2

Table 38 Semi-quantitative analysis of the phases of $Cu_{10.5}Ni_{1.5}Sb_4S_{11.5}Se_{1.5}$ annealed sample.

Expected formula of the sample	Cu(at%)	Ni(at%)	Sb(at%)	S(at%)	Se(at%)	Matrix chemical formula
$Cu_{12}Sb_4S_{13}$	42.0±0.5		14.4±0.2	43.6±0.6		$Cu_{12.2\pm0.1}Sb_{4.2\pm0.1}S_{12.6\pm0.2}$
$Cu_{11.5}Ni_{0.5}Sb_4S_{13}$	40.1±0.5	1.9±0.3	14.2±0.3	43.9±0.7		$Cu_{11.6\pm0.2}Ni_{0.6\pm0.1}Sb_{4.1\pm0.1}S_{12.7\pm0.2}$
$Cu_{12}Sb_4S_{12.5}Se_{0.5}$	40.6±0.3		14.1±0.2	44.1±0.5	1.2±0.2	$Cu_{11.8\pm0.1}Sb_{4.1\pm0.1}S_{12.8\pm0.1}Se_{0.4\pm0.1}$
$Cu_{11.5}Ni_{0.5}Sb_4S_{12.5}Se_{0.5}$	40.2±0.4	1.4±0.1	13.9±0.2	43.2±0.5	1.3±0.2	$Cu_{11.7\pm0.1}Ni_{0.4\pm0.1}Sb_{4.0\pm0.1}S_{12.5\pm0.1}Se_{0.4\pm0.1}$
$Cu_{11}NiSb_4S_{13}$	39.0±0.4	2.6±0.2	13.8±0.2	44.7±0.6		$Cu_{11.3\pm0.1}Ni_{0.8\pm0.1}Sb_{4.0\pm0.1}S_{13.0\pm0.2}$
$Cu_{11}NiSb_4S_{12.5}Se_{0.5}$	38.4±0.5	3.8±0.3	14.4±0.2	41.9±0.6	1.6±0.2	$Cu_{11.1\pm0.1}Ni_{1.1\pm0.1}Sb_{4.2\pm0.1}S_{12.2\pm0.2}Se_{0.5\pm0.1}$
$Cu_{12}Sb_4S_{12}Se$	38.9±0.5		12.7±0.3	44.7±0.7	3.7±0.3	$Cu_{11.3\pm0.2}Sb_{3.7\pm0.1}S_{13.0\pm0.2}Se_{1.1\pm0.1}$
$Cu_{11.5}Ni_{0.5}Sb_4S_{12}Se$	39.4±0.4	2.1±0.2	13.7±0.2	42.0±0.5	2.8±0.2	$Cu_{11.4\pm0.1}Ni_{0.6\pm0.1}Sb_{4.0\pm0.1}S_{12.2\pm0.2}Se_{0.8\pm0.1}$
$Cu_{12}NiSb_4S_{12}Se$	37.3±0.5	4.7±0.3	13.9±0.2	41.6±0.6	2.5±0.2	$Cu_{10.8\pm0.1}Ni_{1.4\pm0.1}Sb_{4.0\pm0.1}S_{12.1\pm0.2}Se_{0.7\pm0.1}$
$Cu_{10.5}Ni_{1.5}Sb_4S_{13}$	37.7±0.5	4.5±0.3	14.3±0.2	43.6±0.6		$Cu_{10.9\pm0.2}Ni_{1.3\pm0.1}Sb_{4.1\pm0.1}S_{12.6\pm0.2}$
$Cu_{10.5}Ni_{1.5}Sb_4S_{12.5}Se_{0.5}$	38.3±0.5	4.0±0.3	14.1±0.2	42.5±0.6	1.2±0.2	$Cu_{11.1\pm0.2}Ni_{1.2\pm0.1}Sb_{4.1\pm0.1}S_{12.3\pm0.2}Se_{0.3\pm0.1}$
$Cu_{10.5}Ni_{1.5}Sb_4S_{12}Se$	37.3±0.5	4.8±0.3	14.2±0.3	41.2±0.6	2.6±0.2	$Cu_{10.8\pm0.2}Ni_{1.4\pm0.1}Sb_{4.1\pm0.1}S_{11.9\pm0.2}Se_{0.7\pm0.1}$
$Cu_{12}Sb_4S_{11.5}Se_{1.5}$	42.6±0.4		13.7±0.2	39.5±0.6	4.3±0.2	$Cu_{12.3\pm0.1}Sb_{4.0\pm0.1}S_{11.5\pm0.2}Se_{1.2\pm0.1}$
$Cu_{11.5}Ni_{0.5}Sb_4S_{11.5}Se_{1.5}$	39.8±0.5	1.4±0.3	14.7±0.2	40.5±0.6	3.6±0.2	$Cu_{11.6\pm0.2}Ni_{0.4\pm0.1}Sb_{4.3\pm0.1}S_{11.7\pm0.2}Se_{1.1\pm0.1}$
$Cu_{11}NiSb_4S_{11.5}Se_{1.5}$	38.4±0.5	3.6±0.3	14.0±0.2	40.1±0.6	3.9±0.3	$Cu_{11.1\pm0.1}Ni_{1.1\pm0.1}Sb_{4.1\pm0.1}S_{11.6\pm0.2}Se_{1.1\pm0.1}$
$Cu_{10.5}Ni_{1.5}Sb_4S_{11.5}Se_{1.5}$	37.5±0.5	4.5±0.3	13.9±0.2	40.3±0.6	3.8±0.3	$Cu_{10.9\pm0.1}Ni_{1.3\pm0.1}Sb_{4.0\pm0.1}S_{11.7\pm0.2}Se_{1.1\pm0.1}$

Table 39 SEM-EDS semi-quantitative analysis of the matrix of annealed samples. The matrix chemical formula was calculated based on the composition and assuming a 29 atoms molecule like tetrahedrite.

Hot-pressed samples

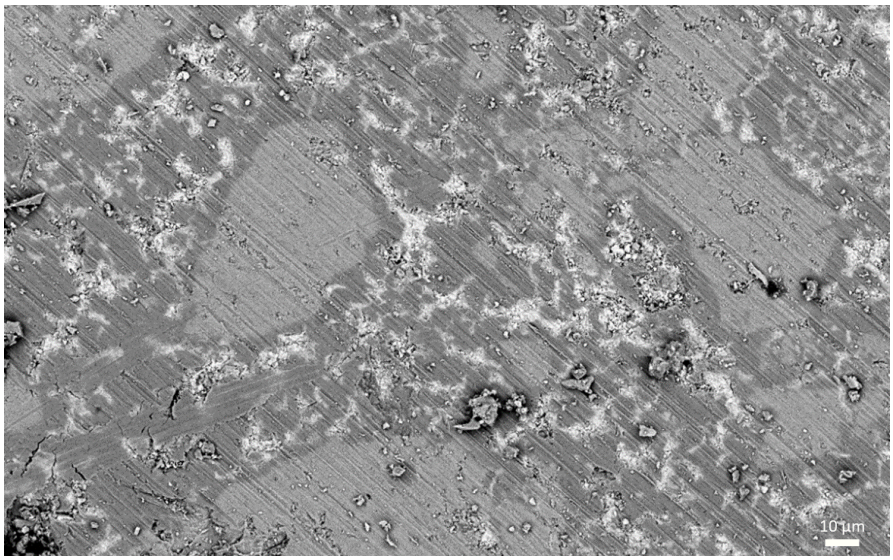

Fig. 151 Microstructures and pores observed in SEM imaging of the $Cu_{11.5}Ni_{0.5}Sb_4S_{13}$ hot-pressed sample with 500x magnification. The dark phases are composed of copper sulphides (Cu_xS_y). The white regions are oxide phases mainly antimony oxide (SbO_2).

Phase	Cu(at%)	Ni(at%)	Sb(at%)	S(at%)	Se(at%)
Matrix	38.2±0.4	3.0±0.2	14.4±0.2	44.5±0.6	
Dark	66.1±0.4			34.0±0.6	

Table 40 Semi-quantitative analysis of the phases of $Cu_{11.5}Ni_{0.5}Sb_4S_{13}$ hot-pressed sample.

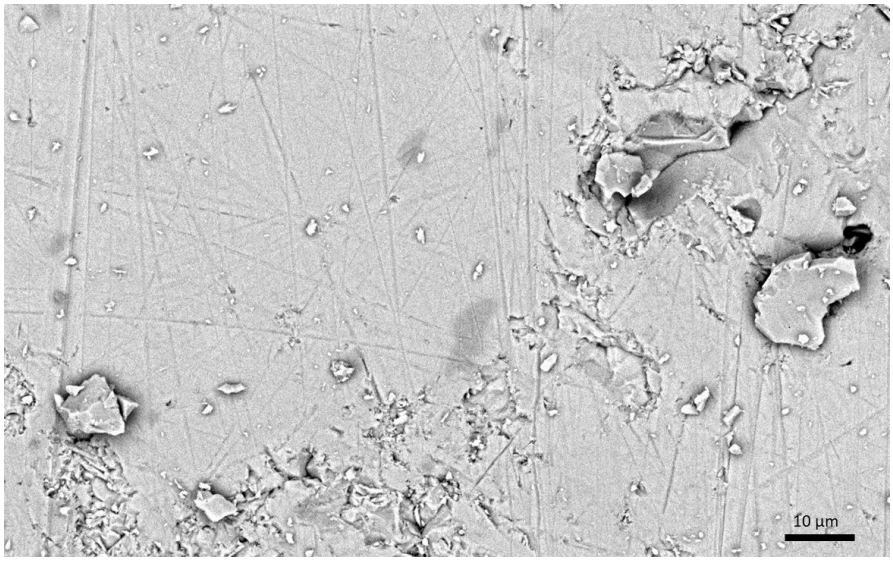

Fig. 152 Microstructures and pores observed in SEM imaging of the $Cu_{12}Sb_4S_{12.5}Se_{0.5}$ hot-pressed sample with 1000x magnification. The dark phases are composed of copper sulphides (Cu_xS_y).

Phase	Cu(at%)	Ni(at%)	Sb(at%)	S(at%)	Se(at%)
Matrix	41.2±0.4		13.7±0.2	42.4±0.6	2.7±0.2
Dark	69.6±0.4			30.5±0.7	

Table 41 Semi-quantitative analysis of the phases of $Cu_{12}Sb_4S_{12.5}Se_{0.5}$ hot-pressed sample.

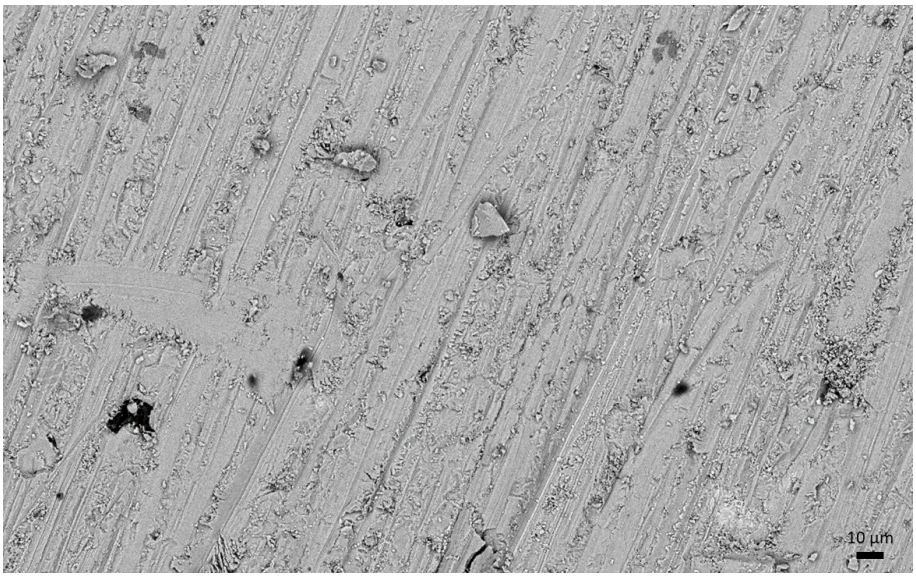

Fig. 153 Microstructures and pores observed in SEM imaging of the $Cu_{11.5}Ni_{0.5}Sb_4S_{12.5}Se_{0.5}$ hot-pressed sample with 380x magnification. The dark phases are composed of nickel sulphides (Ni_xS_y).

Phase	Cu(at%)	Ni(at%)	Sb(at%)	S(at%)	Se(at%)
Matrix	38.7±0.4	1.2±0.3	13.8±0.2	42.2±0.6	4.1±0.2
Dark	3.3±0.3	29.2±0.3		62.4±0.5	5.2±0.2

Table 42 Semi-quantitative analysis of the phases of $Cu_{11.5}Ni_{0.5}Sb_4S_{12.5}Se_{0.5}$ hot-pressed sample.

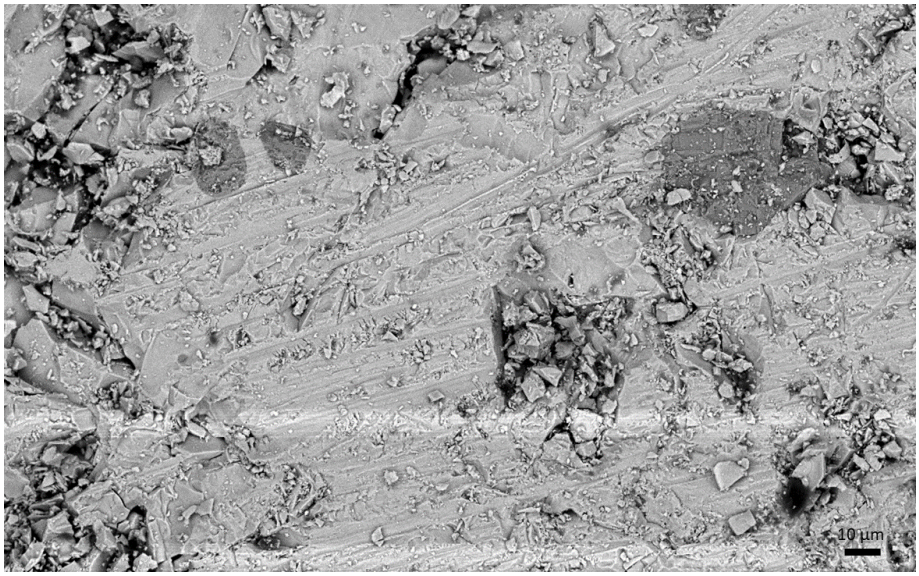

Fig. 154 Microstructures and pores observed in SEM imaging of the $Cu_{11}NiSb_4S_{13}$ hot-pressed sample with 500x magnification. The dark phases are composed of nickel sulphides (Ni_xS_y).

Phase	Cu(at%)	Ni(at%)	Sb(at%)	S(at%)	Se(at%)
Matrix	40.5±0.4	2.0±0.2	14.2±0.2	43.3±0.6	
Dark	1.7±0.3	33.7±0.3		64.6±0.5	

Table 43 Semi-quantitative analysis of the phases of $Cu_{11}NiSb_4S_{13}$ hot-pressed sample.

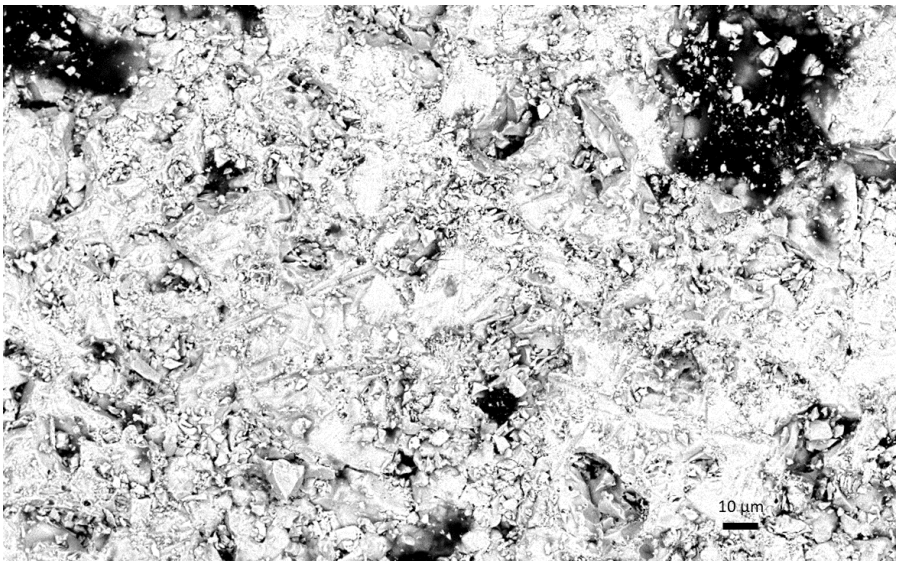

Fig. 155 Microstructures and pores observed in SEM imaging of the $Cu_{11}NiSb_4S_{12.5}Se_{0.5}$ hot-pressed sample with 500x magnification. The dark phases are a secondary tetrahedrite phase without Se.

Phase	Cu(at%)	Ni(at%)	Sb(at%)	S(at%)	Se(at%)
Matrix	37.5±0.4	2.5±0.3	13.9±0.2	42.3±0.6	3.8±0.2
Dark	37.8±0.5	3.3±0.3	17.75±0.2	41.2±0.6	

Table 44 Semi-quantitative analysis of the phases of $Cu_{11}NiSb_4S_{12.5}Se_{0.5}$ hot-pressed sample.

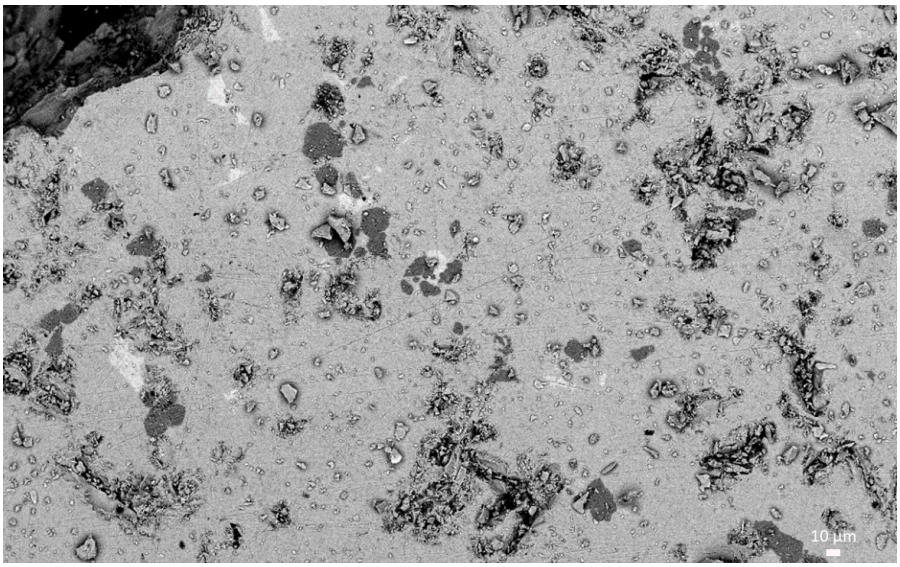

Fig. 156 Microstructures and pores observed in SEM imaging of the $Cu_{11.5}Ni_{0.5}Sb_4S_{12}Se$ hot-pressed sample with 200x magnification. The dark phases are composed of nickel sulphides (Ni_xS_y). The light phases are composed of chalcostibite ($CuSbS_2$).

Phase	Cu(at%)	Ni(at%)	Sb(at%)	S(at%)	Se(at%)
Matrix	39.2±0.4	1.6±0.3	14.3±0.2	41.0±0.6	3.9±0.2
Dark	2.9±0.3	28.2±0.3		63.5±0.5	5.3±0.2
Light	26.3±0.4		26.2±0.2	35.1±0.6	15.7±0.3

Table 45 Semi-quantitative analysis of the phases of $Cu_{12}Sb_4S_{12}Se$ hot-pressed sample.

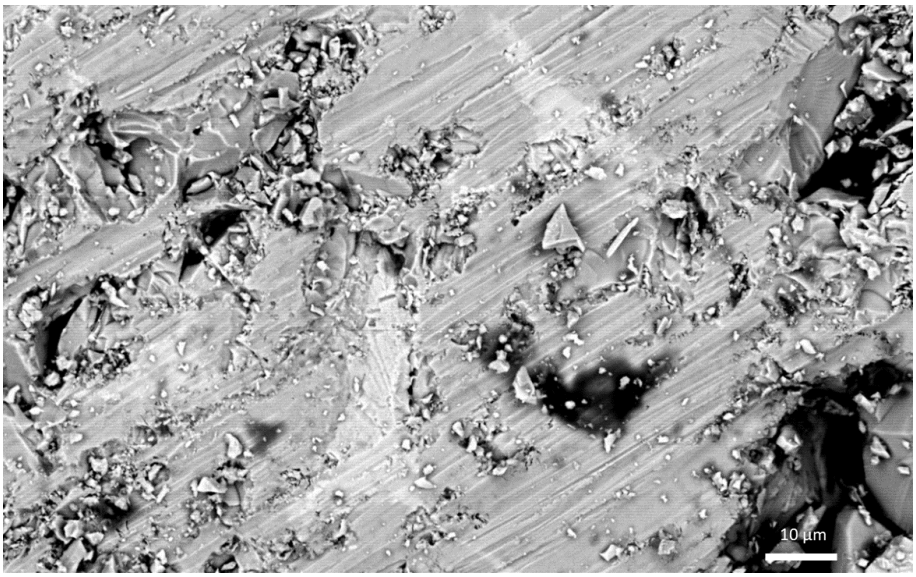

Fig. 157 Microstructures and pores observed in SEM imaging of the $Cu_{11}NiSb_4S_{12}Se$ hot-pressed sample with 1000x magnification. The light phases are composed of chalcostibite ($CuSbS_2$).

Phase	Cu(at%)	Ni(at%)	Sb(at%)	S(at%)	Se(at%)
Matrix	37.1±0.4	3.3±0.3	13.8±0.2	41.2±0.6	4.7±0.2
Light	25.5±0.4		26.6±0.2	42.0±0.6	9.4±0.3

Table 46 Semi-quantitative analysis of the phases of $Cu_{12}Sb_4S_{12}Se$ hot-pressed sample.

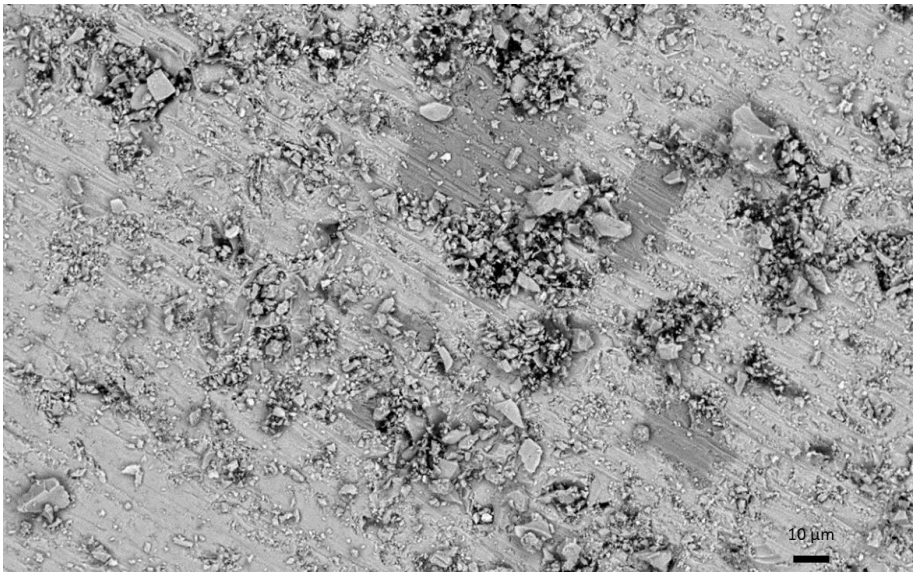

Fig. 158 Microstructures and pores observed in SEM imaging of the $Cu_{10.5}Ni_{1.5}Sb_4S_{13}$ hot-pressed sample with 500x magnification. The dark phases are composed of nickel sulphides (Ni_xS_y).

Phase	Cu(at%)	Ni(at%)	Sb(at%)	S(at%)	Se(at%)
Matrix	36.9±0.4	3.9±0.2	14.2±0.2	45.0±0.6	
Dark	9.8±0.3	40.2±0.4	1.3±0.2	48.8±0.6	

Table 47 Semi-quantitative analysis of the phases of $Cu_{10.5}Ni_{1.5}Sb_4S_{13}$ hot-pressed sample.

Fig. 159 Microstructures and pores observed in SEM imaging of the $Cu_{10.5}Ni_{1.5}Sb_4S_{12.5}Se_{0.5}$ hot-pressed sample with 500x magnification. The dark phases are composed of nickel sulphides (Ni_xS_y). The light phases are composed of ullmannite (NiSbS).

Phase	Cu(at%)	Ni(at%)	Sb(at%)	S(at%)	Se(at%)
Matrix	37.4±0.4	4.0±0.3	13.6±0.2	41.3±0.6	3.8±0.2
Dark	3.7±0.3	47.5±0.4		48.8±0.6	
Light	2.3±0.5	34.9±0.6	39.7±0.3	26.1±0.9	4.3±0.3

Table 48 Semi-quantitative analysis of the phases of $Cu_{10.5}Ni_{1.5}Sb_4S_{12.5}Se_{0.5}$ hot-pressed sample.

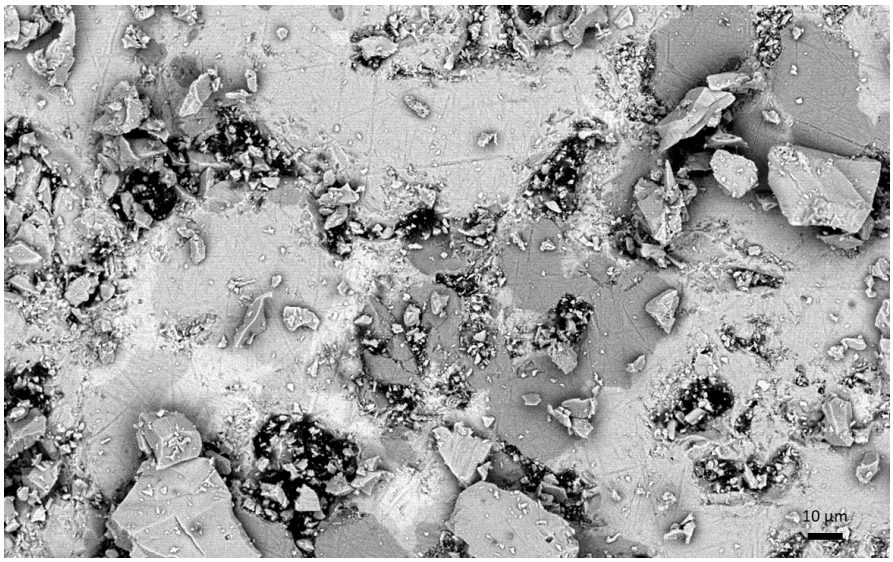

Fig. 160 Microstructures and pores observed in SEM imaging of the $Cu_{10.5}Ni_{1.5}Sb_4S_{12}Se$ hot-pressed sample with 500x magnification. The dark phases are composed of nickel sulphides (Ni_xS_y). The light phases are composed of chalcostibite ($CuSbS_2$).

Phase	Cu(at%)	Ni(at%)	Sb(at%)	S(at%)	Se(at%)
Matrix	36.1±0.4	3.5±0.3	13.9±0.2	42.0±0.6	4.5±0.2
Dark	0.8±0.3	46.6±0.4		46.7±0.6	6.0±0.2
Light	26,5±0.4	1.2±0.3	25.9±0.2	38.3±0.6	11.6±0.3

Table 49 Semi-quantitative analysis of the phases of $Cu_{10.5}Ni_{1.5}Sb_4S_{12}Se$ hot-pressed sample.

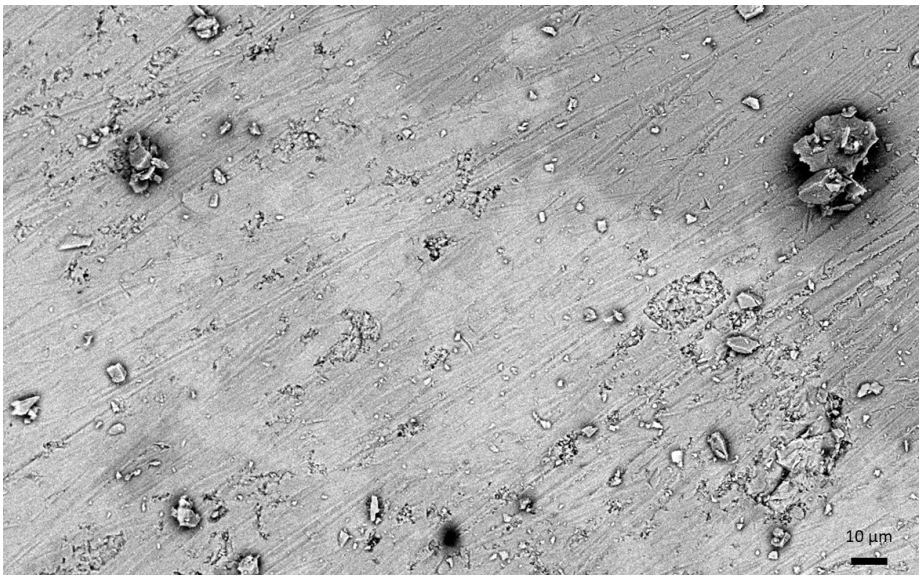

Fig. 161 Microstructures and pores observed in SEM imaging of the $Cu_{12}Sb_4S_{11.5}Se_{1.5}$ hot-pressed sample with 500x magnification. The dark phases are composed of copper sulphides (Cu_xS_y).

Phase	Cu(at%)	Ni(at%)	Sb(at%)	S(at%)	Se(at%)
Matrix	39.7±0.5		14.2±0.2	39.0±0.6	7.1±0.2
Dark	70.6±0.4			29.5±0.7	

Table 50 Semi-quantitative analysis of the phases of $Cu_{12}Sb_4S_{11.5}Se_{1.5}$ hot-pressed sample.

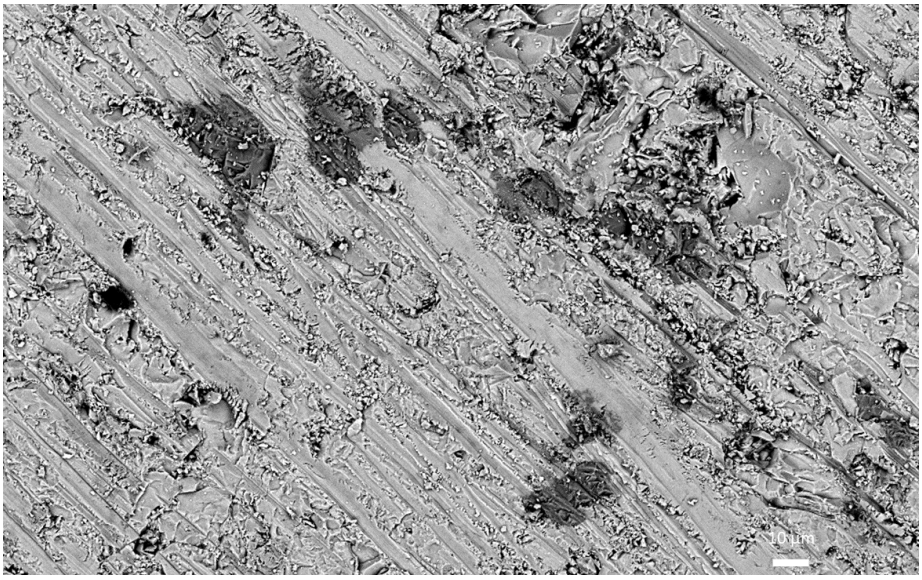

Fig. 162 Microstructures and pores observed in SEM imaging of the $Cu_{11.5}Ni_{0.5}Sb_4S_{11.5}Se_{1.5}$ hot-pressed sample with 500x magnification. The dark phases are composed of nickel sulphides (Ni_xS_y).

Phase	Cu(at%)	Ni(at%)	Sb(at%)	S(at%)	Se(at%)
Matrix	44.1±0.5	0.8±0.3	12.6±0.2	37.2±0.6	5.4±0.2
Dark	3.7±0.3	35.5±0.4		56.4±0.5	4.4±0.2

Table 51 Semi-quantitative of the phases of $Cu_{11.5}Ni_{0.5}Sb_4S_{11.5}Se_{1.5}$ hot-pressed sample.

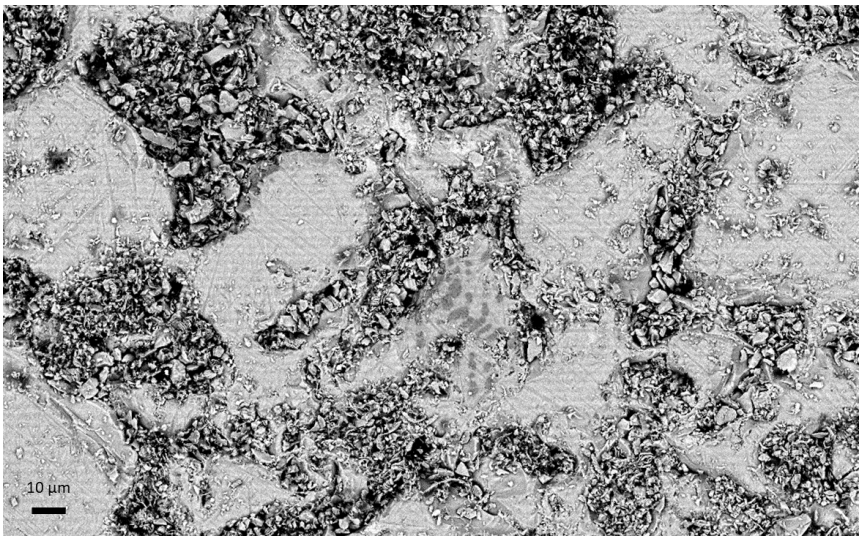

Fig. 163 Microstructures and pores observed in SEM imaging of the $Cu_{11}NiSb_4S_{11.5}Se_{1.5}$ hot-pressed sample with 500x magnification. The dark phases are composed of nickel sulphides (Ni_xS_y) and lighter phases are composed of chalcostibite ($CuSbS_2$).

Phase	Cu(at%)	Ni(at%)	Sb(at%)	S(at%)	Se(at%)
Matrix	37.3±0.5	2.9±0.23	14.0±0.2	39.5±0.6	6.2±0.2
Dark	2.1±0.3	47.8±0.4		50.1±0.6	
Light	27.0±0.4		29.1±0.3	33.9±0.6	14.3±0.3

Table 52 Semi-quantitative analysis of the phases of $Cu_{10.5}Ni_{1.5}Sb_4S_{12}Se$ hot-pressed sample.

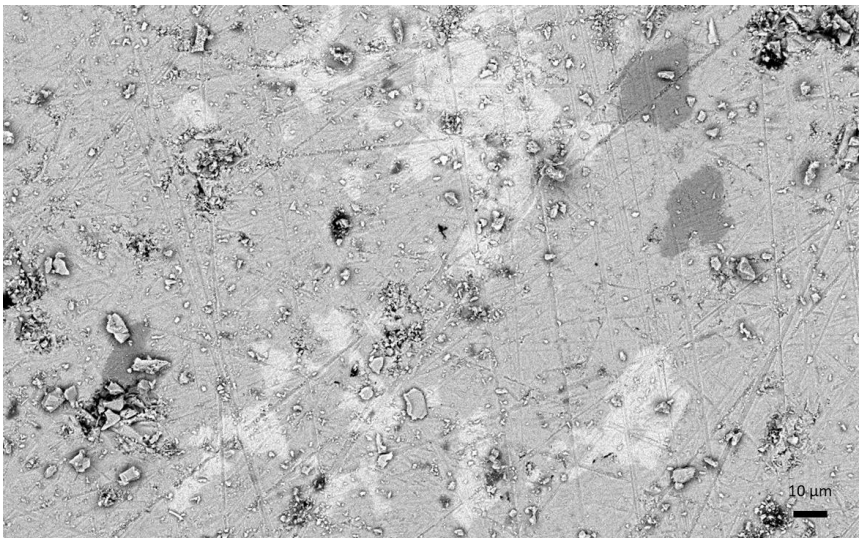

Fig. 164 Microstructures and pores observed in SEM imaging of the $Cu_{10.5}Ni_{1.5}Sb_4S_{11.5}Se_{1.5}$ hot-pressed sample with 500x magnification. The dark phases are composed of nickel sulphides (Ni_xS_y) and lighter phases are composed of chalcostibite ($CuSbS_2$).

Phase	Cu(at%)	Ni(at%)	Sb(at%)	S(at%)	Se(at%)
Matrix	35.6±0.5	4.0±0.3	14.3±0.2	39.2±0.6	6.9±0.2
Dark	1.9±0.3	48.9±0.4		43.0±0.6	6.2±0.2
Light	27.1±0.4		25.7±0.2	38.7±0.6	11.7±0.3

Table 53 Semi-quantitative analysis of the phases of $Cu_{10.5}Ni_{1.5}Sb_4S_{11.5}Se_{1.5}$ hot-pressed sample.

Expected formula of the sample	Cu(at%)	Ni(at%)	Sb(at%)	S(at%)	Se(at%)	Matrix chemical formula
$Cu_{11.5}Ni_{0.5}Sb_4S_{13}$	38.2±0.4	3.0±0.2	14.4±0.2	44.5±0.6		$Cu_{11.1\pm0.1}Ni_{0.9\pm0.1}Sb_{4.2\pm0.1}S_{12.9\pm0.2}$
$Cu_{12}Sb_4S_{12.5}Se_{0.5}$	41.2±0.4		13.7±0.2	42.4±0.6	2.7±0.2	$Cu_{11.9\pm0.1}Sb_{4.0\pm0.1}S_{12.3\pm0.2}Se_{0.8\pm0.1}$
$Cu_{11.5}Ni_{0.5}Sb_4S_{12.5}Se_{0.5}$	38.7±0.4	1.2±0.3	13.8±0.2	42.2±0.6	4.1±0.2	$Cu_{11.2\pm0.1}Ni_{0.4\pm0.1}Sb_{4.0\pm0.1}S_{12.3\pm0.2}Se_{1.2\pm0.1}$
$Cu_{11}NiSb_4S_{13}$	40.5±0.4	2.0±0.2	14.2±0.2	43.3±0.6		$Cu_{11.7\pm0.1}Ni_{0.6\pm0.1}Sb_{4.1\pm0.1}S_{12.6\pm0.2}$
$Cu_{11}NiSb_4S_{12.5}Se_{0.5}$	37.5±0.4	2.5±0.3	13.9±0.2	42.3±0.6	3.8±0.2	$Cu_{110.9\pm0.1}Ni_{0.7\pm0.1}Sb_{4.0\pm0.1}S_{12.3\pm0.2}Se_{1.1\pm0.1}$
$Cu_{11.5}Ni_{0.5}Sb_4S_{12}Se$	39.2±0.4	1.6±0.3	14.3±0.2	41.0±0.6	3.9±0.2	$Cu_{11.4\pm0.1}Ni_{0.5\pm0.1}Sb_{4.2\pm0.1}S_{11.9\pm0.2}Se_{1.1\pm0.1}$
$Cu_{12}NiSb_4S_{12}Se$	37.1±0.4	3.3±0.3	13.8±0.2	41.2±0.6	4.7±0.2	$Cu_{10.8\pm0.1}Ni_{0.9\pm0.1}Sb_{4.0\pm0.1}S_{11.9\pm0.2}Se_{1.4\pm0.1}$
$Cu_{10.5}Ni_{1.5}Sb_4S_{13}$	36.9±0.4	3.9±0.2	14.2±0.2	45.0±0.6		$Cu_{10.7\pm0.1}Ni_{1.1\pm0.1}Sb_{4.1\pm0.1}S_{13.1\pm0.1}$
$Cu_{10.5}Ni_{1.5}Sb_4S_{12.5}Se_{0.5}$	37.4±0.4	4.0±0.3	13.6±0.2	41.3±0.6	3.8±0.2	$Cu_{10.8\pm0.1}Ni_{1.2\pm0.1}Sb_{3.9\pm0.1}S_{12.0\pm0.2}Se_{1.1\pm0.1}$
$Cu_{10.5}Ni_{1.5}Sb_4S_{12}Se$	36.1±0.4	3.5±0.3	13.9±0.2	42.0±0.6	4.5±0.2	$Cu_{10.5\pm0.1}Ni_{1.0\pm0.1}Sb_{4.0\pm0.1}S_{12.2\pm0.2}Se_{1.3\pm0.1}$
$Cu_{12}Sb_4S_{11.5}Se_{1.5}$	39.7±0.5		14.2±0.2	39.0±0.6	7.1±0.2	$Cu_{11.5\pm0.1}Sb_{4.1\pm0.1}S_{11.3\pm0.2}Se_{2.1\pm0.1}$
$Cu_{11.5}Ni_{0.5}Sb_4S_{11.5}Se_{1.5}$	44.1±0.5	0.8±0.3	12.6±0.2	37.2±0.6	5.4±0.2	$Cu_{12.8\pm0.1}Ni_{0.2\pm0.1}Sb_{3.7\pm0.1}S_{10.8\pm0.2}Se_{1.6\pm0.1}$
$Cu_{11}NiSb_4S_{11.5}Se_{1.5}$	37.3±0.5	2.9±0.2	14.0±0.2	39.5±0.6	6.2±0.2	$Cu_{10.8\pm0.1}Ni_{0.9\pm0.1}Sb_{4.1\pm0.1}S_{11.5\pm0.2}Se_{1.8\pm0.1}$
$Cu_{10.5}Ni_{1.5}Sb_4S_{11.5}Se_{1.5}$	35.6±0.5	4.0±0.3	14.3±0.2	39.2±0.6	6.9±0.2	$Cu_{10.3\pm0.1}Ni_{1.2\pm0.1}Sb_{4.2\pm0.1}S_{11.4\pm0.2}Se_{2.0\pm0.1}$

Table 54 SEM-EDS semi-quantitative analysis of the matrix of hot-pressed samples. The matrix chemical formula was calculated based on the composition and assuming a 29 atoms molecule like tetrahedrite.

ATTACHMENT 4: MEASUREMENTS OF ELECTRICAL RESISITIVITY

Annealed samples- Electrical resistivity (ρ)

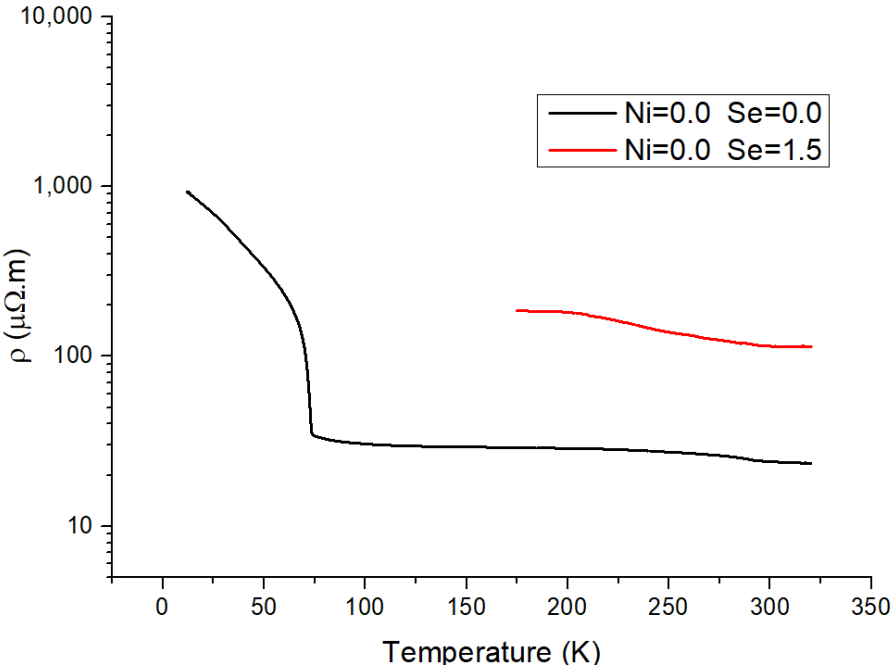

Fig. 165 Temperature dependence of Electrical resistivity of annealed samples following the formula $Cu_{12}Sb_4S_{13-y}Se_y$.

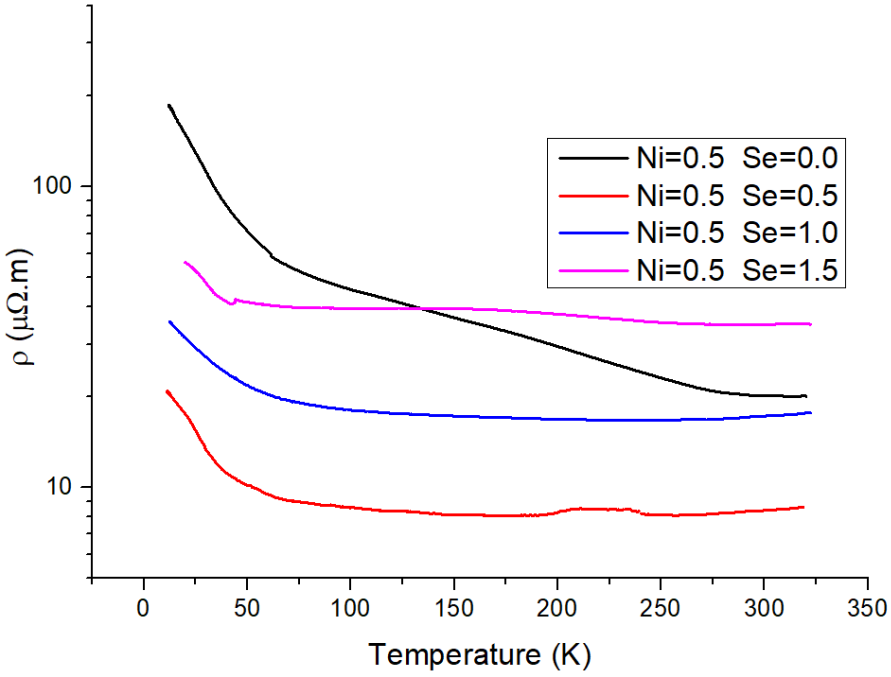

Fig. 166 Temperature dependence of Electrical resistivity of annealed samples following the formula $Cu_{11.5}Ni_{0.5}Sb_4S_{13-y}Se_y$.

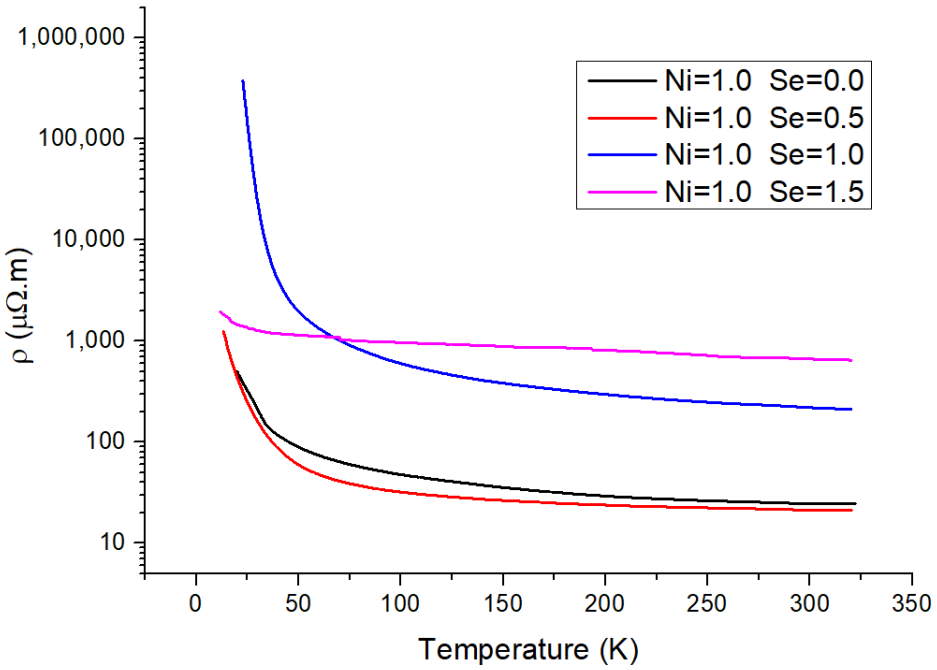

Fig. 167 Temperature dependence of Electrical resistivity of annealed samples following the formula $Cu_{11}NiSb_4S_{13-y}Se_y$.

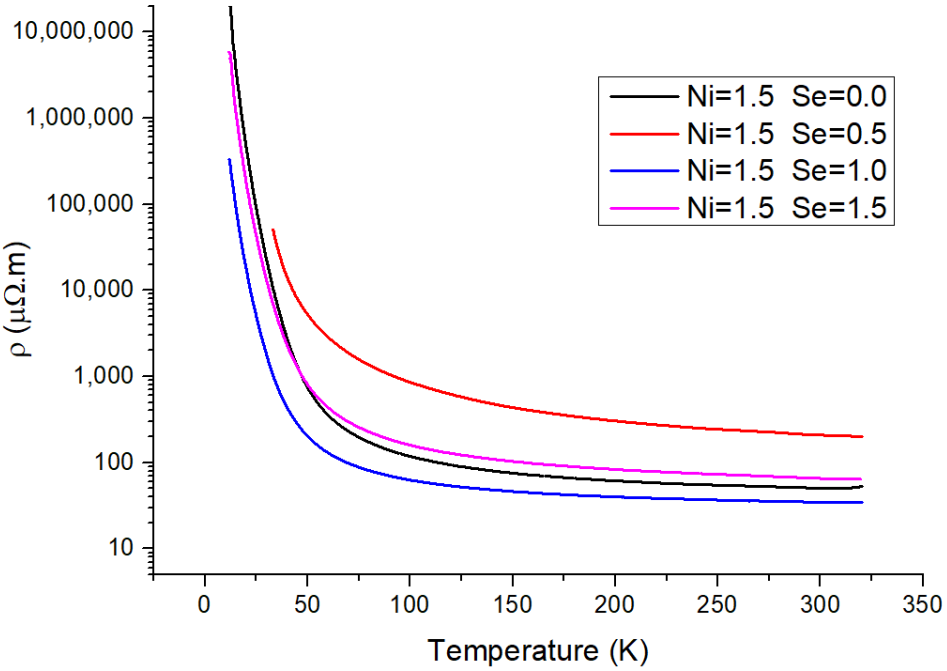

Fig. 168 Temperature dependence of Electrical resistivity of annealed samples following the formula $Cu_{10.5}Ni_{1.5}Sb_4S_{13-y}Se_y$.

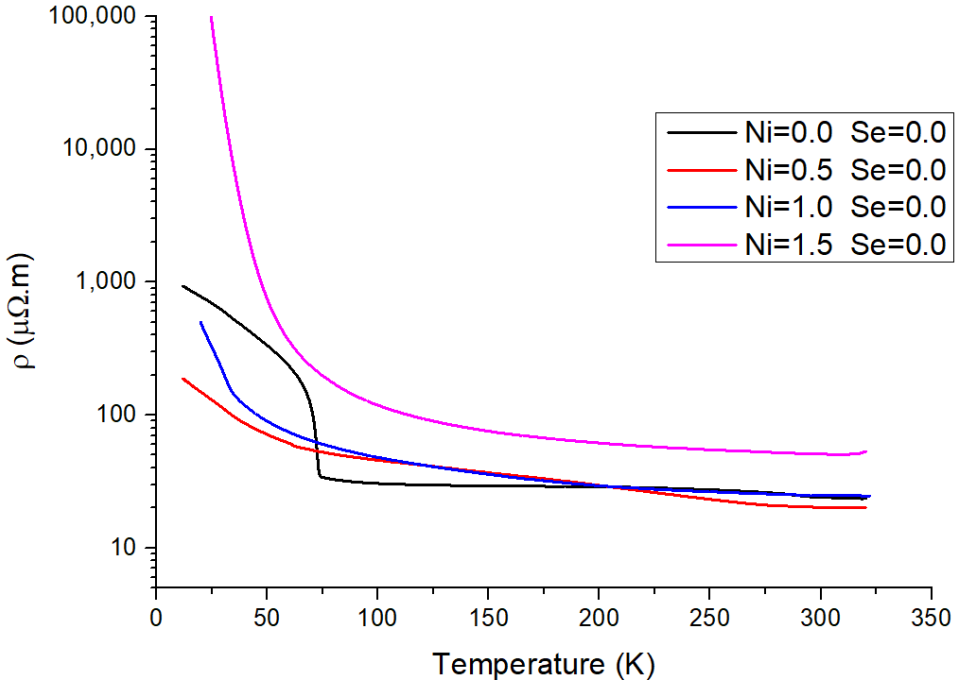

Fig. 169 Temperature dependence of Electrical resistivity of annealed samples following the formula $Cu_{12-x}Ni_xSb_4S_{13}$.

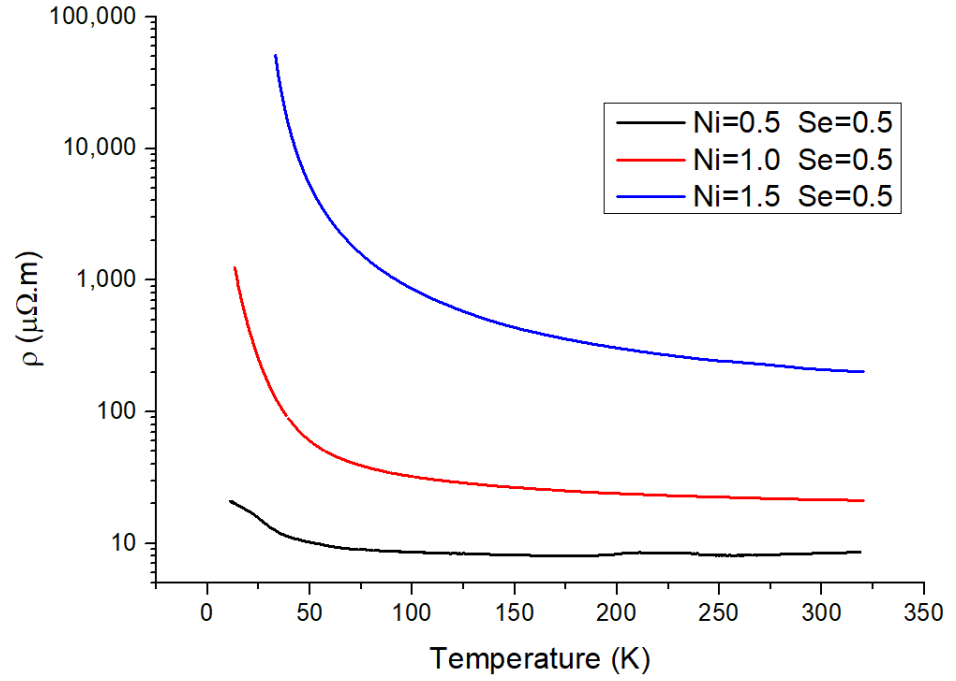

Fig. 170 Temperature dependence of Electrical resistivity of annealed samples following the formula $Cu_{12-x}Ni_xSb_4S_{12.5}Se_{0.5}$.

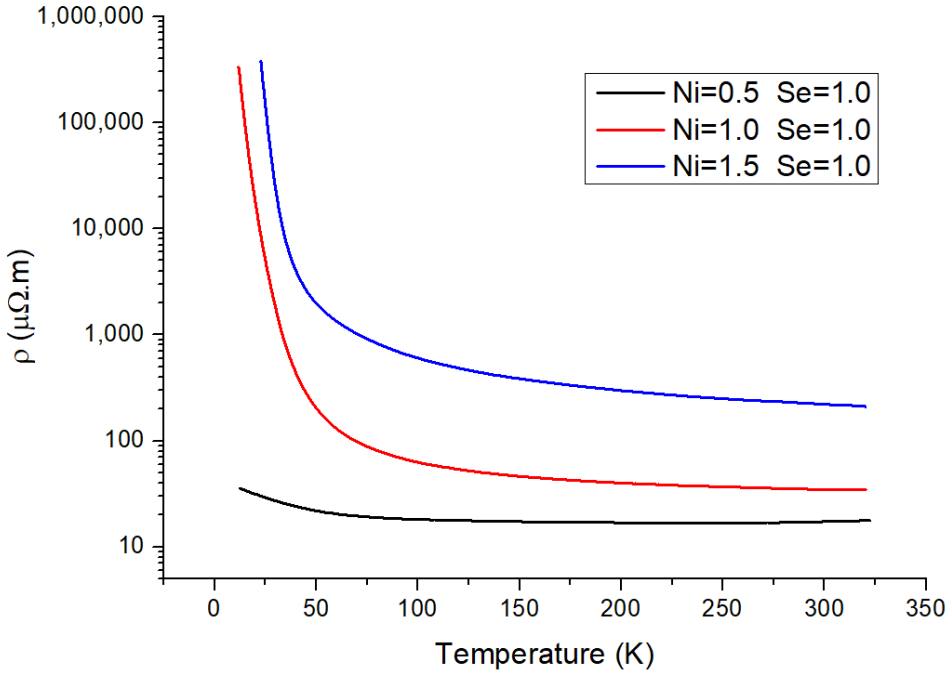

Fig. 171 Temperature dependence of Electrical resistivity of annealed samples following the formula $Cu_{12-x}Ni_xSb_4S_{12}Se$.

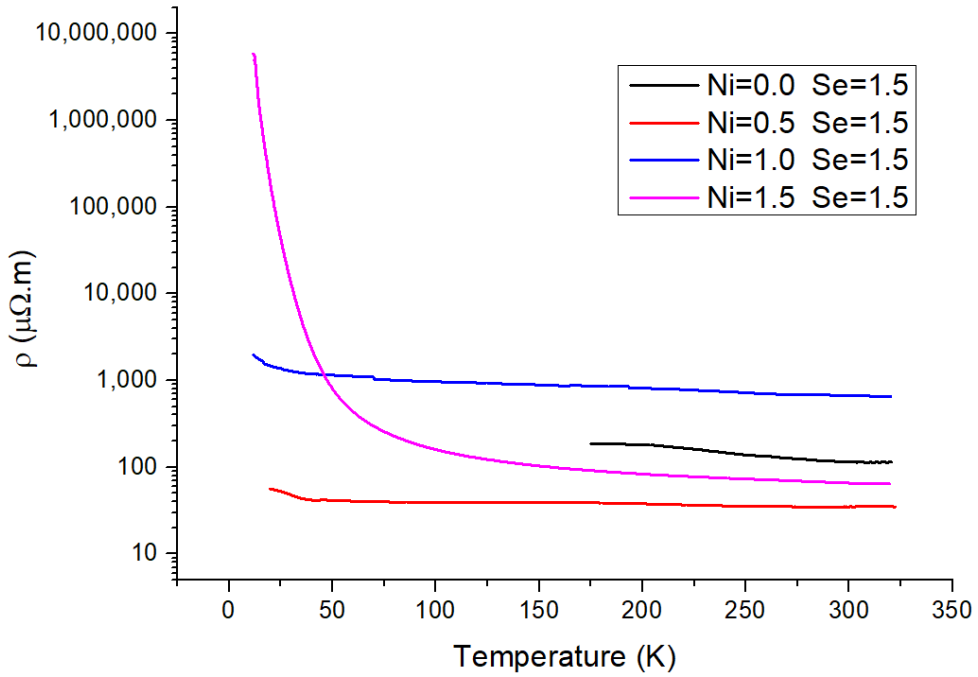

Fig. 172 Temperature dependence of Electrical resistivity of annealed samples following the formula $Cu_{12-x}Ni_xSb_4S_{11.5}Se_{1.5}$.

Hot-pressed samples-Electrical resistivity (ρ)

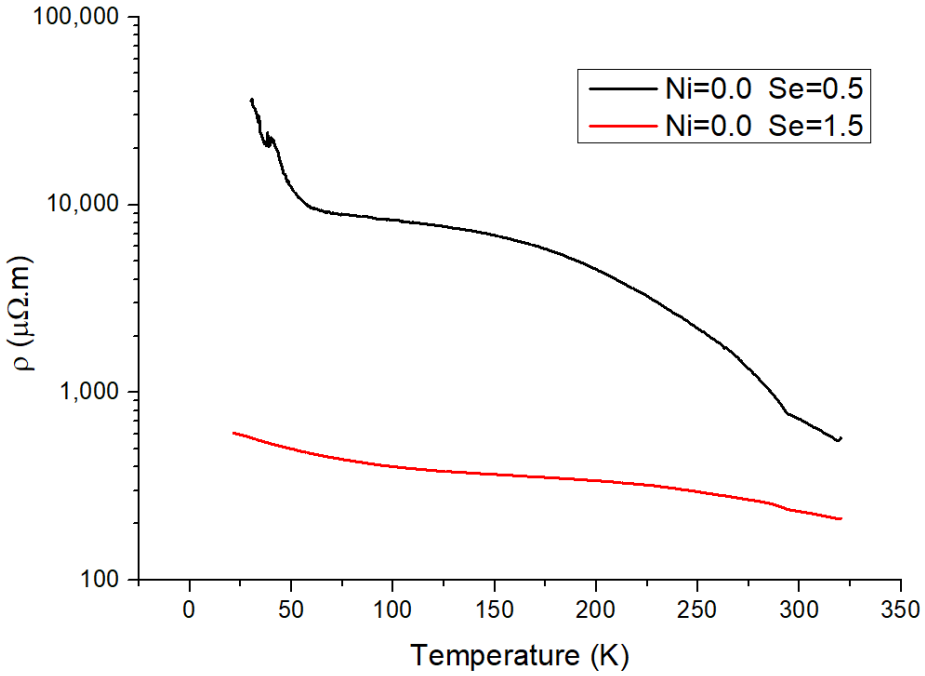

Fig. 173 Temperature dependence of Electrical resistivity of hot-pressed samples following the formula $Cu_{12}Sb_4S_{13-y}Se_y$.

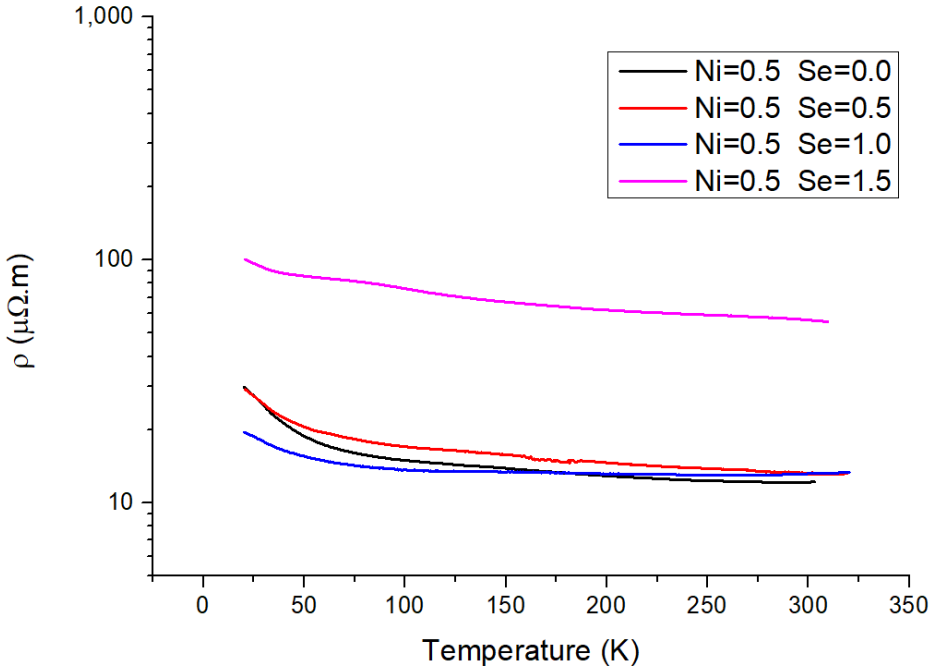

Fig. 174 Temperature dependence of Electrical resistivity of hot-pressed samples following the formula $Cu_{11.5}Ni_{0.5}Sb_4S_{13-y}Se_y$.

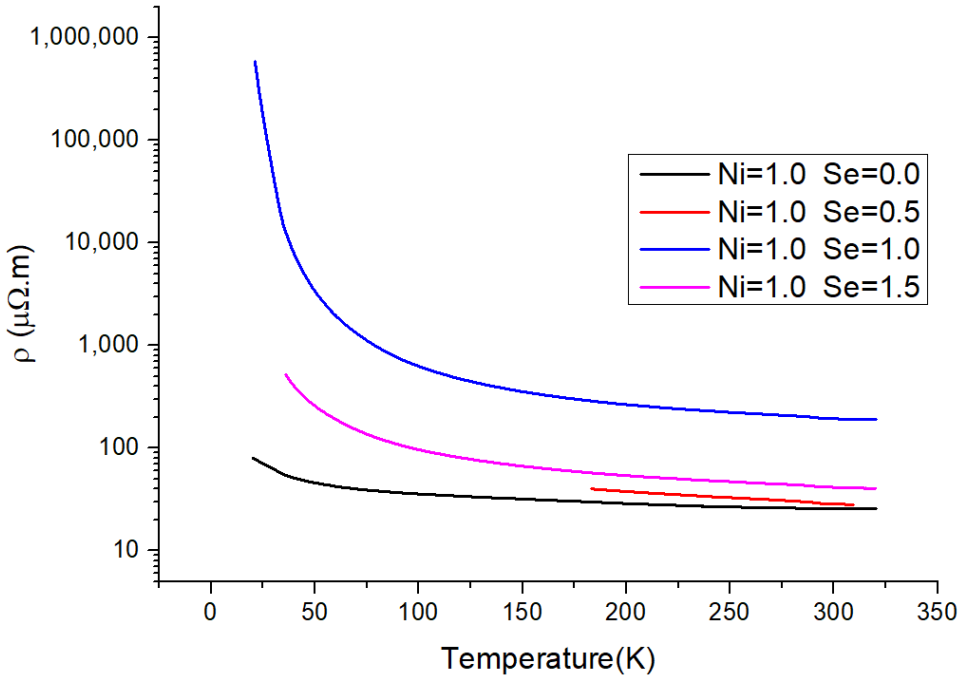

Fig. 175 Temperature dependence of Electrical resistivity of hot-pressed samples following the formula $Cu_{11}NiSb_4S_{13-y}Se_y$.

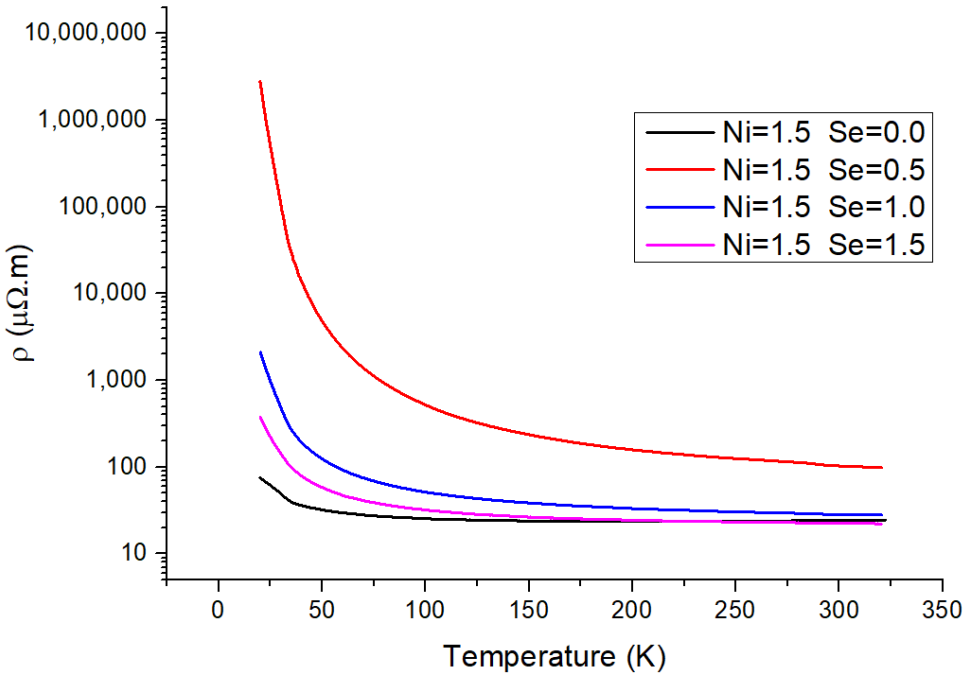

Fig. 176 Temperature dependence of Electrical resistivity of hot-pressed samples following the formula $Cu_{10.5}Ni_{1.5}Sb_4S_{13-y}Se_y$.

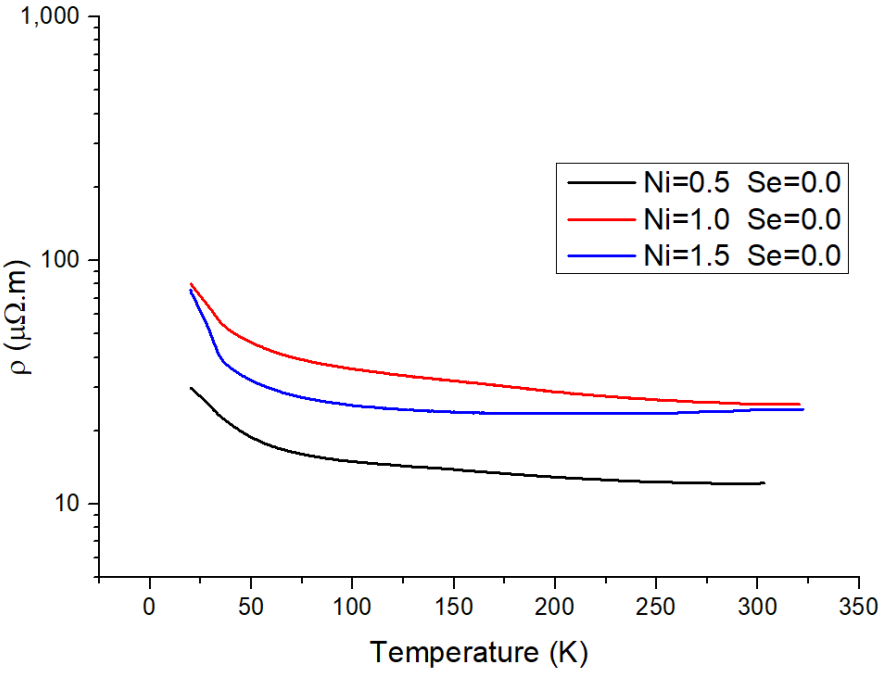

Fig. 177 Temperature dependence of Electrical resistivity of hot-pressed samples following the formula $Cu_{12-x}Ni_xSb_4S_{13}$.

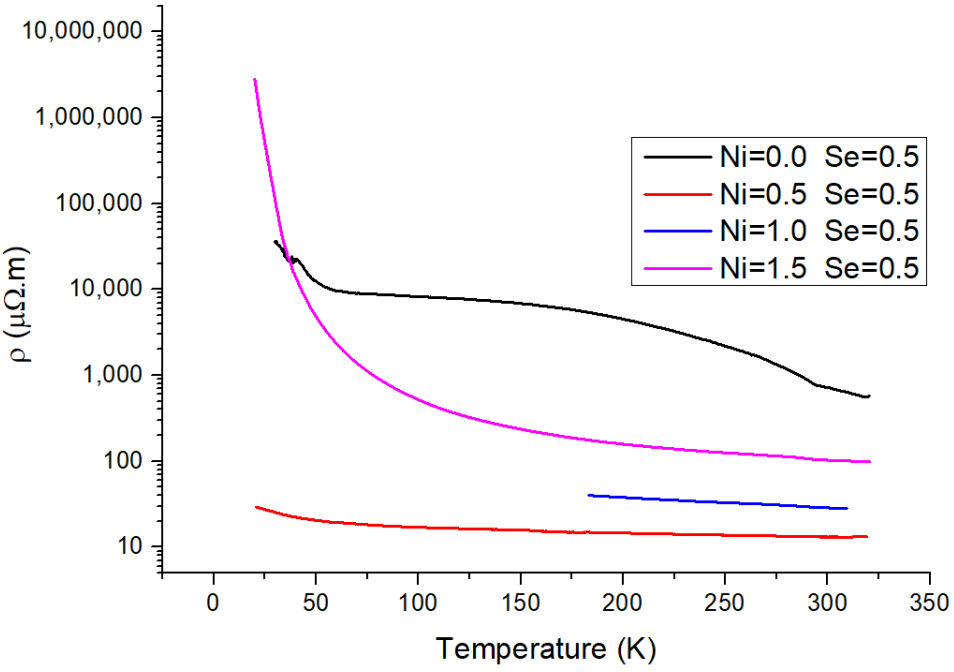

Fig. 178 Temperature dependence of Electrical resistivity of hot-pressed samples following the formula $Cu_{12-x}Ni_xSb_4S_{12.5}Se_{0.5}$.

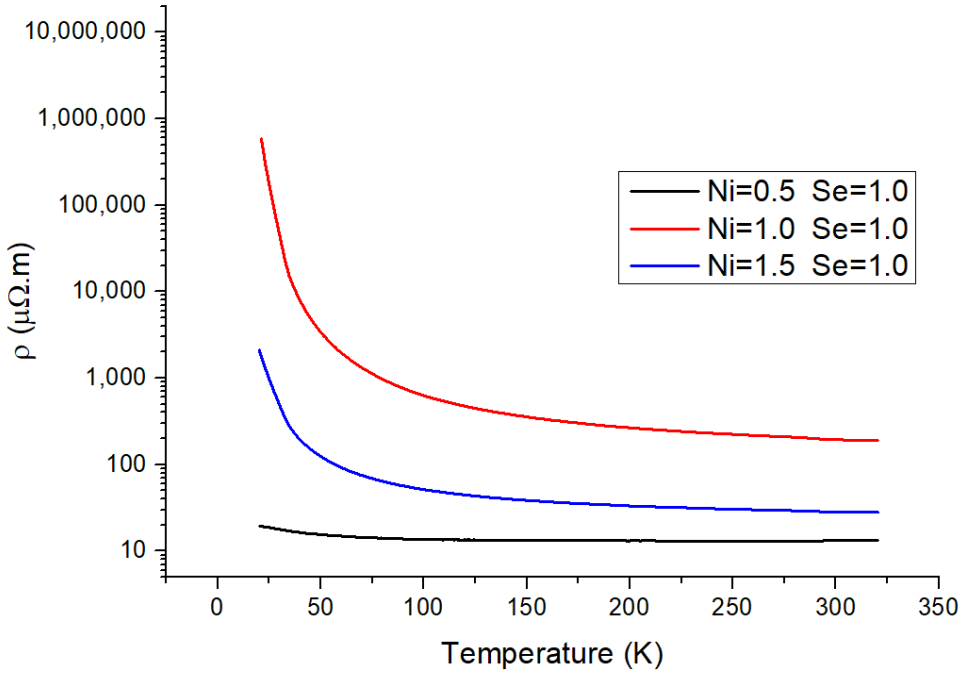

Fig. 179 Temperature dependence of Electrical resistivity of hot-pressed samples following the formula $Cu_{12-x}Ni_xSb_4S_{12}Se$.

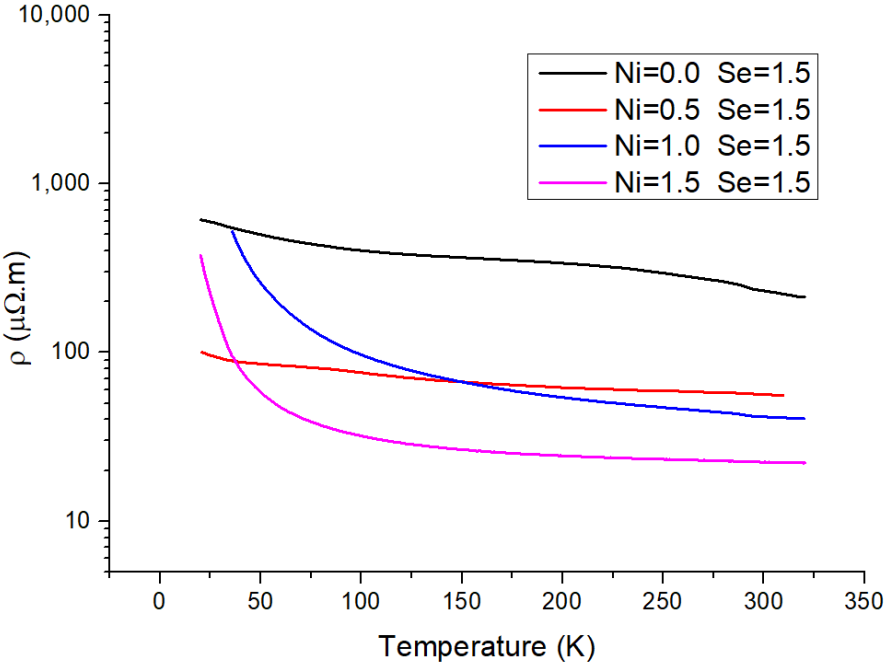

Fig. 180 Temperature dependence of Electrical resistivity of hot-pressed samples following the formula $Cu_{12-x}Ni_xSb_4S_{11.5}Se_{1.5}$.

ATTACHMENT 5: MEASUREMENTS OF SEEBECK COEFFICIENT

Annealed samples- Seebeck Coefficient

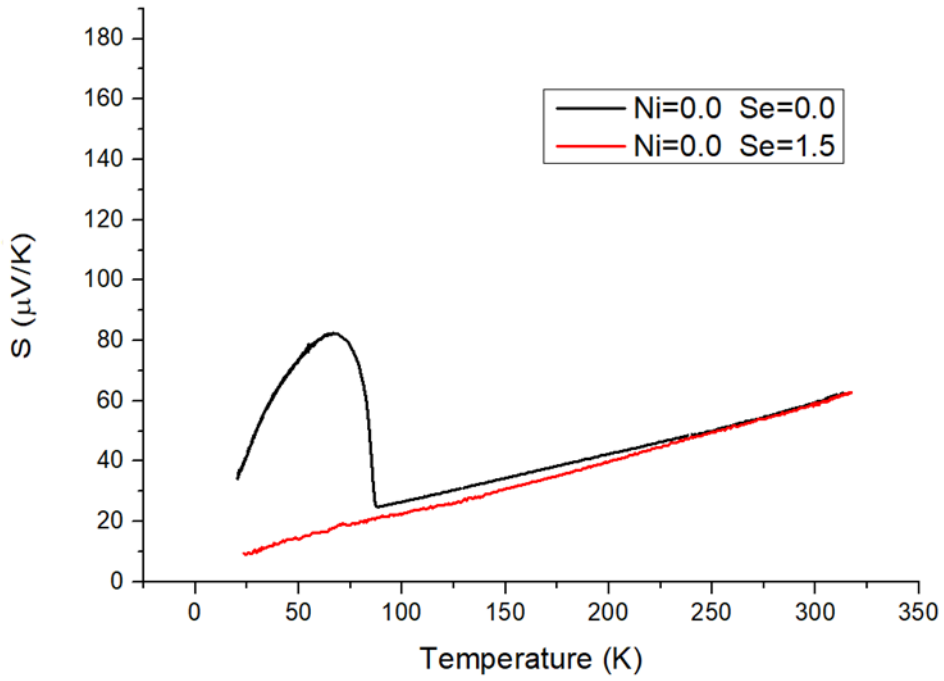

Fig. 181 Temperature dependence of Seebeck coefficient of annealed samples following the formula $Cu_{12}Sb_4S_{13-y}Se_y$.

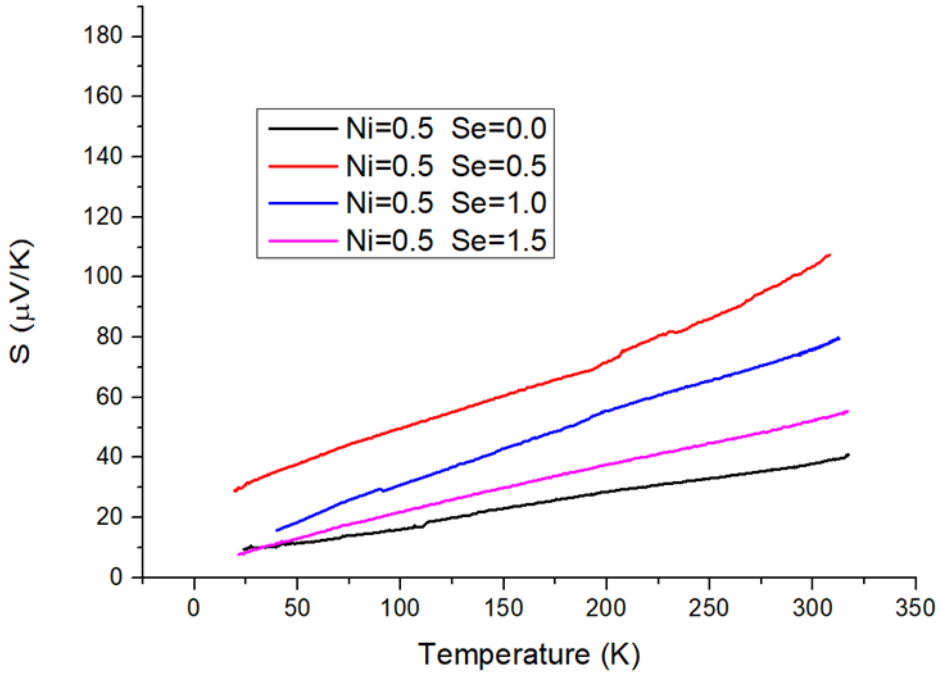

Fig. 182 Temperature dependence of Seebeck coefficient of annealed samples following the formula $Cu_{11.5}Ni_{0.5}Sb_4S_{13-y}Se_y$

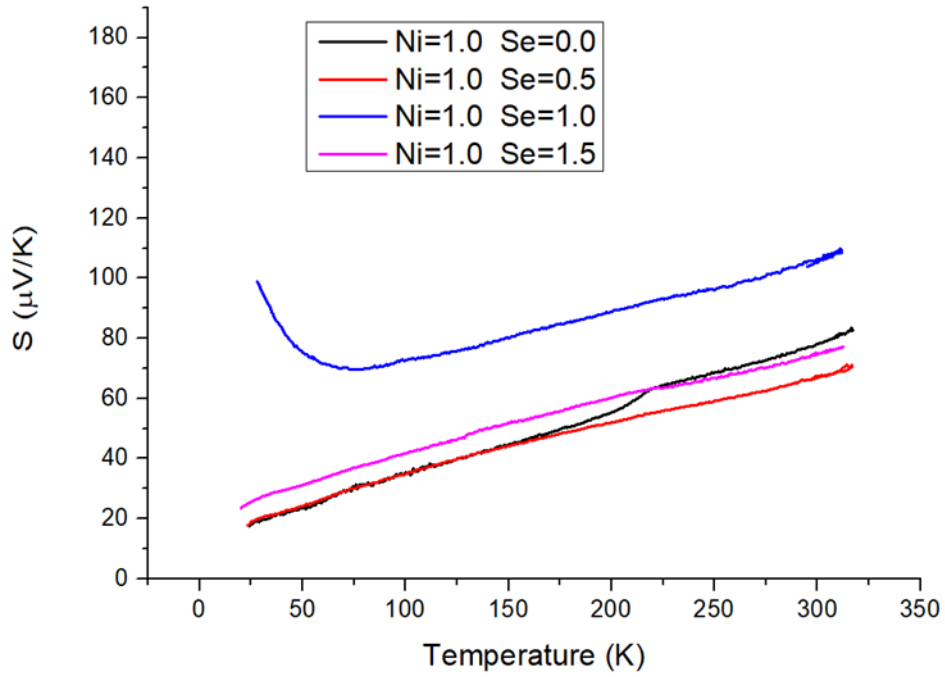

Fig. 183 Temperature dependence of Seebeck coefficient of annealed samples following the formula $Cu_{11}NiSb_4S_{13-y}Se_y$

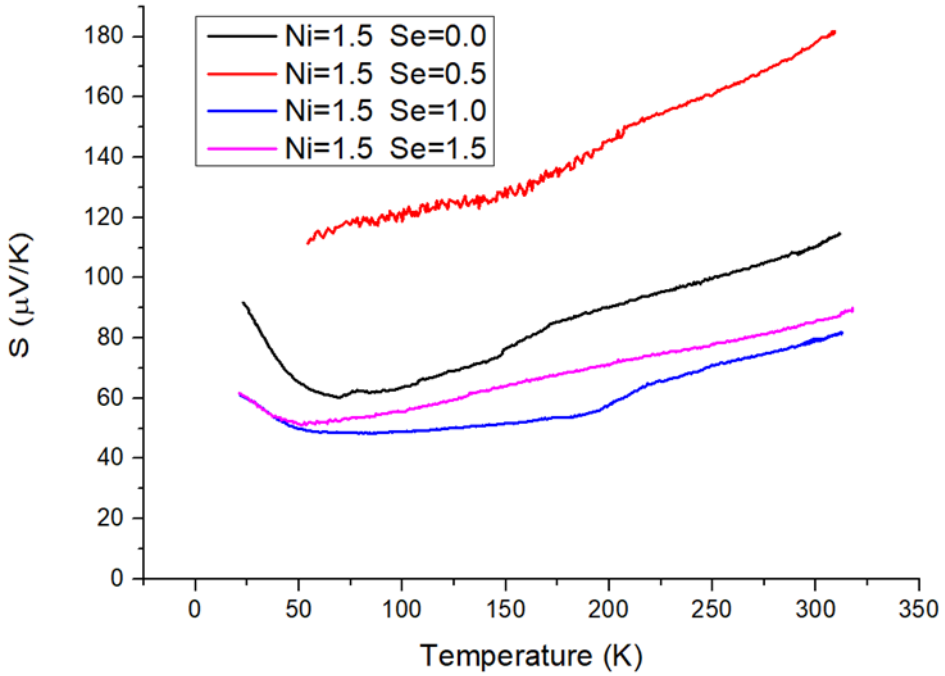

Fig. 184 Temperature dependence of Seebeck coefficient of annealed samples following the formula $Cu_{10.5}Ni_{1.5}Sb_4S_{13-y}Se_y$

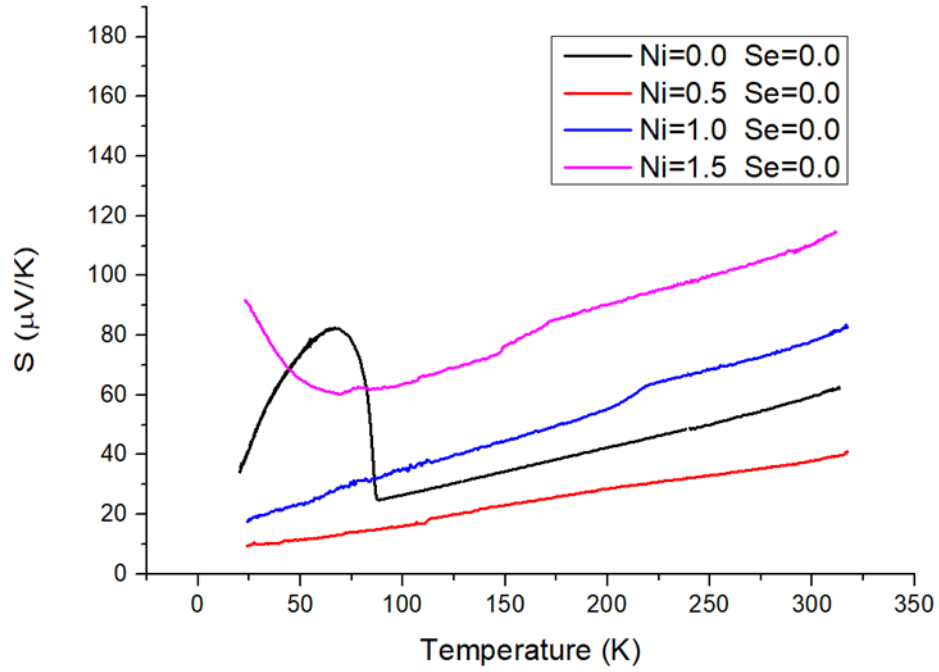

Fig. 185 Temperature dependence of Seebeck coefficient of annealed samples following the formula $Cu_{12-x}Ni_xSb_4S_{13}$

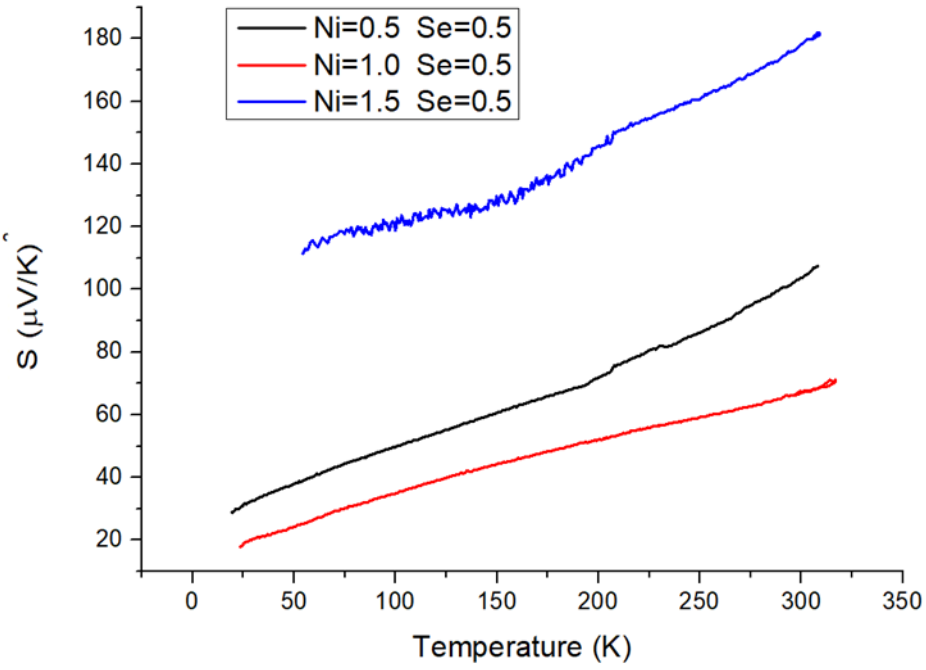

Fig. 186 Temperature dependence of Seebeck coefficient of annealed samples following the formula $Cu_{12-x}Ni_xSb_4S_{12.5}Se_{0.5}$

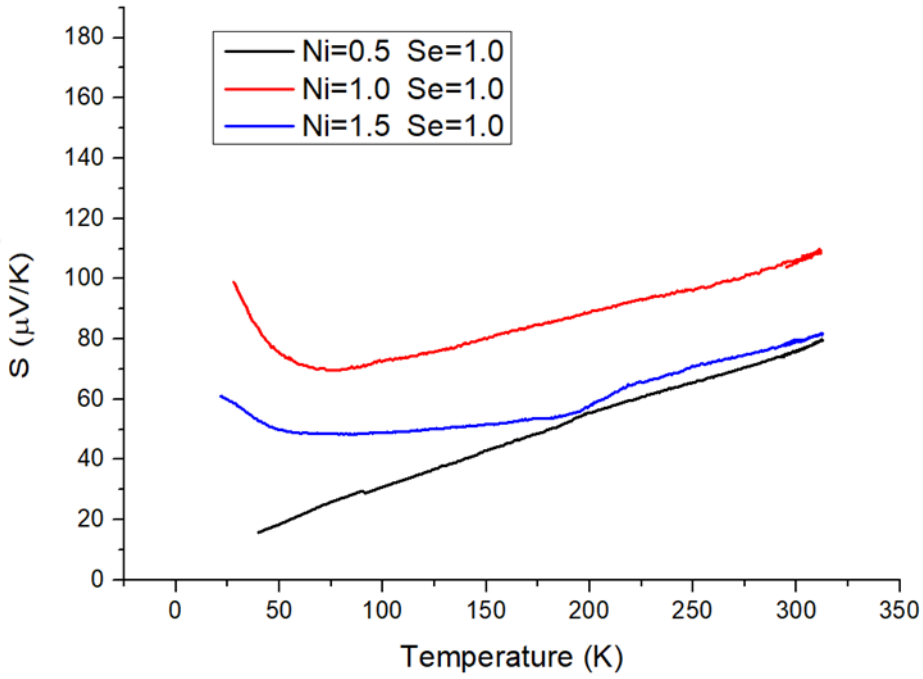

Fig. 187 Temperature dependence of Seebeck coefficient of annealed samples following the formula $Cu_{12-x}Ni_xSb_4S_{12}Se$

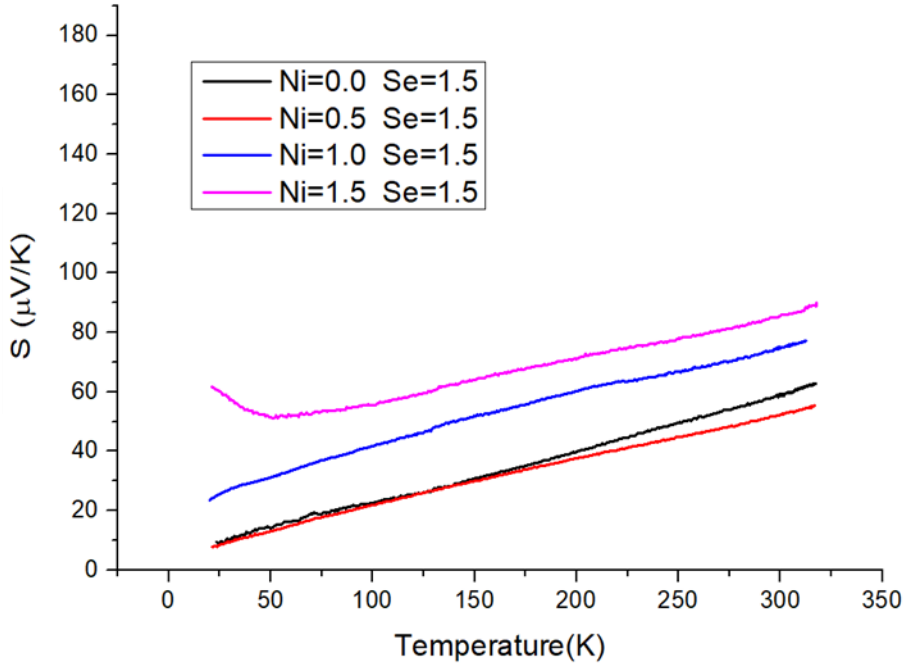

Fig. 188 Temperature dependence of Seebeck coefficient of annealed samples following the formula $Cu_{12-x}Ni_xSb_4S_{11.5}Se_{1.5}$

Hot-pressed samples- Seebeck Coefficient

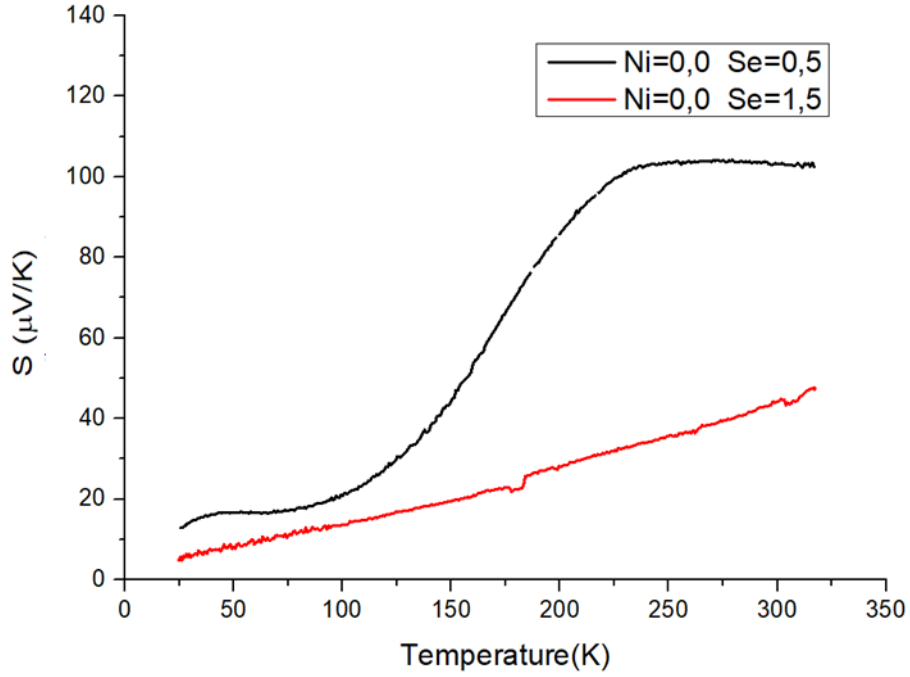

Fig. 189 Temperature dependence of Seebeck coefficient of hot-pressed samples following the formula $Cu_{12}Sb_4S_{13-y}Se_y$.

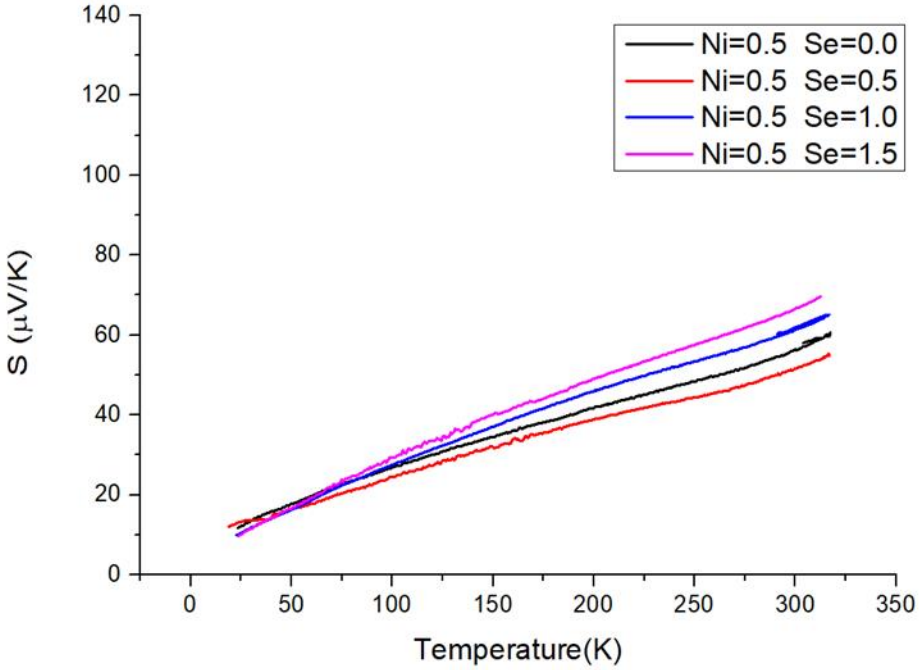

Fig. 190 Temperature dependence of Seebeck coefficient of hot-pressed samples following the formula $Cu_{11.5}Ni_{0.5}Sb_4S_{13-y}Se_y$

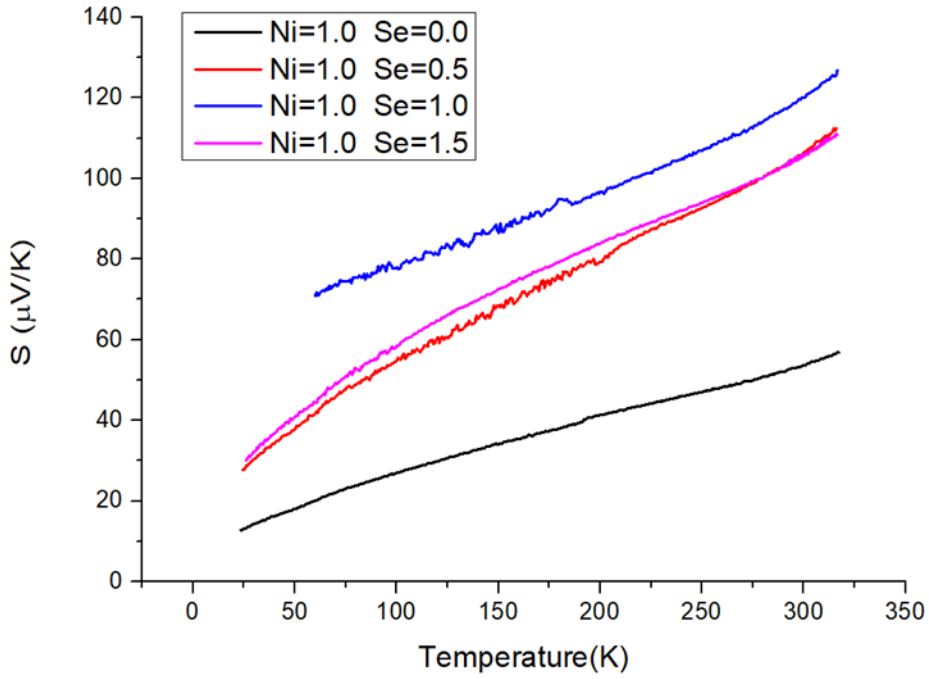

Fig. 191 Temperature dependence of Seebeck coefficient of hot-pressed samples following the formula $Cu_{11}NiSb_4S_{13-y}Se_y$

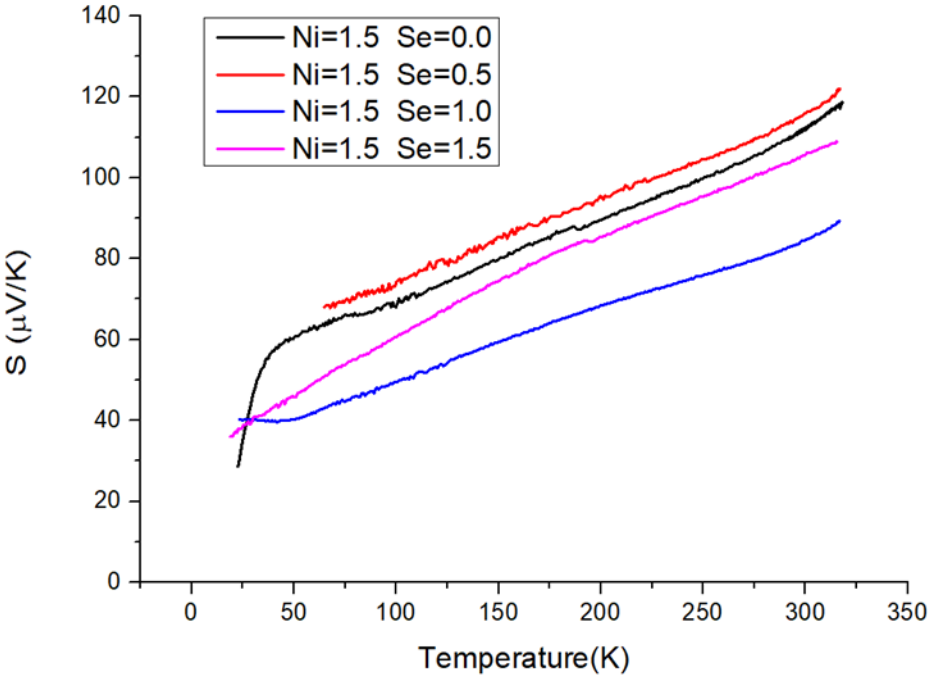

Fig. 192 Temperature dependence of Seebeck coefficient of hot-pressed samples following the formula $Cu_{10.5}Ni_{1.5}Sb_4S_{13-y}Se_y$

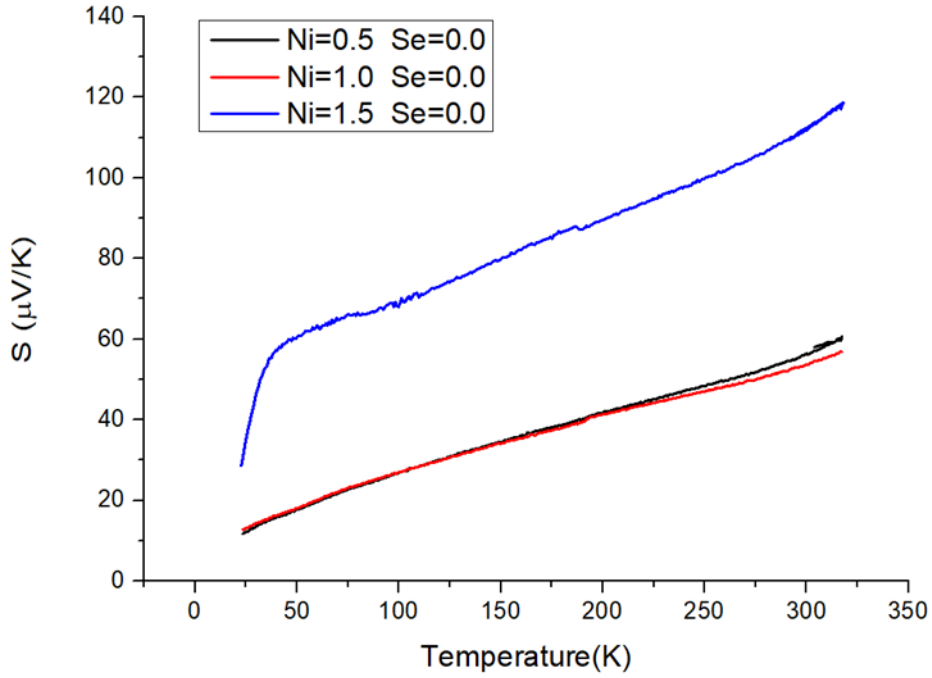

Fig. 193 Temperature dependence of Seebeck coefficient of hot-pressed samples following the formula $Cu_{12-x}Ni_xSb_4S_{13}$

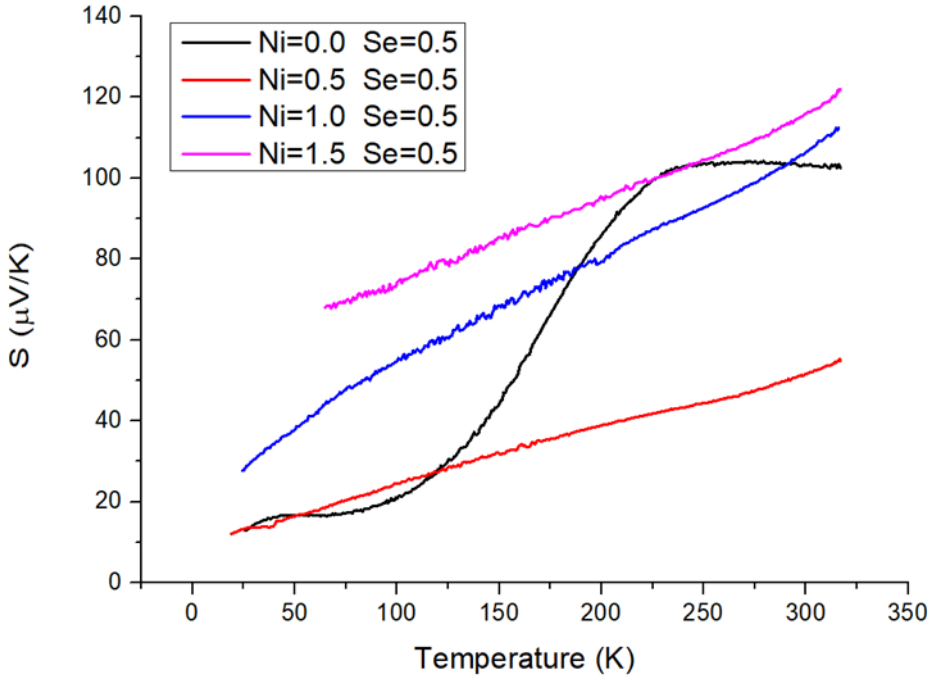

Fig. 194 Temperature dependence of Seebeck coefficient of hot-pressed samples following the formula $Cu_{12-x}Ni_xSb_4S_{12.5}Se_{0.5}$

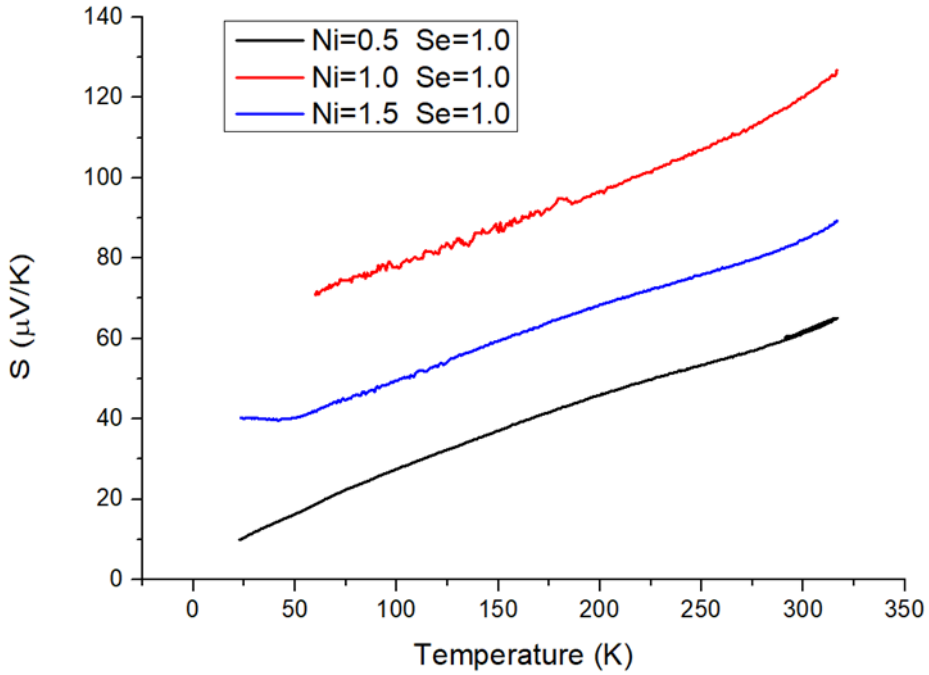

Fig. 195 Temperature dependence of Seebeck coefficient of hot-pressed samples following the formula $Cu_{12-x}Ni_xSb_4S_{12}Se$

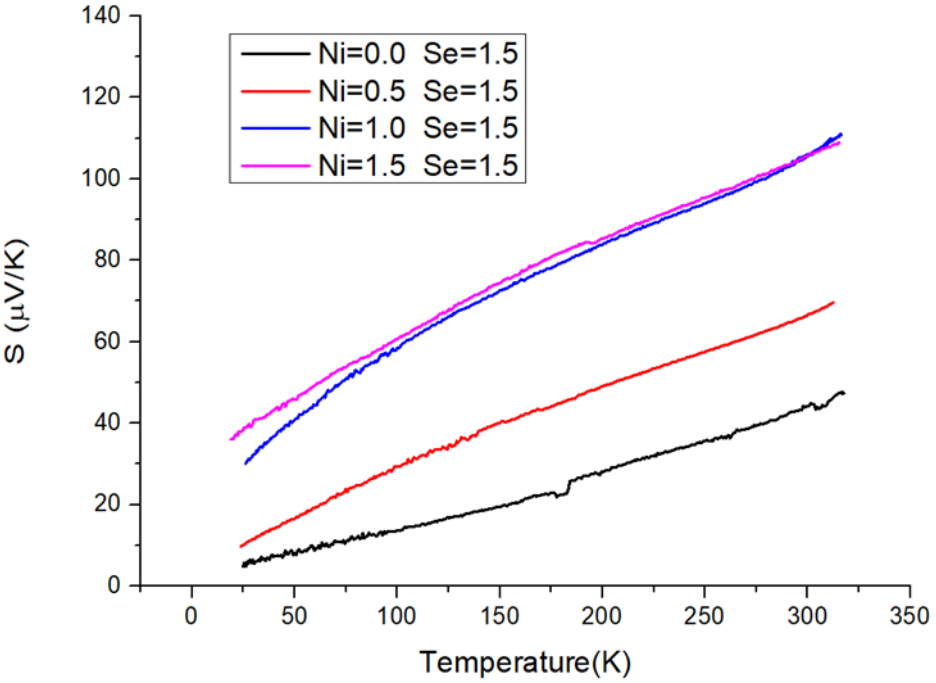

Fig. 196 Temperature dependence of Seebeck coefficient of hot-pressed samples following the formula $Cu_{12-x}Ni_xSb_4S_{11.5}Se_{1.5}$

ATTACHMENT 6: POWER FACTOR

Annealed samples-Power Factor

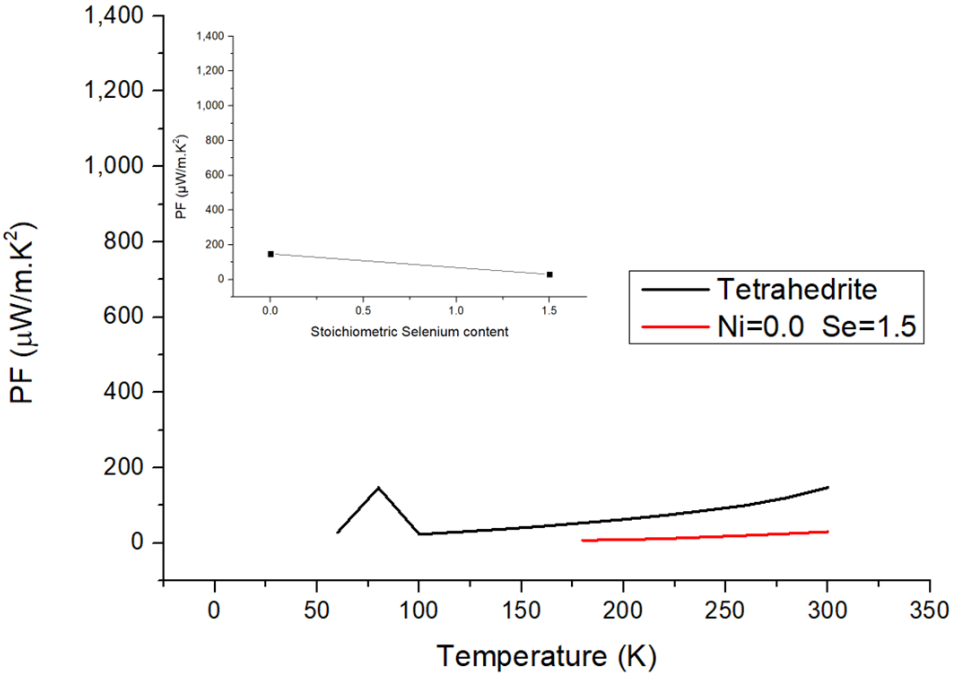

Fig. 197 Temperature dependence of PF of annealed samples following the formula $Cu_{12}Sb_4S_{13-y}Se_y$. In closed, the PF at 300 K shown as a function of stoichiometric Selenium content (y)

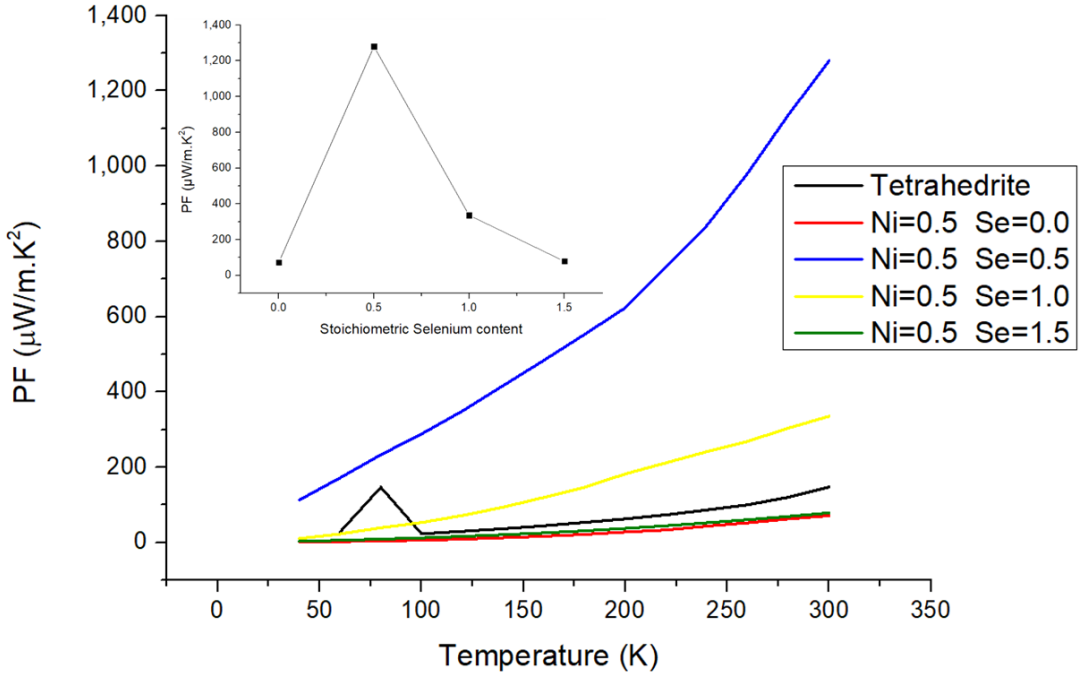

Fig. 198 Temperature dependence of PF of annealed samples following the formula $Cu_{11.5}Ni_{0.5}Sb_4S_{13-y}Se_y$ compared to undoped tetrahedrite ($Cu_{12}Sb_4S_{13}$). In closed, the PF at 300 K shown as a function of stoichiometric Selenium content (y)

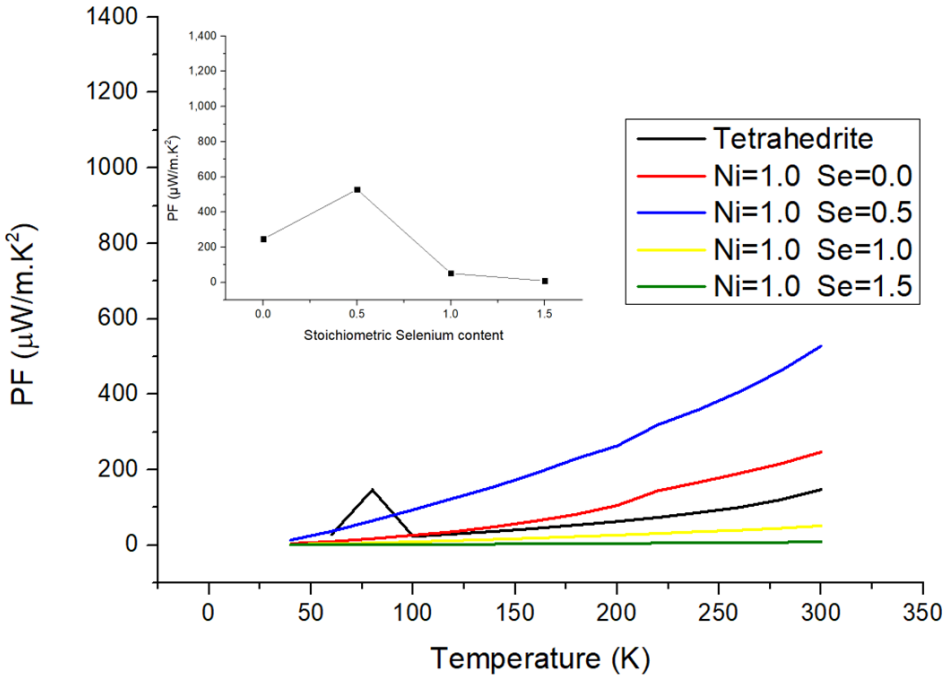

Fig. 199 Temperature dependence of PF of annealed samples following the formula $Cu_{11}NiSb_4S_{13-y}Se_y$ compared to undoped tetrahedrite ($Cu_{12}Sb_4S_{13}$). In closed, the PF at 300 K shown as a function of stoichiometric Selenium content (y)

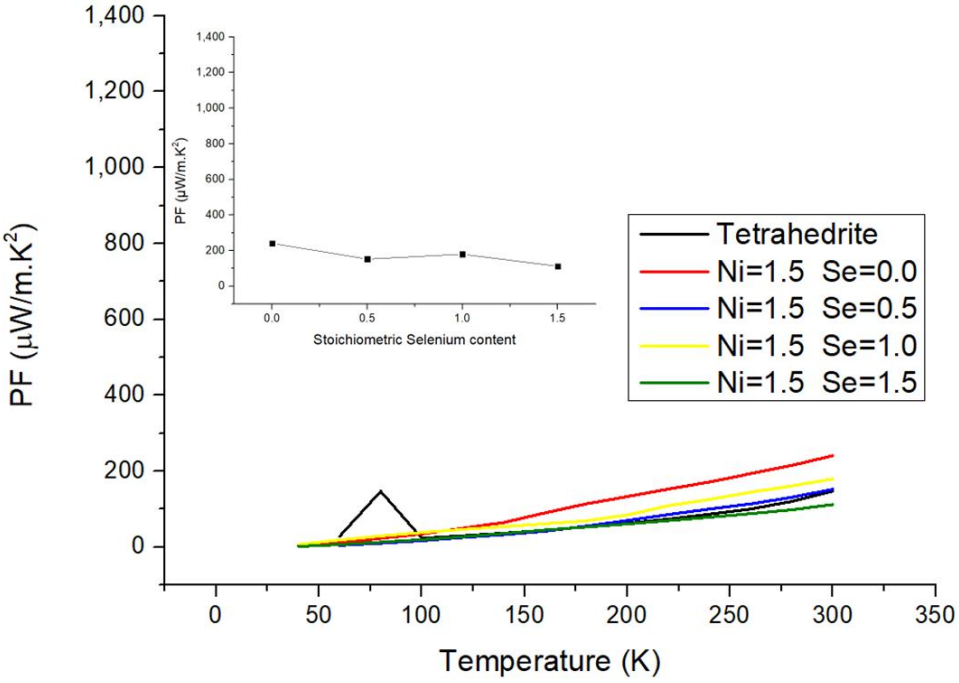

Fig. 200 Temperature dependence of PF of annealed samples following the formula $Cu_{10.5}Ni_{1.5}Sb_4S_{13-y}Se_y$ compared to undoped tetrahedrite ($Cu_{12}Sb_4S_{13}$). In closed, the PF at 300 K shown as a function of stoichiometric Selenium content (y)

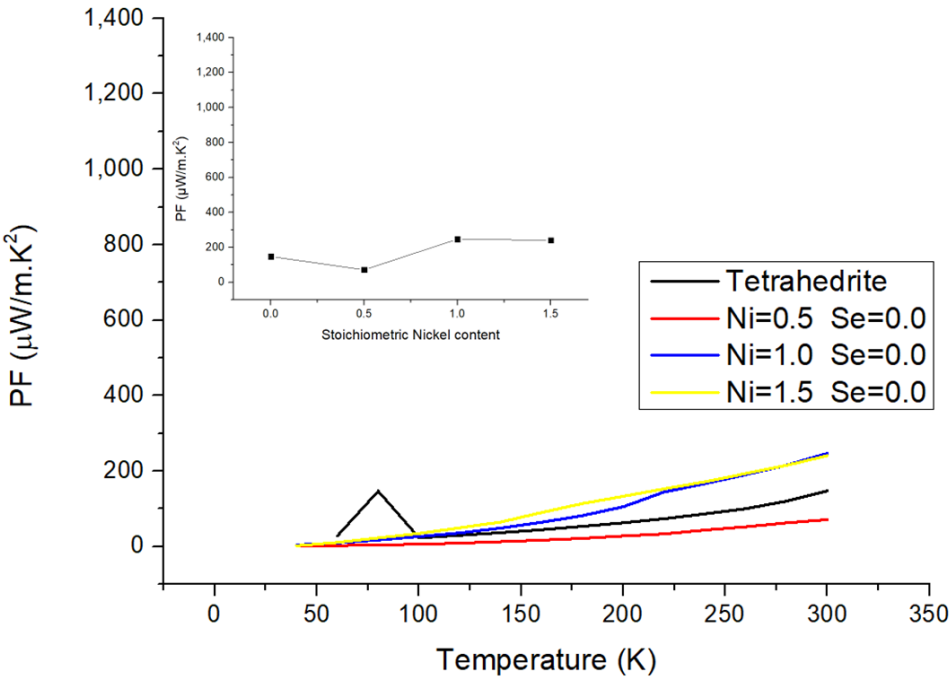

Fig. 201 Temperature dependence of PF of annealed samples following the formula $Cu_{12-x}Ni_xSb_4S_{13}$ compared to undoped tetrahedrite ($Cu_{12}Sb_4S_{13}$). In closed, the PF at 300 K shown as a function of stoichiometric Nickel content (x)

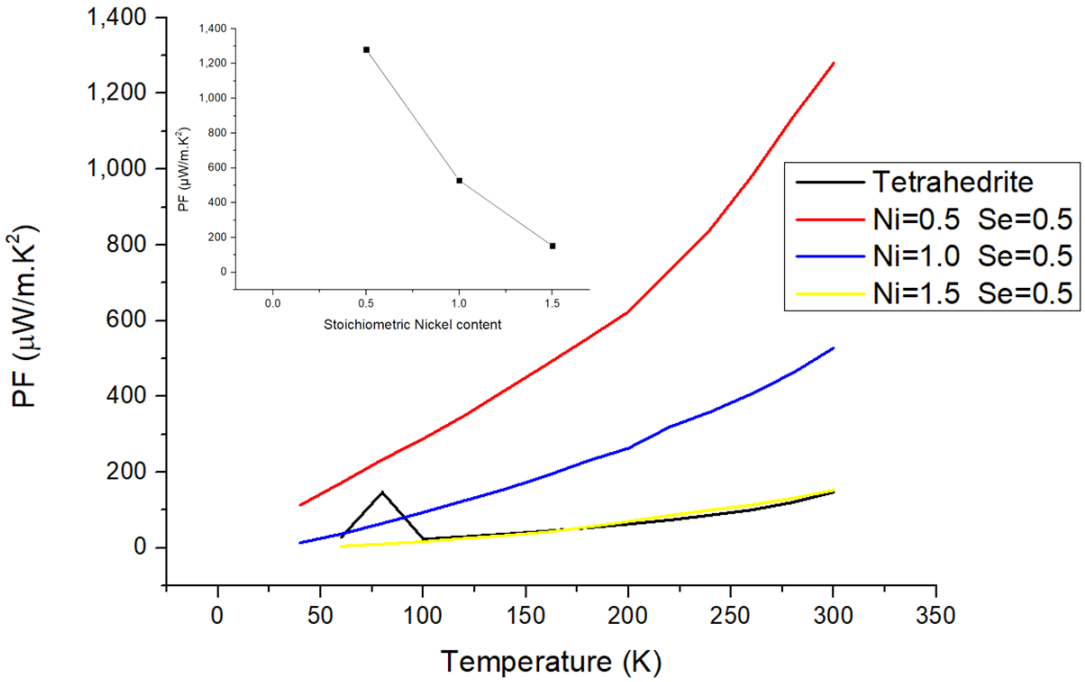

Fig. 202 Temperature dependence of PF of annealed samples following the formula $Cu_{12-x}Ni_xSb_4S_{12.5}Se_{0.5}$ compared to undoped tetrahedrite ($Cu_{12}Sb_4S_{13}$). In closed, the PF at 300 K shown as a function of stoichiometric Nickel content (x)

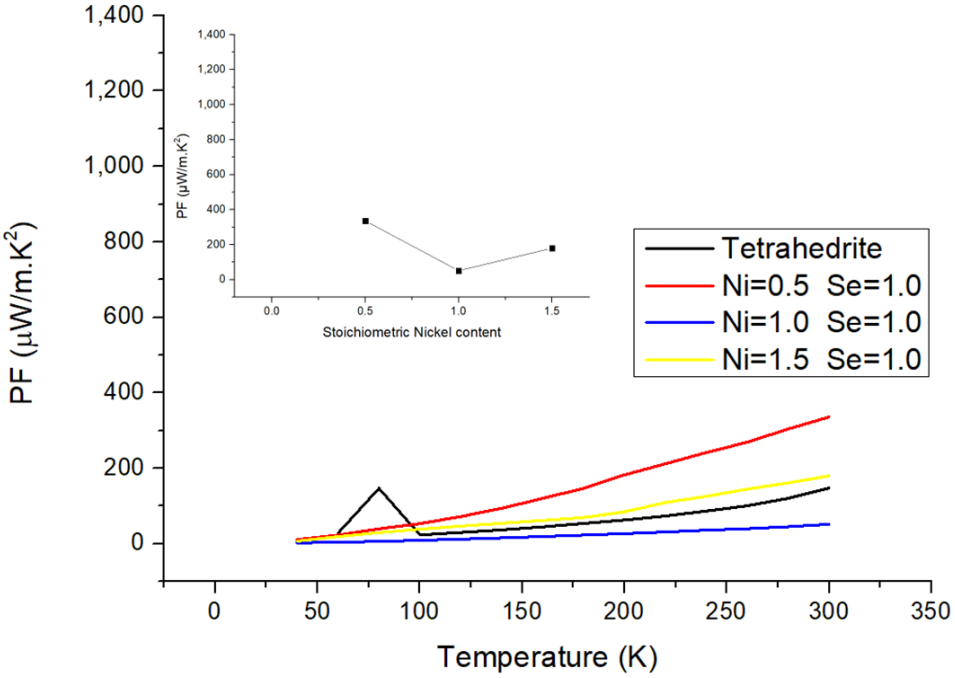

Fig. 203 Temperature dependence of PF of annealed samples following the formula $Cu_{12-x}Ni_xSb_4S_{12}Se$ compared to undoped tetrahedrite ($Cu_{12}Sb_4S_{13}$). In closed, the PF at 300 K shown as a function of stoichiometric Nickel content (x)

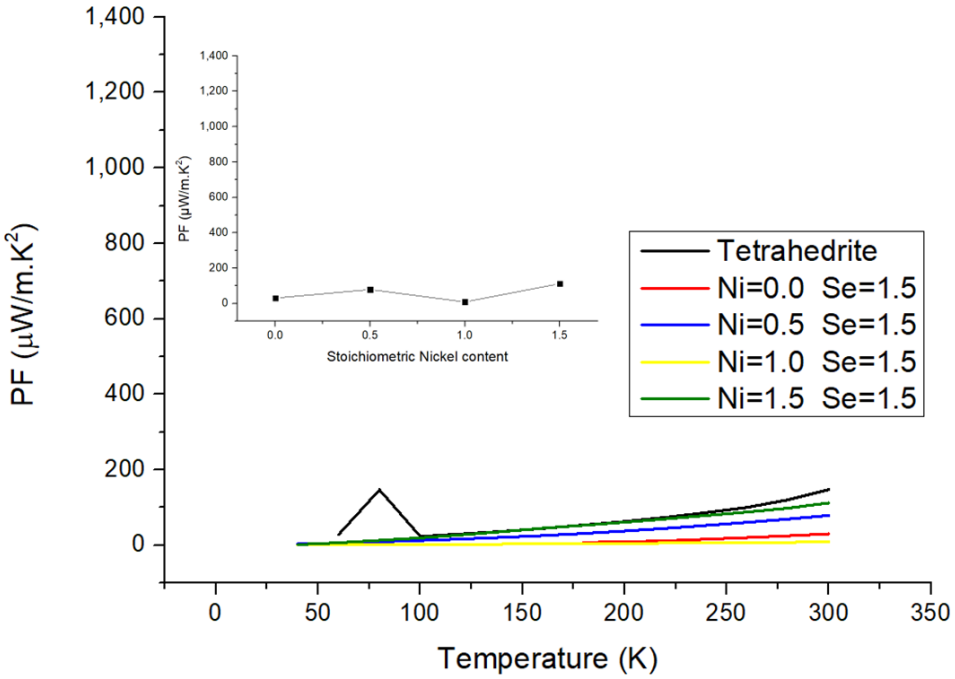

Fig. 204 Temperature dependence of PF of annealed samples following the formula $Cu_{12-x}Ni_xSb_4S_{11.5}Se_{1.5}$ compared to undoped tetrahedrite ($Cu_{12}Sb_4S_{13}$). In closed, the PF at 300 K shown as a function of stoichiometric Nickel content (x)

Hot-pressed samples- Power factor

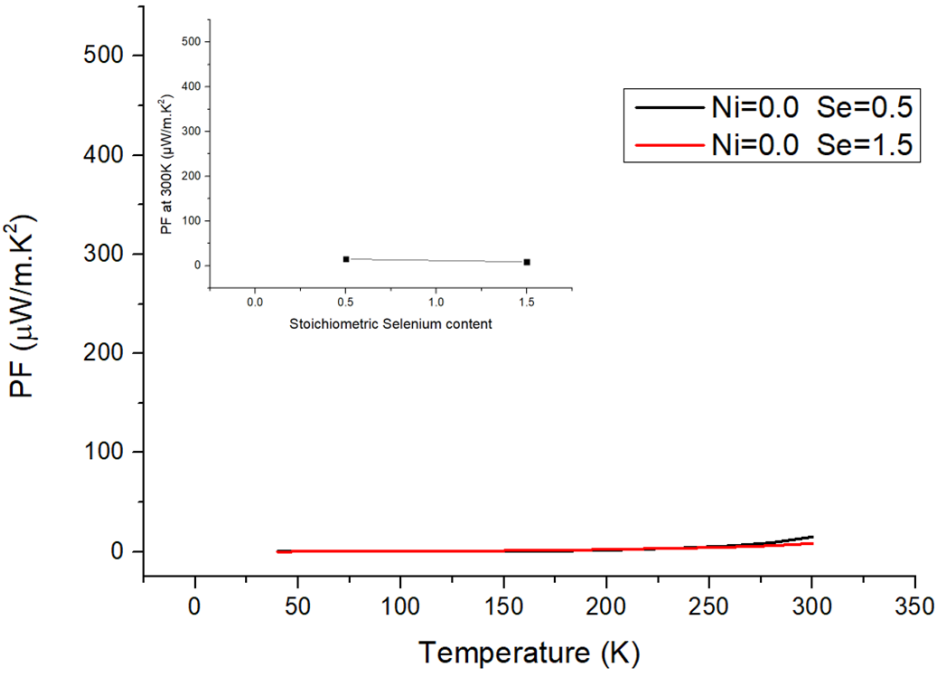

Fig. 205 Temperature dependence of PF of hot-pressed samples following the formula $Cu_{12}Sb_4S_{13-y}Se_y$. In closed, the PF at 300 K shown as a function of stoichiometric Selenium content (y)

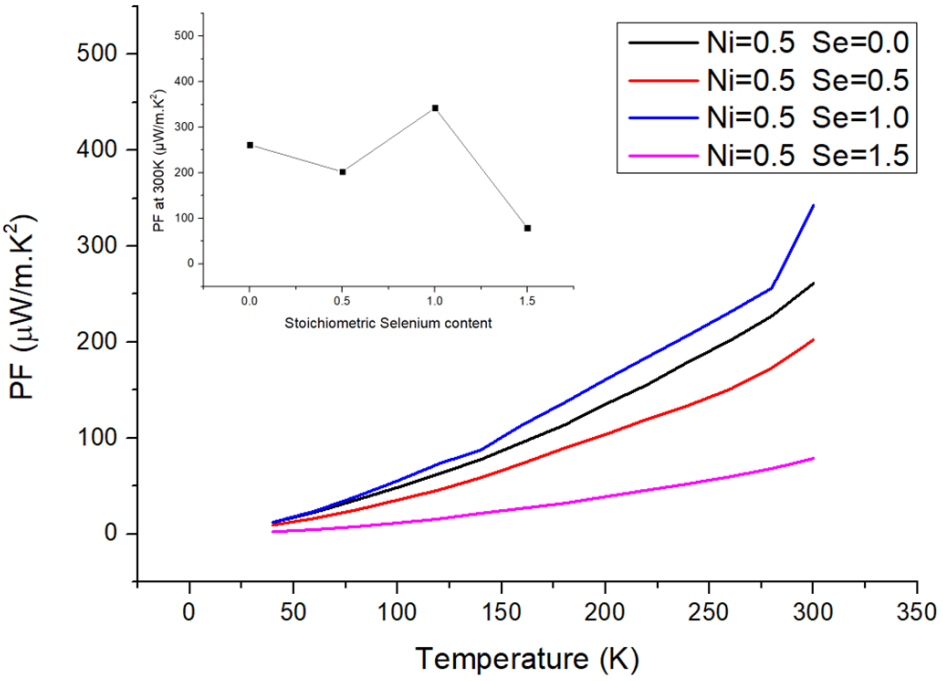

Fig. 206 Temperature dependence of PF of hot-pressed samples following the formula $Cu_{11.5}Ni_{0.5}Sb_4S_{13-y}Se_y$. In closed, the PF at 300 K shown as a function of stoichiometric Selenium content (y)

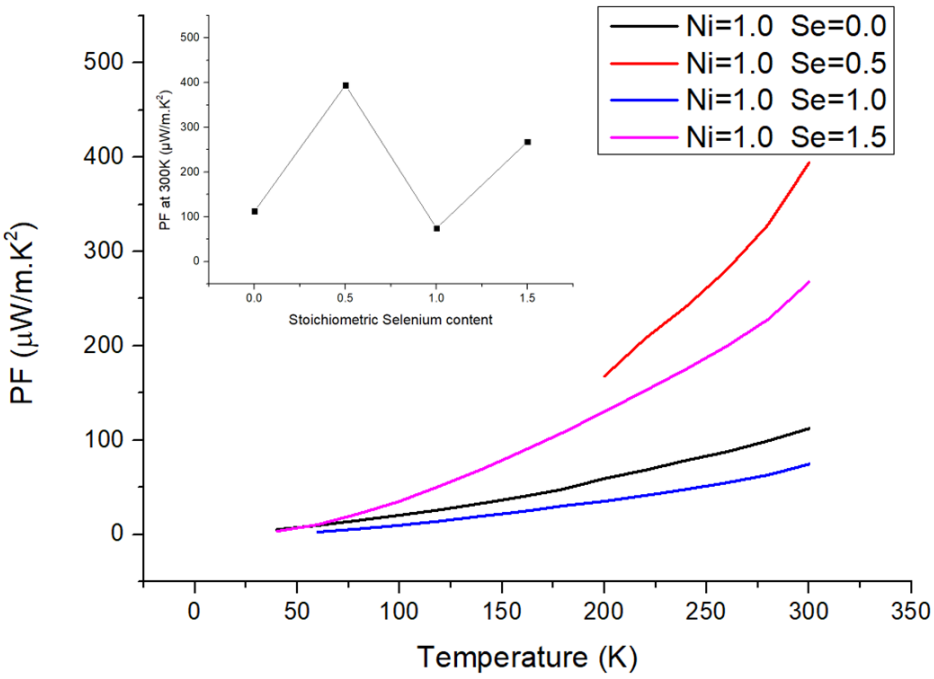

Fig. 207 Temperature dependence of PF of hot-pressed samples following the formula $Cu_{11}NiSb_4S_{13-y}Se_y$. In closed, the PF at 300 K shown as a function of stoichiometric Selenium content (y)

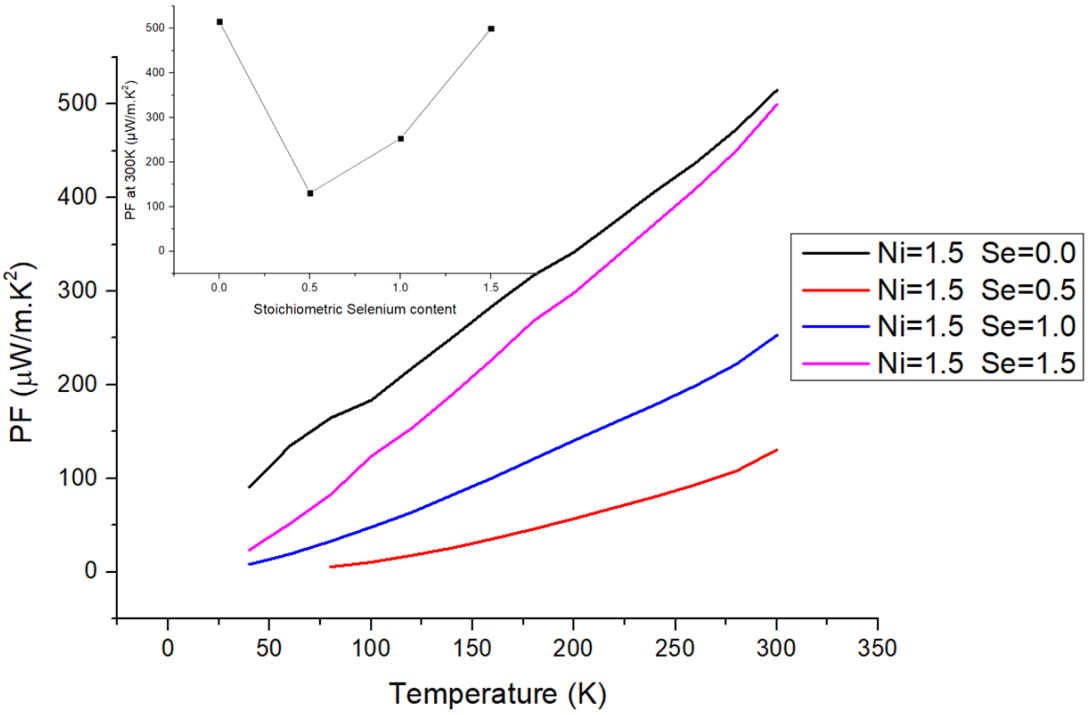

Fig. 208 Temperature dependence of PF of hot-pressed samples following the formula $Cu_{10.5}Ni_{1.5}Sb_4S_{13-y}Se_y$. In closed, the PF at 300 K shown as a function of stoichiometric Selenium content (y)

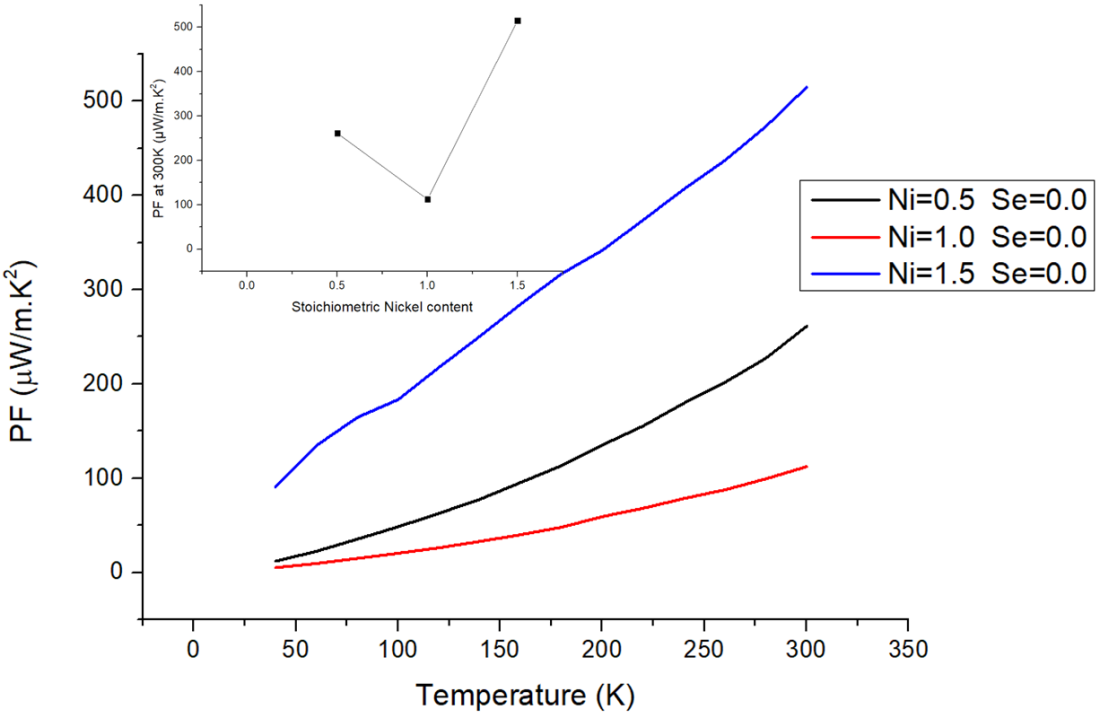

Fig. 209 Temperature dependence of PF of hot-pressed samples following the formula $Cu_{12-x}Ni_xSb_4S_{13}$. In closed, the PF at 300 K shown as a function of stoichiometric Nickel content (x)

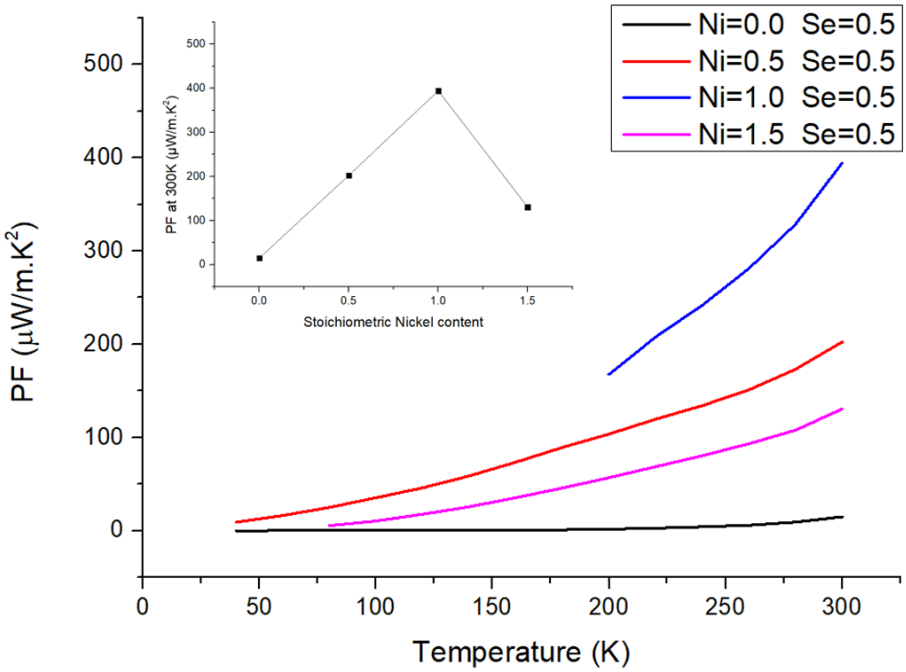

Fig. 210 Temperature dependence of PF of hot-pressed samples following the formula $Cu_{12-x}Ni_xSb_4S_{12.5}Se_{0.5}$. In closed, the PF at 300 K shown as a function of stoichiometric Nickel content (x)

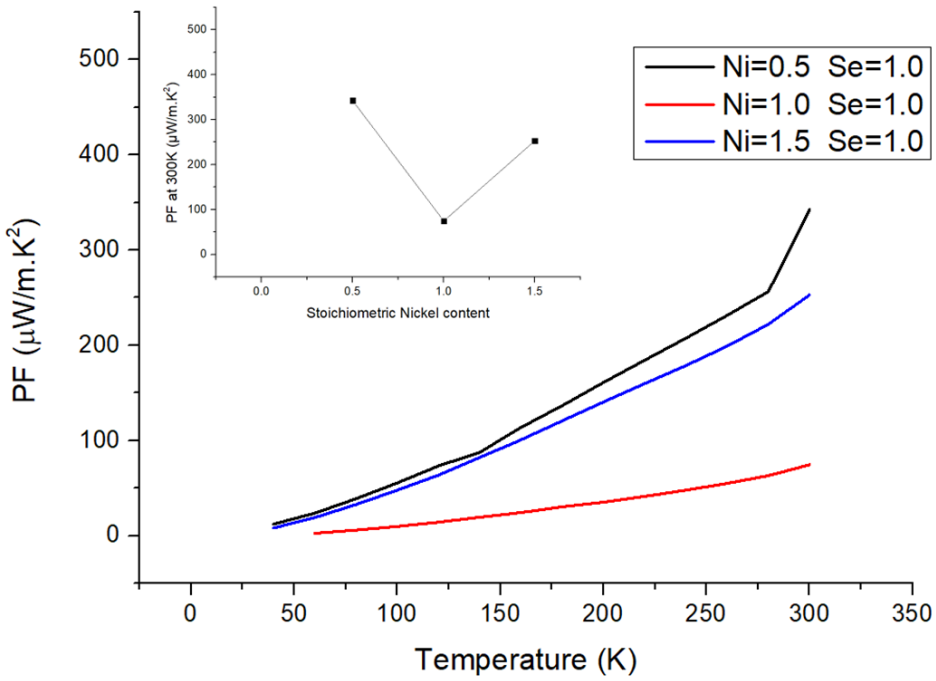

Fig. 211 Temperature dependence of PF of hot-pressed samples following the formula $Cu_{12-x}Ni_xSb_4S_{12}Se$. In closed, the PF at 300 K shown as a function of stoichiometric Nickel content (x)

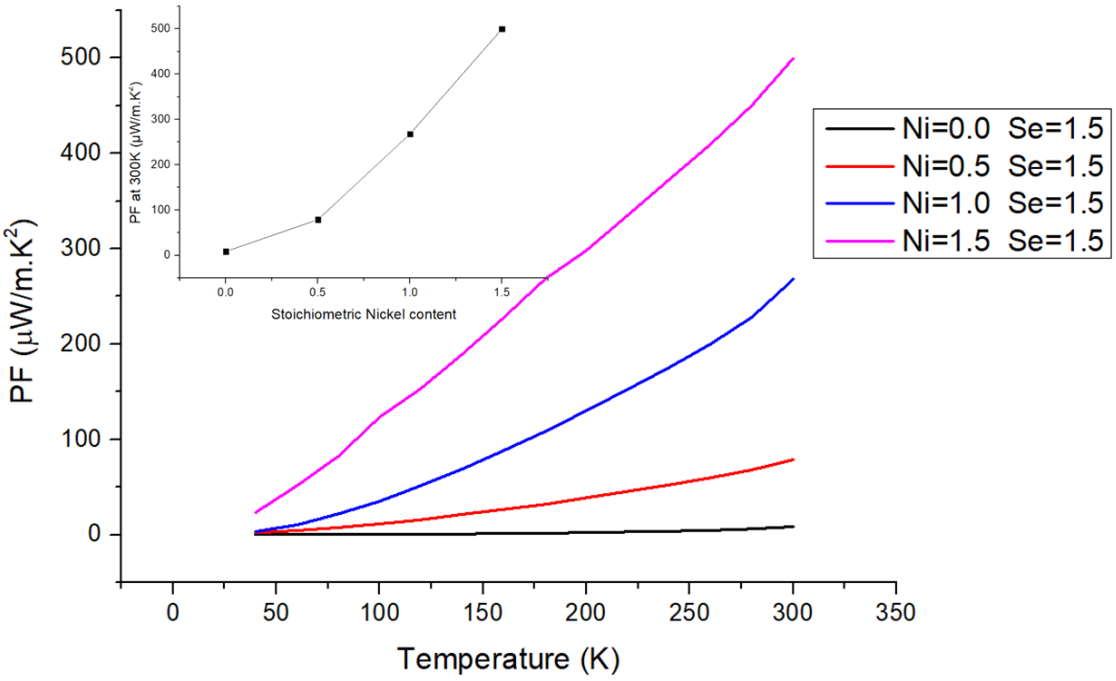

Fig. 212 Temperature dependence of PF of hot-pressed samples following the formula $Cu_{12-x}Ni_xSb_4S_{11.5}Se_{1.5}$. In closed, the PF at 300 K shown as a function of stoichiometric Nickel content (x)

ATTACHMENT 7: FIGURE OF MERIT

Annealed samples-Figure of Merit

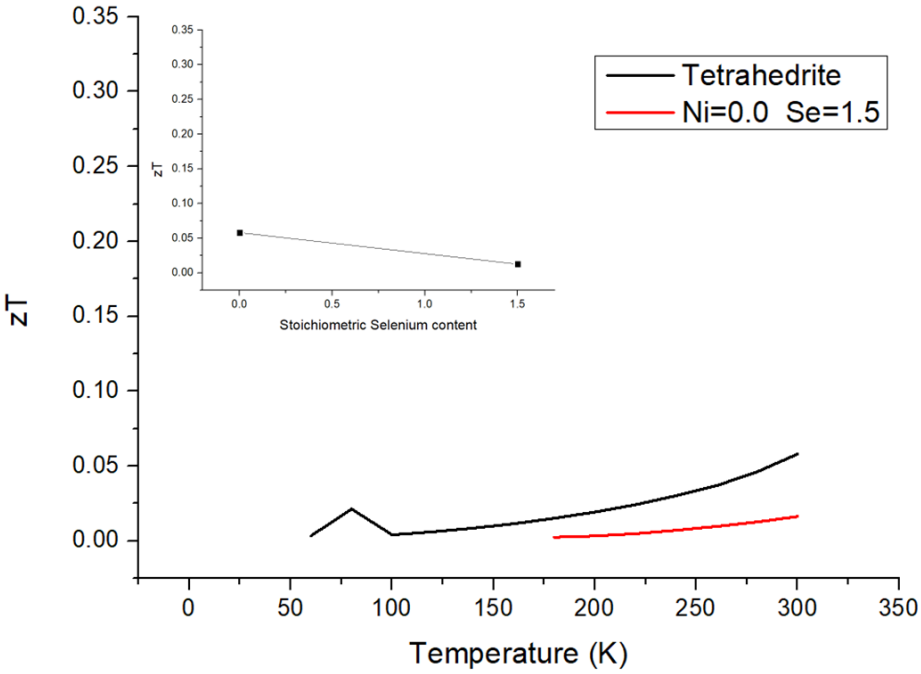

Fig. 213 Temperature dependence of zT of annealed samples following the formula $Cu_{12}Sb_4S_{13-y}Se_y$ In closed, the zT at 300 K shown as a function of stoichiometric Selenium content (y)

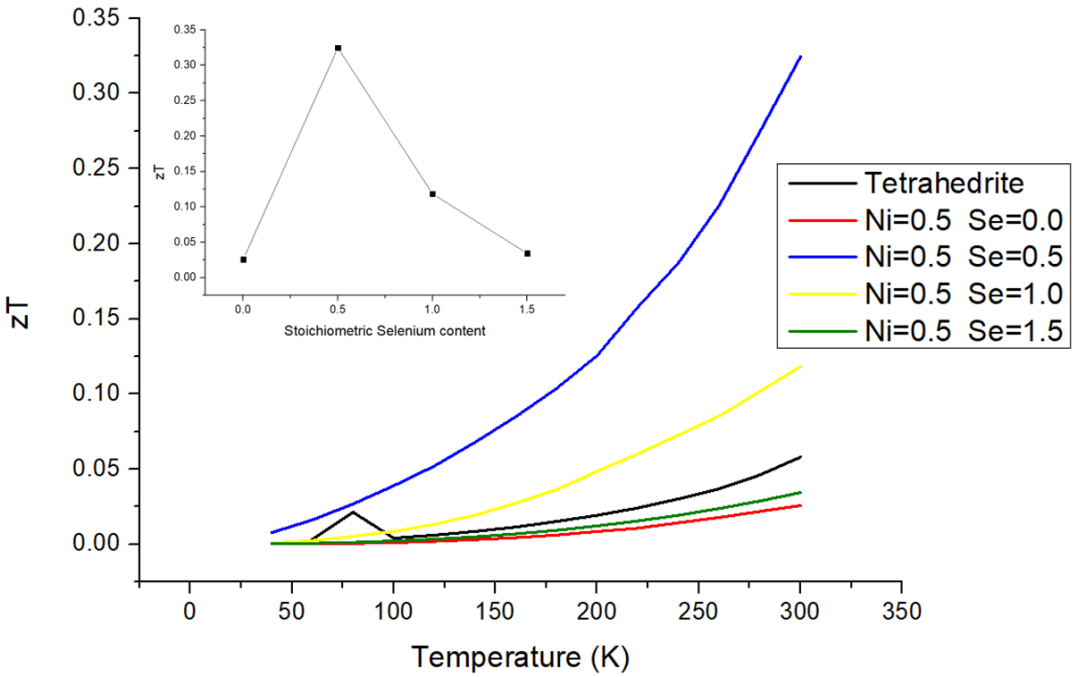

Fig. 214 Temperature dependence of zT of annealed samples following the formula $Cu_{11.5}Ni_{0.5}Sb_4S_{13-y}Se_y$ compared to undoped tetrahedrite ($Cu_{12}Sb_4S_{13}$). In closed, the zT at 300 K shown as a function of stoichiometric Selenium content (y)

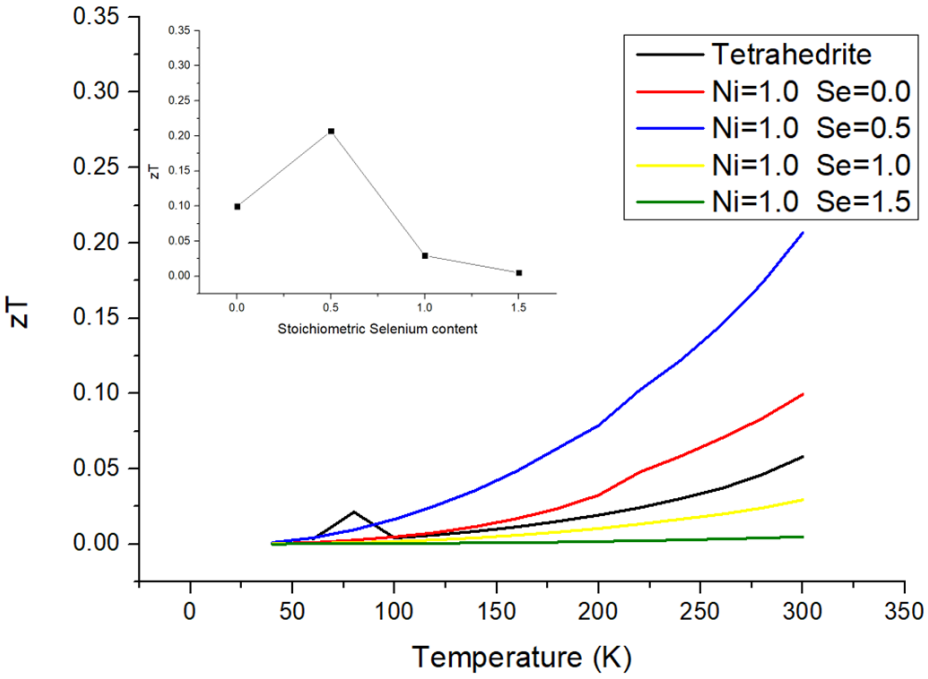

Fig. 215 Temperature dependence of zT of annealed samples following the formula $Cu_{11}NiSb_4S_{13-y}Se_y$ compared to undoped tetrahedrite ($Cu_{12}Sb_4S_{13}$). In closed, the zT at 300 K shown as a function of stoichiometric Selenium content (y)

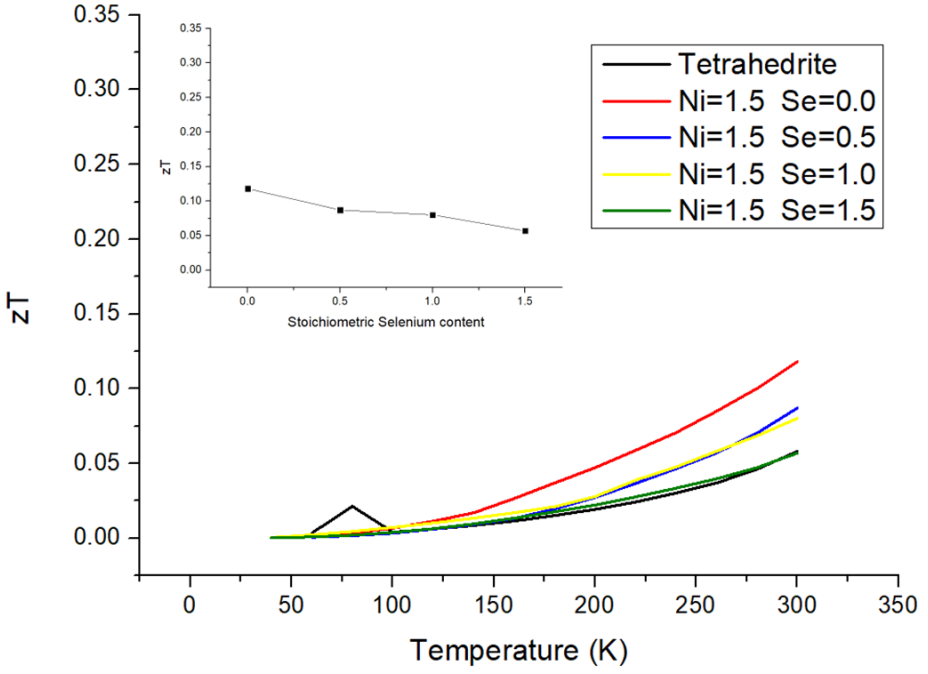

Fig. 216 Temperature dependence of zT of annealed samples following the formula $Cu_{10.5}Ni_{1.5}Sb_4S_{13-y}Se_y$ compared to undoped tetrahedrite ($Cu_{12}Sb_4S_{13}$). In closed, the zT at 300 K shown as a function of stoichiometric Selenium content (y)

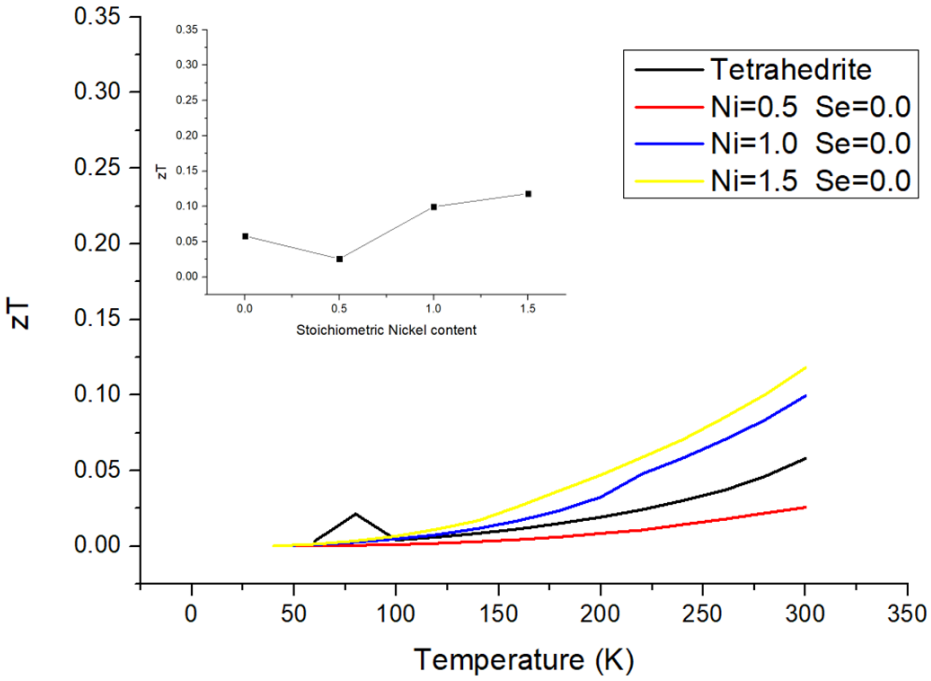

Fig. 217 Temperature dependence of zT of annealed samples following the formula $Cu_{12-x}Ni_xSb_4S_{13}$. In closed, the zT at 300 K shown as a function of stoichiometric Nickel content (x)

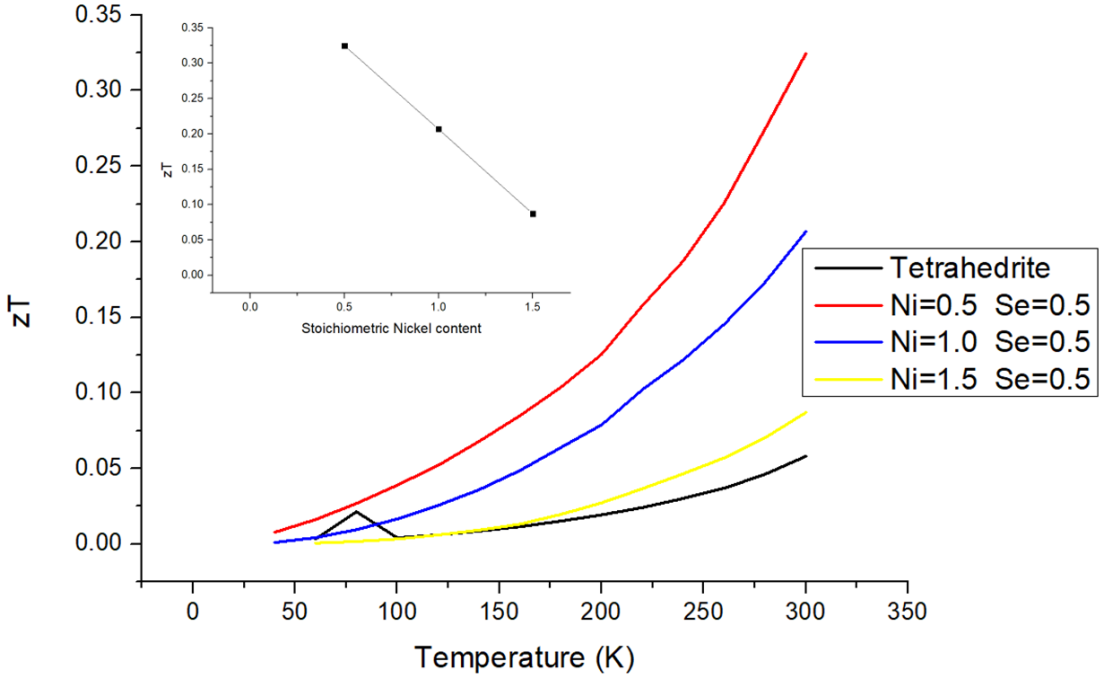

Fig. 218 Temperature dependence of zT of annealed samples following the formula $Cu_{12-x}Ni_xSb_4S_{12.5}Se_{0.5}$ compared to undoped tetrahedrite ($Cu_{12}Sb_4S_{13}$). In closed, the zT at 300 K shown as a function of stoichiometric Nickel content (x)

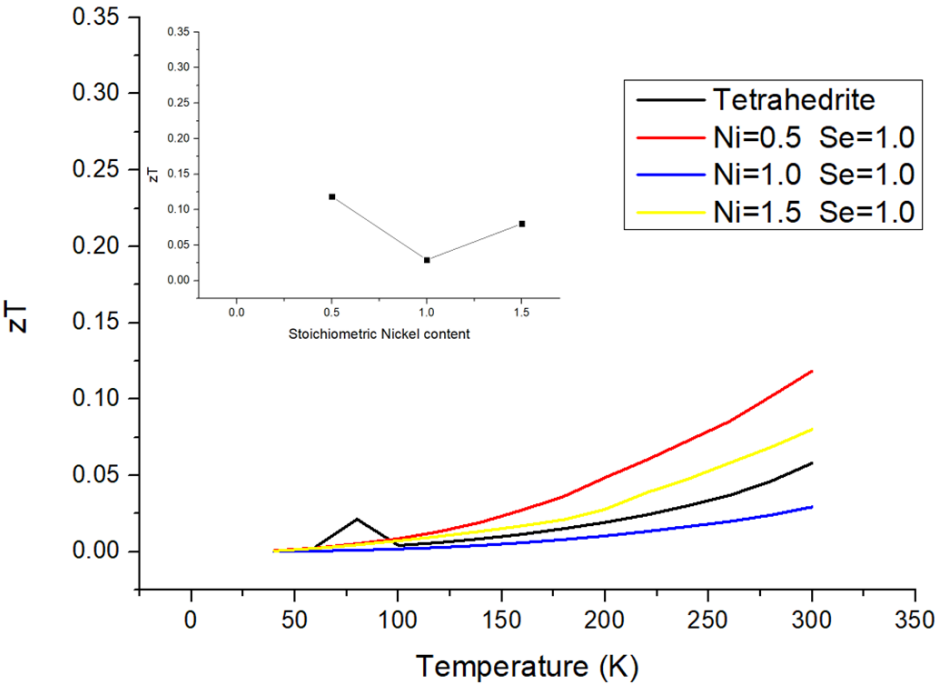

Fig. 219 Temperature dependence of zT of annealed samples following the formula $Cu_{12-x}Ni_xSb_4S_{12}Se$ compared to undoped tetrahedrite ($Cu_{12}Sb_4S_{13}$). In closed, the zT at 300 K shown as a function of stoichiometric Nickel content (x)

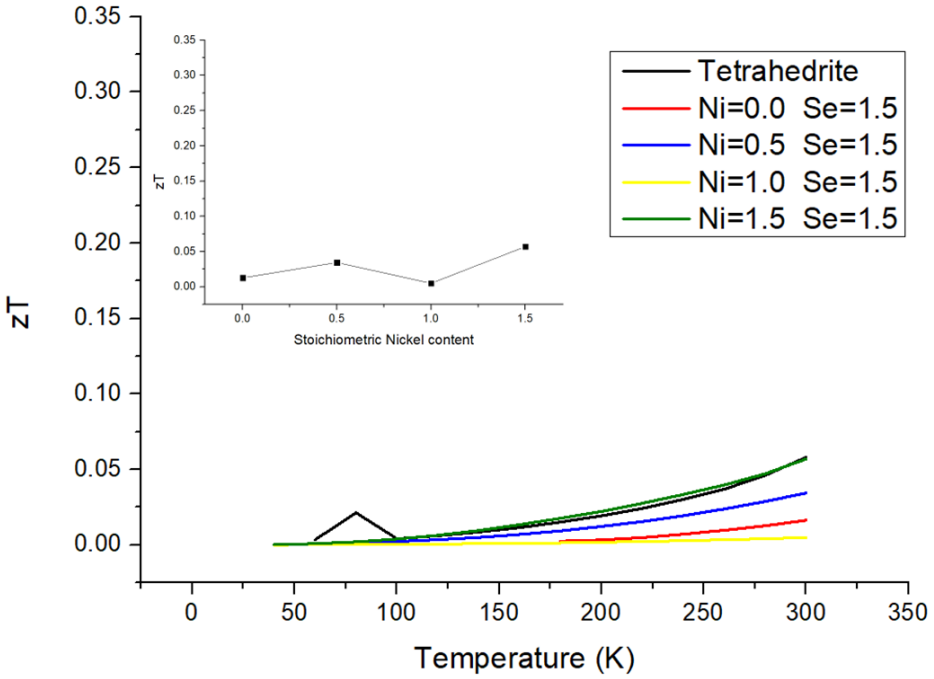

Fig. 220 Temperature dependence of zT of annealed samples following the formula $Cu_{12-x}Ni_xSb_4S_{11.5}Se_{1.5}$ compared to undoped tetrahedrite ($Cu_{12}Sb_4S_{13}$). In closed, the zT at 300 K shown as a function of stoichiometric Nickel content (x)

Hot-pressed samples-Figure of merit

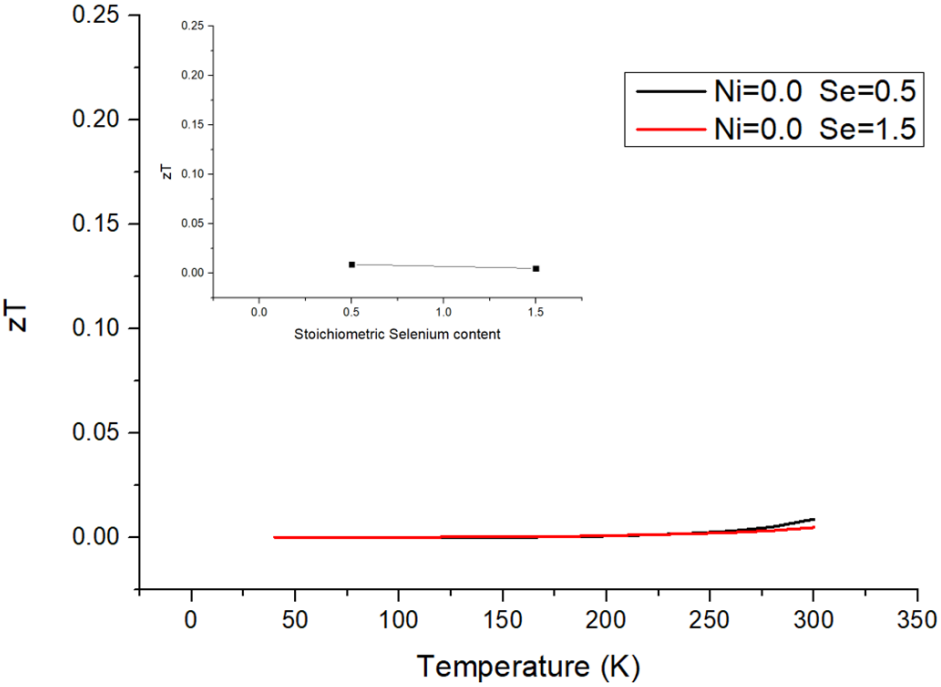

Fig. 221 Temperature dependence of zT of hot-pressed samples following the formula $Cu_{12}Sb_4S_{13-y}Se_y$. In closed, the zT at 300 K shown as a function of stoichiometric Selenium content (y)

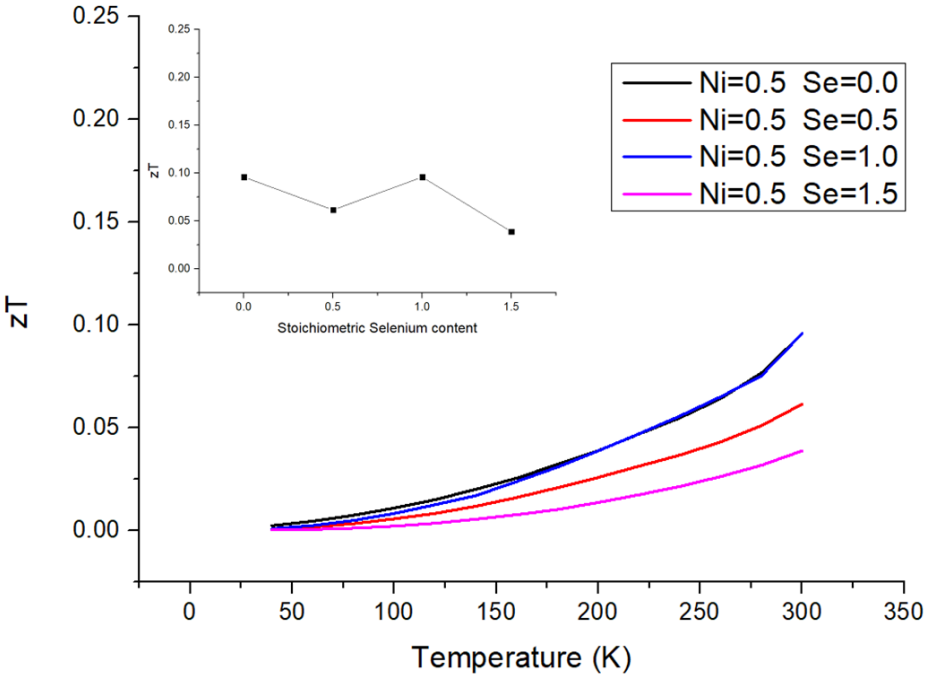

Fig. 222 Temperature dependence of zT of hot-pressed samples following the formula $Cu_{11.5}Ni_{0.5}Sb_4S_{13-y}Se_y$. In closed, the zT at 300 K shown as a function of stoichiometric Selenium content (y)

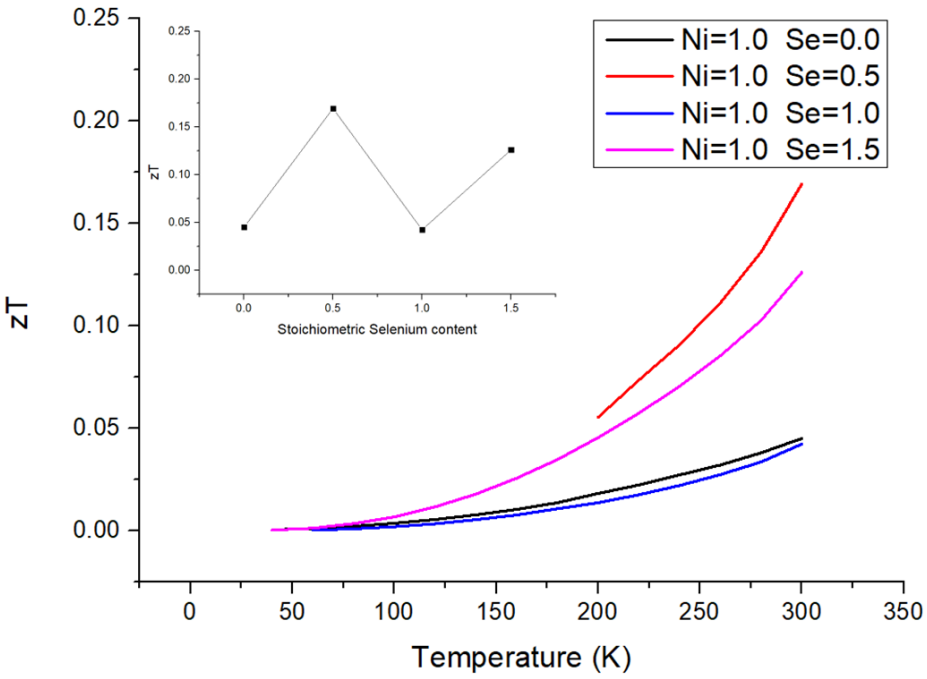

Fig. 223 Temperature dependence of zT of hot-pressed samples following the formula $Cu_{11}NiSb_4S_{13-y}Se_y$. In closed, the zT at 300 K shown as a function of stoichiometric Selenium content (y)

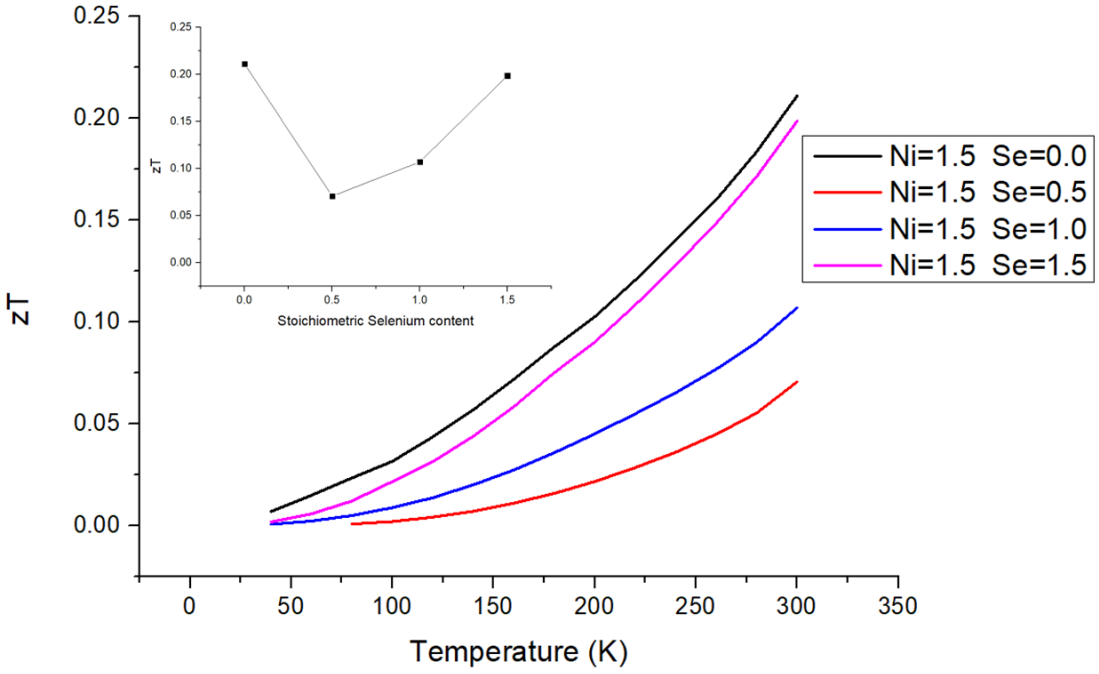

Fig. 224 Temperature dependence of zT of hot-pressed samples following the formula $Cu_{10.5}Ni_{1.5}Sb_4S_{13-y}Se_y$. In closed, the zT at 300 K shown as a function of stoichiometric Selenium content (y)

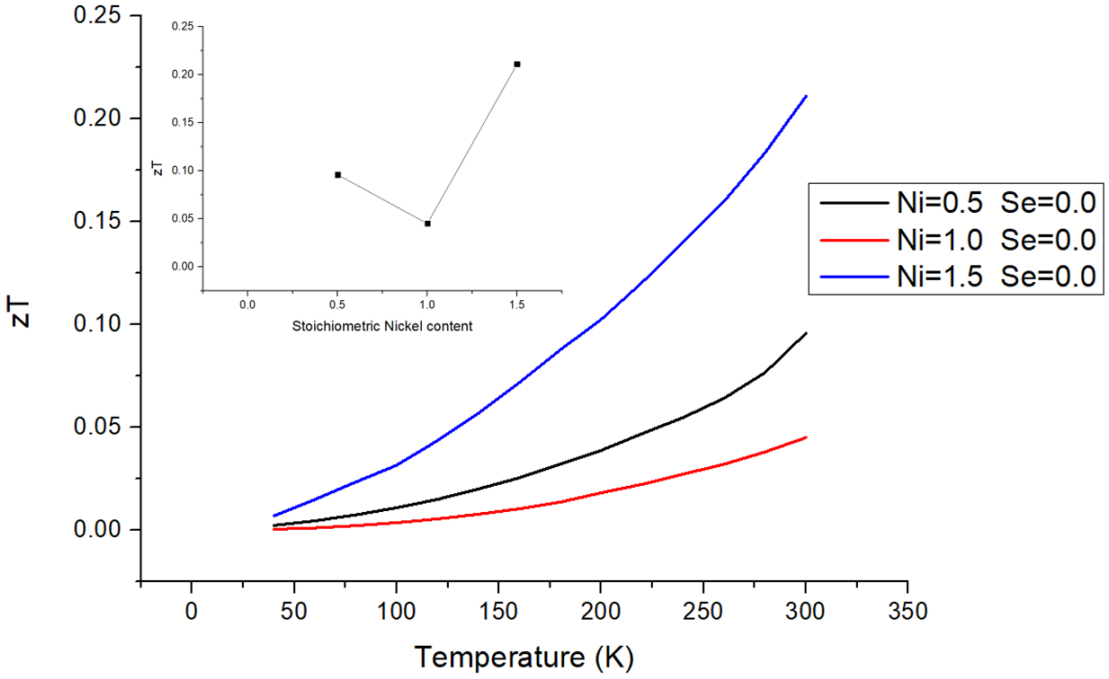

Fig. 225 Temperature dependence of zT of hot-pressed samples following the formula $Cu_{12-x}Ni_xSb_4S_{13}$. In closed, the zT at 300 K shown as a function of stoichiometric Nickel content (x)

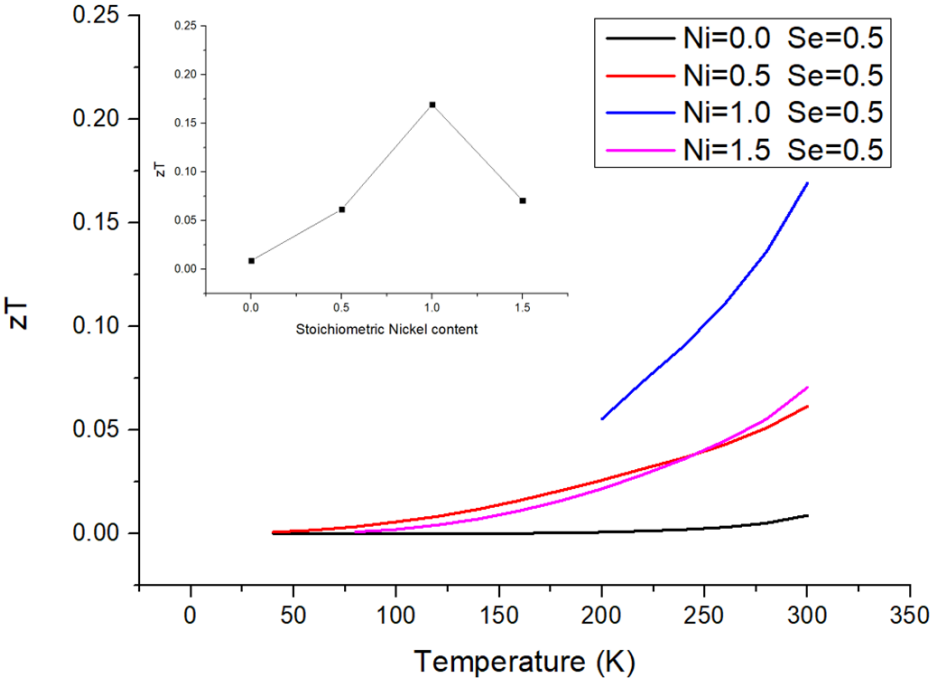

Fig. 226 Temperature dependence of zT of hot-pressed samples following the formula $Cu_{12-x}Ni_xSb_4S_{12.5}Se_{0.5}$. In closed, the zT at 300 K shown as a function of stoichiometric Nickel content (x)

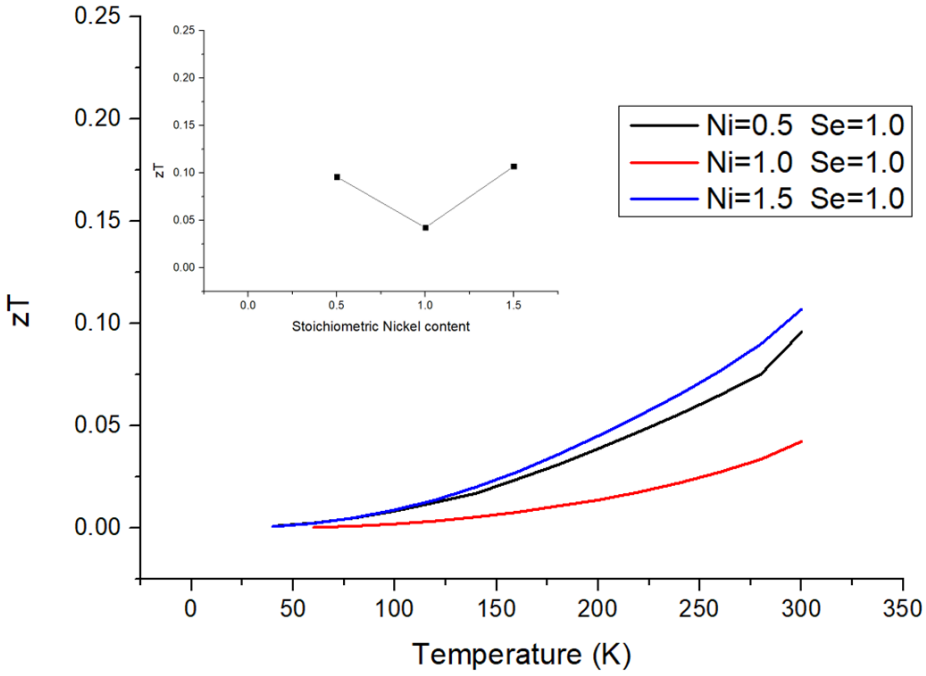

Fig. 227 Temperature dependence of zT of hot-pressed samples following the formula $Cu_{12-x}Ni_xSb_4S_{12}Se$. In closed, the zT at 300 K shown as a function of stoichiometric Nickel content (x)

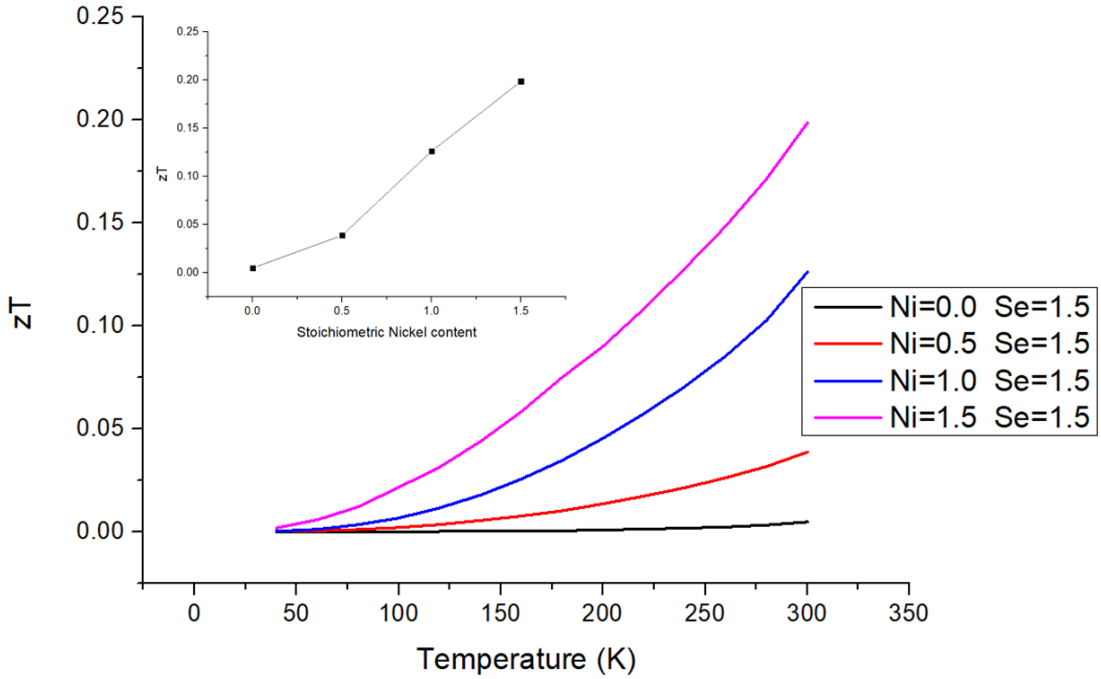

Fig. 228 Temperature dependence of zT of hot-pressed samples following the formula $Cu_{12-x}Ni_xSb_4S_{11.5}Se_{1.5}$. In closed, the zT at 300 K shown as a function of stoichiometric Nickel content (x)

ATTACHMENT 8: WEIGHTED MOBILITY

Annealed samples-Weighted mobility

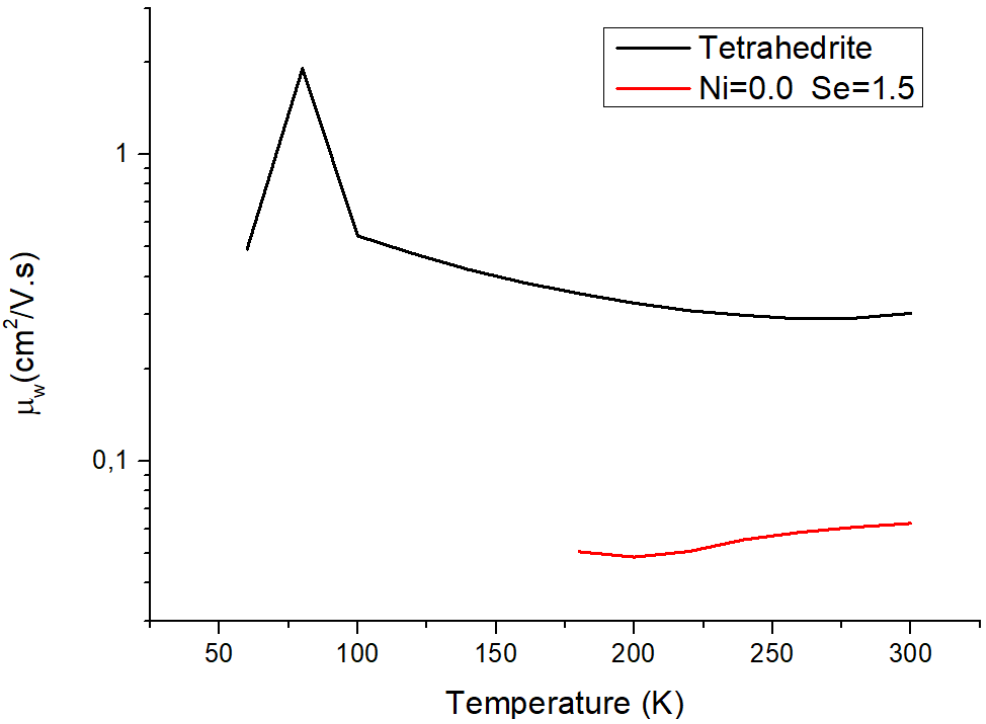

Fig. 229 Temperature dependence of Weighted mobility of annealed samples following the formula $Cu_{12}Sb_4S_{13-y}Se_y$ compared to undoped tetrahedrite ($Cu_{12}Sb_4S_{13}$).

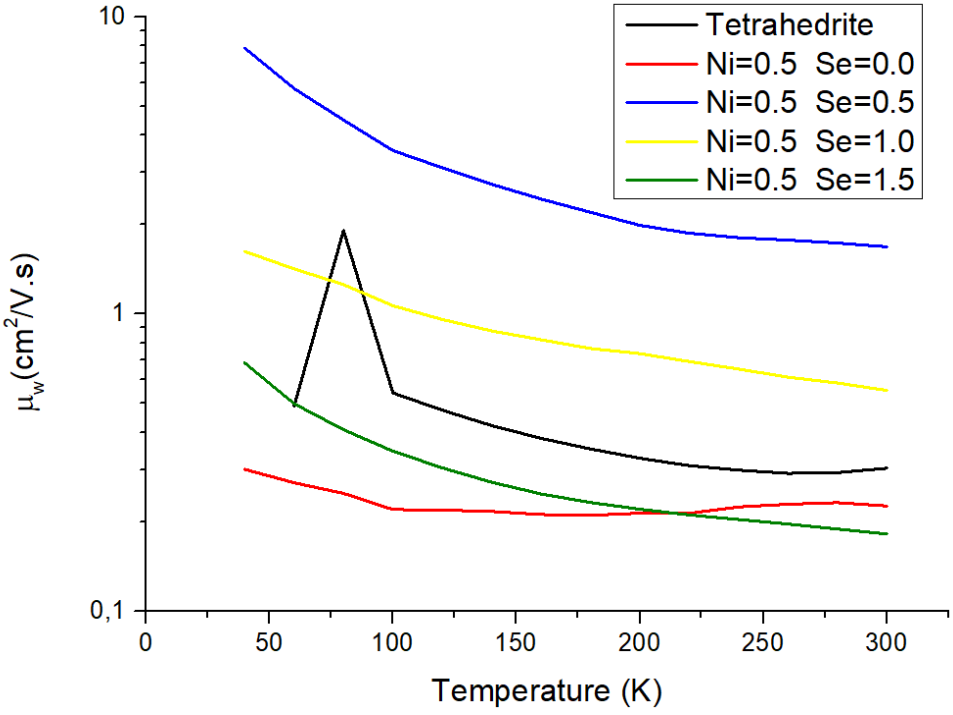

Fig. 230 Temperature dependence of Weighted mobility of annealed samples following the formula $Cu_{11.5}Ni_{0.5}Sb_4S_{13-y}Se_y$ compared to undoped tetrahedrite ($Cu_{12}Sb_4S_{13}$).

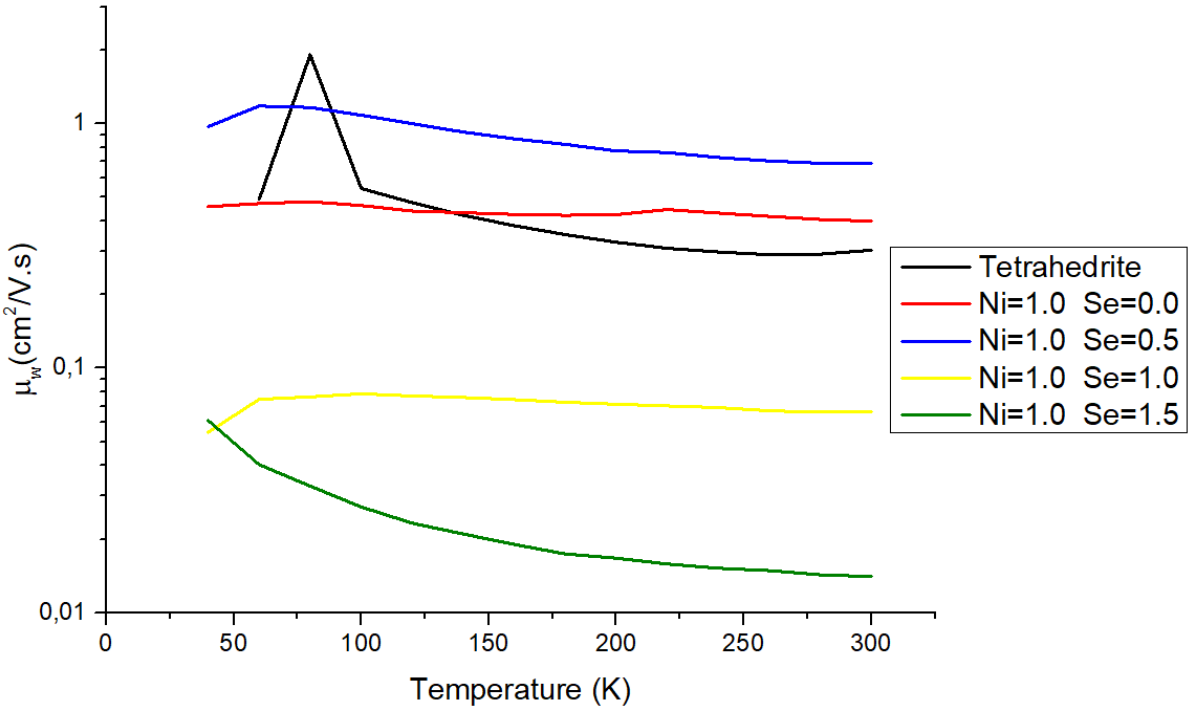

Fig. 231 Temperature dependence of Weighted mobility of annealed samples following the formula $Cu_{11}NiSb_4S_{13-y}Se_y$ compared to undoped tetrahedrite ($Cu_{12}Sb_4S_{13}$).

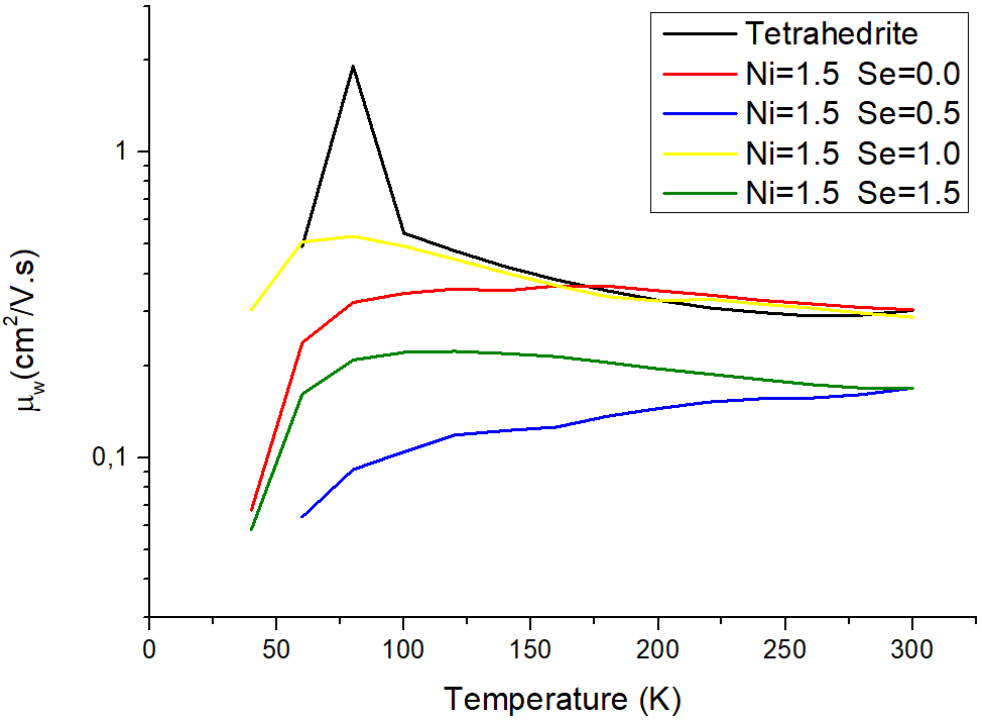

Fig. 232 Temperature dependence of Weighted mobility of annealed samples following the formula $Cu_{10.5}Ni_{1.5}Sb_4S_{13-y}Se_y$ compared to undoped tetrahedrite ($Cu_{12}Sb_4S_{13}$).

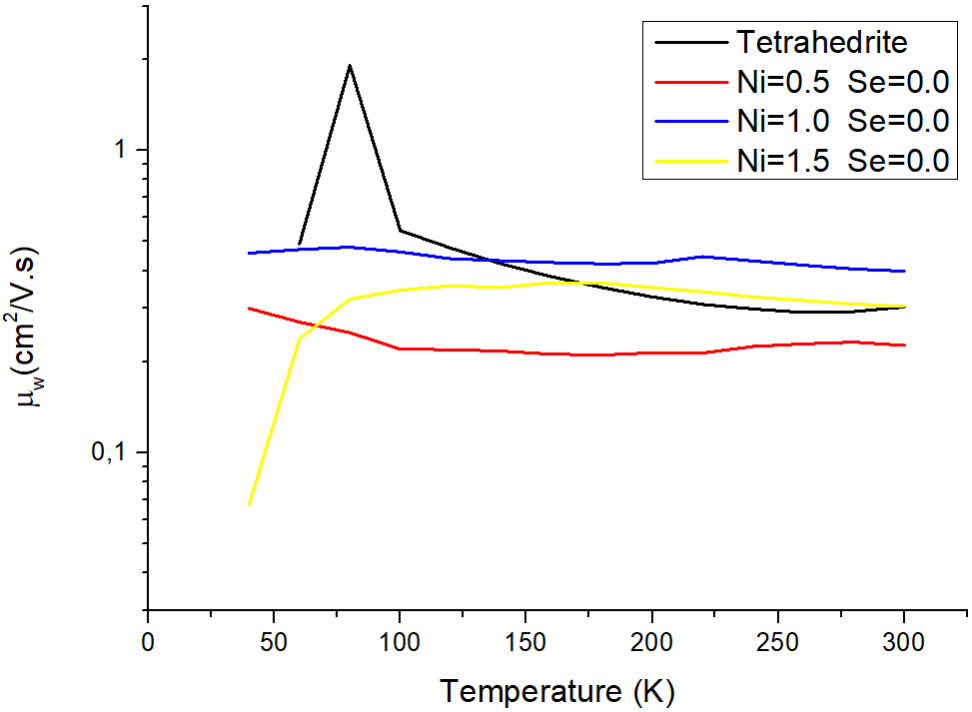

Fig. 233 Temperature dependence of Weighted mobility of annealed samples following the formula $Cu_{12-x}Ni_xSb_4S_{13}$ compared to undoped tetrahedrite ($Cu_{12}Sb_4S_{13}$).

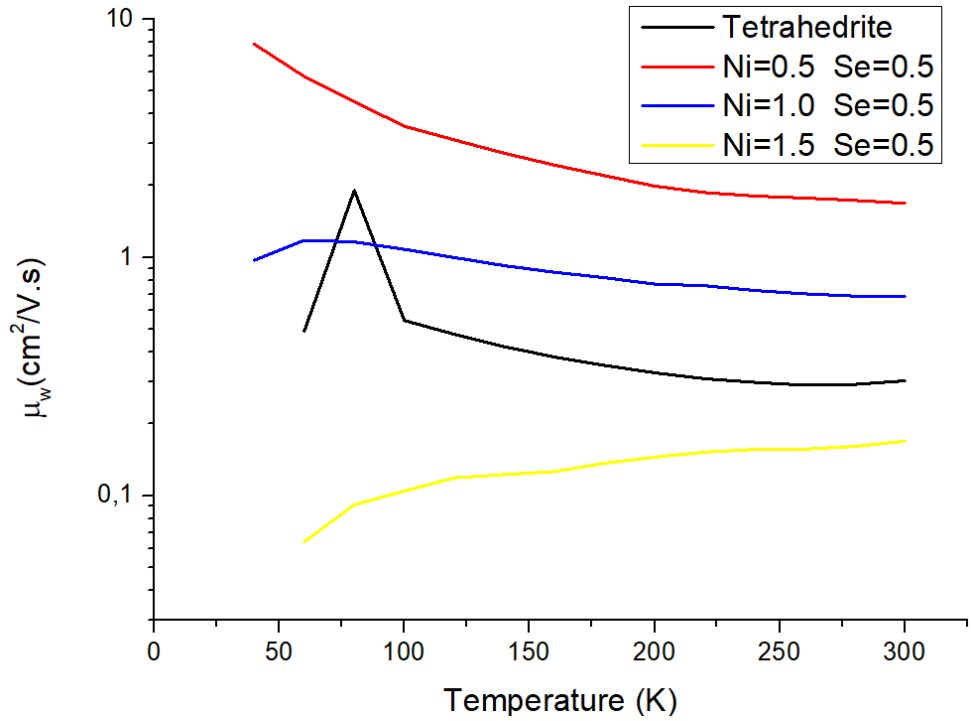

Fig. 234 Temperature dependence of Weighted mobility of annealed samples following the formula $Cu_{12-x}Ni_xSb_4S_{12.5}Se_{0.5}$ compared to undoped tetrahedrite ($Cu_{12}Sb_4S_{13}$).

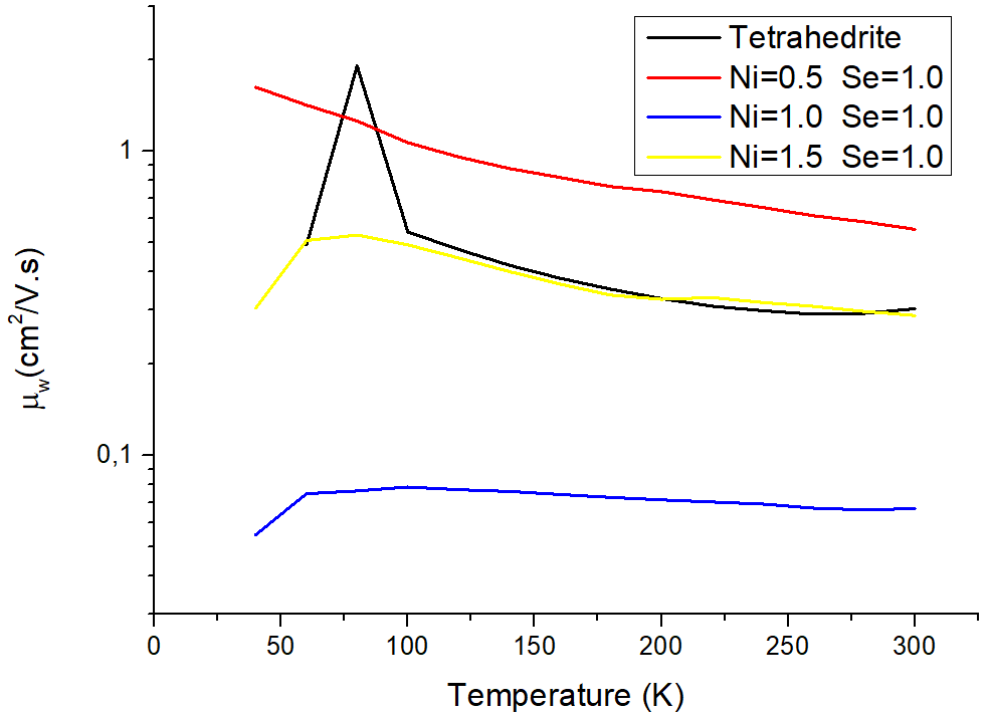

Fig. 235 Temperature dependence of Weighted mobility of annealed samples following the formula $Cu_{12-x}Ni_xSb_4S_{12}Se$.

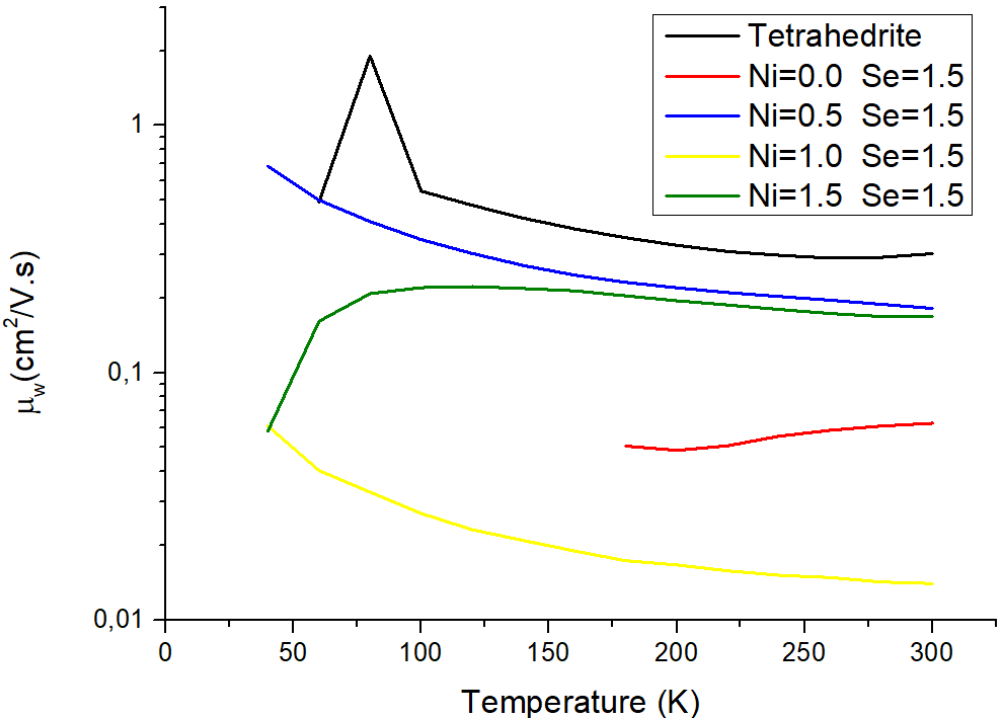

Fig. 236 Temperature dependence of Weighted mobility of annealed samples following the formula $Cu_{12-x}Ni_xSb_4S_{11.5}Se_{1.5}$ compared to undoped tetrahedrite ($Cu_{12}Sb_4S_{13}$).

Hot-pressed samples- Weighted mobility

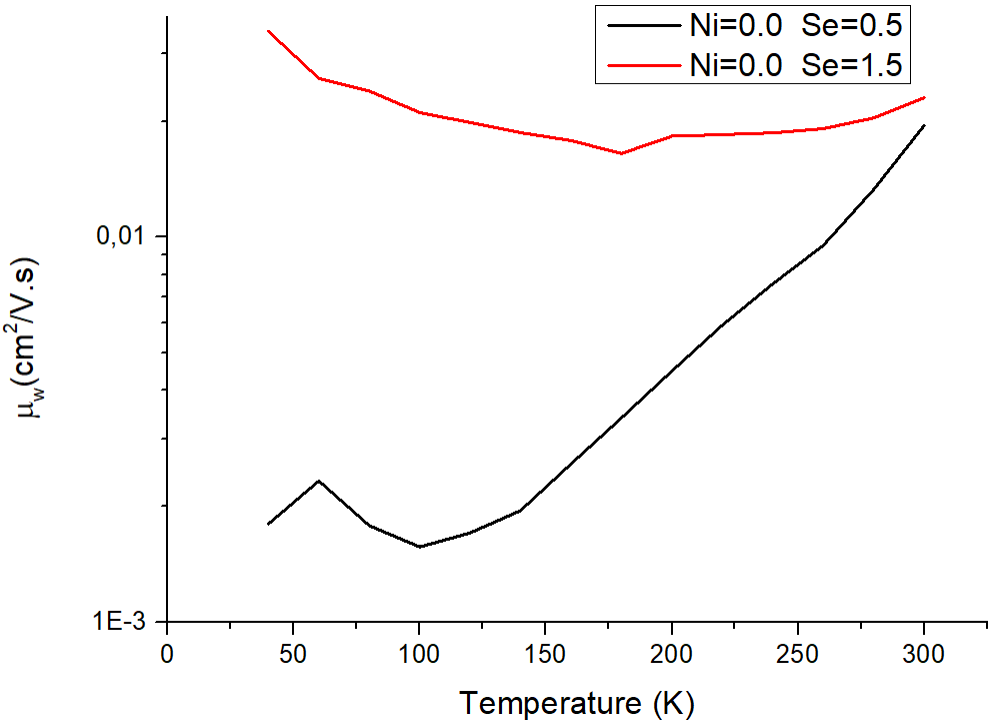

Fig. 237 Temperature dependence of Weighted mobility of hot-pressed samples following the formula $Cu_{12}Sb_4S_{13-y}Se_y$.

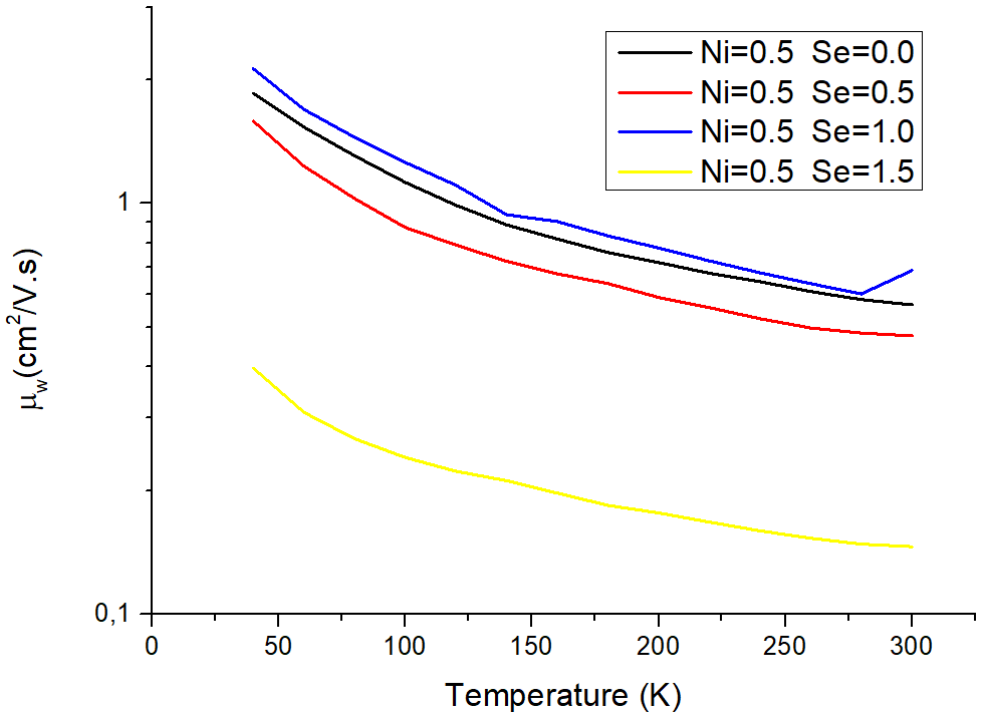

Fig. 238 Temperature dependence of Weighted mobility of hot-pressed samples following the formula $Cu_{11.5}Ni_{0.5}Sb_4S_{13-y}Se_y$.

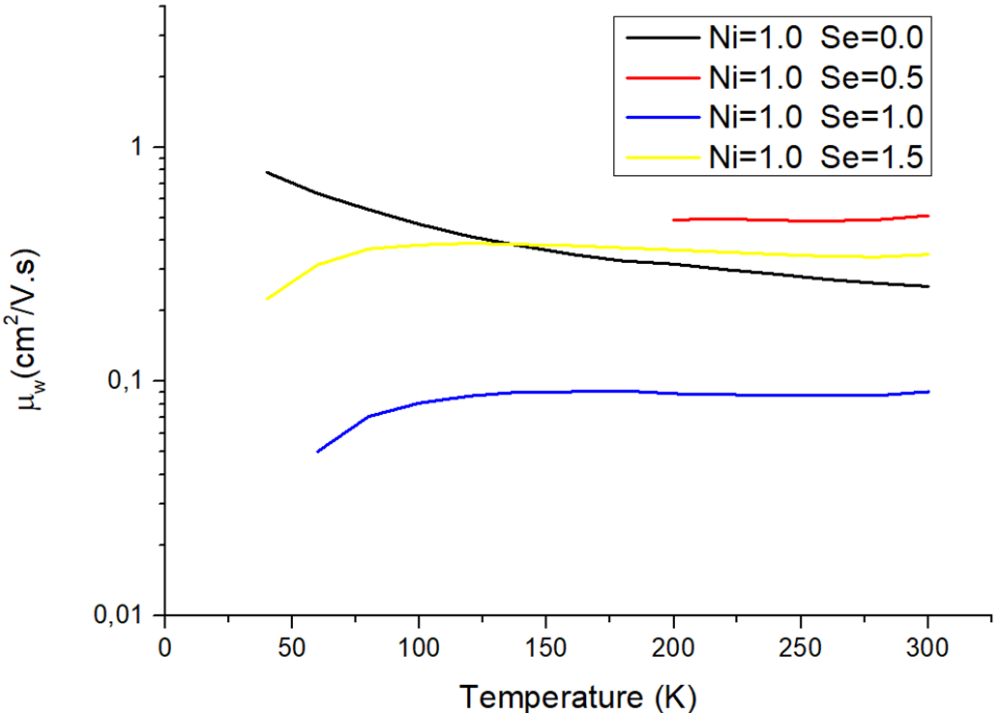

Fig. 239 Temperature dependence of Weighted mobility of hot-pressed samples following the formula $Cu_{11}NiSb_4S_{13-y}Se_y$.

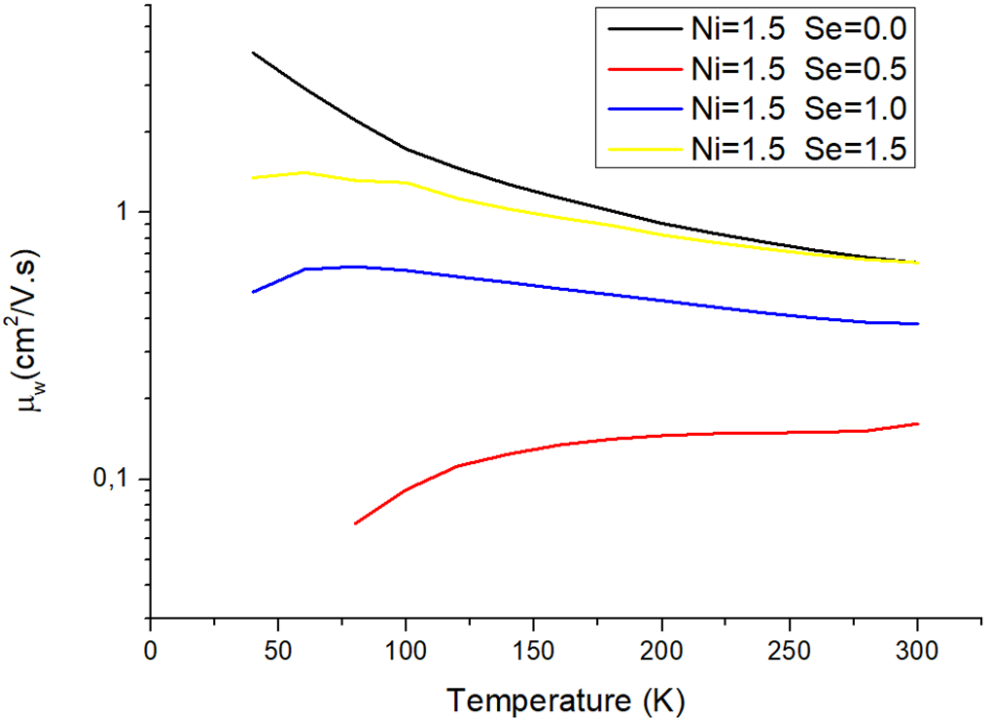

Fig. 240 Temperature dependence of Weighted mobility of hot-pressed samples following the formula $Cu_{10.5}Ni_{1.5}Sb_4S_{13-y}Se_y$.

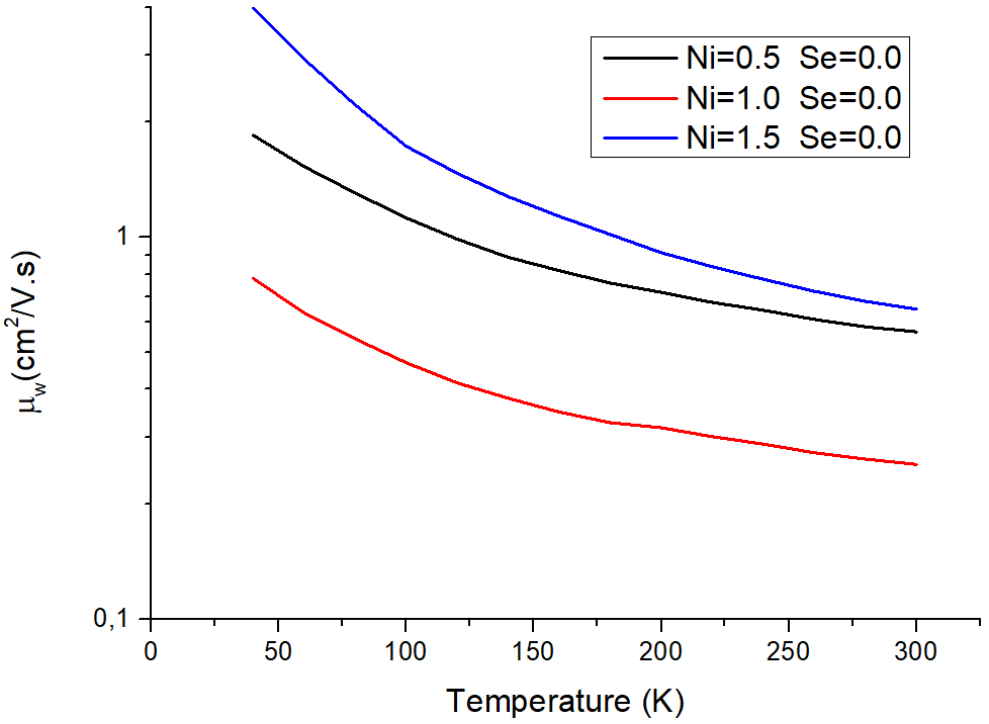

Fig. 241 Temperature dependence of Weighted mobility of hot-pressed samples following the formula $Cu_{12-x}Ni_xSb_4S_{13}$.

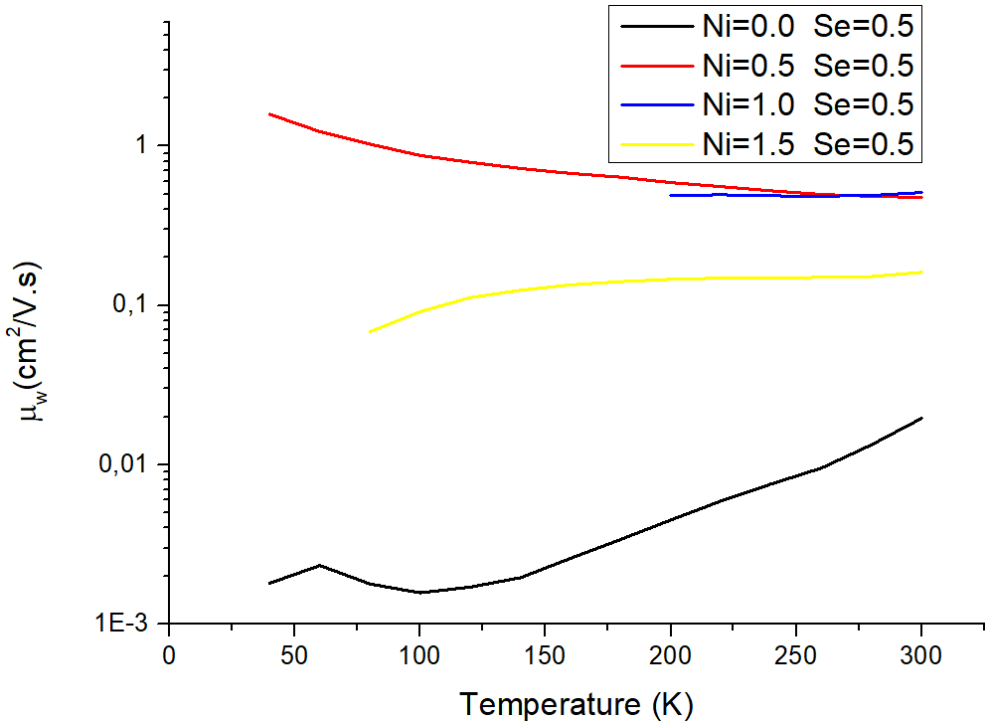

Fig. 242 Temperature dependence of Weighted mobility of hot-pressed samples following the formula $Cu_{12-x}Ni_xSb_4S_{12.5}Se_{0.5}$.

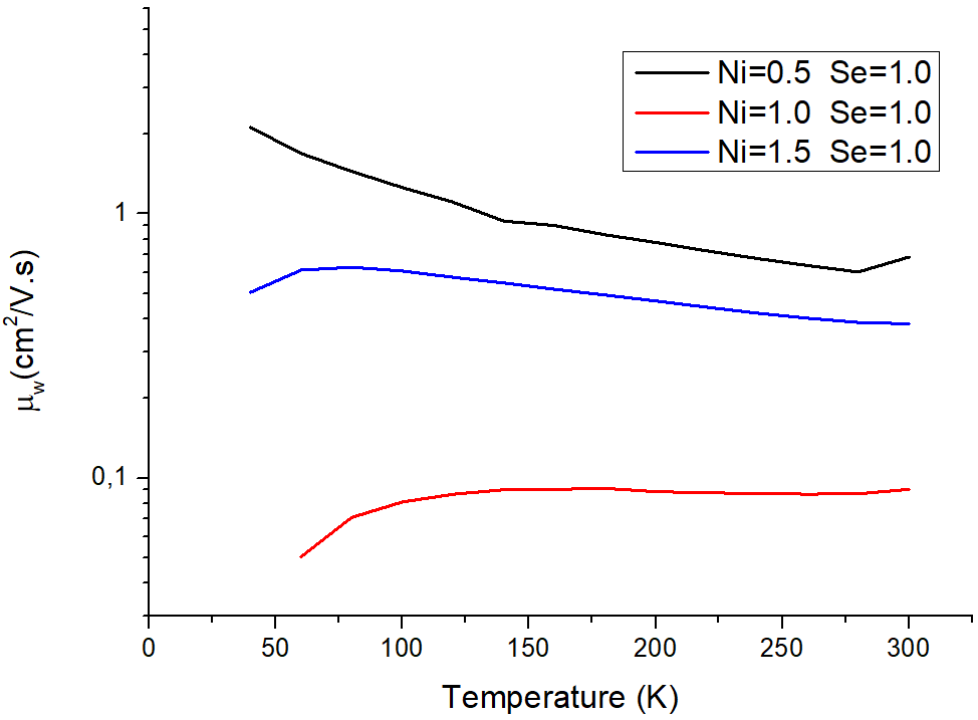

Fig. 243 Temperature dependence of Weighted mobility of hot-pressed samples following the formula $Cu_{12-x}Ni_xSb_4S_{12}Se$.

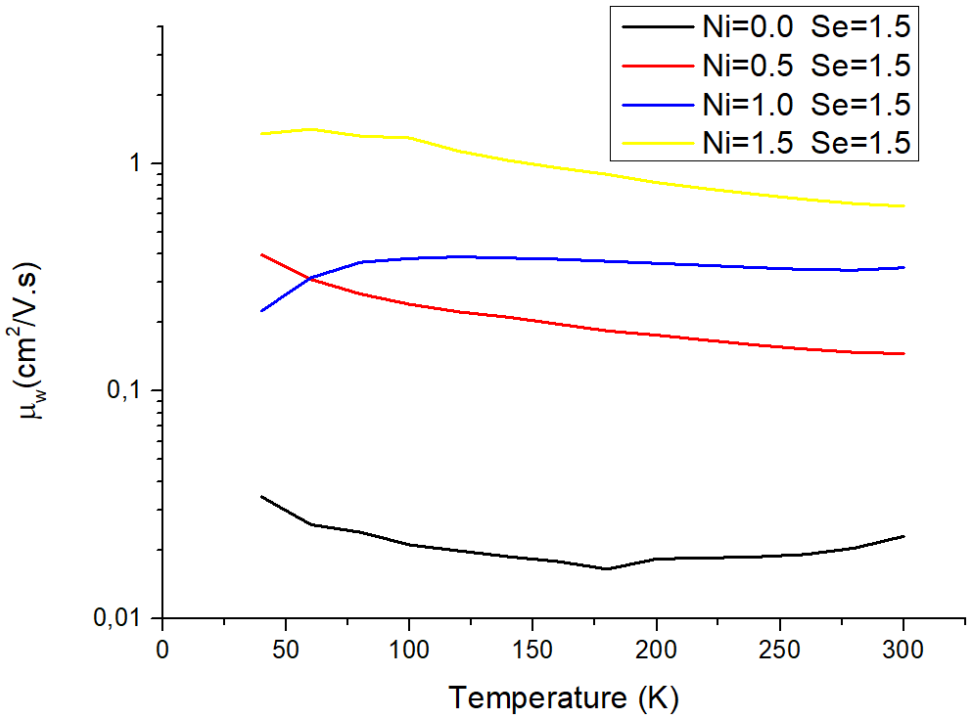

Fig. 244 Temperature dependence of Weighted mobility of hot-pressed samples following the formula $Cu_{12-x}Ni_xSb_4S_{11.5}Se_{1.5}$.